An investigation of the magnetic field of full flux penetration of superconducting materials for radio-frequency cavities

Daniel Andrew Turner, MSc, BSc (Hons)
Department of Engineering
Lancaster University

A thesis submitted for the degree of
Doctor of Philosophy

June 2026

I dedicate this thesis to my parents.

Declaration

I declare that the work presented in this thesis is, to the best of my knowledge and belief, original and my own work. The material has not been submitted, either in whole or in part, for a degree at this, or any other university. This thesis does not exceed the maximum permitted word length of 80,000 words including appendices and footnotes, but excluding the bibliography. A rough estimate of the word count is: 62436

_____

Daniel Andrew Turner

An investigation of the magnetic field of full flux penetration of superconducting materials for radio-frequency cavities

Daniel Andrew Turner, MSc, BSc (Hons).
Department of Engineering, Lancaster University
A thesis submitted for the degree of *Doctor of Philosophy*. October, 2024

Abstract

The material of choice for current SRF accelerators is bulk Nb which is reaching the theoretical limits in terms of maximum accelerating gradient, E_{acc}. To increase E_{acc}, the magnetic field, B, on the accelerating cavity wall, B_{surf}, must be increased. There are multiple methods to increase B_{surf} such as new, novel materials. One method to increase E_{acc} is to use multilayer structures, which consist of superconducting thin films (smaller than the London penetration depth) on the surface that screens B_{surf}, such that the superconducting substrate will see a reduced B than on the surface. The increased B_{surf} results in a larger E_{acc}, whilst the bulk substrate is still witness to the same B.

As the RF performance is related to B, it is appropriate to investigate the response of a superconductor to an external magnetic field. Whilst commercial magnetometry exists, it consists of limitations. These include flux enhancements, sample alignment, and B penetrating through insulating layers of multilayer structures such that the screening effect will not be observed. These limitations can be mitigated, such as using sample geometries with will known geometries such as ellipsoids. Multilayer structures are difficult to deposit in a 3D geometry, thus a magnetometry system must be designed to be able to accommodate planar multilayer samples by applying B from one side of the sample to the other.

A field penetration facility has been designed, built and commissioned at Daresbury laboratory. A DC field is applied from one side of the sample using a C-shaped dipole magnet, similar to that of an RF cavity. Hall probes measure both the applied and the penetrated field. The system underwent a rigorous commissioning process which indicated the system has a random error of 0.9 %. The facility has then been used to investigate new materials for SRF applications.

Publications

Two publications, shown below, have been created directly from the thesis, from which large portions of this published work is used within chapters 3 and 4 respectively:

D. A. Turner, G. Burt, and T. Junginger, "No interface energy barrier and increased surface pinning in low temperature baked niobium," *Scientific reports*, vol. 12, no. 1, pp. 1–9, 2022

D. A. Turner, O. B. Malyshev, G. Burt, *et al.*, "A facility for the characterisation of planar multilayer structures with preliminary niobium results," *Superconductor Science and Technology*, vol. 35, no. 9, p. 095 004, 2022

D. A. Turner, O. B. Malyshev, G. Burt, *et al.*, "Investigating the superconducting properties and surface morphology of sputtered Nb films on Cu due to laser treatment," *IEEE Transactions on Applied Superconductivity*, vol. 33, no. 4, pp. 1–12, 2023. DOI: 10.1109/TASC.2023.3243459

The following proceedings have been generated while developing the thesis, which are either wholly the authors own work, or that which the author contributed to:

D. Turner, O. Malyshev, G. Burt, *et al.*, "Characterization of flat multilayer thin film superconductors," in *Proc. SRF 2019*, 2019

R. Valizadeh, A. Hannah, S. Aliasghari, *et al.*, "PVD depostion of Nb3Sn thin film on copper substrate from an alloy Nb3Sn target," *Proc. IPAC'19*, pp. 2818–2821, 2019

The following reports have been generated while developing this thesis:

O. Malyshev, R. Valizadeh, D. Turner, *et al.*, "Final report on thin film technology, ARIES delivery report D15.4," *Horizon 2020 Research Infrastructures*, 2021. [Online]. Available: available%20at:%20https://edms.cern.ch/document/1820620/1.0 (visited on 03/14/2022)

Acknowledgements

Throughout my time performing the work presented within this thesis, I have worked and had the pleasure of meeting a number of people who deserve acknowledgement of the effect they had.

First and foremost, I would like to thank Dr. Tobias Junginger for not only giving me the opportunity to perform this research, but also for the continued supervision from afar. I would like to express my gratitude to Professor Graeme Burt for taking over the mantle and for the excellent supervision ever since. Similarly, the supervision of Dr. Oleg Malyshev must also be acknowledged, who always had me thinking from another perspective and driving the laboratory work forward. I cannot express my gratitude enough to the three named above. Their continued supervision, guidance, imparted knowledge and passion have moulded me into the researcher I am today.

Next, I would like to thank the staff and students from Daresbury laboratory who made the experience what it was. Special mentions go to Dr. Taaj Sian and Daniel Seal for making the experience all the more enjoyable; from Tuesday coffee mornings (remote or in person) and the fruitful discussions. Additionally to Dr. Reza Valizadeh for producing samples and Liam Smith for the aid in maintaining and running the facility. I would also like to acknowledge Stephen Bibby-Trevor for all the work he performed, especially the machining of the facility.

I would like to express my thanks to Dr. Alick Macpherson for the support in finishing whilst working alongside him. The support over the final hours are greatly appreciated.

I would like to thank the friends and colleagues I met at CERN, with special thanks to Daniel Flailing and Stephanie Kwan. Without your addition I would have not 'touched grass' or explored the area half as much as we have.

I would like to thank the friend group from University of Central Lancashire. You made the course all the more enjoyable, and it is fair to say that without you I would not have started on this career path. So thank you for being there over the years, and making sure I enjoy the time away from work.

I would like to thank my parents, family and in-laws, who helped in any way they could, making the whole process that bit easier.

And finally, I would like to thank Amy. From being there to vent after a bad day, to accompanying me on work trips. Without you, none of this would have been possible, who has encouraged and believed in me from the very start. I cannot express my gratitude enough.

It is not the strength of the body,
but the strength of the spirit.

J.R.R. Tolkien

Ever tried. Ever failed. No matter.
Try Again. Fail again. Fail better.

Samuel Beckett

Contents

List of Figures

List of Tables

Chapter 1

Introduction

1.1 Particle accelerators

Particle accelerators are machines that use large electromagnetic fields to accelerate charged particles such as electrons, protons or ions. The first particle accelerators used electrostatic fields, while modern day particle accelerators use alternating electromagnetic fields in the form of radio-frequency waves. The swap from static fields to oscillating fields was to avoid voltage breakdown and also to reduce the size of the accelerators. More than 30,000 accelerators currently exist around the world with only 1 % being used for research purposes [7] such as the Large Hadron Collider at CERN, Switzerland, and the SuperKEKB at KEK in Japan. The other 99 % of accelerators are used in energy, health, industry and security applications [7].

1.1.1 Types of particle accelerator

There are 2 main types of particle accelerators, circular accelerators and linear accelerators (Linacs). The bunches of charged particles pass through the accelerating structures (cavities) multiple times in circular accelerators, accelerating on each pass of the cavities. Circular accelerators produce high energy particles without having to be extremely long, as the bunches will pass through the accelerating cavities multiple times, such that less accelerating cavities are required when compared to a linear accelerator whilst reaching the same final velocity. Circular accelerators also provide multiple places where beams can cross to create collisions, and the beam does not have top be dumped after each use as it can be re-used.

The beam in circular accelerators are directed using a magnetic field, which is the limiting factor for circular accelerators. For heavy charged particles such as protons, the magnitude of the magnetic field to bend the beam is the limiting factor for a set size. To increase the energy of the protons, the bend radius of the accelerator needs

to be increased to ensure the particles can be kept within the accelerator. On the other hand, electrons are ≈ 1000 times lighter than protons, and thus require a much smaller magnetic field to bend the beam. As the electrons travel in a circular path they emit synchrotron radiation, which limits the maximum energy of the electrons. This is the case for all charged particles in a magnetic field, however it is not the limiting factor for particles with a larger mass. To increase the energy of the beam requires either stronger magnets to reduce the beam path (which is limited by the strength of the magnets), reducing the diameter of a circular accelerator, or increasing the radii of a circular accelerator. Both of these options increase the capital cost.

Linear accelerators (Linac) only allow the beam to pass through the each of the accelerating structures once [8]. If a sufficient accelerating gradient (E_{acc}) can be produced, Linacs can have a cheaper capital cost than circular accelerators [7] as they are much smaller in size and require less infrastructure such as tunnels and buildings to house the accelerator. Additionally, linacs do not require the large magnets to direct the beam into a circular path.

In a Linac, the bunches only see the accelerating structures once, as the accelerator is not a closed loop. Hence, more RF power is required to accelerate the bunches to a similar energy. Thus, Linacs require to be extremely long for the beam to reach energies comparable to that of circular accelerators, and have a high cost per MeV of acceleration, such that it is more expensive to accelerate hadrons at relativistic energies [8]. Circular accelerators allow the beam to be re-used, as the bunches pass through the accelerating structures multiple times. Increasing the maximum E_{acc} of an accelerating structure can reduce the cost per MeV of acceleration, whilst reducing the total length of the accelerator and therefore the capital cost.

1.2 Accelerating cavities

1.2.1 Normal conducting cavities

Accelerating cavities are the key components to accelerate charged particles within the beam. Modern particle accelerators use radio frequency (RF) as the method of acceleration. There are numerous modes of operation, such as short pulse, long pulse ($>10\,\mu s$) [9], and continuous wave.

Copper is the most common material to make normal conducting cavities due having low electrical resistance and high thermal conductivity for removing heat from the cavity surface, produced by the RF power also accelerating the charge carriers in the surface layer of the cavity. For cavities that use RF in short pulses ($<1\,\mu s$), the accelerating gradient can be as high as $100\,MV\,m^{-1}$ ($\approx 200\,ns$ pulse) [9]. Normal conducting cavities that are required to run a large accelerating gradient can only be used with a low duty factor, $< 0.1\,\%$. Copper cavities can run in a continuous

wave/long pulse mode, however the maximum accelerating gradient is limited to $\approx$1 MV m^{-1} [9]. This is due to the average RF heating on the cavity surface. The heated cavity surface can lead to vacuum degradation and stresses [9], which then lead to the cavity detuning due to the thermal expansion, which can change the resonant frequency of the cavity. Thus, it is uneconomical to run a normal conducting cavity at a high gradient for long time periods.

1.2.2 Superconductivity

Superconductivity was discovered early in the 20$^{\text{th}}$ century, and was aptly named due to the abrupt disappearance in electrical resistance when cooled below the transition temperature (T_c) of the material [10]. It was found 20 years later that superconductors do not actually display perfect conductivity, as an externally applied magnetic field is expelled from the superconductor when cooled below T_c. The initial discovery of superconductors was found for elements with low T_c values, however in recent years more materials have been found with higher T_c values, up to 134 K for cuprates, known as high temperature superconductors (HTS)[11], which further expanded the possibilities of the applications in which superconductors could be used. Due to the absence of DC resistance and the ability to carry large currents with a low voltage, superconductors became the perfect materials for high field magnets as the cost of cooling becomes cheaper than the Cu counter parts [11]. The most common use of superconductors is magnetic resonance imaging (MRI) and nuclear magnetic resonance (NMR) in medical applications [11]. Both of these applications use NbTi, which is a has a low T_c.

1.2.2.1 Superconducting cavities

One main advantage of superconducting radio-frequency (SRF) cavities is that (even considering the cryogenic plant) the operating cost (and therefore energy consumption) is much lower than for normal conducting cavities [8] for high duty cycle applications, which is key in the modern day drive to be environmentally friendly. For high power machines with a high duty cycle, the energy argument becomes more important [8], especially if the machine is required to be efficient.

If a particle accelerator requires an accelerating gradient of a few MV m^{-1} whilst operating in either the long pulse or continuous wave modes, superconducting cavities excel over normal conducting cavities [9]. The surface resistance (R_{surf}) of SRF cavities is magnitudes of orders lower than that of Cu cavities. The performance of SRF cavities is determined by the quality factor (Q_0) of a cavity, which is the ratio of the stored energy within the cavity to the power dissipated in the cavity walls per RF cycle [12]. Because R_{surf} is much lower for SRF cavities than Cu cavities, Q_0 is much greater, $\approx 10^9$-10^{10} range [12] compared to 10^4 range [13] for normal conducting

cavities. The reduction in resistance also decreases the amount of heating generated within the cavity, making the cavity more efficient as more of the RF is applied to accelerating the beam rather than a fraction of the RF being deposited in the cavity wall, generating heat. The beam apertures are also larger in superconducting cavities, which cause less disturbance on the beam as it passes through. Additionally, as the apertures are larger, there is no concern with an increased shunt impedance.

However, SRF cavities have their limitations. The large EM fields required for acceleration produce a parallel magnetic field across the cavity surface (in the TM_{010} mode) known as B_{surf}. Whilst superconductors expel the magnetic field (B) in the Meissner state, if B_{surf} becomes too large, the B enters the cavity and produces losses. Additionally, SRF cavities do not perform up to their theoretical limits as B enters at a value lower than theoretical, therefore reducing the Q_0 of the cavities. Many techniques have been implemented to mitigate the reduction in Q_0 for large B such as polishing [12] and performing baking techniques [14], [15], which have in turn increased the performance of Nb cavities close to the theoretical limits. Thus, to increase E_{acc} of SRF cavities new materials must be utilised to aid or replace Nb cavities.

1.2.2.2 Multilayer structures

One theory to increase the maximum E_{acc} is to use multilayer structures, proposed by Gurevich [16]. A multilayer structure consists of a bulk superconducting substrate, such as Nb, with superconducting thin films (smaller than the London penetration depth, λ_L) on the surface. There are two types of multilayers; superconducting-insulating-superconducting structures named SIS structures, and superconducting-superconducting structures, known as SS bi-layers. Thin films smaller than λ_L are 'magnetically transparent', such that normal conducting regions cannot be created within the film, allowing the thin films to remain in the superconducting state to much higher applied parallel B. The B passing through the thin film decays such that the bulk superconducting substrate is witness to a smaller B than on the surface of the structure.

It was long thought that low temperature baking (LTB) techniques affected the surface layers of the cavity and produced a similar structure to a SS bi-layer, as LTB was found to remove the high field Q slope (HFQS). However, through this work it has been determined that LTB techniques do not produce an increase in the field of first vortex penetration (B_{vp}) [1], whilst other bi-layers consisting of distinct, separate layers have also been investigated such as MgB_2 on Nb [17] which showed an increase in B_{vp} in a superconducting quantum interference device (SQUID) magnetometer, and Nb_3Sn which showed an increase in muon spin rotation (μSR) [18].

1.3 Magnetometry techniques

To determine if materials are suitable to be used for RF cavities, the quality of the superconductor must first be investigated. Whilst full cavities can be produced, they are expensive and take a long time to fabricate and test. It is beneficial to test small samples for deposition parameter optimisation; to increase the speed and decrease the cost of fabrication. Many commercial magnetometry facilities have been built with the premise to test and measure small superconducting samples. The most notable commercial magnetometer is a SQUID magnetometer, which can also run in a vibrating sample magnetometer (VSM) configuration. Both systems use a similar set up, measuring the induced EMF from a pick up coil due to the response of the sample. The main difference between the systems is that a SQUID magnetometer measures a voltage though a Josephson junction. The Josephson junction allows the measurement of small voltages, corresponding to a B, allowing the SQUID magnetometer to measure the magnetic moment down to $< 8 \times 10^{-8}$ emu [19].

However, commercial magnetometry is not built with thin film superconductors in mind, and consequently some disadvantages are present when testing thin films. For example, the sample is placed in the centre of a solenoid such that the applied magnetic field (B_{app}) is uniform over the sample. This requires the sample to be placed perfectly vertical to ensure the superconducting surface is parallel to B_{app}. If the sample is not perfectly parallel, the B_{app} will produce a normal component on the surface and enter the sample at a much lower magnetic field than expected. The field at which the B_{app} enters the sample is known as the field of first flux penetration (B_{vp}). More limitations produced by testing superconducting thin films using commercial magnetometry consist of:

- The B_{app} is over the whole sample, such that B is applied to both faces of a SC (assuming a parallel B_{app} set up). If a sample has been deposited, B may enter the superconductor (SC) from the surface in contact with the substrate - i.e. not the face which would witness the RF in a SRF cavity, and produce a B_{vp} lower than expected.
- If the superconductor is not directly in the centre of the pickup coils (such as slightly to one side) the measurements can be distorted.
- If the sample shape consists of edges (such as most samples that have been cut from a larger sample) flux enhancements with an unknown demagnetization factor can be present. Thus, B_{vp} is lower than the true value, which cannot be accounted for using a demagnetisation factor.
- If the sample is not perfectly parallel with the magnetic field, a normal component will be present on the surface of the SC which will produce a B_{vp} at a lower B_{app} than expected.

Whilst commercial magnetometry can produce a highly sensitive insight into the quality of superconducting samples, there are some limitations that are dependant on the facility. Removing/reducing the effects of these limitations allow the quality of superconducting samples to be investigated with greater accuracy.

1.4 Aims of the project

The main aim of the project was to investigate the field of first full flux penetration (B_{fp}) in thin film structures using DC magnetometry. Commercial magnetometry exists, and also consist of limitations listed in the previous section. Testing multilayer samples using commercial magnetometry means that B_{app} will enter the multilayer at the insulating boundaries and the effect of screening on the surface will not be present. Whilst geometries exist which can reduce these limitations (such as using geometries with well known demagnetisation factors), it is difficult to create these geometries as multilayers.

Thus, a cryogen free facility had to be designed and built which could apply a magnetic field parallel to the surface of a superconductor to try and allow optimisation of the deposition process of superconductors. The first field penetration facility was a continuation of a previous students project (Lewis Gurran) who designed the magnet and staff members (Oleg Malyshev and Ninad Pattalwar) who designed the insert and the cryostat, such that some of the work had already been performed. Due to complications with the facilities and not operating as expected, a new facility was designed, built and commissioned at STFC Daresbury Laboratory within this project. An identical magnet to the first facility was used for the second facility, with a new cryogenic facility design.

It was demonstrated that the new facility can be used for evaluating performance of superconducting thin films, and aid in the deposition parameter optimisation process.

Chapter 2

Background

2.1 Superconductivity

2.1.1 Discovery and hallmarks

Superconductivity was initially discovered by H. Kamerlingh-Onnes in 1911 whilst measuring the electrical resistance of Mercury at low temperatures [20]. Onnes wanted to determine how small a resistance could become if all thermal noise was removed by using a high purity metal [20] such as Hg, Pb and Sn. The results determined that once the metals reached a certain temperature, the electrical resistance abruptly disappeared. This is known as the transition temperature (T_c). If DC currents are generated in the superconductor, it has been found using nuclear resonance that the currents should not decay in $10^{10^{10}}$ years [21]. Thus, perfect conductivity, and is the first hallmark property of superconductivity. This was eloquently put in a mathematical expression by F. and H. London in 1935 [22].

2.1.2 Critical temperature

Superconductivity is a state which only some materials can exhibit. The superconducting (SC) state has multiple phases, which depend on the type of superconductor, Type I or Type II. Currently, no superconductors exist at room temperature and atmospheric pressure. For superconductors to enter the Meissner state they must be cooled below the T_c. In the absence of an external magnetic field (B_{ext}), the transition is a thermodynamic second order transition [23] as there is no latent heat present during the transition. The transition from the normal conducting (NC) state to the SC state can be explained using the Gibbs free energy. When a SC is cooled below T_c, the SC becomes more ordered than the previous NC state, reducing the free energy of the medium [13]. The medium wants to have the lowest possible energy

state, such that the medium transitions into the superconducting regime due to having a lower energy. This can be described by using the Gibbs free energy, given by [10]:

$$F = U_{int} - TS \tag{2.1}$$

Which leads to:

$$dF = dU_{int} - TdS - SdT = -SdT - pdV \tag{2.2}$$

Where S is the entropy, p is the pressure and V is the volume. The variation in p is much easier to use than V, such that the p is introduced as the independent variable, such that the Gibbs function for the enthalpy (f) becomes Eqn 2.4 [10]:

$$F = U_{int} - TS + pV \tag{2.3}$$

$$df = -SdT + Vdp \tag{2.4}$$

Only the electrons within k_bT of the Fermi energy are involved, such that the energy change due to entropy is small [13]. Whilst an B_{ext} affects the free energy of the superconductor, a term should be included to account for B and the induced magnetic moment (m) due to an B_{ext}. This is not relevant for T_c. At T_c, $B_{ext} = 0$, and the Gibbs free energy energy in the SC and NC state must be equal, $F_s = F_n$ respectively. When the free energy of both systems are equal, the sample transitions from the NC state to the SC state, indicating T_c.

2.1.3 Meissner effect

The second hallmark of superconductivity was discovered by W. Meissner and R. Ochsenfeld in 1933 [24]. When a superconductor is cooled below T_c, B_{ext} is expelled from the bulk [20] due to supercurrents forming in the surface that oppose the B_{ext}. Simply, a superconductor behaves as perfect diamagnet. This is known as the Meissner effect/state. The London brothers were able to mathematically describe the Meissner effect, with the derivation and the result shown in the next section. As B was experimentally determined to be expelled from a superconductor, the solution to the London equation must be that B decays exponentially over a few London penetration depths (λ_L), which typically ranges up to a few hundred nm [25].

The Meissner effect is where a superconductor differs from a perfect conductor. When B_{ext} is applied to both a perfect conductor and a superconductor in the Meissner state, B is screened and does not enter sample [13] due to Lenz's law. However, if a perfect conductor and a superconductor are cooled below T_c in the presence of B_{ext}, which is subsequently removed, a perfect conductor and a superconductor behave differently. A perfect conductor will not expel the B_{ext} from the bulk of the material as it transitions below T_c. As B_{ext} is removed the flux would be trapped, resulting

in the perfect conductor producing its own B equal to the previously applied B_{ext}. In the same situation, a superconductor will experience the Meissner effect, and B will be expelled from the sample as it cooled below T_c. For a perfect superconductor (containing no defects or impurities), no flux is trapped when the B_{ext} is removed, and the superconductor does not produce its own field [13].

2.1.4 Theories of Superconductivity

2.1.4.1 London model

Although superconductors were discovered in 1911, the first mathematical expression to describe superconductivity was produced in 1935 by F. and H. London [22]. As there is no resistance in a superconducting state, it can be determined that an electrical field (**E**) will accelerate the charge carriers (in this case electrons) in a sample without any resistance, and can be defined as:

$$\boldsymbol{F} = m_e \frac{\partial \mathbf{v}}{\partial t} = e\mathbf{E} \tag{2.5}$$

Where m_e, v and e is the is the mass, velocity and charge of the electron respectively. The superconducting current ($\boldsymbol{J_s}$) can therefore be given by:

$$\boldsymbol{J_s} = n_s e \boldsymbol{v} \tag{2.6}$$

Where n_s is the density of superconducting charge carriers. Differentiating Eqn. 2.6 with respect to time, re-arranging and combining with Eqn. 2.5 produces:

$$\frac{\partial}{\partial t}(\boldsymbol{J_s}) = n_s e \frac{\partial v}{\partial t} = \frac{n_s e^2}{m_e}\boldsymbol{E} \tag{2.7}$$

This is the first London equation [22], which describes a perfect conductor. Using Maxwell's equation ($\boldsymbol{\nabla} \times \boldsymbol{E} = -\partial \boldsymbol{B}/\partial t$) and taking the curl of Eqn. 2.7 allows the magnetic field (**B**) inside the superconductor to be described. Thus, the perfect conductivity equation becomes:

$$\frac{\partial}{\partial t}(\boldsymbol{\nabla} \times \boldsymbol{J_s}) = \frac{n_s e^2}{m_e}(\boldsymbol{\nabla} \times \boldsymbol{E}) = -\frac{n_s e^2}{m_e}\frac{\partial \boldsymbol{B}}{\partial t} \tag{2.8}$$

$$\frac{\partial}{\partial t}(\boldsymbol{\nabla} \times \boldsymbol{J_s} + \frac{n_s e^2}{m_e}\boldsymbol{B}) = 0 \tag{2.9}$$

$$\boldsymbol{\nabla} \times \boldsymbol{J_s} + \frac{n_s e^2}{m_e}\boldsymbol{B} = 0 \tag{2.10}$$

Equation 2.9 describes the internal magnetic field of a perfect conductor due to the supercurrents. As there is no resistance, Eqn. 2.9 must be time independent, which leads to Eqn. 2.10, which is London's second equation. The Ampere-Maxwell law (Eqn. 2.11) for static fields can then be subbed into Eqn. 2.10.

$$\nabla \times \boldsymbol{B} = \nabla \times \mu_0 \boldsymbol{H} = \mu_0 \boldsymbol{J} \tag{2.11}$$

Such that Eqn. 2.10 becomes:

$$\boldsymbol{\nabla} \times \boldsymbol{\nabla} \times \boldsymbol{B} = -\frac{\mu_0 n_s e^2}{m_e} \boldsymbol{B} \tag{2.12}$$

The vector identity for $\boldsymbol{\nabla} \times \boldsymbol{\nabla} \times \boldsymbol{B} = \boldsymbol{\nabla} \cdot (\boldsymbol{\nabla} \cdot \boldsymbol{B}) - \boldsymbol{\nabla^2 B}$, where the 1st term on the right hand side is 0, due to Gauss's law. The final equation becomes:

$$\boldsymbol{\nabla^2 B} = \frac{\mu_0 n_s e^2}{m_e} \boldsymbol{B} = \frac{1}{\lambda_L^2} \boldsymbol{B} \tag{2.13}$$

Where λ_{L} is the London penetration depth and has units of length. Solving Eqn. 2.13 produces 2 solutions. Either the magnetic field is constant, or decays exponentially over λ_{L}. The B has been observed experimentally to be expelled from the superconductor, thus B must decay over the λ_{L}. Thus the magnitude of B can be found over a distance (d) within a superconductor using Eqn. 2.14.

$$\boldsymbol{B} = \boldsymbol{B_0 e^{-d/\lambda_L}} \tag{2.14}$$

Equation 2.14 predicts that B is exponentially suppressed within a superconductor and predicts the Meissner effect, Section 2.1.3.

Whilst the London brothers had produced the first equations to explain the behaviour of superconductors, the first microscopic theory was only produced 40 years after the initially discovery of superconductors, by Bardeen, Cooper and Schreiffer, and is known as the BCS theory. This is due to small gaps having to be filled, which later played an important part in producing the full BCS theory.

2.1.4.2 Pippard model

As $T \to \mathrm{T_c}$, it is expected that the density of superconducting charge carriers $n_s \to 0$. Therefore λ_{L} diverges as $T \to \mathrm{T_c}$, following Eqn. 2.15 [21].

$$\lambda(T) \approx \lambda_L(0\,\mathrm{K}) \left[1 - \left(\frac{T}{T_c} \right)^4 \right]^{-\frac{1}{2}} \tag{2.15}$$

Comparing experimental estimations of $\lambda_{\mathrm{L}}(0\,\mathrm{K})$ to the values predicted by Eqn. 2.14 showed that there was some discrepancy in the results. This led to Pippard

to introduce non-local electrodynamics to account for these discrepancies. The current at a point **r** also depends on the electric field at a second point, **E(r')** [21], and that the interaction length between **r** and **r'** must have the dimension ξ_0, the coherence length. Therefore n_s can vary significantly over the distance ξ_0.

Pippard argued that the wave function of the SC must have a dimension similar to that of ξ_0. Only the electrons within kT_c of the Fermi energy are involved at the transition at T_c, which have a momentum $\Delta\rho \approx kT_c/v_f$, where v_f is the Fermi velocity. Substituting the momentum into the Heisenberg uncertainty principle ($\Delta x \geq \hbar/\Delta p$), the ξ_0 can be found to be [21]:

$$\xi_0 = a\frac{\hbar v_f}{kT_c} \tag{2.16}$$

Where a is a constant, which Pippard found for Sn and Al to be 0.15, and was later confirmed by the BCS theory (described in section 2.1.4.5) to be 0.18.

2.1.4.3 Energy Gap

The next step that was required for the first microscopic theory was the discovery of the SC energy band gap, Δ, that is of the order kT_c between the ground state and the quasipartile excitation's of the superconductor [21]. The first experimental evidence of Δ arose from specific heat measurements [26]. At low temperatures, the specific heat contribution of metals is dominated by the electronic specific heat (C_e) which has a linear dependence with T. However, the specific heat of superconductors does not follow this dependence when cooled below T_c, but decays exponentially. The NC charge carriers were no longer contributing to C_e, indicating that the SC charge carriers do not behave the same as electrons. As the decay was exponential, it was determined that that the electrons must condense into pairs, which are known as Cooper pairs. Each pair has a minimum excitation energy of $\approx 1.5\ kT_c$.

Glover and Tinkham [27] performed measurements of electromagnetic absorption in the region of 0.3 - 40 kT_c (in the infrared and microwave lengths), which could be interpreted to produce an energy gap of 3-4 kT_c. These results were consistent with those produced by the calorimetric measurements produced by Corak et al., as the calorimetric measurements are for each statistically individual particle, where as the EM absorption determines that the excitation's were produced in pairs, thus obeying Fermi statistics. As the excitation's were produced in pairs determined that the charge carriers were paired. Hence, the energy to create a pair of excitation's can be denoted by the condensation energy of a pair of charge carriers (E_c), where as the calorimetric measurements measured $E_c/2$.

2.1.4.4 The isotope effect

E. Maxwell [28] observed experimentally that two different isotopes of Hg (198 and natural - with an average atomic weight of 200.6) produced 2 different T_c's by extrapolating a critical magnetic field (B_c) vs T graph. It was determined that the high purity $Hg^{200.6}$ had a $T_c = 4.157\,K$, where as the T_c for the lighter Hg^{198} was greater, $T_c = 4.167\,K$. It was inferred that lighter isotopes produced an increased T_c, indicating an interaction between the charge carriers and the lattice of the superconductor.

2.1.4.5 Bardeen Cooper Schreiffer theory

After the confirmation of the band gap, Bardeen, Cooper and Schreiffer made the first microscopic theory for the behaviour of SC's, over 40 years after the initial discovery [29]. Simply, the electrons which occupy the same state now interact, and have equal and opposite momentum and spin [21]. The paired electrons are named 'Cooper pairs', and are the SC charge carriers with a distance separating each electron of ξ_0.

In a simple static system, it can be can be visualised as 2 electrons in different areas. Each electron attracts the neighbouring nuclei in the surrounding lattice, distorting the lattice. The distorted lattice can be described as being polarised [10], as the negative charge has produced an accumulation of positive charge around it. The accumulation of positive charge in each area attracts the electron from the opposite area; i.e.- the electrons are attracted to each other, which form the Cooper pair.

In a mobile system, the Cooper pairs can be envisioned by electrons moving through the lattice. As the electrons travel, neighbouring nuclei are attracted to the electrons due to the Coulomb force, and the lattice distorts similar to in a static system. The ions are larger and heavier than the electrons, and therefore move slowly towards the electron. As the ion takes a time to move towards the electron, the electron has moved away in the time it takes for the ion to reach the original point of the electron. The ion creates an excess of positive charge in the space it has moved to, which will in turn attract another electron, causing it to change its direction of motion [20], which can be shown in Fig. 2.1. Only electrons which are far apart (relative to the lattice dimensions) are attracted to the areas of positive charge. Due to the initial electron causing the ion to move followed by the second electron only being attracted by the ion once there is an area of increased positive charge. I.e.- the initial electron must have moved away for the second electron to be attracted towards the area of increased charge. The initial electron must have moved away or else the negative charge would dominate the interaction and cause the electrons to repel each other. This causes the electrons to be attracted to each other due to an electron-phonon interaction [20].

The distance between the electrons in the Cooper pair is the coherence length,

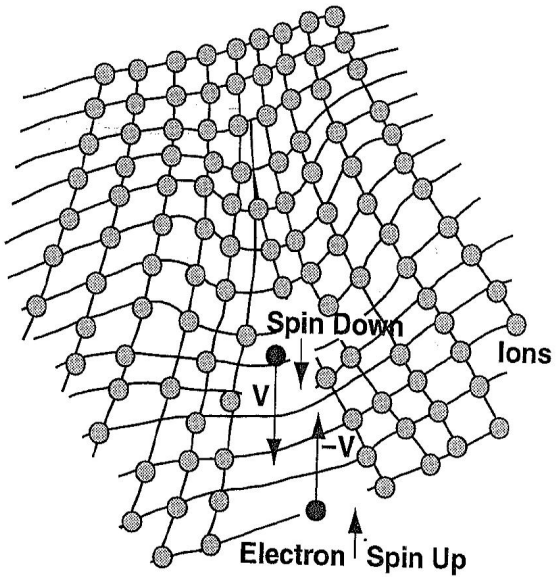

Figure 2.1: A visual representation of electrons distorting the lattice to form Cooper pairs. Image taken from Ref. [13].

denoted by ξ_0, which is different for each superconductor [20]. The coherence length is much larger than the distance between atoms. For example, Nb is a type II superconductor which has a body centered cubic (BCC) lattice structure, with 2.95 Å between atoms [30]. The London penetration depth and coherence length for Nb is 40 nm and 35 nm respectively [31]. Lead is a type I superconductor with a face centered cubic (FCC) lattice structure with atoms 4.95 Å apart. The London penetration depth and coherence length for Pb is 30.5 nm and 96 nm respectively [32]. Other materials which are discussed throughout this thesis are shown in Table 2.1 alongside Nb and Pb for a comparison.

2.1.4.6 Ginzburg Landau Theory

A second important theory of superconductivity is the Ginzbury-Landau (GL) theory, which is today more known as the Ginzburg-Landau-Abrikosov-Gor'kov (GLAG) theory. The original theory was published in 1950 [45], however only gained traction after a microscopic theory (BCS) had been published. The GL theory utilised that the SC state can be described in terms of a wave function with a phase. The GL theory is an extension of the London equations [22], in which a spatially constant density for the charge carriers were assumed [10].

The GL theory was used to predict an intermediate state present in Type II superconductors by Abrikosov [46] (known as the vortex state), and Gor'kov determined

Property	**Pb**	**Nb**	**Nb_3Sn**	**NbTiN**
Type	I	II	II	II
T_c [K]	7.20 [33]	9.25 [34]	18.0 [35]	16 - 18 [36], [37]
λ_L [nm]	30.5 [32]	35.0 [34]	69.0 [38]	150-200 [39]
ξ_0 [nm]	96.0 [32]	43.0 [34]	5.7 - 7.7 [40]	2.4 [41]
B_{c1} [mT] [K]	-	174.0 [42]	38.0 [35]	30 [39]
B_c [mT] [K]	80.3 [33]	199.3 [34]	520.0 [35]	500 [43]
B_{sh} [mT]	-	240 [44]	440.0 [44]	439 [43]

Table 2.1: A table with the superconducting parameters of multiple materials of interest that are tested throughout this thesis.

that for T near T_c, the GL theory can be derived from the BCS theory [47]. These extensions to the theory are why they are included in GLAG theory.

Landau had developed a theory in which the T_c transition was a second order phase transition. This theory included an order parameter that increased from 0 at T_c continuously up to 1 at $T = 0\,K$. Ginzburg and Landau defined the SC phase order parameter to be Ψ. The free energy of the SC state is a minimum at T_c, thus Ψ is also at a minimum. For $T \approx T_c$, and for cases where B is absent, the free energy of the medium can be expanded using the Taylor series of the density $|\Psi|^2$ [10]:

$$F_s = F_n + \alpha|\Psi|^2 + \frac{\beta}{2}|\Psi|^4 \tag{2.17}$$

For $T \geq T_c$, $|\Psi|^2 = 0$, and $F_s = F_n$. As the superconductor must be stable at T_c in the SC state, and must be analytic at $\Psi = 0$ [21], the expansion only includes the even powers [48]. For the theory to be useful, $\beta > 0$, or else the lowest free energy would only occur for large values of $|\Psi|^2$ [21]. The free energy density variation depends on the sign of α [48]. If $\alpha > 0$, the minimum free energy occurs at $|\Psi|^2 = 0$, and corresponds to the NC state. In the SC state, as $\beta > 0$, $\alpha < 0$, or else F_s would always be larger than F_n. Both α and β can be expanded in the Taylor series of the temperature [10], such that α and β can be written as:

$$\begin{aligned} \alpha &= \alpha(T)\left(\frac{T}{T_c} - 1\right) \\ \beta(T) &= \beta = \text{constant} \end{aligned} \tag{2.18}$$

Sufficiently far away from the interface, Ψ can be denoted Ψ_∞, such that $|\Psi_\infty|^2 = n_s$, the number of charge carriers [10].

$$F_s = F_n + \alpha|\Psi_\infty|^2 + \frac{\beta}{2}|\Psi_\infty|^4 \tag{2.19}$$

The minimum free energy in the SC state can be found by differentiating Eqn. 2.19 with respect to $|\Psi_\infty|^2$, and occurs at $d(F_s)/d|\Psi_\infty|^2 = 0$.

$$\begin{aligned} \frac{d(F_s)}{d(|\Psi_\infty|^2)} = 0 = \alpha + \beta|\Psi_\infty|^2 \\ n_s = |\Psi_\infty|^2 = -\frac{\alpha}{\beta} \end{aligned} \tag{2.20}$$

This minimum in the free energy can then be attributed to the thermodynamic critical field, B_c by substituting in the minimum $|\Psi_\infty|^2$ into Eqn. 2.19:

$$\begin{aligned} F_n - F_s = -\alpha|\Psi_\infty|^2 - \frac{\beta}{2}|\Psi_\infty|^4 = -\alpha \cdot \left(-\frac{\alpha}{\beta}\right) - \frac{\beta}{2} \cdot \left(-\frac{\alpha}{\beta}\right)^2 \\ F_n - F_s = \frac{\alpha^2}{\beta} - \frac{\alpha^2}{2\beta} = \frac{\alpha^2}{2\beta} = \frac{B_c^2}{8\pi\mu_0} \end{aligned} \tag{2.21}$$

If a superconductor is in the presence of B, and Ψ is small and varies slowly in free space, the free energy can be expanded to be Eqn. 2.22 [21].

$$F_s = F_n + \alpha|\Psi|^2 - \frac{\beta}{2}|\Psi|^4 + \frac{1}{2m^*}\left|\left(\frac{\hbar}{i}\nabla - e^*\boldsymbol{A}\right)\Psi\right|^2 + \frac{B^2}{8\pi\mu_0} \tag{2.22}$$

Where m^* and e^* represent the mass and charge respectively of the charge carriers, and are double the mass and charge of an electron, as the charge carriers are Cooper pairs. The final term in Eqn. 2.22 is the correction to F_n for a finite B, and the third term is the kinetic energy of the Cooper pairs, where $\boldsymbol{A}$ is the vector potential of the screening currents within the superconductor due to B_{ext}.

Using variational procedure to minimise F_s in Eqn. 2.22, two non-linear second order differential equations are produced, shown in Eqns. 2.23 and 2.24, where Ψ^* is the complex conjugate:

$$\frac{1}{2m^*}\left(\frac{\hbar}{i}\nabla - e^*\boldsymbol{A}\right)^2\Psi + \alpha|\Psi|^2 + \frac{\beta}{2}|\Psi|^4 \tag{2.23}$$

$$J_s = \frac{e^*\hbar}{2mi}(\Psi^*\nabla\Psi - \Psi\nabla\Psi^*) - \frac{e^{*2}}{m^*}\Psi^*\Psi\boldsymbol{A} \tag{2.24}$$

Normalising Ψ to Ψ_{inf} in Eqn. 2.23 yields Eqn. 2.25 from Ref. [10], where Eqn. 2.20 has been used to substitute $\alpha = \beta|\Psi_{\text{inf}}|$.

$$\frac{1}{2m^*}\Big(\frac{\hbar}{i}\nabla - e^*\boldsymbol{A}\Big)^2\psi + \alpha\psi - \alpha|\psi|^2\psi = 0 \tag{2.25}$$

Dividing both sides by α, and moving $\hbar$ out the brackets produces:

$$\frac{\hbar^2}{2m^*\alpha}\Big(\frac{1}{i}\nabla - \frac{e^*}{h}\boldsymbol{A}\Big)^2\psi + \psi - |\psi|^2\psi = 0 \tag{2.26}$$

The constants in the first term produce the units of (length)^2, which is taken to be the Ginzburg-Landau coherence length (ξ_{GL}):

$$\xi_{GL} = \sqrt{\frac{-\hbar^2}{2m^*\alpha}} \tag{2.27}$$

The surface energy determines how the superconductor will behave in B_{ext}, which depends on λ_{L} and ξ_{GL}, and is given by the Ginzburg-Landau parameter, κ_{GL}:

$$\kappa_{GL} = \frac{\lambda_L}{\xi_{GL}} \tag{2.28}$$

If $\xi_{GL} > \lambda_L$ then the boundary has a positive surface energy (Type I superconductors), and negative when $\xi_{GL} < \lambda_L$ (Type II superconductors) [13]. The crossover κ_{GL} occurs at $1/\sqrt{2}$, such that:

$$\begin{aligned} \kappa_{GL} &< \frac{1}{\sqrt{2}} \text{ Type I superconductors} \\ \kappa_{GL} &> \frac{1}{\sqrt{2}} \text{ Type II superconductors} \end{aligned} \tag{2.29}$$

2.1.5 Critical magnetic fields, Type I and Type II

As mentioned previously, the Meissner state is reversible, implying that the SC state can also be destroyed by a B. The B at which the Meissner state breaks down depends on both the bulk and surface energy of the superconductor.

2.1.5.1 Thermodynamic critical field, B_c

In the presence of B_{ext}, the Cooper pairs form a super-current (J_{s}) to oppose B_{ext} and shield the bulk of the superconductor. The induced J_{s} increases the bulk free energy of the superconductor. When the increase in the free energy of the superconductor is equal to the condensation energy of the Cooper pairs, the Cooper pairs break. The magnitude of J_{s} at which the Cooper pairs break is known as the depairing current density (J_{d}). As the the Cooper pairs have broken, no screening current is present

and the B enters the bulk of the superconductor all at once [12]. Superconductivity breaks down due to the normal conducting regime having a lower free energy than the SC state when a B_{ext} >B_c is applied. This transition is known as the thermodynamic critical field (B_c) as only the bulk free energy of the system is considered, which varies for each superconductor. Equating the free energies at a set temperature, B_c can be written as shown in Eqn. 2.30.

$$F_s(B) = F_n = F_s(B = 0\,\mathrm{mT}) + \mu_0 V_s \int_0^{B_c} \boldsymbol{B} dB \tag{2.30}$$

The work done on the superconductor to establish supercurrents can be wrote as:

$$F_n - F_s(B = 0\,\mathrm{mT}) = \frac{\mu_0 V_s B_c^2}{2} \tag{2.31}$$

The B_c has a temperature dependence, which has been found to have a good approximation to T^2, such that:

$$B_c(T) = B_c(0\,\mathrm{K})\left[1 - \left(\frac{T}{T_c}\right)^2\right] \tag{2.32}$$

Whilst the thermodynamic free energy of the system defines the B_c, the interface energy of the superconductor also plays a part in the entry of B_{ext} due to the n_s at the surface. The affect of the interface energy on the free energy is incorporated into the Ginzburg-Landau equation (third term in Eqn. 2.22).

Materials that have a $\kappa_{GL} < 1/\sqrt{2}$ have $\xi_0 > \lambda_L$ are known as Type I superconductors, which have a positive surface energy. In the absence of B the Meissner state has a lower free energy than in the the NC regime, such that increasing B_{ext} reduces the free energy of the system. Due to $\xi_0 > \lambda_L$ there is a low density of Cooper pairs near the surface layers [20].

Alternatively, materials which have a $\lambda_L > \xi_0$ have a negative surface energy, and a $\kappa_{GL} > 1/\sqrt{2}$. Unlike Type I superconductors, there is a greater n_s in the surface layers. It is energetically favourable to allow B_{ext} to enter the SC at a B < B_c.

2.1.5.2 Lower critical field, B_{c1}

Whilst the bulk free energy of a system determines B_c, the interface energy due to n_s in the surface layers also play a part in when B_{ext} can enter the superconductor. Type I superconductors have a $\xi_0 > \lambda_L$, such that they have a positive surface energy, such that it is energetically favourable for B to enter a Type I superconductor when B>B_c. Thus, B will enter a Type I superconductor abruptly at B_c. However, Type II superconductors have $\lambda_L > \xi_0$, which corresponds to a negative surface energy such that it is energetically favourable to allow B to enter the superconductor at B<B_c.

The B at which it is energetically favourable to enter a Type II superconductor is known as the lower critical field (B_{c1}). Applying a B_{ext} to a increases the internal energy as screening currents are formed to oppose B_{ext}. To lower the internal energy of the system, Type II superconductors split into superconducting/normal-conducting boundaries known as vortices. Because B enters the medium in the form of vortices and is not forced to reduce to 0 inside the superconductor, less energy is required to expel the flux [12], thus reducing the bulk free energy of the system. Vortices can be thought of as normal conducting cone-like structures containing 1 flux quantum (ϕ_0, shown in Eqn. 2.33) and require energy to be formed [13]. This state is known as the Shubnikov phase and/or the Abrikosov state.

$$\phi_0 = \frac{h}{2e} = 2.07 \times 10^{-15}\,\mathrm{Wb} \tag{2.33}$$

Each fluxoid has a surface area related to the mediums ξ_0, shown in Eqn. 2.34.

$$A_{fluxoid} \approx \frac{\pi \xi_0^2}{2} \tag{2.34}$$

The vortex has a radius corresponding to ξ_0, which is due to the Cooper pair having a kinetic energy greater than the binding energy [13]. As B_{ext} is increased, the number of vortices increases to reduce the bulk free energy of the system, allowing the medium to have a lower energy than the NC regime. Provided κ_{GL} is large and both λ_L and ξ_0 are known, B_{c1} an be estimated by using Eqn. 2.35 [13].

$$B_{c1} \approx \frac{\phi_0}{4\pi\mu_0\lambda_L^2}(\ln \kappa_{GL}) = \frac{B_c}{\sqrt{2}\kappa_{GL}} \ln \kappa_{GL} \tag{2.35}$$

Provided there is no pinning or defects, the vortice distribution is a triangular array due to providing the lowest free energy [21]. The Shubnikov phase is maintained for B up to the upper critical field (B_{c2}). However, another effect can take place.

2.1.5.3 Superheating field, B_{sh}

Although it is energetically favourable for the flux to enter the superconductor at B_{c1}, a Type II superconductor can remain in the Meissner state above B_{c1} in a metastable state up to the superheating field (B_{sh}) [49]. This is due to the Bean-Livingston surface barrier, which can be visualised as an image vortex being formed outside the superconductor that creates a force opposing the real vortice from penetrating into the superconductor. Whether the superconductor can reach B_{sh} depends on the impurities and dislocations in the surface of the superconductor. The magnitude of B_{sh} depends on κ_{GL}, and has been calculated by Matricon and Saint-James in Ref. [50], presented in Ref. [13] and below:

$$\begin{aligned} B_{sh} &\approx \frac{0.89}{\sqrt{\kappa_{GL}}} B_c \text{ for } \kappa_{GL} \ll 1 \\ B_{sh} &\approx 1.2 B_c \text{ for } \kappa_{GL} \approx 1 \\ B_{sh} &\approx 0.75 B_c \text{ for } \kappa_{GL} \gg 1 \end{aligned} \tag{2.36}$$

The time period of an RF wave takes $\approx 0.1\,\%$ of the time period it takes for fluxoids to nucleate, it is more likely that the metastable Meissner state will exist up to B_{sh} [13]. It is expected that the critical radio frequency field ($B_{rf,crit}$) is the same as B_{sh} [13], and is thus the limiting factor of E_{acc}.

2.1.5.4 Upper critical field, B_{c2}

Increasing B_{ext} whilst a Type II is in the Shubnikov phase increases the number of vortices present within the medium, which re-arrange the structure of the vortices such that they are equally spread out (assuming a pin free sample) to reduce the internal energy. As B_{ext} increases, the density of the vortices increase up until the NC cores overlap, at which the medium has transitioned to the NC state and superconductivity breaks down. The vortex cores overlap at the upper critical field (B_{c2}). The B field where B_{c2} occurs can be found using Eqn. 2.37 [12], provided ξ_0 is known.

$$B_{c2} = \frac{\phi_0}{2\pi\mu_0\xi_0^2} \tag{2.37}$$

Both B_c and B_{c2} can be related using Eqn. 2.38:

$$B_{c2} = \frac{\phi_0}{2\pi\mu_0\xi_0^2} = B_c\sqrt{2}\kappa_{GL} \tag{2.38}$$

However, at a metal-superconductor boundary superconductivity can remain in the parallel B up to a surface critical field (B_{c3}).

2.1.5.5 Surface critical field, B_{c3}

Saint James and de Gennes [51] determined in 1963 that a superconducting sheath can nucleate at a metal-superconductor boundary, with a parallel B. This surface critical field (B_{c3}) can be maintained up to $B_{c3} = 1.695B_{c2}$ [21], such that the nucleation occurs at a B much greater than in the bulk. A superconductor in $B_{c2} < B < B_{c3}$ may still be able to carry a supercurrent, even though superconductivity cannot be detected. To avoid B_{c3} the sample surface must be plated with a normal metal (i.e. not SC). The NC metal behaves as a pair breaking inhibitor, as any Cooper pairs formed in the surface diffuse into the normal conductor and are consequently destroyed. Thus,

surface superconductivity is destroyed. This ensures that no flux is trapped within the superconductor.

2.1.6 Thin films, $d < \lambda$

Superconducting thin films with a thickness (d) less than λ_L can exceed B_c (in a parallel B_{ext}) by a large factor provided that the ratio of d/λ_L is small enough [21], due to the film having a small increase in the internal free energy compared to an equal volume of a bulk superconductor. Films with a $d < \lambda_L$ have an increased B_{c1} [52], such that the equation for B_{c1} becomes:

$$B_{c1} = \frac{2\phi_0}{\pi d^2} \ln\left(\frac{d}{\hat{\xi}}\right) \tag{2.39}$$

Where $\hat{\xi} = 1.07\xi_0$ [16]. For example, a 20 nm NbN thin film with $\xi_0 = 5$ nm has a $B_{c1} = 4.2$ T [16].

Superconducting thin films still behave similar to bulk superconductors, as the B penetrates into the volume and decays exponentially over λ_L. As the thin films have a $d < \lambda_L$, B does not decay to 0 mT within the film. Additionally, vortices are not thermodynamically stable in a parallel B for films with a $d < \lambda_L$ [52]–[54]. Finally, it has been found experimentally by Stejic et al. [53] that the J_c of thin films depends greatly on the orientation of B with respect to the film surface, and also the thickness of the superconductor. Films with a $d< \lambda_L$ produce an increased J_c than the bulk counterpart for a B applied with any orientation to the surface. As the sample face becomes more parallel to B, the J_c of the thin films begins to increase, producing a peak J_c when B is parallel to the film surface. The peak increase in J_c is much greater for the thin films compared to the bulk superconducting counterparts relative to the perpendicular B.

2.2 Materials for SRF Cavities

2.2.1 Why SRF?

Superconducting radio-frequency cavities are beneficial for continuous wave applications that require a large E_{acc} ($>$ a few MV m^{-1}). Whilst superconductors have no DC resistance, they produce a none zero resistance under RF conditions - R_{surf}. The Cooper pairs flow through the surface with no resistance, however they have a mass of 2 electrons ($2m_e$), and therefore a momentum. When E alternates direction, forces are applied to the Cooper pairs such that B_{surf} is not perfectly screened and a time varying E is present within the surface of the cavity [13]. Superconductors have a R_{surf} many orders of magnitude lower than Cu cavities [12], as NC cavities also experience

this effect whilst the electrons scatter off the lattice. Thus, less RF power is dissipated in the cavity walls compared to a NC cavity. For an E_{acc} of $1\,MV\,m^{-1}$, the power dissipated in a Cu cavity is $\approx 4 \times 10^4$ greater than a Nb cavity per meter [13]. Once the cryogenic plant has also been accounted for to produce the LHe to cool the SRF cavities, there is still a net reduction in the power required to operate SRF cavities compared to normal conducting cavities [12]. For continuous wave operations using a Cu cavity, E_{acc} is generally kept to $< 1\,MV\,m^{-1}$ [13]. High E_{acc} can be produced in Cu cavities for short periods of time due to the required RF power becoming prohibitive, as well as the possibility of the cavity become damaged. If the amount of heat deposited in a Cu cavity becomes excessive, the cavity can become damaged due to the thermal expansion and stresses in the walls.

From a beam dynamics perspective, accelerating structures disturb the particle bunches as they pass through the structure. As SRF cavities can reach much larger $MV\,m^{-1}$, the accelerator can be shorter, reducing the amount of disruption on the beam [12].

2.2.2 Bulk Nb and Low temperature baking techniques

Currently, most SRF cavities are made out of Nb due to having the largest T_c of any element [55] and the largest B_{c1} for any known superconductor. For clean Nb, $T_c = 9.25\,K$ and $B_{c1} \approx 174\,mT$ at $0\,K$ [34], [42], with a $\kappa_{GL} \approx 1$ which produces a $B_{sh} \approx 1.2\ B_c$. Thus, for Nb with $B_c \approx 199.3 \pm 10\,mT$ at $0\,K$ [34], B_{sh} can persist up to $\approx 240\,mT$ at $0\,K$. For a typical Tesla shape Nb cavity the limit is $4.2\,mT\,MV^{-1}\,m$ [13], which allows us to calculate the maximum theoretical E_{acc} for Nb:

$$E_{acc} = \frac{240}{4.2}\frac{mT\,MV}{mT\,m} = 57.1\,MV\,m^{-1} \tag{2.40}$$

More detailed calculations within Ginsburg-Landau theory can be found in Ref. [44]. To produce a good quality cavity, high purity Nb must be used to reduce losses in the cavity and increase the maximum E_{acc} that the cavity can reach. There are multiple techniques that can be used to determine if the Nb is clean and high purity, which reduces the R_{surf}.

2.2.2.1 Residual resistance ratio

The quality of the Nb used to make a cavity is measured using the residual resistance ratio (RRR) which compares the electrical resistance at room temperature and at a temperature just above T_c. The RRR measurements give insight into the imperfections and dislocations in the lattice structure, and also an insight into the purity of the metal. The resistance must be extrapolated to $4.2\,K$ as it is

possible the superconductor will have transitioned, therefore having no resistance. The measurements compare the electrical resistance (R) producing Eqn. 2.41 [56]:

$$RRR = \frac{R_{300K}}{R_{4.2K}} \tag{2.41}$$

When performing RRR measurements on superconductor's, the resistance must be extrapolated for 4.2 K as the superconductor will have transitioned into the Meissner state and therefore DC resistivity will have disappeared. Another possibility is to compare at room temperature and just above T_c. For example, RRR_{300K}/RRR_{10K} for Nb [57]–[59]. Niobium with a RRR = 300 is high purity [56], and will correspond to a $B_{rf,crit}$ of 200 mT, in turn corresponding to a $E_{acc} \approx 46\,MV\,m^{-1}$ at 1.3 GHz for a Tesla shaped cavity [60]. This is a theoretical limit due to other possible imperfections on the surface such as scratches, dislocations, impurities etc.

During cavity fabrication, imperfections, impurities and dislocations can be introduced by machining, welding and drawing out the bulk Nb. Imperfections on the surface can create flux enhancements such that B will enter at a lower B_{ext}, and impurities can create pinning centers allowing early entry of B. Both cases decrease $B_{rf,crit}$, therefore limiting E_{acc}.

This has led to improved technology in electron beam welding and surface preparation techniques [60]. Currently the maximum E_{acc} for bulk Nb cavities is reaching its theoretical limits, with single cell cavities able to reliably reach over $40\,MV\,m^{-1}$ [61], with some single cell cavities producing $E_{acc} \approx 59\,MV\,m^{-1}$ [12], [62] at 1.3 GHz, which corresponds to a peak B_{surf} of 206.5 mT. These results were produced by a re-entrant shaped cavity, and do not follow the same equation for E_{acc}/B_{surf} as the Tesla shaped cavity mentioned above.

Another practice for accelerating cavities is to use micrometer thick films of Nb, which can be deposited onto existing Cu cavities by magnetron sputtering [9]. This method reduces the cost of cavity fabrication. The cavities have a greater thermal stability due to being deposited on Cu. Micrometer thick film cavities have been implemented in LEP-II with 272 sputtered cavities with an operational frequency of 352.2 MHz [63], with an average accelerating gradient of $7.5\,MV\,m^{-1}$ and some cavities reaching $9\,MV\,m^{-1}$ at 4.5 K [64]. Low β cavities have also been made for ALPI [9] and sputtered Nb quarter wave resonators are in use in HIE-ISOLDE [65].

2.2.2.2 Magnetic flux pinning

Although superconductors expel an external magnetic field once they transition past T_c, it is possible for some flux lines to become trapped within the superconductor.

The amount of trapped flux can be seperated into 2 regimes; The number of areas that allow magnetic flux to be trapped, known as pinning sites. This is a material property (Impurities, grain size etc). The second is the flux pinning

mechanisms such as T gradient and the cooling rate. Flux pinning has a significant effect on the performance of SRF cavities, thus the material and fabrication process must be carefully considered to ensure the number of pinning sites is low. The amount of trapped flux can be reduced by controlling the cool down dynamics of the superconductor. The spatial thermal gradient (∇T=dT/dx·dx/dv) acts as a de-pinning force during the transition from the NC to SC state, with a greater thermal gradient improving flux expulsion in vertical cryostats [66], [67]. There are 2 proposed models to explain this behaviour. One is that the NC/SC wavefront acts as a de-pinning force that expels the flux line [68]. The second is that as the NC/SC wavefront moves, there is a mixed state domain. The large ∇T causes a reduced mixed state domain, thus reducing the probability of a flux line becoming trapped [69]. Once flux is pinned within a superconductor it can only be fully released by increasing the superconductor above its T_c. Trapped flux can be moved throughout the superconductor if a force is applied to the flux line that is greater than the pinning force. Once the flux line is de-pinned from its pinning site, it will jump to another pinning site where it will become pinned again. This is known as a flux jump.

2.2.2.3 High field Q-slope

The RRR impacts the R_{surf} of a cavity. This is due to flux becoming trapped at impurities and dislocations when cavities are cooled down [70] in an externally applied B, such as the earths B. Thus forming localised NC regions in which the Cooper pairs have to flow around. When applying RF to a cavity, the B component interferes with the trapped flux causing it to oscillate [70], in turn increasing R_{surf}. An increased R_{surf} increases the amount of RF power lost in the cavity walls, reducing the Q_0 of the cavity which is the ratio of the energy stored (U) in the cavity to the power dissipated in the cavity walls (P_c) per RF cycle [12].

$$Q_0 = \frac{\omega_0 U}{P_c} = \frac{G}{R_{surf}} \tag{2.42}$$

Where G is the geometry factor of the cavity. It can be seen for a given geometry of cavity, the Q_0 relies on the R_{surf} of the cavity. The alternating E_{acc} produced by the RF, is not always perfectly screened by the superconductor such that some resistance is present. The Cooper pairs having a mass and a momentum that flow in the surface. When E_{acc} alternates and the Cooper pairs de-accelerate and B_{surf} is not perfectly screened, such that a time varying E exists in the skin layer of the superconductor. The E couples to the NC electrons that are accelerated/de-accelerated, and thus dissipate power, reducing the Q_0. The P_c is related to R_{surf} with [13]:

$$P_c = \frac{1}{2} R_{surf} \int_A \left| \frac{B}{\mu_0} \right| dA \tag{2.43}$$

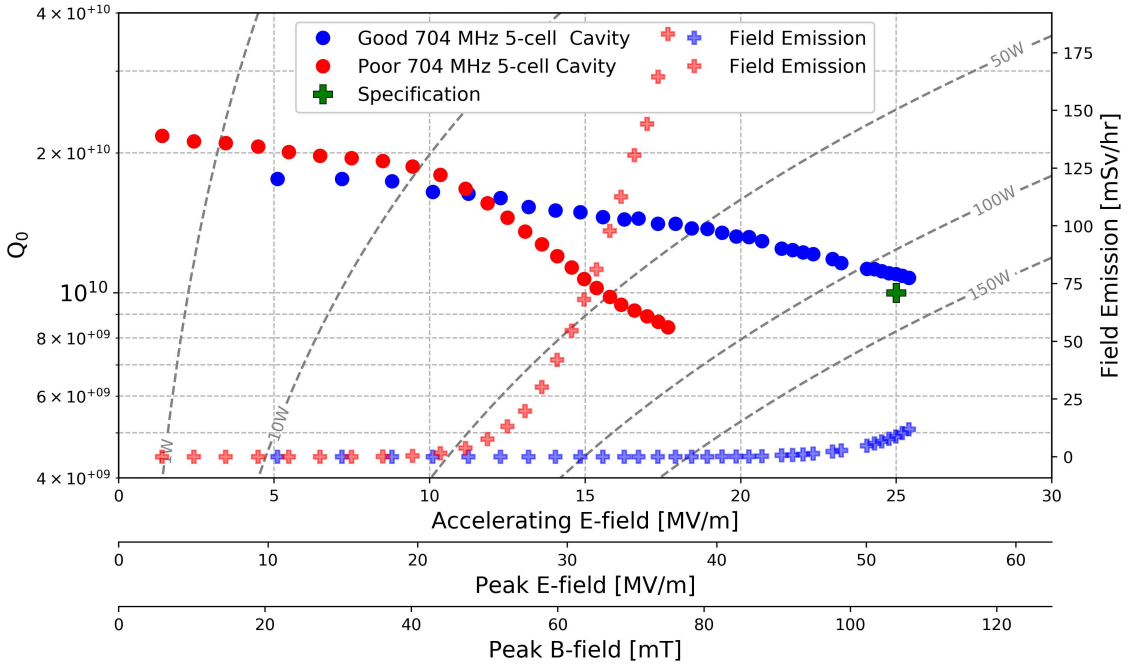

Figure 2.2: The quality factor Q_0 of a good and poor quality cavity plotted against E_{acc} and the peak B, courtesy of CERN [71], from [70].

Where A is the surface area. Typical values of Q_0 for bulk Nb range between $\approx 10^9 - 10^{10}$. The Q_0 is usually plotted on the y-axis, with either the B_{surf} [mT] or E_{acc} [MV m^{-1}] on the x-axis, which presents a phenomenon known as the high field Q slope (HFQS) which is shown clearly by the 'poor' cavity in Fig. 2.2. As E_{acc} (and therefore B_{surf}) is increased, the Q_0 decays slightly (known as the mid-field Q slope) as more power dissipates in the walls due to higher fields, shown by the 'good' cavity in Fig. 2.2. Eventually, there is a rapid fall in the Q_0, which indicates the losses in the cavity have become too large. This has been observed for cavities that have undergone electropolishing (EP) and buffer-chemical polishing (BCP) [72]. The current experimental data is best described by a theory of nano-hydrides proximity coupled to the Nb lattice [73], which once the EM fields produced by the RF in the cavity become so large, they are above the breakdown field for the nano-hydrides, so that they become NC [74]. The sudden change in the hydrides becoming NC increase the R_{surf}, producing the HFQS.

2.2.2.4 Low temperature baking

It is standard practice to perform a low temperature bake (LTB) as a final preparation step to reach large accelerating gradients. This consists of heating the cavity to 120 °C

for 48 hours in ultra-high vacuum [75]. A two-step baking process has shown to produce accelerating gradients larger than a single LTB [76]. The two-step baking process starts by baking a cavity at 75 °C for 4 hours before undergoing the LTB previously described.

The best Nb cavities prepared by LTB produce a maximum $E_{acc} \approx 50\,MV\,m^{-1}$ whilst operating at 2 K, which corresponds to a maximum $B_{surf} \approx 200\,mT$ [14]. This is above B_{c1} for Nb at 2 K and approximately 10 % lower than the the B_{sh}, which is the expected maximum value.

Another method which is classed as a LTB technique, however it is not performed under vacuum, but in the presence of N, and is referred to as nitrogen infusion. Nitrogen infusion can produce E_{acc} and Q_0 in excess to what can be obtained with LTB at 120 °C. The cavity is heated to 800 °C under high vacuum for 3 hours for H degassing and to separate any Nb_2O_5. The cavity is then cooled and held between 120-200 °C with a pressure of 25mTorr of N [15].

The increased B_{surf} due to LTB techniques can be due to a number of possibilities. For example, baking could avoid dissipative Nb hydrides forming [74], eliminating the HFQS. Additionally, LTB produces a change in λ_L [77], reducing the surface current, in turn delaying (or completely preventing) localized quenching and dissipation [72]. The surface layers affected by the baking could also introduce an interface energy barrier, between the 'dirty' (LTB affected regions) and the clean regime (bulk material, unaffected by the LTB), thus delaying flux penetration to larger B [78]. For a sufficiently thick dirty layer it might be possible for two distinct energy barriers to be present. Calculations from Checchin suggest that the dirty layer should have a thickness $\approx 60\,nm$ [48], which is comparable to what LE-μSR studies suggest.

2.2.3 Micrometer thick Nb on Cu

One alternative to bulk Nb is to deposit Nb thin films on a Cu cavity, as the RF only affects a few microns on the surface, typically less than 1 µm [39]. For clean Nb with a $\lambda_L = 40\,nm$ the ratio of B/B_0 can be found to be 14×10^{-12} using Eqn. 2.14, thus showing only a small amount of Nb is required to screen the magnetic field. Deposition of Nb has a few benefits compared to bulk Nb cavities, such as;

- A reduction in cost - Cu is cheaper than Nb, and the manufacturing costs for Cu cavities are also cheaper than bulk Nb cavities.
- Increased thermal stability - Cu has a greater thermal conductivity than Nb, reducing the temperature gradient from the cavity surface to the LHe bath [39]. The increased thermal conductivity allows the thin film to be more resistant to both multipacting and field emission.
- Insensitive to the earths magnetic field [55], [79], such that complex magnetic shielding is not required.

- Free from impurities in the Nb, such as steel, nickel and some oxide compounds [39] which can be sites for early flux entry in cavities. These substances can be present within bulk Nb sheets/ingots, and can be uncovered by etching. They can also be introduced during the manufacturing process of the cavities [80]. There are process' which remove these impurities, however this increases the manufacturing cost. Deposition under vacuum can avoid these impurities being included in the cavity.

Micrometer thick Nb cavities still consist of limitations. For example, the Q-slope limits Nb film cavities to a low E_{acc}. Sputtered films typically replicate the morphology of the substrate underneath, such that the substrate can have an affect on the RF performance. Previous studies have been performed in WP15 of the ARIES collaboration on how the quality of a Cu substrate affects the superconducting performance in DC magnetic studies [81]–[83]. Finally, the atoms of the gas present in DC magnetron sputtering can be embedded in the film, which can affect the RF performance of the films [84].

2.2.3.1 Post deposition laser treatment

Due to the micrometer thick films replicating the morphology of the of the substrate, the films may not be ideal for RF performance. It is possible that the structure of the Nb can be altered post deposition by using laser treatment to irradiate the sample. The laser produces heating in the sample surface, rapidly annealing localised areas that recrystallise into a desired structure upon cooling. Laser treatment has also been found to reduce the surface roughness of Nb. Laser treatment has already been performed for bulk Nb [85], [86] and micrometer thick Nb films [87]–[89]. Previous DC magnetometry tests using a VSM have been performed on laser treated samples [90], [91] produced by the ARIES work package that indicated promising results.

2.2.4 Increasing the accelerating gradient

The maximum E_{acc} of superconducting cavities is limited by the field of first flux penetration (B_{vp}). Increasing B_{vp} in turn can increase E_{acc}. There are multiple theories on how to increase B_{vp}. One method is to use materials with a larger T_c or larger critical fields known as A15 compounds, or to use multilayer structures to screen the magnetic field.

2.2.4.1 A15 superconductors

Alternative materials with a larger T_c could increase E_{acc}. Good candidate superconductors must have low resistivity in the NC state to minimise RF losses, a high T_c and a small κ_{GL} value [39].

The majority of A15 materials have B_{c1} lower than Nb, but much larger B_c values. For example, Nb_3Sn has a $B_c = 540\,mT$ [39]. As $\xi_{GL} \ll \lambda_L$ (4 and 80-100 nm respectively [39]), $B_{sh} \approx 0.75 B_c \approx 405\,mT$. Although B_{sh} is reduced due to the properties of the material, A15 compounds have the possibility to remain in the Meissner state in a metastable regime to B fields which are greater than that of Nb. Therefore E_{acc} can theoretically be increased past the current limits for Nb. Present results show Nb_3Sn have shown $E_{acc} = 24\,MV\,m^{-1}$ in continuous wave operation [92], which correlates to $\approx 100\,mT$. Whilst the E_{acc} is much lower than the theoretical value, the $B_{surf} > B_{c1} = 38\,mT$ [93].

Both B_{c1} and B_c depend on the ratio T/T_c. Therefore a cavity made out of an A15 compound can run at a higher T, reducing the cooling power (and the losses produced) required to run the cavity at fields similar to that of Nb. A new alternative is to use cryocoolers to cool cavities, which further reduces the cryogenic costs to run the cavity [92] whilst also minimising the amount of LHe required for operation.

2.2.4.2 Multilayer structures

Another possibility is to aid bulk Nb to increase E_{acc}. One theory has been proposed by A. Gurevich [16] to use multilayer structures, which consists of superconducting thin films (with a thickness $d < \lambda_L$) on the surface of a bulk substrate. There are two types of multilayers; superconducting-insulating-superconducting (SIS) structures, and superconducting-superconducting structures (SS bi-layers). In a parallel B_{ext}, films with a $d < \lambda_L$ have an extremely large B_{c1} as shown in Section 2.1.6, such that vortices can only be created in the film at extremely large B_{ext}. The thin films can remain in the superconducting state to much higher applied B. Thus, a parallel B passing through the thin film decays exponentially over the depth of a film. A general equation for multilayer structures is Eqn. 2.44, assuming that the thin films are the same material and the same thickness.

$$B = B_0 e^{-Nd/\lambda_L} \tag{2.44}$$

Where N is the number of thin film layers of the same material. As λ_L varies for different materials, this equation must be repeated/altered if a multilayer consists of different superconductors. The bulk substrate will still be witness to the same magnitude of B, however the B on the surface of the multilayer structure will be larger, such that a larger E_{acc} is produced within the cavity. The behaviour of B through a multilayer structure is shown in Fig. 2.3.

The main difference between multilayer and bi-layer structures is the presence of an insulating layer. The insulating layer is thought to intercept a vortex and localise the dissipation in the thin film layer [78]. The insulating layer stops vortices producing an avalanche effect and penetrating through the whole structure as more energy is

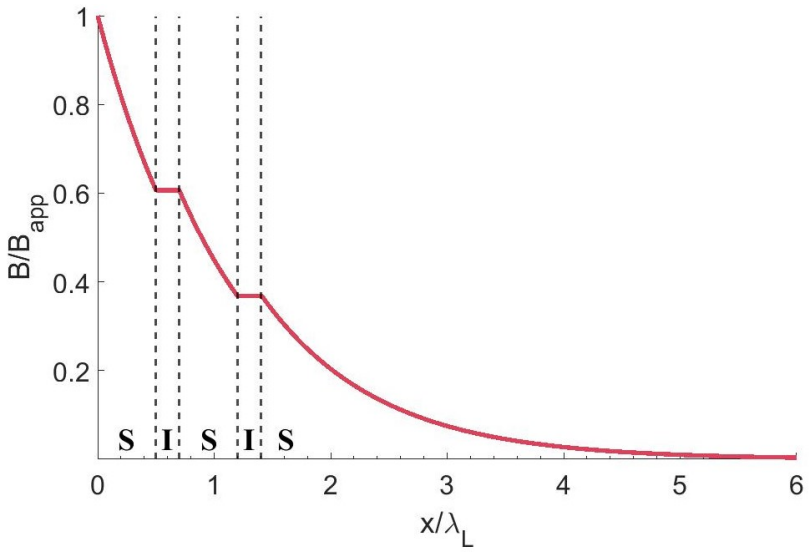

Figure 2.3: The magnetic field decay with B applied from one side of a multilayer consisting of two thin films (S) and two insulating layers (I) to a bulk substrate.

required at the next superconducting boundary to form new vortices. It should be noted that whilst thin films have a high B_{c1}, impurities or dislocations can allow vortices to form in localised areas.

It was long thought that LTB techniques affected the surface layers of the cavity, producing a similar structure to a SS bi-layer. It is known that all LTB processes described above yield a larger λ_L, and therefore a reduced screening current in the outer layer exposed to the RF field. The larger λ_L in the surface layers could be interpreted as an SS bi-layer, and thus a SS interface energy barrier for flux penetration could be present at the boundary between the dirty layer and the clean bulk superconductor. The interface energy barrier between the two regimes could be similar to the Bean-Livingston barrier at the superconductor-vacuum interface [78]. This interface energy barrier could further increase B_{vp}, such that there is a greater B_{surf} and a greater E_{acc}. It has been argued that only the interface energy barrier can prevent B_{vp} at defects as the order parameter can recover in the localised area of the defect at the interface, but not at the boundary [18]. The study by Junginger et al. involved bilayers composed of two different superconductors, whereas the results they produced on LTB Nb only showed a small increase in B_{vp}, this could be due to pinning centres present in the sample surface.

2.3 Magnetometry

To determine if new materials are suitable for SRF conditions, they must first be investigated. To test under RF conditions full size cavities can be deposited and tested, or large flat samples can be deposited for tests in a quadrupole resonator (QPR) or a choke cavity. However, depositing full cavities is expensive and requires a dedicated deposition facility. Additionally, RF tests take a long time which do not allow parameter optimization during deposition.

The B_{surf} is the limiting factor for SRF cavities. To increase E_{acc} of the cavities, B_{surf} must be increased. Thus, it is logical to try and increase B_{vp} in a DC magnetic field. This allows samples smaller than a full size cavity to be deposited reducing time and cost of deposition. Additionally, DC magnetometry tests are typically much faster than RF tests, which if done properly, can allow deposition parameter optimisation. Whilst magnetometry exists commercially, it is not designed for the investigation for certain SRF materials, such that new in house facilities have also been made to investigate SC's for SRF applications.

2.3.1 Vibrating Sample Magnetometry

Vibrating sample magnetometry (VSM) was first developed by Simon Foner in 1955 and reported in 1959 [94]. Although the VSM was developed 60 years ago, it is one of the most sensitive commercial instruments for magnetometry, allowing magnetic moments down to $\times 10^{-5}$ and $\times 10^{-6}$ emu [94] to be detected, with only a few changes to the original design in recent years. The original design consisted of a pickup coil placed between the poles of a dipole magnet (much larger than the pickup coil, shown in Fig. 2.4). The sample would be weighed, then glued to a sample mount and placed inside the pickup coil, however in modern magnetometry samples can also be mounted using friction in removable sample straws, see Section 3.3.1. A B is applied perpendicularly to the direction of oscillation, which in turn induces a magnetic moment (m) in response to B_{ext}. The sample is oscillated repeatedly through the pickup coil by using the loudspeaker with a set frequency, which in turn which induces a voltage in the pick up coil.

Simultaneously, a reference sample oscillates through the reference coils (4 and 6 respectively in Fig. 2.4), and the sample and reference sample have a common member [94]. The induced voltages in both coils are directly related in phase and amplitude, with the known voltage induced in the reference coils being phased to balance the voltage from the pickup coils. This voltage is the directly proportional to the magnetic moment of the sample [94].

Modern, commercial VSM's no longer use a loudspeaker, and instead use an oscillator to drive the sample. An amplifier is used to amplify the signal generated in

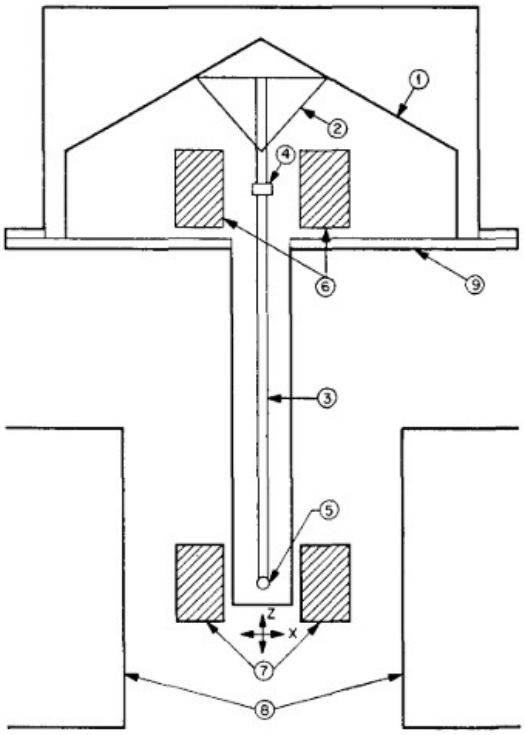

Figure 2.4: A schematic set up of the vibrational sample magnetometer by Foner in 1955 [94]. 1) Loudspeaker transducer 2) Conical Paper cup support 3) Drinking straw 4) Reference sample 5) Sample 6) Reference coils 7) Sample coils 8) Magnet poles 9) Metal container, [94]

the pick up coils, and a lock in amplifier is used to pick up the signals produced at the driving frequency. This removes all other frequencies which may be present such as a turbo pump, lights etc. Additionally, commercial VSM can also come with a DC SQUID sensor option, which can detect m down to 8×10^{-8} emu at 7 T [19] due to measuring the fluctuations in the magnetic field associated with one flux quantum (Eqn. 2.33). This is due to a SQUID consisting of 2 Josephson junctions connected in parallel in a superconducting loop [95].

Figure 2.5 shows the coil configuration inside a modern VSM with a DC SQUID sensor. There are four coils in total. A DC field is applied by the use of a large superconducting coil much larger than the sample. An AC field can be applied to the sample by a smaller coil which is still larger than the sample, and is usually normal conducting due to the heat load generated by an AC current being larger in a superconducting wire than a normal conducting wire. Finally, there are 2 inner coils (measuring coils in Fig. 2.5) wound in opposite directions. When B_{ext} is applied by

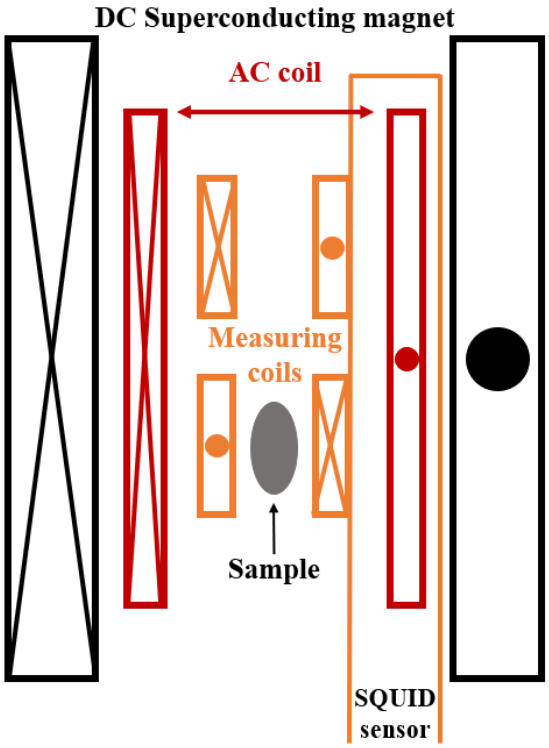

Figure 2.5: The coil configuration inside a VSM with a SQUID magnetometer. The crosses indicate the coil moving into the page, and the dots indicate the coil moving out of the page.

either the AC/DC coil, no voltage (V) is induced in pickup coils due to being counter wound with the same number of turns. A SQUID sensor can be damaged in a strong magnetic field so they are screened with the variations in the field transferred to the SQUID through the measuring coils [20].

2.3.1.1 Limitations

VSM's suffer some technical limitations. As the sample is placed in a B produced by a coil with a geometry larger than the sample as shown in Fig. 2.5, the B_{app} is produced over the whole sample, which can produce edge effects on the sample. Edge effects are localised flux enhancements due to the geometry of the sample. Flux enhancements can be accounted for if the demagnetisation factor is known, however it is difficult to determine for small, irregular shapes. The local increase in B can cause a breakdown in the Meissner state at a lower B_{ext}. Therefore B would enter the sample at a lower field, producing a lower B_{vp} than expected.

Samples are mounted in straws and packed in by a person, so it is possible that

the sample will not be perfectly parallel with B_{ext}. Thus, a normal component of the magnetic field will be present on the sample surface, which can also produce an early B_{vp}. There has been multiple discussions on the measurement procedure to accurately determine B_{vp} [96]–[100].

To investigate superconducting films, the small samples which are tested in a VSM are usually cut from a larger sample to fit inside the sample straw. During the machining process impurities can be introduced to the samples from the machining tools, which again can cause early B_{vp}.

One of the main limitations is that the B in a cavity is applied only from one side of the superconducting film, while in VSM the B is applied to both sides. When a B is applied from both sides of a sample, the flux may not break in through the superconducting face that is not the face of interest. For example, the boundary between sputtered Nb and a Cu substrate. Additionally, for multilayer samples, B would penetrate through the insulating layer such that the shielding expected to be produced by the thin films [16] would not be observed, as shown in Fig. 2.6.

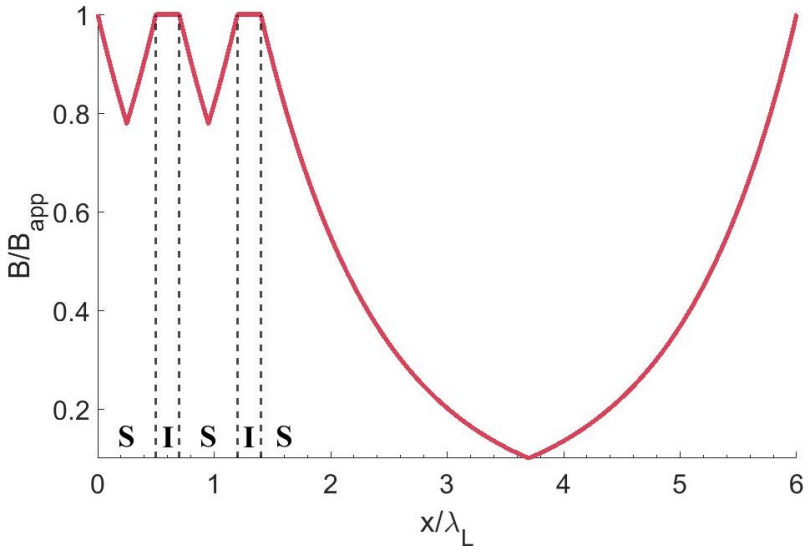

Figure 2.6: The magnetic field through a multilayer in a VSM. The multilayer consists of two thin films (S) and two insulating layers (I) to a bulk substrate

2.3.2 Localised magnetometry systems

As previously discussed, one limitation present in commercial magnetometry is that a magnetic field is applied over the whole sample. To bypass these limitations a few magnetometry facilities have been developed with the main aim of producing a

localised B to a sample surface. Thus, B is only applied to one side of the sample, and much smaller than the total sample size.

2.3.2.1 Cylindrical tube facilities

One method to overcome unknown flux enhancements is to use long SC cylinders, which are longer than the measurement coil. One of these systems has been developed by A.S. Dhavale et al at Jefferson Laboratory which tests hollow, cylindrical samples in a DC magnetic field which removes the demagnetisation factor and improves field homogeneity during testing [101]. Unlike a VSM, this system requires to only have 1 measurement coil or else the signal would not be picked up.

A second facility has been previously suggested by Gurevich and built at Daresbury Laboratory utilising tubular samples [102], [103]. Similar to the previous measurements, a relatively long (≈20 cm long and ≈12 mm diameter) sample tube is placed in the middle of a short (3 cm in length) superconducting magnetic coil, such that B_{ext} is parallel to the outer surface of the cylinder. It was demonstrated that this method allows field penetration measurements where a parallel B is applied from only one side, whilst also ensuring edge effects are negligible. The tube does not oscillate to induce a V. Instead, two magnetic field strength sensors (e.g. Hall-effect sensor/probe) were placed on the central plane of the magnet: one inside of the superconducting cylinder and the other outside to measure the applied field to the surface and the penetrated field respectively. The main disadvantage of this facility is that samples must be deposited on the outside wall, which requires a dedicated deposition facility and deposition conditions. These parameters are not directly translatable to the coating on a RF cavity.

2.3.2.2 Third Harmonic systems

C. Antoine et al. have developed an AC magnetic susceptibility and third harmonic measurement system [104]–[108] to study flux dynamics in superconducting samples. The system uses a normal conducting solenoid with a diameter much smaller than the sample, and is placed at a normal to the sample surface. The measurements can be performed without edge effects being present [105]. The solenoid applies an alternating current for both excitation and detection in B_{vp} [109].

In the Meissner state the SC sample behaves as a 'magnetic mirror', and the alternating B is expelled from the sample. The sample temperature is slowly increased until the superconductor transitions into the Abrikosov state, in which the alternating B enters the sample. If the frequency of the AC is low (kHz), the vortices that are present due to the superconductor being in the Abrikosov state change the coil impedance, distorting the voltage induced in the coil which is independent of current

polarity [109]. The distortion produces odd number harmonic components, with the third harmonic having the largest signal.

The aim for this facility was to be able to produce B> 200 mT at temperatures as low as 2 K [109], however this proved difficult as the peak B produced was 114 mT [105]. The peak B is the limiting factor of this system, as Ito et al. [105] found that the minimum temperature the measurements could be produced was ≈ 5 K. However, their results were comparable to previous measurements of B_{c1} [34] of Nb indicating that third harmonic measurements are a valuable technique.

2.3.2.3 Field penetration facility - Solenoid

A joint team from Old Dominion University and Thomas Jefferson National Laboratory have built a DC penetration measurement set-up [110] which also applies B using a coil at a normal to the sample surface. This system uses a SC solenoid to apply a much larger B, up to 600 mT on the sample surface. This technique has simulated the B on the sample surface for various currents, and B_{fp} is measured by Hall probe sensors placed on the opposing side of the sample, sensitive perpendicular to the sample surface.

This facility is cooled by using liquid helium (LHe), and therefore operates at 2.00 and 4.35 K [110] which is one of the limiting factors.

Limitations

Magnetic field penetration facilities that use a coil placed at a normal to the surface of a SC must apply a perpendicular field to a certain degree. This does not matter whilst a thick SC in the Meissner state, as the sample behaves as a magnetic mirror - i.e the perpendicular field is cancelled out and the parallel component remains. However, it is possible for the normal component of B to break through the superconductor much earlier than when a parallel B is applied. To investigate multilayer structures which contain thin films, the B will not be parallel in the surface of the thin films and the effect of screening would be reduced.

2.3.2.4 Field penetration facility - Daresbury Laboratory

As mentioned previously in this section, whilst other commercial and in-house magnetometry exists, they consist of limitations. The tubular facility built at Daresbury laboratory (mentioned above) [102], [103] demonstrated that direct measurements of both the applied and penetrated field can be measured by Hall probe sensors. However, the tubular samples required a dedicated deposition facility which was not directly translatable to cavities. Thus, a new facility has been designed, built and commissioned at Daresbury Laboratory with the aim to produce a facility

that reduced these limitations. A DC magnetic field would be generated by a superconducting solenoid to ensure a minimal heat load to the cryogenic system, whilst using a high carbon C-shaped yoke with a small gap to direct B parallel to the sample surface from one side of the sample to the other, similar to that in a cavity. The poles of the magnet are detachable, so that new poles can be made to accommodate different sample geometries, such that curved samples or cavity cut outs could possibly be tested. The small gap between the poles reduces the stray fields produced by the magnet and constrains the fields to be parallel to the sample surface. Thus edge effects are negligible and should not affect the results.

The system investigates the field of first full flux penetration (B_{fp}), which is the magnitude of the magnetic field applied to the surface of the sample at which B penetrates from one side to the other. Both the applied and penetrated field are measured directly by Hall probe sensors, similar to the tubular facility.

The initial idea was to produce a facility with a fast sample turn-around, such that parameter optimisation can happen in real time. As discussed in Section (4.4) the first facility could not be cooled to a low enough temperature to run the magnet. Further development was undertaken to cool the samples to a lower temperature using a new cryogenic facility. The samples were mounted directly to a cryo-cooler to allow sufficient cooling and ensure low temperatures could be reached, with the trade off that the system takes longer to reach the desired temperatures. The design, testing and commissioning of the system is described in Chapters 4 and 5.

Chapter 3

Low temperature baked ellipsoid measurements

A Quantum Design Physical Magnetic Property Measurement System (MPMS) 3 user facility is housed at Rutherford Appleton Laboratory (RAL). This facility was used for testing small superconducting samples in the VSM set up, using the SQUID sensor read out. The first objective was to determine the T_c of the samples. If the sample transitioned into the superconducting state, the next test was to determine B_{vp} to try and determine the quality of the superconducting sample. Whilst many samples were tested using this method, only the most well prepared and well known samples are reported. The majority of this chapter has been published in [1].

The aim of this study was to investigate whether the increase in E_{acc} caused by different LTB processes could be correlated to an increased B_{vp}, and could be measured with DC magnetometry. To ensure the results were reliable, high temperature annealed ellipsoidal samples were used. Ellipsoids were used to eliminate unknown flux enhancements at sharp edges. Additionally, the flux enhancement at the equator of the ellipse is also is also well known. Each sample was made to be 10 mm tip to tip of the ellipsoid, with a 4 mm diameter at the equator.

3.1 Sample preparation

Four ellipsoids were machined from the same Nb piece. Each ellipsoid was hand polished to remove any edges that were produced by machining. Each ellipse then underwent buffer chemical polishing (BCP) to remove any damaged surface layers. Annealing samples at high T has been found to remove pinning [42], thus the ellipsoids were annealed for 5 hours at 1400 °C to remove stresses within the Nb that were either present before machining or introduced during the machining process. To remove any contaminants that could have been introduced from the oven during the annealing

process another round of BCP was performed which removed ≈10 µm. From this point forward, each ellipse had a variation in the treatments that followed.

One ellipsoid saw no further treatment to be used as a baseline sample to compare all further treatments too, and is referred to as 'baseline', and weighed 768.4 mg.

One ellipsoid was baked at 120 °C for 48 hours only, and is referred to as 120 °C, which weighed 768.2 mg. A second LTB ellipse underwent a two step bake under vacuum. The two step bake consisted of a 75 °C for 5 hours followed by a 120 °C bake for 48 hours, and is labelled 75/120 °C, which weighed 772.7 mg.

The remaining ellipse was sent to Fermi National Accelerator Laboratory (FNAL) for N infusion. The sample was heated to 800 °C under vacuum and remained under high vacuum for 3 hours. The temperature was then reduced to 120 °C and 33.3 mbar of N was injected into the furnace. The pressure and temperature was maintained for 48 hours [15]. This sample is labelled as the 'N infused' ellipse, and weighs 770.4 mg.

3.2 Testing considerations

The MPMS 3 uses a solenoid to produce a uniform B with a volume that is much larger than the sample. Thus the sample is placed in a uniform B. However this uniform B will be distorted when a superconducting sample is present. A superconducting ellipse will expel any external flux whilst in the Meissner state. The inner diameter of the coil does not change, but the free cross sectional area will vary as the diameter of the ellipse varies from tip to tip. At the equator of the ellipse, the free space between the ellipse and the solenoid is at a minimum, and the flux lines will the much more dense than at the tips. Thus, B at the equator (B_{eq}) is denser than the external magnetic field (B_{ext}). The demagnetization factor N relates B_{eq} to B_{ext} by $B_{eq} = B_{ext}/(1-N)$ [97], where N = 0.13 for the ellipsoids used in this study. The MPMS 3 is ideally suited for samples with length shorter than 5 mm, due to the size of the measurement solenoids [19]. For longer samples the magnetic moment will be underestimated as the samples will induce a small V in the oppositely wound measurement coil, that slightly opposes the induced V in the measurement coil in which the sample is situated. These samples are 10 mm long. The expected magnetic moment for a perfect diamagnet assuming a demagnetization factor of N=0.13 would be about 20 % higher than the data obtained for an irreversible magnetization curve.

3.3 Method

3.3.1 Sample mounting

The samples were mounted inside a plastic straw using a guide to ensure the sample was at roughly the correct height. The sample was moved within the sample straw using cotton buds to move the sample to the correct height shown on the guide to ensure that the sample is situated inside one of the pick-up coils. The sample was packed into the straw using off cuts of the straw to wedge the sample in place, whilst trying to keep the tip of the ellipse as close to vertical as possible when the sample straw was mounted in the MPMS 3. The end of the straw was sealed using Kapton tape to ensure the sample cannot fall out during testing. The straw was attached to the sample rod, again using friction, which was then installed inside the MPMS 3. The system then performs a 'latscan'. During the latscan the sample is slowly moved through the measurement coils to induce a V, which is then found as a function of distance through the measurement coils. This allows a fine adjustment by the sample height within the system to ensure the centre of the sample is in the centre of the measurement coil. The facility can then be cooled to a defined set point by the user.

3.3.2 Transition temperature

Once a sample has been installed in the system, T_c is the first property of the sample that is measured to ensure the sample is superconducting, and to ensure that when the sample is warmed up in later tests all the flux that is trapped/pinned in the superconductor is expelled. The sample is held at a $T > T_c$ (by assuming a theoretical value for T_c) for 5 minutes to ensure the sample is in thermal equilibrium. An $B_{ext} = 10\,mT$ is applied by the solenoid, inducing a magnetic moment (m) in response. The B is sustained as T is slowly reduced. When T is reduced to $T_c(10\,mT)$, the superconducting sample transitions into the Meissner state which expels the B flux, thus increasing the magnetic moment.

For a rough estimate, T_c can be estimated using the last point in the normally conducting state before the m changes, as this is the upper estimate for T_c and is the onset of superconductivity. Thus, when when the sample is warmed up to remove any trapped flux, it should be above this T. This analysis allows an approximate T_c to be quickly determined if it is required for further tests, such as hysteresis curves. However it is not an accurate way to report T_c as the transition is not always sharp.

For a thorough analysis of T_c, the mid-point of the transition (between the maximum and the minimum m, therefore known as $T_c(50\,\%)$) must be used. Additionally, the temperatures from 10 and 90 % of the change in moment can then be determined and used to show the error in the measurement/the quality of the sample. All three of these lines are shown in Fig. 3.1 for the 75/120 °C baked ellipse. If the

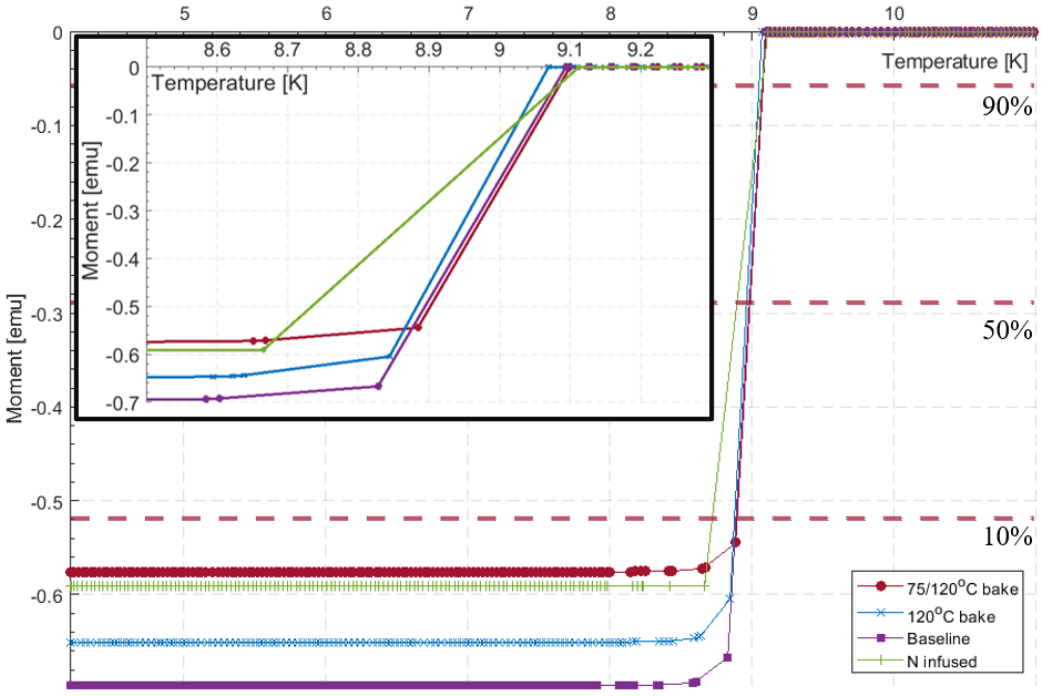

Figure 3.1: The transition temperature curve for Nb with various LTB performed, and the 10, 50 and 90 % lines shown to determine the corresponding T_c values, which are shown in Table. 3.1.

sample produces a sharp transition, the T_c(10 %) - T_c(90 %) error is extremely small. Samples with a transition over a large T range have a greater error. This method underestimates T_c as it is not the onset of superconductivity that is reported, however this is difficult to report with applied fields.

The T_c results for the LTB ellipses are shown in Table 3.1.

Label	$\mathbf{B_{eq}}$(mT)	$\mathbf{T_c}$(10 %) [K]	$\mathbf{T_c}$(50 %) [K]	$\mathbf{T_c}$(90 %) [K]
75/120 °C bake	11.502	8.895	8.986	9.077
120 °C bake	11.494	8.851	8.948	9.045
Baseline	11.469	8.860	8.955	9.066
N Infused	11.502	8.710	8.889	9.068

Table 3.1: The final point equal to the normal conducting moment during the T_c tests as shown in Fig. 3.1.

The same process should be repeated whilst the sample is heated from $T \rightarrow T_c$, then averaged with the data from cooling the sample, as this reduces the error due to

the thermal lag. Thus producing a more accurate T_c measurement. Due to insufficient time on the facility, the warming data was not performed.

3.3.3 Hysteresis curves

3.3.3.1 Method

Samples were cooled in the absence of B_{ext} - a zero field cool-down (ZFC) - before for each sample underwent a 5 quadrant hysteresis loop measurement at fixed T. The reported B_{ext} is determined by the current known to be passing through the solenoid at a given time, that is generating B. However, the B_{ext} could be different due to the history of the magnet, as flux could be trapped within the solenoid [19]. In an attempt to minimise the trapped flux within the solenoid the magnet was degaussed after each temperature run. After the degauss the sample was heated above T_c to remove any pinning that could be present in the sample. The samples were held at $T > T_c$ to ensure the ellipsoids were in thermal equilibrium and that all trapped flux had been removed. The samples were then warmed up, and held at 12 K for 5 minutes to expel any flux that could be trapped within the sample, before undergoing ZFC again. As B_{ext} is swept it does not stabilise at a specific value, hence the reported B_{ext} are calculated averages [19].

Each testing cycle begins at $B_{ext} = 0$ mT, such that no m is generated. Next, B_{ext} is slowly increased resulting in the superconductor producing a perfect diamagnetic response shown in Fig. 3.2 by the initial curve (the straight line in fourth quadrant starting from the origin, shown in red). It can be observed that as B_{ext} is initially increased, the resulting m is not perfectly linear, which has been observed for each sample. When the B on the surface of the superconductor reaches B_{vp}, B enters the superconductor dividing the ellipse into normal conducting/superconducting regions in the form of vortices. Once the vortices have entered the sample, the superconductor has transitioned from the Meissner state to the Abrikosov state and the response of m(B) is no longer linear. This is due to more vortices penetrating into the superconductor, in turn reducing the superconducting volume. As B_{ext} continues to be increased, m continues to increase up until B_{c2}, where m becomes slightly positive due to the paramagnetic response of the Nb in the normal conducting state. The B_{ext} is then decreased. Decreasing B causes the flux within the ellipse to be expelled from the superconductor, and m becomes negative again. In the case of a perfect superconductor with no pinning centers, impurities etc., the m produced by the decreasing would be the same for both increasing and decreasing B_{ext}. It can be seen in Fig. 3.2 that this is not the case for these carefully prepared ellipsoids. The absolute value of the m is reduced compared to the initial curve. This is due to flux trapped within the sample.

After B_{ext} has been reduced back to zero, B is ramped at a faster rate with reversed

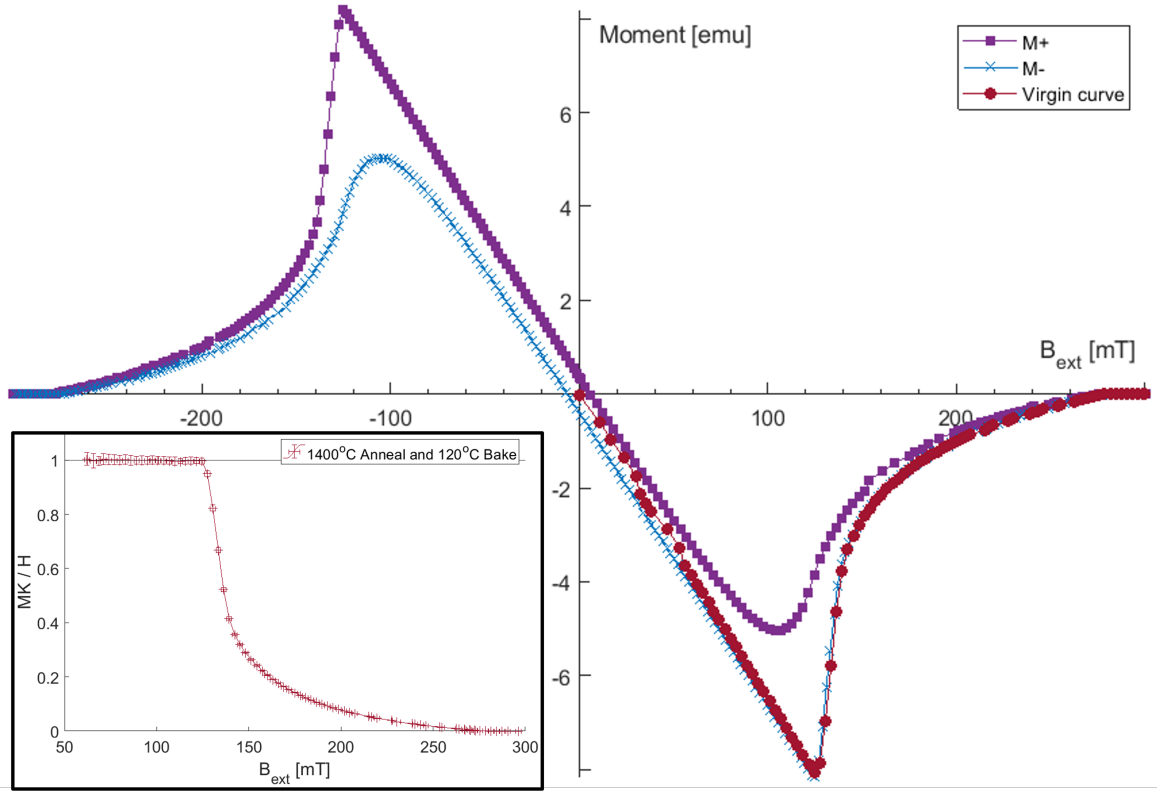

Figure 3.2: The hysteresis loop for the 120 °C baked ellipse. The initial increase from $0 \rightarrow B_{max}$ is shown in red. The positive and negative m used to determine pinning strength are shown in purple and blue respectively. The standardisation curve used to determine B_{vp} is shown in the bottom left quadrant, which is determined from the initial increase in B from 0 mT. The last point within error of the normalised value (1) is taken as B_{vp}.

polarity (B is applied in the opposite direction). These results are shown by the purple and blue curves in Fig. 3.2. Each hysteresis cycle ends by repeating the initial virgin curve to ensure that the sample has not moved during the test.

3.3.4 Determining the field of first flux penetration

To determine the field of first vortex penetration, B_{vp}, only the initial curve produced by increasing B_{ext} is used as the superconductor has no magnetic history which can affect the results. Whilst in the Meissner state, the response of the superconductor is linear due to B_{ext}, and can be described as $m = K^* B_{ext}$ [111], where K^* is a constant which is proportional to the superconducting volume and can vary slightly between samples. The normalisation produces $1 = mK^*/B$ in the Meissner state and is shown

in the bottom left quadrant of Fig. 3.2. The B_{vp} can be determined by the last point to be within error of the normalised values. Once B_{ext} has been found, the local field must be found for the increased B at the equator of the ellipse. For an ellipse, the demagnetisation factor N=0.13. Thus, $B_{eq} = B_{vp}/0.87$. This method was repeated for each sample at each temperature.

3.3.5 Determining irreversible pinning strength

In an ideal pin-free superconductor, once B_{ext} has been increased above B_{c2} and is then decreased, the m produced by the sample is identical to the initial magnetisation loop. Realistically, samples are not pin-free, such that the return loop for the magnetisation curve will differ from the virgin curve. This was observed for all the hysteresis loops for each ellipse. To determine the pinning strength produced by each treatment the irreversible magnetisation was calculated using the hysteresis loops shown in Fig. 3.2, using both the positive and negative moment, M^+ and M^- respectively, where M^+ is the magnetic moment once B_{ext} has been increased up to a maximum in a 'positive' orientation and is being decreased to a maximum in a negative orientation, and M^- is the opposite. The irreversible magnetisation is then found using $M_{ir} = (M^+ - M^-)/2$ [112], with both M^+ and M^- shown in Fig. 3.2, and M_{ir} plotted as a function of B_{ext} for each sample at 4.2 K in Fig. 3.6.

The largest M_{ir} is observed at B_{vp}, as the return loop does not follow the virgin curve due to pinning within the sample. The amount of flux pinning within a sample is determined when B_{ext} has been removed, thus $M_{ir}(0\,mT)$ is the pinning strength (M_{pin}). This is because the the sample is producing a m without a B_{ext}. Table 3.3 shows M_{pin} for each treatment.

3.4 Results

A hysteresis loop was performed at 2, 3, 4.2, 5, 6, 7, 8, and 9 K for all samples except the 120 °C baked ellipse, which was only tested at 4.2 K. Figure 3.3 shows the effect of temperature on each hysteresis loop.

It can be seen that the increase in T reduces the critical fields of the ellipses. Additionally, the hysteresis loops produced for the Baseline, 120 °C bake and the 75/120 °C bake have similar looking curves across all T. I.e. each ellipse generates a smooth transition as B_{ext} is varied. This is not the case for the N infused sample. Once the sample had been witness to $B_{ext} > B_{c2}$, there are sharp transitions in m visible in the first and fourth quadrant, and at low B_{ext} shown in Fig. 3.3. The sudden transitions indicate flux jumps, which are only visible for the measurements performed at 2 K. Flux jumps indicate that some B was trapped within the sample which suddenly moves within the sample from one pinning centre to another. The

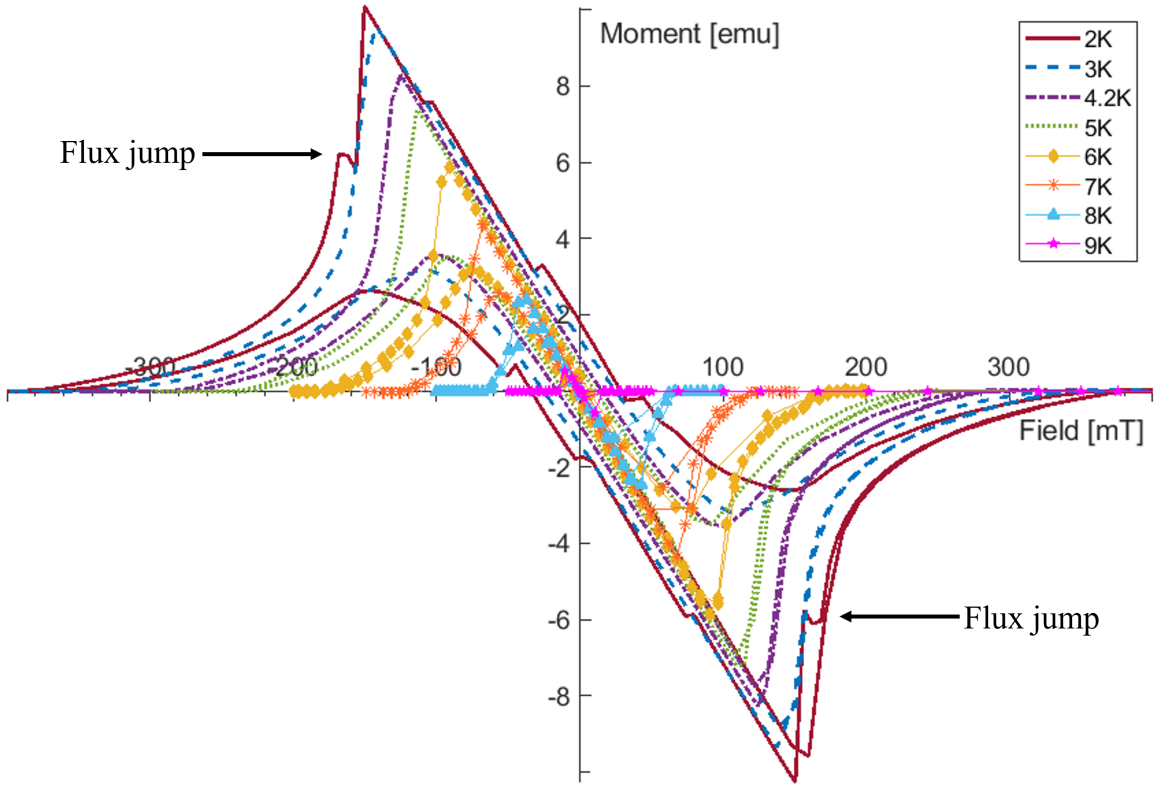

Figure 3.3: The hysteresis loops performed on the N infused sample at varying temperatures. Flux jumps can be seen once the sample had been taken above B_{c2} for the 2 K data only.

sudden movement is due to a change of forces as B_{ext} is varied. It is shown in Fig. 3.3 that the flux jumps appear when B_{ext} is being ramped, indicating that the flux is moving from one pinning centre to another to allow more vortices to enter the ellipse. This only happens after the ellipse has been witness to $B_{ext} > B_{c2}$, such that the superconductor had previously transitioned into the normal conducting regime. As no flux jumps are present in the virgin curve, but are present once the ellipse had transitioned into the NC state, it can be assumed that the flux was been trapped after the sample has transitioned back into the NC state from the SC state.

The B_{vp} was found for each sample at various temperatures by using the standardisation curve method described in Section 3.3.4. Once B_{vp} was determined, B_{eq} was found by accounting for the demagnetisation factor, and $B_{eq}(T)$ could be plotted, shown in Fig. 3.4. It was determined that B_{eq} followed a T^2 dependence, the same dependence as B_c shown in Eqn. 2.32, such that $B_{eq}(T) = B_{eq}(0K)(1-(T/T_c)^2)$. Other dependence's of $B_{eq}(T)$ were investigated, such as one proposed by French [113]. Similarly to French, the authors found the proposed fit unsuited to the presented data,

as French found in Ref. [113]. The $B_{eq}(T^2)$ produced a *pvalue* $= 3.1 \times 10^{-7}$, thus determining the data is statistically significant. Fitting a straight line to $B_{eq}(T^2)$ allows $B_{eq}(0\,K)$ and T_c to be derived by determining the intersection of the Y and X axis respectively. Figure 3.4 and Table 3.2 show that there is no significant difference in B_{eq} produced by LTB or N-infusion compared to a baseline sample when tested in DC magnetometry. Table 3.2 also shows that there is no change between extrapolated T_c between samples.

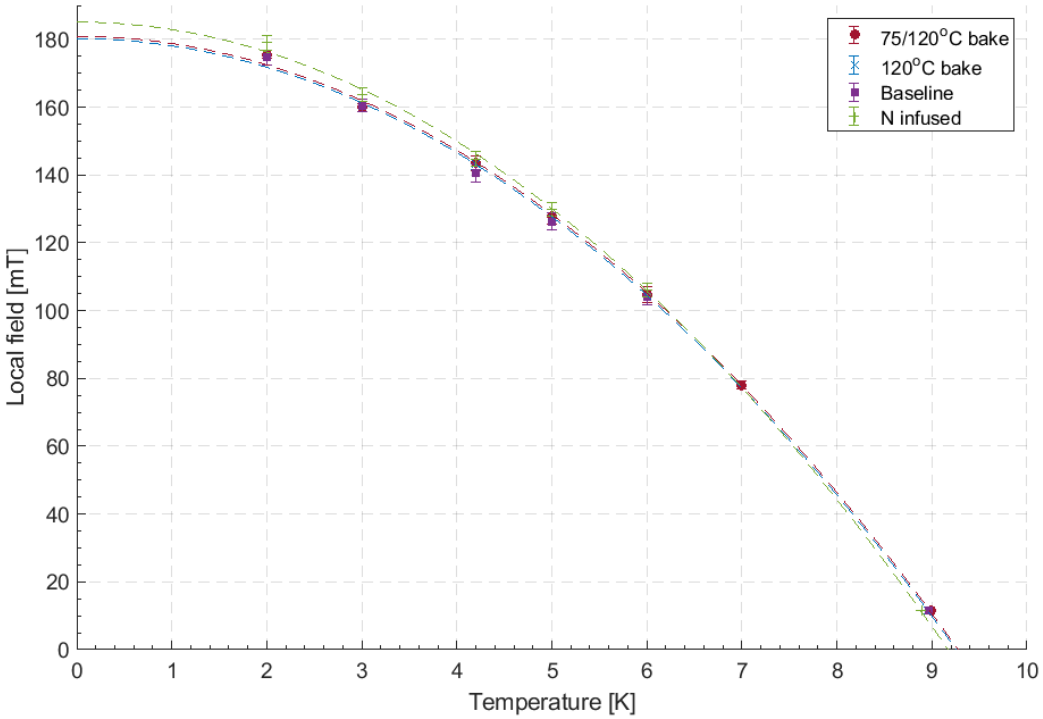

Figure 3.4: The local magnetic field of first flux penetration as a function of temperature for all 4 samples. The line of best fit is shown for each sample except the 120 °C baked sample as only 2 points were taken.

One clear difference between the four samples is the pinning strength, which is shown as an inset in Fig. 3.5 and is also presented in Table 3.3. The difference in m for increasing/decreasing B_{ext} indicates the pinning strength. A pin free sample would produce m = 0 for B_{ext}= 0 in both cases. The sample with the weakest pinning is the baseline sample. The 120 °C and 75/120 °C samples have a similar pinning strength, and a greater amount of pinning than the baseline sample. The N infused sample produces the greatest amount of pinning for this set of samples.

	$\mathbf{B_{eq}(T)}$, mT **for each treatment**			
T, K	**Baseline**	120 °C **bake**	75/120 °C **bake**	**N infusion**
2	174.6 ± 2.19	-	175.5 ± 1.21	179.0 ± 2.06
3	160.5 ± 1.84	-	159.9 ± 1.09	163.7 ± 2.07
4.2	140.7 ± 2.64	143.1 ± 1.55	143.4 ± 2.30	144.7 ± 2.18
5	126.3 ± 2.41	-	127.7 ± 2.18	129.9 ± 2.07
6	104.0 ± 2.18	-	104.7 ± 2.19	106.16 ± 2.07
7	-	-	78.0 ± 1.09	-
$\mathbf{T_c}$ (0 mT)	9.24 ± 0.04	-	9.24 ± 0.03	9.17 ± 0.03

Table 3.2: The local magnetic field of full flux penetration for each set temperature and the critical temperature determined by using a linear dependence for $B_{eq}(T^2)$.

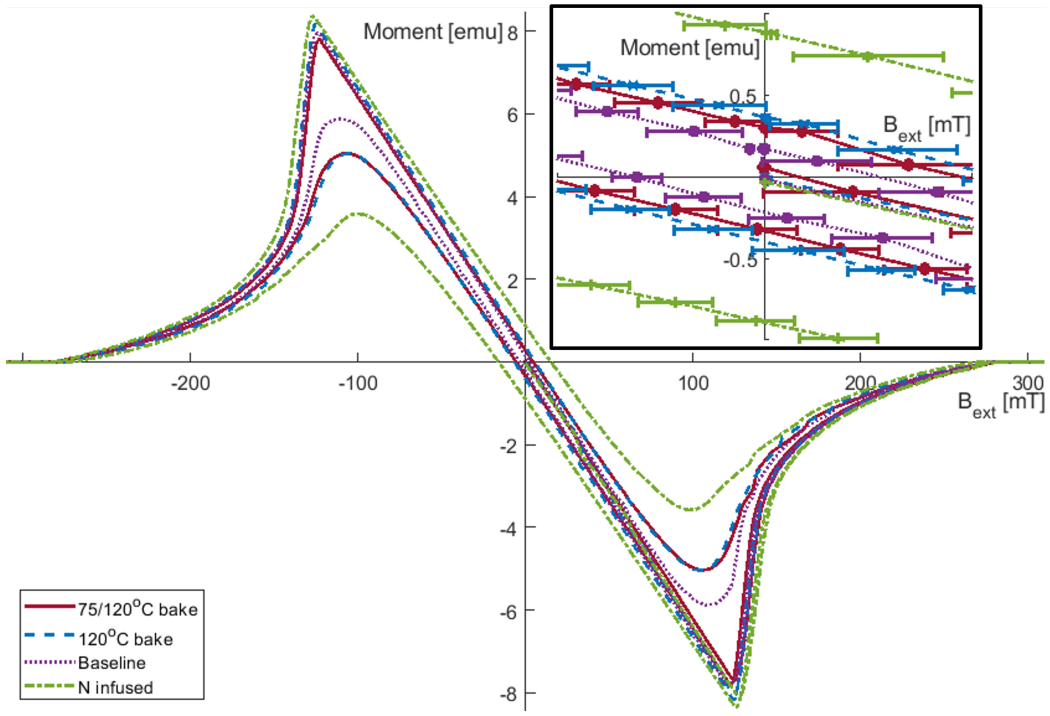

Figure 3.5: The hysteresis loops at 4.2 K for all four samples, with a magnified inset image in the second quadrant depicting the residual m at $B_{ext} = 0$ mT.

3.5 Discussion

Four Nb ellipsoids have been well prepared to investigate the effects of LTB. Each sample was machined from the same piece of Nb. The samples were annealed to eliminate pinning within the samples that was either already present or produced

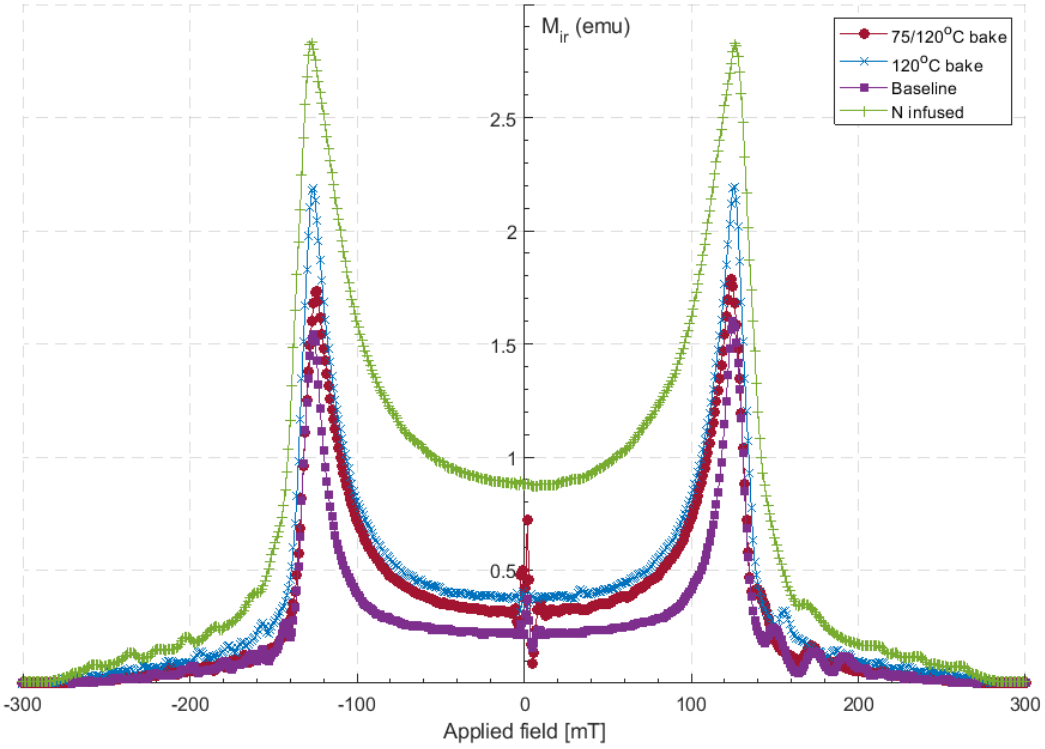

Figure 3.6: The irreversible pinning (M_{ir}) for each LTB treatment for measurements performed at 4.2 K.

	M_{pin}, **emu for each treatment**			
T, K	**Baseline**	120 °C **bake**	75/120 °C **bake**	**N infusion**
2	0.44 ± 0.016	-	0.82 ± 0.0076	1.9 ± 0.0063
3	0.24 ± 0.0063	-	0.50 ± 0.0071	1.7 ± 0.0085
4	0.22 ± 0.0058	0.39 ± 0.0090	0.2847 ± 0.013	0.88 ± 0.0051
5	0.94 ± 0.0075	-	0.18 ± 0.0057	0.64 ± 0.0056
6	0.082 ± 0.0084	-	0.14 ± 0.0055	0.37 ± 0.0058
7	0.076 ± 0.0058	-	0.067 ± 0.0066	0.19 ± 0.0058
8	-	-	0.035 ± 0.0055	0.055 ± 0.0055

Table 3.3: Irreversible magnetic moment obtained at B_{ext}=0 mT indicative of the pinning strength.

during the machining process to produce accurate results. Three of the four samples saw further LTB treatments. One Nb ellipse witnessed a single 120 °C bake for 48 hours, a second ellipse witnessed a two step bake which included an initial 75 °C for 5 hours followed by a 120 °C for a further 48 hours. Both baking process were

performed under vacuum. The final ellipse was sent to FNAL for N infusion, which consists of heating the sample to 800 °C for 3 hours under vacuum. After this step the temperature is reduced to 120 °C and 33.3 mbar is injected into the furnace. Both the temperature and N pressure was maintained for 48 hours.

All four samples were tested using a MPMS 3 VSM using a SQUID sensor readout. The ellipsoids underwent a field cool-down to determine a T_c(10 mT), where B was small to produce a value close to T_c(0 mT). Table 3.1 shows that the T_c is similar across all samples. The N infused sample has a greater T_c(10 %) - T_c(90 %) due to a measurement error by the facility.

Hysteresis loops were performed on the samples at set T points. Initially the samples were held at a set T before a hysteresis loop was performed to ensure the sample was in thermal equilibrium. The initial ramp up in B was used to determine B_{vp} due to the samples having no magnetic history, whilst also taking the well defined demagnetization factor into account. The B_{eq}(T) for each sample is shown in Table 3.2 and Fig. 3.4.

The B_{eq} had a linear dependence on T^2. The line of best fit was extrapolated to 0 K, such that the baseline sample produced a B_{eq}(0 K)=179.9 mT. This is comparable to previous B_{c1} measurements using muon spin rotation (μSR) of 174 mT [42] and using magnetometry 173.5 mT [34]. Comparing B_{eq} for all 4 samples determines that there is no significant increase in B_{eq} produced by the LTB. Thus, LTB does not produce an interface energy barrier for flux penetration that can be observed using DC magnetometry.

Studies performed by Tan et al. [17] and Junginger et al. [18] using bilayer ellipsoids consisting of distinct MgB_2 and Nb_3Sn thin films on bulk niobium are useful to compare to the LTB studies reported here as both tests were completed using a MPMS SQUID magnetometer. These studies found that a layer of MgB_2 with a thickness of 200 nm on Nb increased B_{vp} by approximately 40 mT compared to uncoated niobium [17]. Thus, a thin film of a second, different superconductor causes a delay in B_{vp} into the bulk of the sample to larger fields.

An increase in B_{vp} could be attributed to the flux being pinned in the surface layers, which cannot be differentiated from an interface barrier being present in DC magnetometry. Flux can be pinned due to other process' other than the surface barrier. For example, flux can be pinned by the surface sheath [51] and surface flux pinning [114].

As there is no increase in B_{vp}, it can be verified that neither the interface energy barrier or surface pinning affects B_{vp}, which agrees with results produced by μSR on MgB_2 and Nb_3Sn bilayers on Nb [18]. The results produced by Junginger et al. suggest that B_{vp} should increase from a $B \approx B_{c1}$ up to $B \approx B_{sh}$ of clean Nb due to the outer SC layer. No dependence on thickness was observed, with a range of 50-3000 nm tested. Thus, it can be deduced that the increase in B_{vp} is due to the interface energy

barrier. Additionally, this study found a 10 mT increase in B_{vp} (from 178 to 188 mT) for 120 °C baked Nb. This increase could possibly be due to flux pinning present in surface layers closer to the SC-vacuum boundary than the implantation depth of the muons, ≈ 0.15 mm. Thus, an interface energy barrier might still be relevant for time varying RF fields. Comparing the results produced by the DC magnetometry studies on bilayers and LTB ellipsoids suggest that the interface energy barrier is only relevant for samples that consist of two distinct superconductors.

Another method used to determine B_{vp} was previously been presented by Roy et al. [99], which uses the square root of the standard deviation of the m from a linear trend as a function of B_{ext}, and is shown for the LTB samples in Fig. 3.7. This analysis method agrees with the technique presented by Wilde et al. [111] with a deviation in B_{vp} up to 5 %. The deviation in B_{vp} depends on T and the baking technique. However, both techniques determine that there is no significant change in B_{vp} due to various LTB techniques.

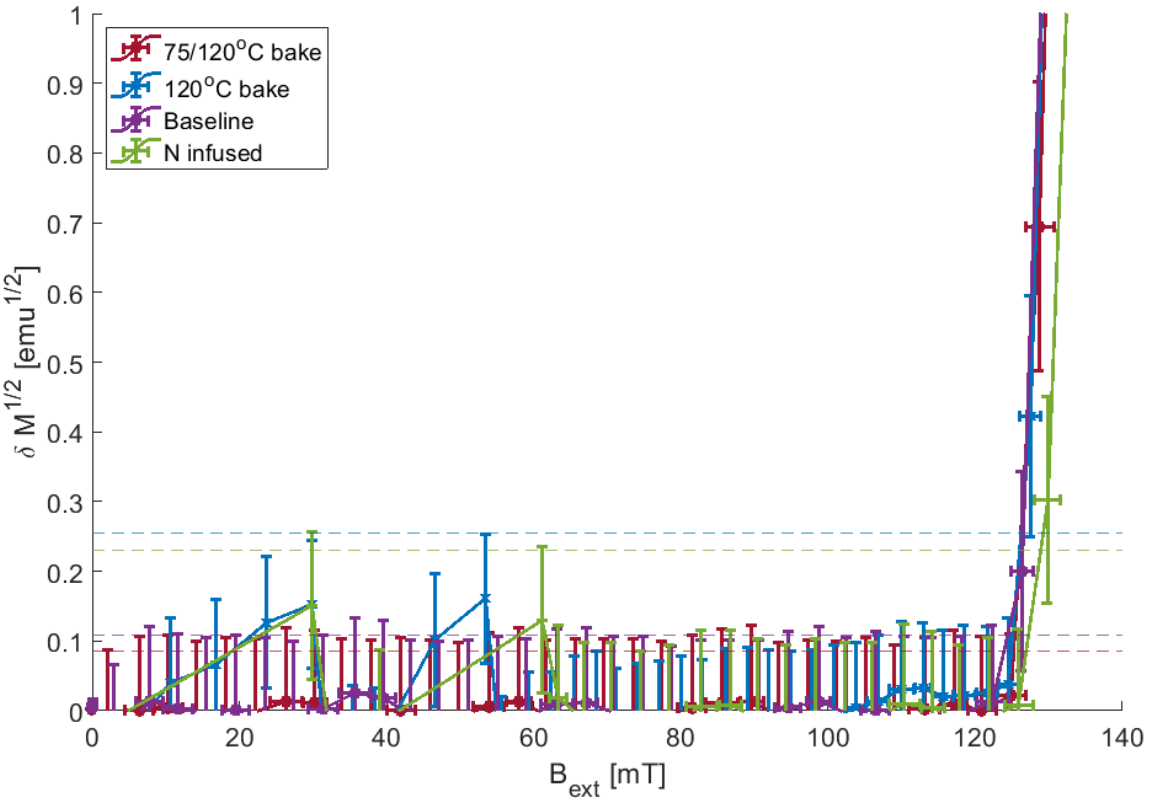

Figure 3.7: Determining B_{vp} using the method presented in Roy, Myneni, and Sahni, Supercond. Sci. Technol 21, 065002 (2008) [99]).

The method presented by Roy et al. also found 2 slopes using the square root

of the deviation method [99], and concluded that the slopes were either due to the Bean-Livingston surface barrier or due to the geometry of the sample. Repeating this analysis technique for the LTB ellipsoids did not produce the two slopes as Roy et al. found, which can be seen in Fig. 3.7. Thus, the initial slope witnessed must be due to the geometry of the samples.

The clear difference between each treatment is the amount of trapped flux produced by each LTB technique, which is shown in Fig. 3.5. Comparing M_{ir} allows the amount of trapped flux to be quantified, with the smallest values representing the least amount of trapped flux. The baseline sample had the lowest amount of trapped flux. The LTB samples had the next greatest M_{pin}, and finally the N infused samples had the largest M_{pin}. As the only variable between the ellipsoids is the LTB techniques which only affects the surface of the ellipsoids, it can be argued that the trapped flux is present in the surface layers of the samples. The pinning of the flux in the surface layers could be attributed to the delayed onset in the HFQS.

The pinning results agree with measurements performed by Furtado [115], in which Nb cylinders were annealed, followed by mechanical and chemical polishing, and finally pulled to produce physical stress to produce dislocations in the lattice. Each treatment was performed to alter the surface of the Nb. The conclusions stated that the condition of the Nb surface was the main factor for increased surface pinning. Mechanical polishing increased the amount of flux trapped within the sample, however a further buffer chemical polish (after machining) removed the flux pinning.

Electropolished cavities produce an onset in HFQS at $\approx 100\,\mathrm{mT}$ [72], and N infusion has been found to delay this HFQS onset up to a peak $B_{surf} \approx 190\,\mathrm{mT}$ [72]. Additionally, using a HF rinse to remove of the surface layers of the cavity returns in the increased HFQS to its previous values, and hence the N infusion only affects a few nanometers in the cavity surface [72]. Thus, the change in M_{pin} between each LTB ellipse must be attributed to changes in the surface layers.

If LTB produces samples which behave as a bi-layer, the depth of the 'dirty layer' produced by the LTB must have an optimal thickness. If the layer is too thin, a nascent vortice can behave as a nucleation site which allows the flux to enter the sample [116]. Checchin has suggested that an effective depth for a bilayer is 60 nm [48], which somewhat agrees with low energy μSR which has determined that LTB changes the magnetic profile in the samples up to 60 nm [77]. On the other hand, it has been observed experimentally that a 50 nm MgB_2 layer on bulk Nb produces an increase in B_{vp} compared to uncoated Nb [18].

Chapter 4

Magnetic Field Penetration Facility Design

4.1 Aims

The limiting factor on SRF cavities is the B_{surf} on the cavity walls, which is directly related to E_{acc} by a constant, such that constant = B_{peak}/E_{acc}. Thus, to increase E_{acc}, the maximum B_{surf} to the cavity surface must be increased, whilst remaining in the Meissner state. Novel materials may be able to provide an increase to B_{surf}, thus increasing E_{acc}. These materials include A15, B2 or other compounds (such as Nb_3Sn, MgB_2, NbTiN, NbN etc), multilayer structures such as SIS structures or SS bi-layers, or even new LTB techniques such as N infusion.

Commercial magnetometry consists of limitations covered extensively in the previous section. Samples are aligned by an operator in a straw, and it is probable that the sample will not be perfectly parallel to B_{ext}. This will create unknown flux enhancements, producing an early B_{vp}. These flux enhancements are difficult to account for if the demagnetisation factor is not known. To reduce (or preferably, eliminate) these limitations, in house magnetometry techniques are required.

In house magnetometry facilities (such as third harmonic systems) struggle to produce a B strong enough to enter a SC sample at $T \ll T_c$. In house RF systems (such as a QPR) apply B from one side of the sample to the other, such that the conditions are similar to that of an accelerating cavity. However, a typical trait for QPRs is the long period of time to fully test a single superconducting sample.

The aim for the project was to create a DC magnetometry method without the limitations present in other techniques, or to a reduced degree. A C-shaped dipole magnet was chosen to apply a DC magnetic field parallel to the face of a superconducting sample. The field must be parallel for 2 reasons:

- A normal component of B on the superconducting surface reduces J_c, thus

reducing the B at which the Meissner state breaks down [53].
- To try and simulate the field inside a SRF cavity.

The dipoles are flat along the bottom, which allow easy alignment of the magnet (and therefore B_{ext}) to the sample surface. The B is produced by using a superconducting solenoid. Whilst in the Meissner state the dynamic heat load due to the large current would be omitted, allowing lower temperatures to be reached during testing. This also allows a reliable reading of the sample temperature as there is no heating directly above the sample. A DC magnetic field is used to further reduce the heating produced compared to using an AC magnetic field, such as in third harmonic systems, which also allows large B to be generated at $T \ll T_c$. The system would use a cryocooler to cool the facility to ensure a fast sample turn around, whilst also reducing the running costs compared to testing with liquid cryogens with no recovery system. Fast sample turn around was desired to allow multiple samples to be tested per day, to allow the optimisation of deposition parameters.

The majority of sections 4.2, 4.5 and 4.5.3 have been published in [2].

4.2 Magnet simulations

The aim was to create a cryogen free environment to cool superconducting samples below T_c, and therefore the cooling capacity of the cryogenic system becomes a limiting factor. A superconducting solenoid was chosen to generate the B field due to having no DC resistance whilst in the SC state. Thus, no Joule heating is produced, in turn reducing the heat load into the system. This was important as initial simulations by Lewis Gurran had determined that 20 A would be required to generate ≈ 500 mT, which would in turn generate a large amount of heating if a normal conducting wire was used. To allow comparison to SRF technology, the B_{app} had specific requirements:

- To try and imitate a SRF cavity by applying B from one side of the sample to the other, such that B_{app} is only seen by one superconducting surface.
- The B_{app} must be parallel to the sample surface, similar to in a SRF cavity.
- The facility should be designed to allow the testing of small samples. A small gap between the dipoles produces a small, constrained magnetic field. Thus, allowing small samples to be tested.
- To minimise the possibility of flux enhancements (and hence early flux entry), B_{app} must be local on the sample surface.
- Allow testing of samples with different geometries. The main focus would be on flat samples, however it could be useful to test cavity cutouts which would be curved, and would require the facility set up to be altered.

The magnet was designed and built by Lewis Gurran, a previous student who was working on this project with these requirements in mind. The yoke was made out of a high carbon steel (C1020) which allows the large B produced by the coil to be maintained throughout the yoke, such that a greater B is produced at the dipoles. A low temperature superconducting (LTS) wire made out of NbTi (Supercon SC-VSF-678) is used to generate the B. The wire is 0.4 mm in diameter (total outer diameter) and contains 672 NbTi filaments embedded within a Cu matrix, which also allows the coil to operate at a $T>T_c$, providing that a low current is used. The coil was wound around the centre of the yoke creating a solenoid with 234 turns over 7 layers, and was wound at STFC RAL by a team of Ben Green, Victoria Bayliss and Josef Boehm.

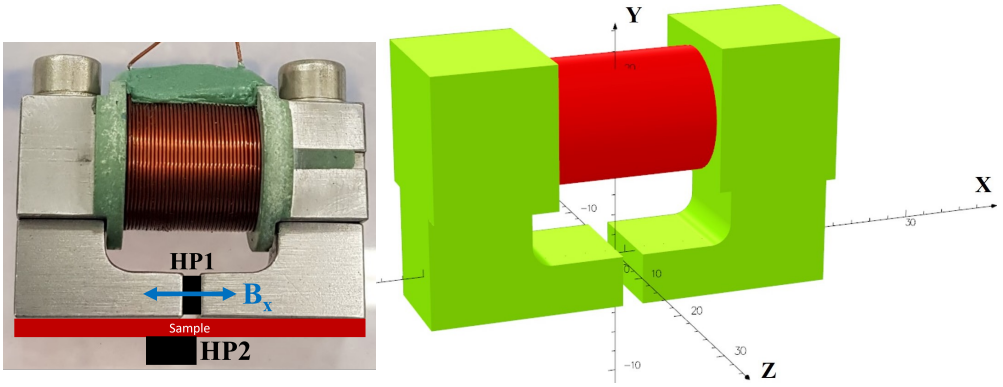

(a) (b)

Figure 4.1: The C-shaped dipole magnet: 4.1a shows the position of the Hall probe sensors and the sample with respect to the magnet, 4.1b shows the simulation of the magnet and the co-ordinate system that is referenced later. The axis centre (0,0,0) is the centre of the dipoles. B_x and B_z are parallel to the sample surface if a sample is present, with B_x being perpendicular to the poles. The vertical component to the sample surface is B_y.

The dipole faces have an area of $5\times10\,mm^2$ to constrain the B into a small area. To ensure B_{app} remains localised, the gap between the poles is 2 mm. If the gap is smaller, then B_{app} would be *over* constrained such that the sample surface would see a lower B than produced between the dipoles. When a superconducting sample is placed under the magnet as shown in Figure 4.1a, B_{app} in the gap is parallel to the sample surface shown in Fig. 4.2, as a sample in the Meissner state behaves as a magnetic mirror.

The applied and penetrated magnetic field are measured by using two Hall probe sensors. The Hall probe sensors are a four wire measurement connected in series, with a small current (20 mA) passed through the circuit during measurements. The

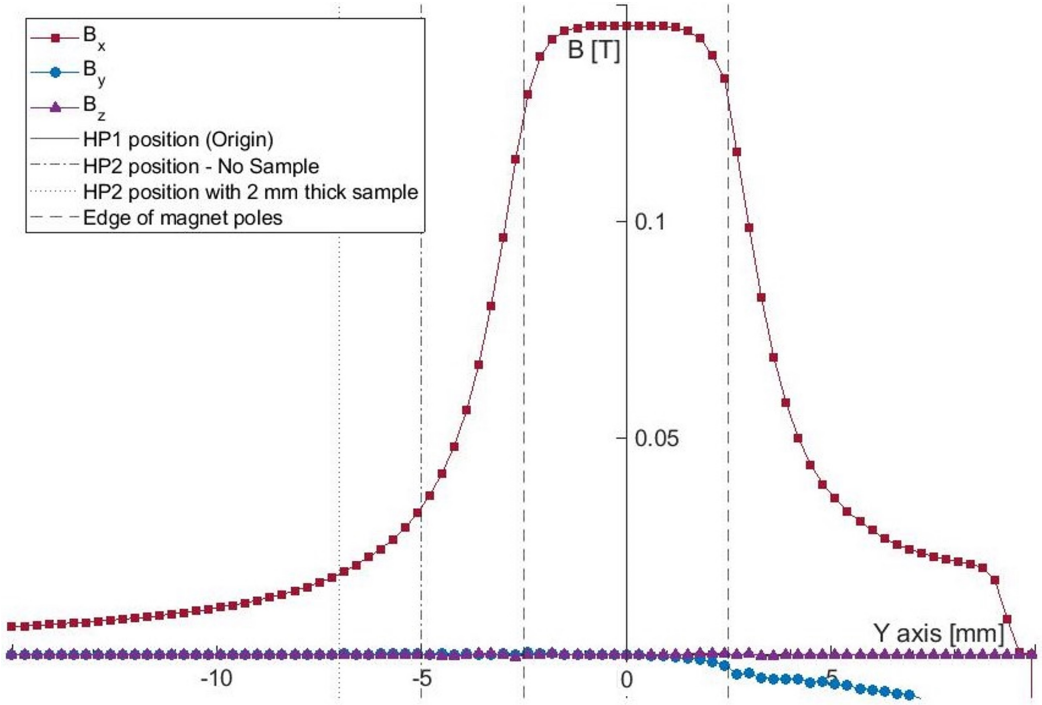

Figure 4.2: Simulation results for the magnetic field vectors through the centre of the gap between the poles in the Y axis of Fig. 4.1, without a sample present and an applied current of 1 A to the coil.

sensors are only sensitive in one direction, and thus must be aligned such that B is perpendicular to the sensitive area on the probes, such that the deflection in the current due to B can be measured by a change in the V - the Hall voltage. Both Hall probe sensors measure the magnetic field perpendicular to the pole faces (B_x), both above and below the sample, such that the B is measured parallel to the sample surfaces, and will not be sensitive to any other vector component of B. The sensitivity of the probes were measured by the manufacturer (Arepoc) at 297, 77 and 4.2 K. The reported B fields are determined using the sensitivity at 4.2 K.

The gap between the dipoles is large enough to place a Hall probe sensor, Hall probe 1, and is further referred to as B_1 in the centre of the dipole. A second Hall probe sensor (Hall probe 2) is placed on the opposite side of the sample to measure once it had fully penetrated though the sample, and is referred to as B_2 throughout. The position of the the Hall probe sensors with respect to a sample and the magnet is shown in Fig. 4.1a.

4.2.1 Modelling the applied magnetic field

The magnet was modelled using Opera SIMULIA to obtain the pattern produced between the dipoles. The magnitude of the vector components of B are shown in Fig. 4.2 when 1 A is applied to the coil. There was no permeability curve for the C1020 yoke, so a permeability curve for another high carbon steel (Steel 1010) was used to model the yoke, and was provided by Opera SIMULIA. The B-H curve is shown in Fig. 4.3.

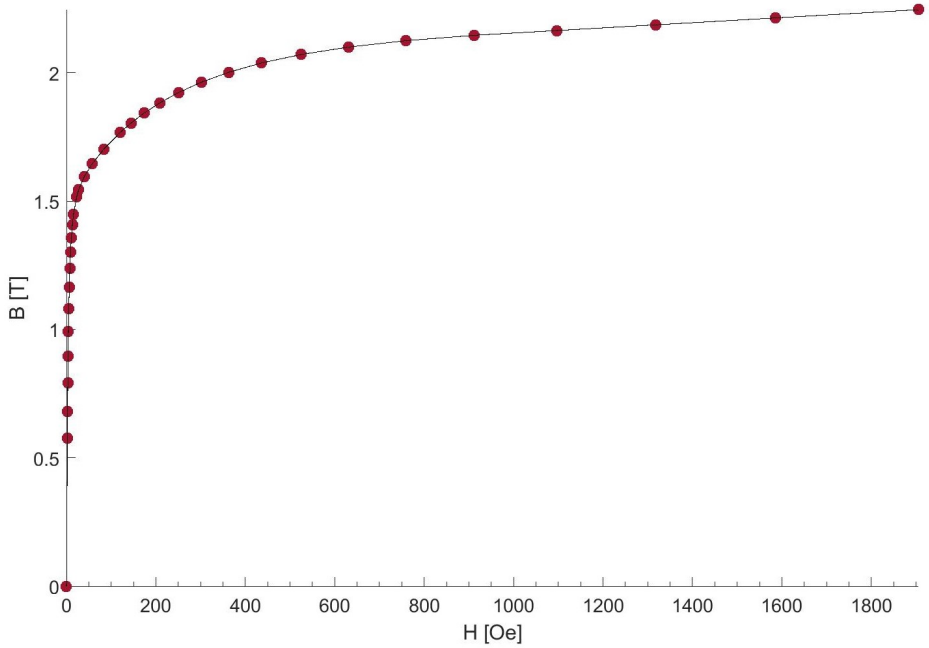

Figure 4.3: The permeability curve for Steel 1010, a high carbon stainless steel, that was used to model the magnet prior to determining the material of the yoke.

All further simulations shown were performed using the permeability curve in Fig. 4.3. At 1 A the coil produced a field of 416.16 mT in the centre of the coil, with peak B fields up to ≈670 mT at the edges close to the coil where the flux lines become denser, which can be seen in Fig. 4.4. This corresponds magnetic flux in the centre of the poles to be 145.6 mT. Figure 4.4 was simulated with the low magnetic permeability sample (μ close to 0), such that the B decays much faster than if there was a sample present. Additionally, the B field vectors are shown in the centre of the yoke, and it can be seen that the flux is much denser towards the inside of the yoke, where as the outer edges of the yoke see little to no flux passing through them.

The vector components are shown for the Y-axis, in the direct centre of the poles due to the diverging at the edges. The components parallel to the sample surface are

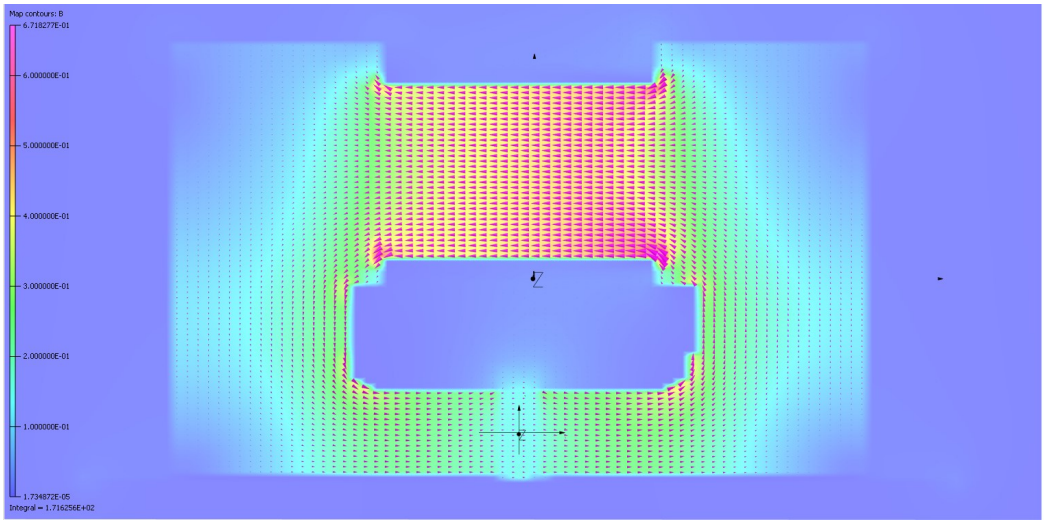

Figure 4.4: A cross section of the yoke whilst 1 A is applied to the coil.

B_x and B_z, where B_x is perpendicular to the pole faces and B_z is parallel to the pole faces. The component perpendicular to the sample surface is B_y. The magnitude of B_1 (B_x) as a function sample thickness and applied current is shown shown in Fig. 4.5.

One of the requirements of the magnet was to produce a strong, localised B between the dipoles. The strong localised B also produces consequences, such as B_1 will reduce rapidly over distance away from the dipole, shown in Fig. 4.2 for the vector components of B, and shown in Table 4.1 for key distances used in the experimental testing. These results are for a coil current of 1 A. The largest B_1 is produced in the centre of the dipoles, shown at y = 0 in Fig. 4.2. There is a plateau between $-1.5\,\text{mm}<y<1.5\,\text{mm}$ for B_x as this is between the poles. The begins to rapidly fall off as the distance away from the centre of the poles is increased, with a % comparison to the applied B_x shown in Table 4.1. Thus, the B_x at the edge of the poles (i.e. on the sample surface, if the sample is normal conducting) is 85.3 % compared to B_1 which is $\approx$122.8 mT, and the B_y component produced is $\approx$44 mT. The B measured by HP2 (B_2) depends on the sample thickness. Thicker samples increase the distance between the source of B_{app} and HP2, such that the B read by HP2 will vary with distance. The difference between B_1 and B_2 is defined as:

$$K_1 = \frac{B_{HP2}}{B_{HP1}}, \text{ for no SC present} \tag{4.1}$$

Thus, K_1 is expected to be in a range of 0.13-0.235 depending on the thickness of the sample being tested, see Fig. 4.6 and Table 4.1. These results are for no magnetic samples present in the facility set up. The magnetic field as a function of I is shown

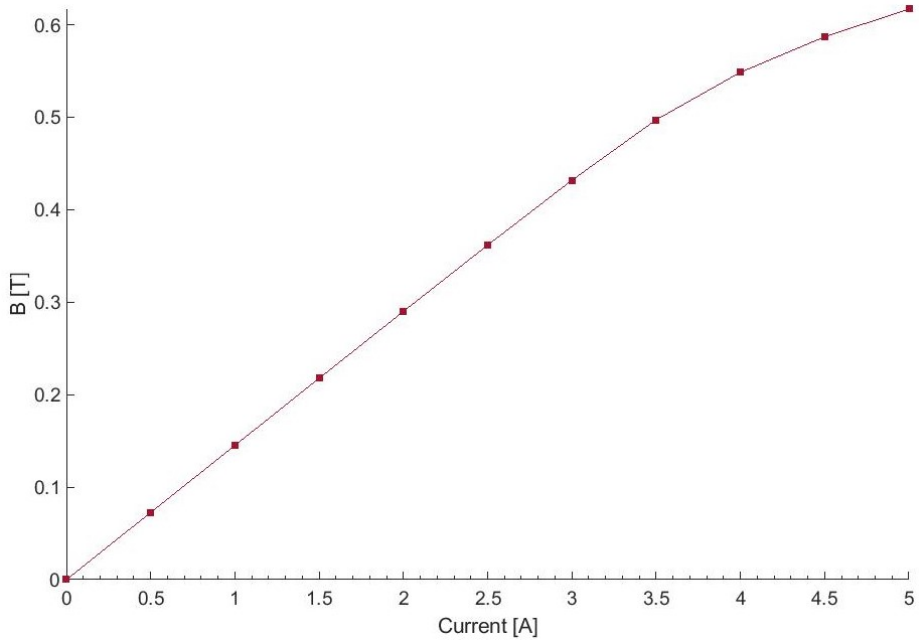

Figure 4.5: Simulation results for B_1 as a function of applied current to the solenoid. This is the magnetic field that is measured by HP1, which correlates to B_x due to Hall probe sensors being direction sensitive.

Table 4.1: Simulation values of K_1 with and applied current of 1 A over distance in the Y-direction away from the poles, with corresponding examples of the distance.

Position	**Distance [mm]**	**% of B_1**
Dipole centre (B_1)	0	100
Dipole edge	2.5	85.3
Sample surface with one Brass spacer	2.8	74.3
HP2 position with no sample	5	23.5
HP2 position with two brass spacers	5.6	19.0
HP2 position for Nb on 2 mm Cu sample	7	13.0

in Fig. 4.5, which shows that B increases linearly with I up to 3 A, which equates to B_1=432 mT. Increasing the current above 3 A produced a non-linear dependence due to the magnet beginning to saturate. A current of 5 A generated a B_1=617 mT which was more than sufficient for magnetic field penetration studies.

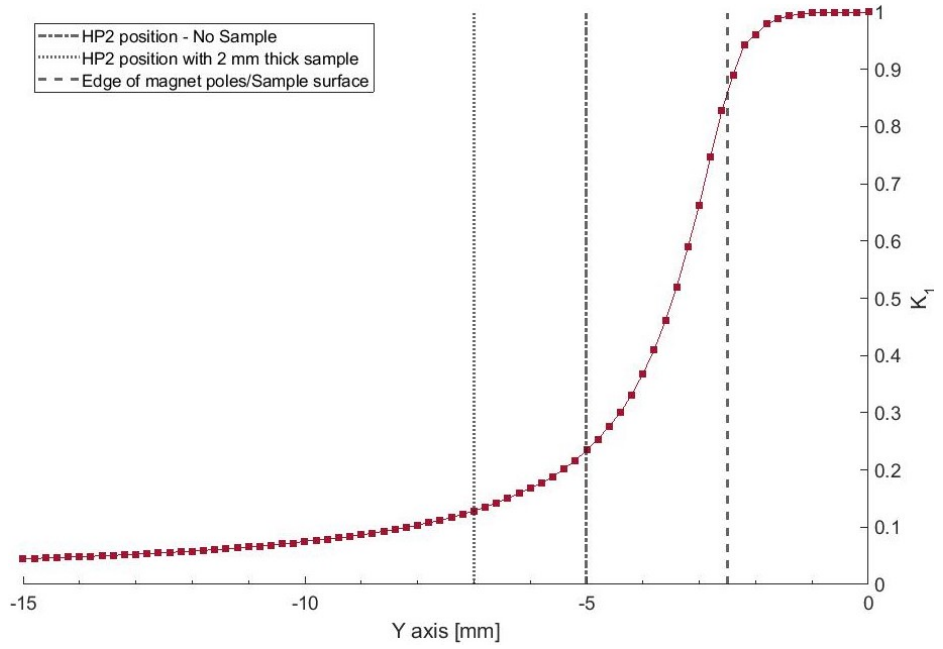

Figure 4.6: Simulation results for the parameter K_1 as a function of distance away from the dipoles.

4.2.2 Magnetic field leakage studies

As the sample sizes are small, an investigation on how small the size of a sample in the Meissner state could be without distorting the results. The two main factors that could skew results would be due to the B_{app} either: 1) producing flux enhancements at the edges of the sample if the sample becomes too small, or 2) too much B leaks around the sample, which is measured by HP2 and masks when the B breaks through the sample. A new parameter, K_2, was created to investigate the effect of B leakage, which has the same properties as K_1 and is shown in Eqn. 4.2, but whilst a sample is in the Meissner state. An infinitely large sample would produce K_2=0 as the sample is much larger than any stray fields that would be produced.

$$K_2 = \frac{B_{HP2}}{B_{HP1}}, \text{ for a SC in the Meissner state} \tag{4.2}$$

Whilst in the Meissner state a superconductor behaves as a perfect diamagnet, thus the magnetic permeability is μ=-1, and can be described as a magnetic mirror, which can be simulated by simulating a second magnet and rotating it 180° in the x-axis. Thus, B_y is cancelled out at the centre, whilst B_x and B_z are maintained. However, this method is difficult to simulate samples of varying size. To investigate the sample size

and geometry on K_2, the samples were simulated with a low permeability (relative μ=1×10^{-200}) such that B is negligible within the sample, such that it would be favourable for B_1 to flow over the sample surface. Because some B penetrates through the simulated low μ sample (unlike in a superconducting sample) the results are not directly comparable. The B leakage was determined using experimental data for a Pb sample shown in Section 4.9, where K_2=B_2/B_1 was found using only the B parallel to the sample surfaces (i.e.- B_x, due to being the only axis the Hall probe sensors are sensitive) where B<B_{fp}. The simulated data for K_2 was calculated the same way, where the B_x was found in the position of each Hall probe sensor to allow a comparison between experimental and simulation. Both simulation and experimental (presented in Section 4.9) results produce a similar trend which are shown by comparing the parameter K_2 as a function of sample area in Fig. 4.7.

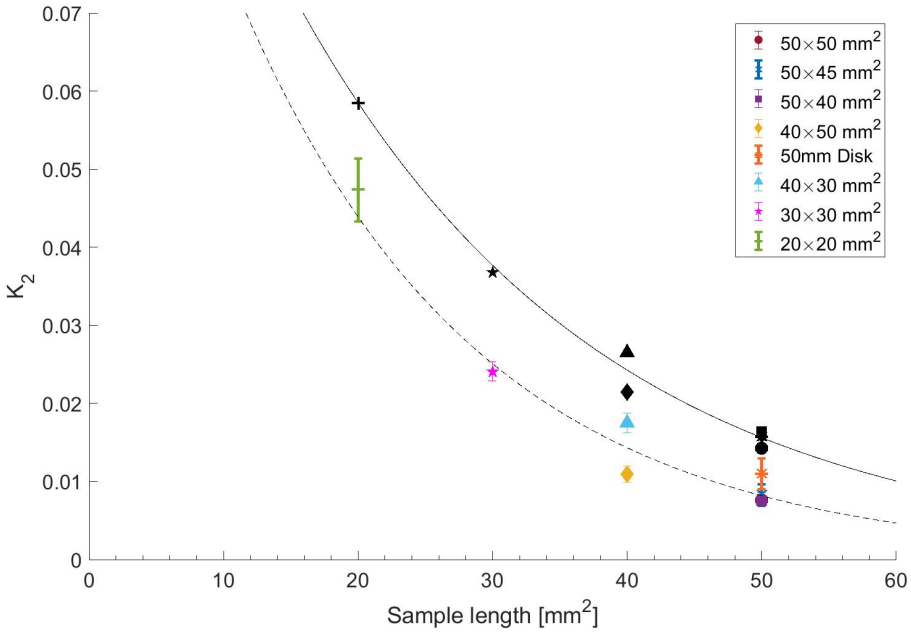

Figure 4.7: The experimental measurements (black dashed line and coloured markers) and the simulated values (black solid line and black markers) for the leakage parameter K_2 as a function of sample length. The legend is given as length×width.

Figure 4.7 shows that as the sample size reduces, K_2 drastically increases, indicating more B is travelling around the sample rather than penetrating through the sample. This indicated that the B will change orientation at the edge of the sample, thus producing fringe fields that could affect the results. It can be seen that K_2 is correlated with the sample length. A comparison of the vertical component

of the magnetic field (B_y) was found for the $20\times20\,mm^2$. It can be seen in Fig. 4.8 that there is little difference in B_y as a function of the X position (perpendicular to the poles) for both above and below the sample whilst outside the pole region ($> \pm10\,mm$), with an increased B_y on the underside of the sample between the poles ($< \pm10\,mm$). This is due to the B moving from the low μ sample to a higher μ area due to being energetically favourable, thus producing a vertical component. The vertical component is negligible within the simulated sample due to the magnetic yoke producing a small vertical component, and the low μ making it unfavourable for the B to enter the sample. Figure 4.9 also shows that there is a peak in B_y up to 30 mT at the $\pm10\,mm$ co-ordinate due to being the edge of the sample. This is much lower than B_1 produced by the magnet, but still large enough to indicate B_{fp} could be obscured.

There is a second peak in B_y in the X-axis at $\pm20\,mm$. This is due to the edges of the magnetic yoke, and must be further investigated for samples of various sample sizes. For samples larger than the length of the yoke, it is expected that these peaks in B would not be present, with results shown later in this section.

The results in the Z-direction (parallel to the poles) shown in Fig. 4.8 indicate that there is less B leaking around the sample in the Z-axis compared to the X-axis. This is expected as the B is applied perpendicular to the Z-axis. There is a peak in B_y at the edge of the sample, but no peak at the inner edge of the pole faces ($\pm5\,mm$). The B_y component is lower under the sample ($\approx10\,mT$) compared to the B_y in the x direction ($\approx30\,mT$). Thus, it can be concluded that the sample length has a greater effect on the B_y component of the field.

Each sample size shown in Fig. 4.7 was simulated to compare with the experimental values. The fringe fields were investigated on each sample surface, and not where the sensitive area of where the Hall probe sensors are present. I.e, the results are simulated to be directly on the sample surface, and not 5 mm higher at the centre of the probe. All samples had a peak B and B_y at the edge of the sample where the B flows over the edge of the sample, shown in Figs 4.8 and 4.9. The largest B and B_y was found for samples with a 40 mm length (thus the edges are at $\pm20\,mm$ in the X-axis), which is identical to the length of the yoke, with the B increased up to $\approx64\,mT$. Comparing this to the values shown in Fig. 4.9b, the major vector component is B_y ($\approx61\,mT$) and thus perpendicular to the low μ sample. This is due to 2 reasons:

1. The edge of the sample is at the edge of the yoke, thus it is favourable for B to go around the yoke and remain vertical until the B is on the opposing side of the sample.
2. The simulated sample is not superconducting, as the B would be screened and not be present on the surface of the sample. Therefore the simulated results using a low μ will produce larger values than for superconducting samples, as the B is not expelled or screened by the sample.

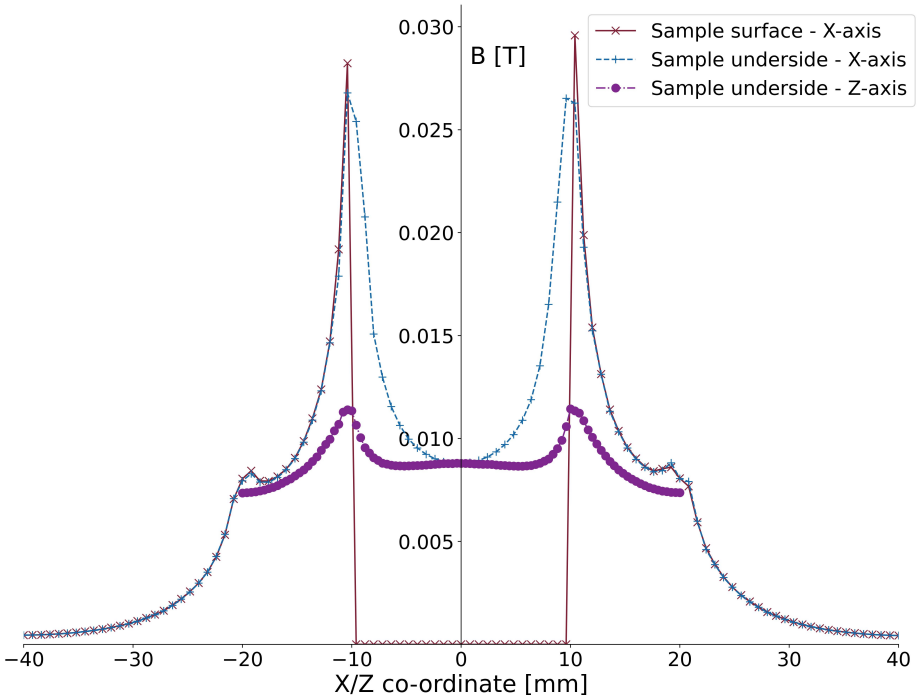

Figure 4.8: The B in both the X and Z direction, parallel to the sample surface. The 'sample surface' data is directly on the sample surface, whereas the 'sample underside' is 0.1 mm away from the sample. These positions are not the position of the Hall probe sensors. The simulated sample is 20×20 mm, thus the edges of the samples are at ±10 mm.

Samples with a length<40 mm (−20 mm<X-axis<20 mm) 2 peaks can be seen; the largest peak at the edge of the sample, and a second, smaller peak at the edge of the yoke. This shows that the edge effects are less than for samples of length=40 mm as the B is flowing around the sample easier and therefore producing a larger B_{leak} and obscuring B_{fp}. Simulations where the length>40 mm show a similar peak at the edge of the sample, which is lower than all other sample sizes. Additionally, $B>B_y$ as shown by comparing Figs. 4.9a and 4.9b, indicating there are multiple B components as the field moves around the sample.

4.2.3 Discussion

Simulations were performed using a high carbon steel yoke with a pre-defined B-H curve. High carbon steel is highly magnetic, allowing a large B to be maintained within the yoke, producing a dense B field in a constrained gap. Changing the material of

the yoke would alter the magnitude of the B within the yoke, and thus also the B within the gap. If the chosen material had a greater permeability, a larger magnetic field would be produced for the same current (provided the saturation B field was not reached). On the other hand, if a lower permeability material was used for the yoke, a smaller magnetic field would be produced for the same current. A change in the material would also alter the saturation field of the yoke, a higher saturation field producing a greater B, and a reduced saturation field producing a lower B. The material could be changed to allow a greater B field to be maintained within the magnet yoke by increasing the saturation field, such that the magnet will not begin to saturate at 5 A. This could allow for greater magnetisation within the yoke, which could affect results as more flux could be trapped within the sample as the sample transitions into the superconducting state, thus causing some error in the measurements.

At 1 A, ≈145 mT is produced within the gap of the yoke, and the magnet only begins to saturate at 5 A, which is ≈617 mT which is more than required for magnetic field penetration studies.

Simulations were performed on low μ samples to determine the effect of the leakage magnetic field (B_{leak}) around a sample. It was determined that samples should be kept as large as possible to reduce the stray B leaking around the sample, whilst also reducing the potential B_y that could punch through a sample whilst in the superconducting state. The results presented here are for a low μ sample and will not behave the same as a SC sample, as a SC sample could not be simulated using Opera for samples of various sizes. If a SC could be simulated, the stray fields would increase as B would be fully expelled in the Meissner state, thus increasing the stray fields on the edge of the samples, and increasing the enhanced flux at the sample edges.

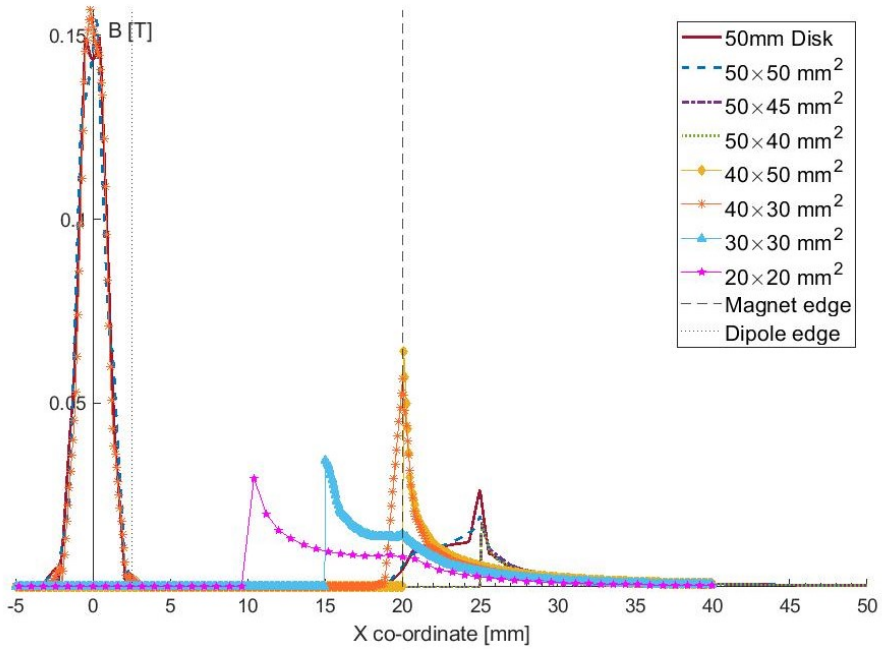

(a) B Fringe fields

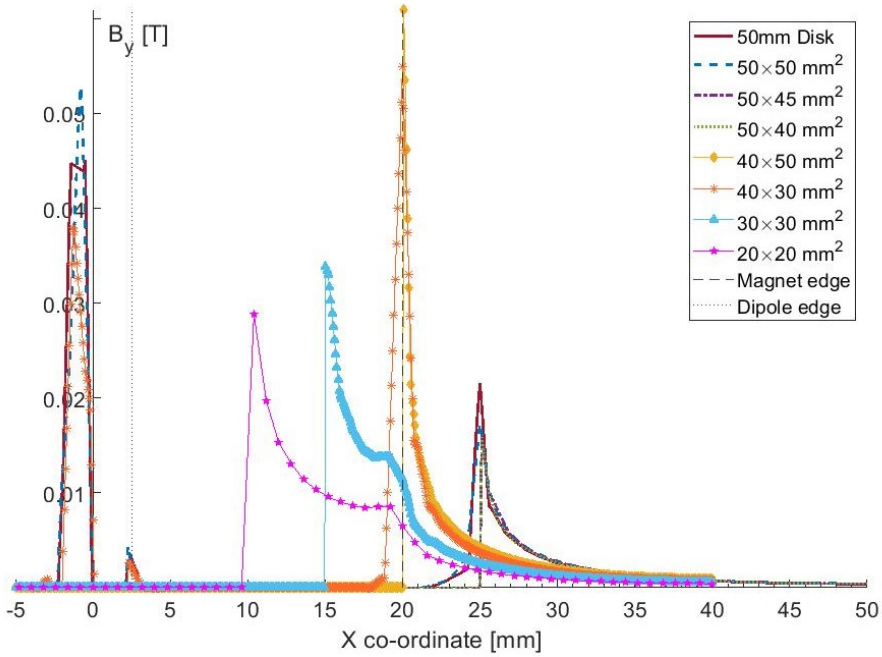

(b) B_y Fringe fields

Figure 4.9: The B and B_y in the X direction, parallel to the sample surface to determine where the fringing magnetic fields are largest. These simulations were performed with 1 A, and thus a B_x=145.6 mT field in the gap.

4.3 Cryogenic facility

Once the magnet had been designed and built, the focus turned to how the sample must be cooled down to an acceptable testing range. Initially a user facility at Daresbury laboratory was planned to cool the experiment by using a variable temperature insert (VTI) described in the next section. After multiple attempts the system could not be cooled to a sufficient temperature for ample testing. To ensure the magnet would be sufficient for the purpose of a field penetration experiment a LHe Dewar was adapted for a small number of tests. Due to no LHe recovery line set up and the rising cost of LHe, a cryogen free facility was designed and built which is described in Section 4.5.

4.4 Variable temperature insert

4.4.1 Design

The first facility designed for the magnetic field penetration experiment (MFPE) was a variable temperature insert (VTI). The aim was to place the VTI into a larger pre-cooled system. The experimental chamber was over pressurised with He gas such that atmosphere could not enter the chamber, before the VTI was inserted or removed before the chamber was closed. A pressure relief valve was always connected to the chamber to ensure it did not over pressurise, and also to help determine when the chamber was ready to open. This allowed the large cryostat to remain cold whilst the sample was being changed. Thus, allowing a rapid sample change over. The cryostat had already been designed and built before I began research at Daresbury Laboratory. The facility was designed as a user facility, such that many people could use it.

The VTI was designed by a team at Daresbury Laboratory before I began the project, but not built, with the skeleton of the insert shown in Fig 4.10. The VTI was designed to reduce the heat load as much as possible over the length such that the sample area would see a minimal heat load. A thin walled steel tube was used to reduce the static heat load from higher T's at the top of the VTI (which is in contact with room temperature (T_{room}) atmosphere on the flange). Baffles made out of Cu are used to reduce the radiative heat load by intercepting photons from higher T's. A thick, spring loaded Cu baffle is situated at the centre of the VTI shown in Fig. 4.10 and labelled in Fig. 4.11. The baffle created the only physical thermal link from the VTI to the S1 plate. The thermal link allowed the VTI to thermalise to S1 inside the cryostat at $\approx 40\,\mathrm{K}$, which should reduce the heat load on the experimental area.

The experimental area is housed at the bottom of the insert, shown on the right of Fig. 4.10. There is no solid connection between the chamber wall and the lowest part of the insert, which is the experimental area. The chamber is only connected

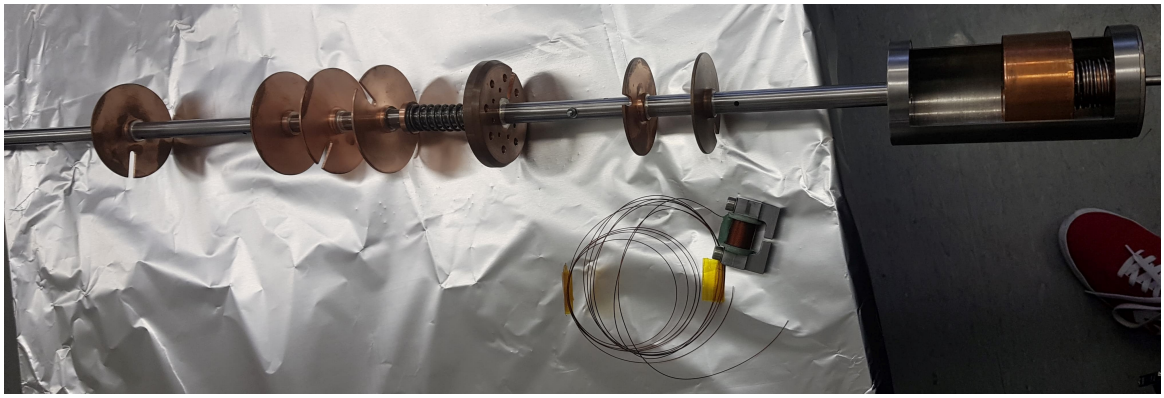

Figure 4.10: Initial VTI and C-shaped dipole magnet before full assembly. The thicker baffle with a spring next to it is the S1 baffle which thermalised the VTI to the S1 plate. The 'cage' on the right is the experimental area.

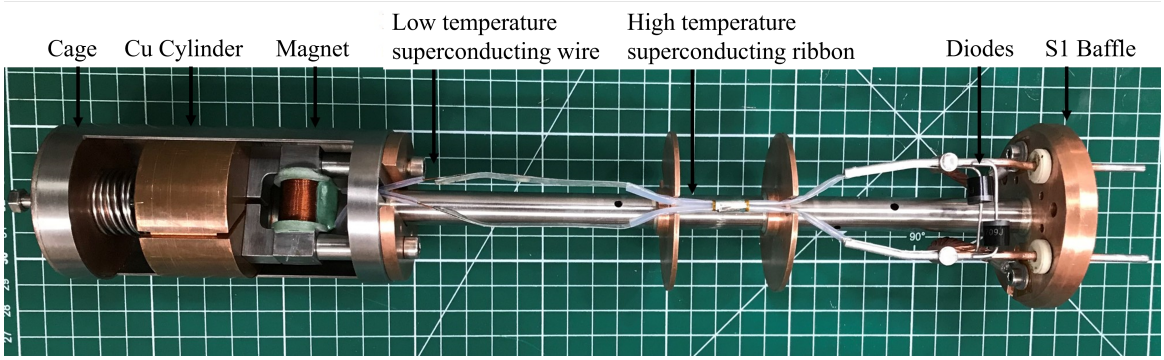

Figure 4.11: The final set up of the VTI.

by thermal strapping, and there is no place on the chamber to bolt the straps such that it must be wrapped around the outside of the chamber. The cage is cooled by convection of He gas within the chamber. When the T of the system becomes stable and the He gas has stratified, the coldest volume of gas will be at the lowest part of the chamber. A large Cu cylinder can be seen at the bottom of the insert, which is used to hold a Hall probe sensor to determine when the field has broke through the sample, a thermometer, and to hold the sample itself. The Cu cylinder is large to create a large thermal inertia such that the sample T cannot rapidly change, which ensured the sample was in thermal equilibrium. To ensure the sample is thermalised to the Cu cylinder, the cylinder was compressed onto the sample by a spring, which in turn was compressed onto the magnet. The spring also ensured that the sample should not move away from the magnet during testing, such that the sample would witness a lower B than measured by HP1. The entire experimental area should be a

similar temperature over the cage, as the distance is not so large that the T of the gas should vary. Two thermometers were used to ensure this, one in the Cu cylinder and one on top of the cage, which allowed the T gradient to be measured over the magnet and the sample during testing.

The final design of the VTI is shown in Fig. 4.11. The stage 1 baffle is shown on the far right of Fig. 4.11, where the normal conducting to superconducting joins are situated. These joins were made by Rutherford Appleton Laboratory by the same team who wound the magnet. As the solenoid is a low temperature superconductor (LTS) and has a $T_c \approx 10\,K$, the magnet had to be joined to a high temperature superconductor (HTS, $T_c \approx 80\,K$) to reduce the heat load from the S1 baffle and ensure the LTS wire would not get damaged during testing at high currents if the LTS wire was still in the normal conducting state higher up the insert. At the S1 baffle a superconducting to normal conducting join was made to allow a current to pass through the circuit. The HTS ribbon was brazed onto OFHC Cu bars to form a connection to the normal conducting power supply. The brazing was done using Indium due to its low melting point (157 °C) which reduces the risk of damaging the superconductor during the brazing process. The connections between the LTS wire, HTS ribbon and normal conducting rods had to be as long as possible to reduce contact resistance between the joins. All of the joins are shown in Fig. 4.11. Normal conducting wire was bolted onto the Cu bars using eyelets/lugs to apply a current from the 'Cryogenics Limited' power supply to the magnet.

A few obstacles were present in this set up. The superconductors had to remain electrically isolated from each other to ensure a short would not be created in the system that would bypass the electromagnet, therefore reducing the B_1 produced. However, the superconductors still had to be thermally connected to ensure there was no thermal gradient between two parts and the wires would transition into the superconducting state, and also to ensure the temperature of the superconductors were known during measurements. The Cu rods were isolated using ceramic screw insulators and attached to the S1 baffle using Cu straps. The Cu straps are electrically isolated by using a layer of Kapton tape, which allowed a thermal connection between the baffle and the rods. Two diodes were connected between the Cu bars such that if there was a quench in the magnet, the diodes would short the circuit so that the magnet would not be damaged. It was later determined that the diodes were not designed to be run at low temperatures, which caused a short in the system, in turn the B produced was smaller than expected.

4.4.2 Dry system

The cryostat was cooled by a RP-082B2 pulse tube cold head, connected to a F-70 indoor water cooled compressor, both designed and manufactured by Sumitomo heavy

industries cryogenic group. The pulse tube has a cooling power of 1 W at 4.2 K on the second stage and 40 W at 45 K on the first stage. Two plates (plate 1 and plate 2 respectively connected to stage 1 and 2 of the cold head) made of OFHC Cu are connected to the pulse tube by Cu strapping. This allows the cold head and plates to cool at different rates without causing damage due to thermal contraction.

The plates are connected using thin walled stainless steel tubing. The tubes provide strength and stability to hold the Cu plates in position whilst minimising the heat load from the external flange to stage 1, and between stage 1 and 2. The final full build of the insert and the corresponding position of the insert inside the cryostat is shown in Fig. 4.12, and the open system is labelled and shown in Fig. 4.13.

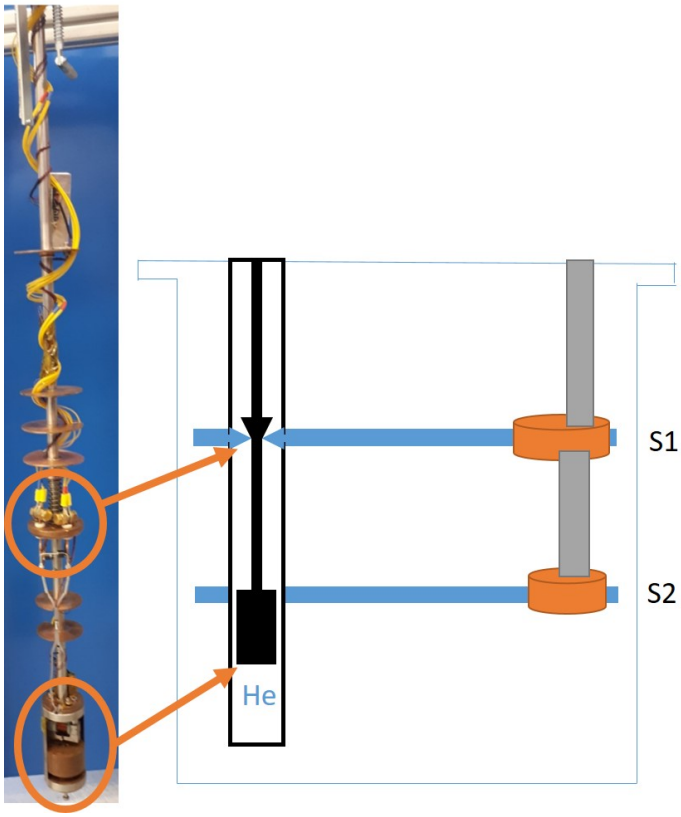

Figure 4.12: Position of the VTI with respect to the cryostat.

The baffle compressed onto stage 1 by a spring is also indicated in the schematic. It should be noted that the baffle is the only physical connection between the VTI and the cold head. Both plates are welded to the outer wall of the VTI chamber, which is a separate volume than the pulse tube and plates. The welds allow heat exchange between the insert chamber and the plates. When the insert is placed in the cryostat (in the separate chamber), He is injected into the VTI chamber which allows heat

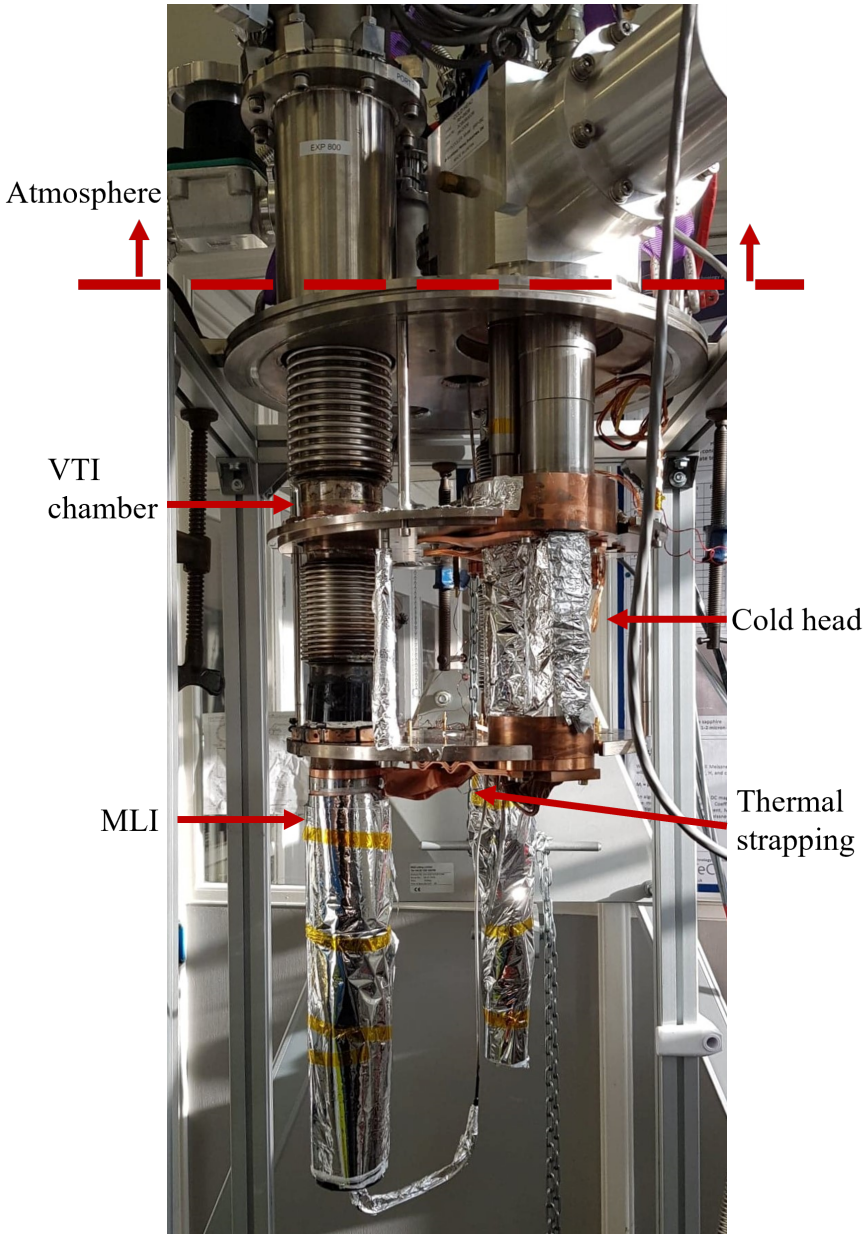

Figure 4.13: The cryostat where the VTI is placed

exchange between the insert and the chamber walls.

The cryostat contains one thermal radiation shield made out of OFHC Cu, wrapped in multi layer insulation (MLI) to reduce the heat load due to thermal radiation. The thermal radiation shield is connected to plate 1 in the cryostat as there is a greater cooling capacity. As thermal radiation (Stefan-Boltzmann law)

increases with T^4, a heat shield only on plate 2 would be too great a heat load for the cold head to remove from the system. The facility is contained within a steel vacuum chamber which is evacuated to $\approx 10^{-4}$ mbar before cooling. Lower pressure is favourable for cooling as it ensures there is no unfavourable substances within the system, however this increases the overall time to cool the system.

4.4.2.1 Dry system summary

Multiple attempts were made to cool the insert using the cryostat. It maintained a difficult challenge to reduce the T of the VTI to that of an acceptable testing range for Nb. Many changes were made to try and reduce the T, such as;

- Cleaning the strapping from the cold head to the plates.
- Increasing the amount of strapping from the cold head to the insert chamber and plates.
- Changing the MLI insulation.
- Adding MLI to the VTI chamber.
- Varying the pressure of He in the VTI chamber.

The lowest temperatures measured in this facility were 3.5 K on S2 of the cold head, 4.4 K on the S2 plate and 4.6 K on the outer wall of the insert chamber. The small variation in T indicated that the system was in thermal equilibrium and with a good thermal link between each component. Without any He inserted into the chamber, the thermometers on the insert read 18.7 K and 38.6 K above the magnet and in the Cu block respectively, also shown in Fig. 4.14.

The larger temperature on the Cu cylinder was likely due to the increased thermal mass of the cylinder, thus taking a longer time to cool down by radiation only. The cylinder would likely still be cooling when this measurement was taken.

Injecting He gas into the chamber significantly reduced the temperature gradient over the experimental area, from 18.7 K and 38.6 K to 8.72 K and 7.55 K respectively, allowing the He gas to produce a thermal link with the chamber wall, such that heat from the VTI was removed. However, this also increased the equilibrium T at other locations such as the outer chamber wall and the S2 cold head, which indicated an increased heat load to the system due to the introduction of gas.

Figure 4.14 shows that the introduction of He increased the T on the S1 plate and cold head, again indicating an increased heat load. This was unexpected as the S1 baffle should have been thermalised to S1 plate via the spring. There are 2 possibilities which explain the increase in T: 1) The S1 baffle on the VTI did not have a good thermal contact to the plate. This would likely be due to the spring becoming brittle at low T, and no longer compressing the baffle onto the plate. The introduction of He therefore increased the thermal conductivity between the VTI and the plate,

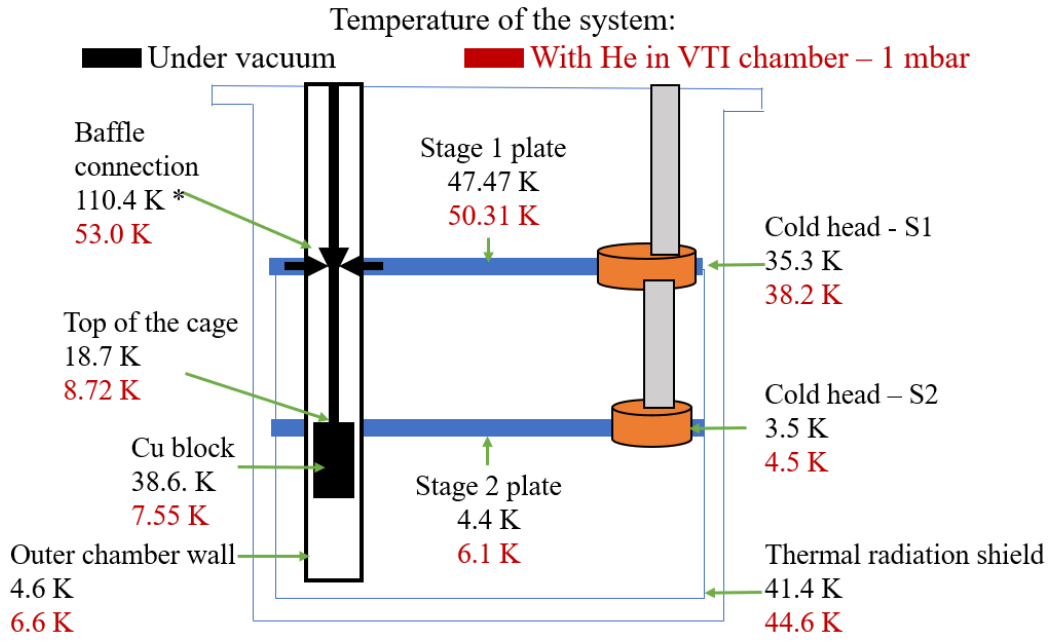

Figure 4.14: A comparison of the temperatures of the VTI and the cryostat under vacuum (black) and with 1mbar of He in the insert chamber (red). These were the lowest temperatures recorded on the insert.

cooling the VTI whilst increasing the heat load onto S1, indicated by an increased T, or 2) If the S1 baffle had a good thermal contact on plate before He was injected, the introduction of He increased the heat load onto the plate, indicating the He had increased the heat load to the system, which was not previously present from the VTI. One explanation for the increased heat load was the large external steel tube in which the VTI was inserted which is visible at the top of Fig. 4.13, which was at T_{room}. The large surface area and T difference would introduce more heat to the internal system, increasing the temperature.

The introduction of He reduced the T of the experimental area due to the introducing a thermal connection between the VTI and S2, thus producing an increased heat load on S2, thus an increased T. There was a 2 K difference between the top of the cage and outer chamber wall (at the bottom of the chamber). The T varied depending on the vertical height the thermometers were placed, thus indicating a vertical T gradient. Whilst the system was in equilibrium, the gas should have stratified, producing a T gradient within the chamber. The coldest gas would be situated at the bottom of the chamber, due to the lower T on the chamber wall. Due to the VTI being shorter than the chamber, the experimental area was situated at a higher T within the chamber. To further reduce the T of the experimental area the

insert should be made longer, such that the experimental area would sit lower within the cryostat, or preferably, the external flange of the insert should sit flush with the top of the cryostat to reduce the heat load introduced by the injected He.

The experimental area reached a minimum of 7.55 K which is approximately the T_c of the LTS wire for the magnet, and only just lower than the T_c of Nb. Thus, the system did not reach a T low enough to perform adequate measurements on the current material for SRF cavities. However, the T is low enough to measure high T_c superconductors. To determine if the experimental set up was viable, a wet system was adapted to ensure the temperature requirement was met for testing.

4.4.3 Wet system

To test if the experimental method would work before more time was spent designing a new cryogenic facility that could reach temperatures low enough for thorough testing, it was decided to use liquid cryogens to cool the experiment. In order to keep the system as simple as possible, a flange was designed to fit an already existing Dewar present at Daresbury Laboratory that would also accommodate the VTI without any modifications being required to be used. Furthermore, to keep the system simple, it was decided for the facility to be an open cycle system. I.e., the liquid He (LHe) would be boiled off to atmosphere rather than being collected. This is not good practice for a long term system which would be used repeatedly due to He being an expensive finite resource. If the system was only to be run using LHe, as a wet system, it should be closed cycle with a recovery system.

The Dewar had been used previously at Daresbury Laboratory, and hence a new flange was designed and made a member of the cryogenic group that would accommodate the insert. The Dewar was cleaned with Isopropanol due to not being used for a long period of time, and the new flange was attached. The vacuum jacket of the Dewar was also pumped down for a week to ensure there was a good enough vacuum and no water was present. The jacket was also leak tested to ensure atmosphere would not enter the jacket during testing.

A level probe was used to determine the height of the LHe in the Dewar at any given time. It was calculated that to fully submerge the sample cage approximately 16.3 L of LHe would need to be in the Dewar. For the first test however, the sample cage sat much higher due to the adapter flange having a greater height than originally stated. An extension was designed made out of thin walled stainless steel tube to extend the total length of the VTI, such that the cage would be situated lower in the Dewar, and hence reduced the amount of LHe required to submerge and cool the experimental area.

Bellows were attached together and used as a transfer line for the He that had boiled off. The transfer line was made long enough that the He leaving would not be

Figure 4.15: The Dewar containing the insert during a cool down.

expelled near any of the users. The final build is shown in Fig. 4.15.

4.4.3.1 Initial results

Magnet testing

The most important test was to ensure that the magnet produced an expected B_1, as at this time the material of the magnet was not known. A Cu disk was used to simulate a superconducting sample not in the Meissner state, to observe how B would decay over the distance between the Hall probe sensors with a sample present.

The magnet was designed by a previous student, and the simulation results from their work were used as for approximate values. It was estimated that 20 A would be required to reach $\approx 500\,\mathrm{mT}$. As the current was increased, B_1 also rapidly increased

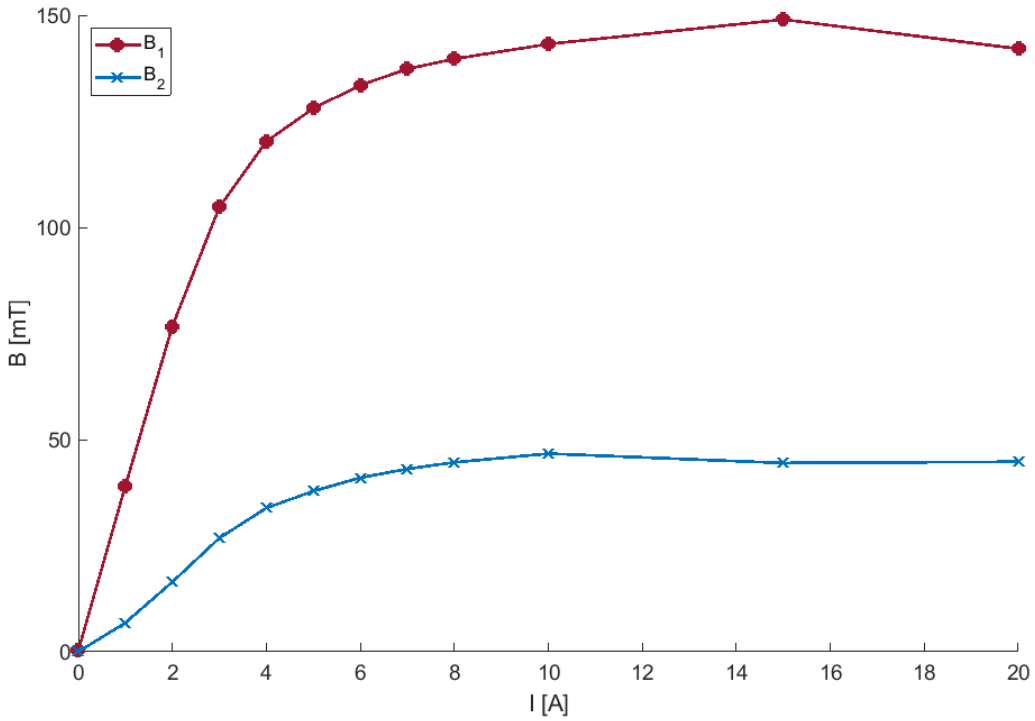

Figure 4.16: The magnetic field observed by both Hall probe sensors as a function of applied current to the magnet with a Cu disk as a sample to simulate the sample.

up to 100 mT at 3 A. Further increasing the current made B_1 begin to saturate at ≈150 mT, between 5 - 10 A, which was much lower than expected, shown in Fig. 4.16. The low B_1 produced could have been due to multiple issues such as; the magnitude of the current not being the same in both polarities, either due to a malfunction of the diodes or due to the power supply, or, the issue could have been due to the magnet itself such as not being made out of the same material as the original simulations.

Hall probe 2 (B_2) was situated 4.5 mm away from the edge of the dipole and saturated the same time as B_1, with a maximum B≈45 mT. This indicated that the Hall probe sensors were both wired correctly and there were no faults with the measurement set up. Yet, B_2 was much larger than expected. Whilst no superconducting sample was present it is expected that $B_2 = 0.1B_1$, however the measured $B_2 \approx 0.3B_1$. Thus, either the sensitivity of HP2 was different than the stated value from the data sheet, or another process was occurring.

4.4.3.2 Niowave Nb disk - Test 1

The first superconducting sample to be tested was a bulk Nb disk from 'Goodfellows Cambridge Ltd'. The disk had a thickness similar to that of the Cu disk was used (≈

1.2 mm), and had a 50 mm diameter. The Nb had a RRR = 400, and thus was a high purity sample. The sample was tested by ramping the current in one polarity, reducing back down to 0 A, reversing the polarity and repeating the test, before reverting the polarity back to the initial run and repeating. The first run was performed in the negative polarity, thus producing a negative B. The results are shown in Fig 4.17. Initially, as B_1 is increased, B_2 increases and decreases in a quadratic relationship (shown by the red line), and there is no sharp transition in B_2. The maximum B_1 measured by HP1 was 150 mT, which is the same as when the Cu gasket was tested. However, B_2 was smaller than when using the Cu gasket (31.7 mT), which indicated that B_1 had been somewhat screened in comparison. The current was then reduced back to 0 A before alternating the polarity.

The results produced from positive polarity run were not as expected. To begin with, as B_1 was increased, B_2 decreased. This was unexpected as both B_1 and B_2 are correlated and should have the same polarity. A sudden increase is present in B_2, which was expected to be B_{fp}. Once the maximum B had been reached, and B_1 began to be ramped down to 0, B_2 continued to increase. Again, this was not expected as B_1 and B_2 should follow the same trend.

The polarity was alternated back to the negative polarity for a final run. It can be seen that B_1 did not start from 0 mT, but 5.3 mT, indicating some hysteresis produced within the sample cage. As B_2 did not reduce down to a B to be considered noise (or zero field), there must have be some magnetisation not produced by the magnet which caused B_2 to remain high. The final ramp up of B_1 produced a quadratic relationship between B_2 and B_1, followed by a rapid change in B_2. Similar to the first test in the negative polarity, the maximum B produced in was 150 mT.

4.4.3.3 Summary of the first test

After the first test, a few theories began to develop based on the results to try and optimise the testing process for further tests. The B_1 was much smaller in the negative polarity (148 mT) than the positive polarity (293 mT) during this test, which brought about 2 theories;

1. Residual magnetisation is present in the magnet, altering B_1.
2. The diodes between the superconducting ribbon are not rated for cryogenic temperatures, creating a short.

In the latter case, both of the diodes could have been creating a short, as B_1 was much lower than simulated in the positive polarity, and even smaller in the negative polarity for the same current. Another possibility was that the magnet yoke was not made out of the same material as simulated by the previous student, which would explain the reduced maximum B compared to the results produced by the simulations.

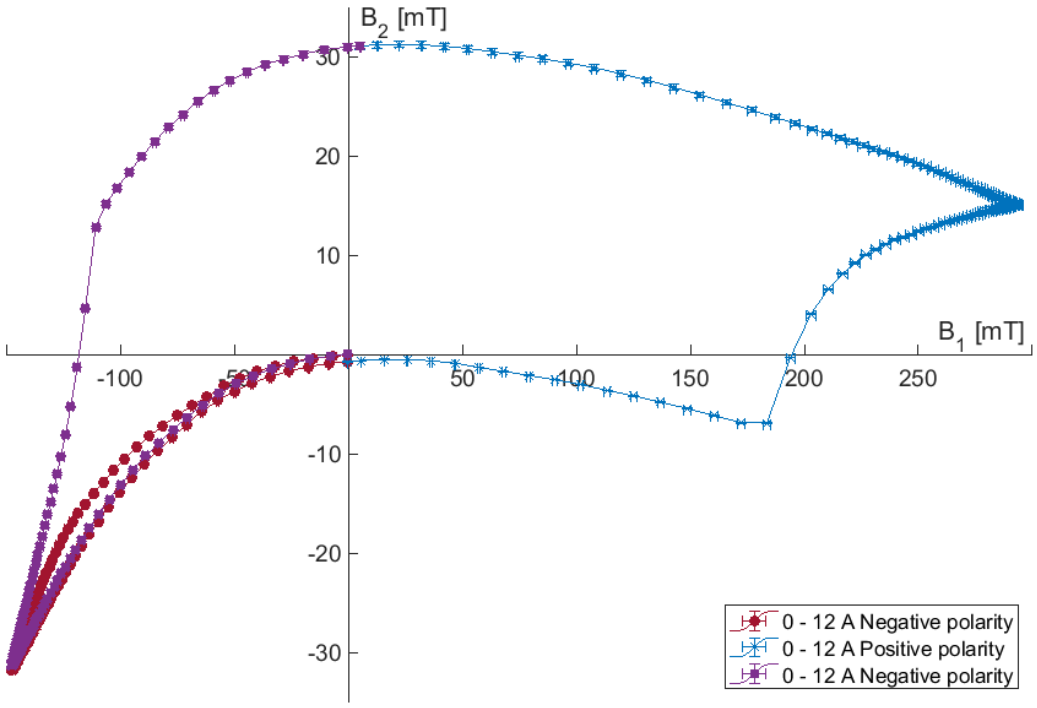

Figure 4.17: The initial test of the Niowave Nb sample, showing B_2 as a function of B_1.

However, this would not explain why the maximum B_1 was not the same in both polarities.

The first run in the negative polarity for both increasing and decreasing B_1 created a similar B_2. This would be expected if B had not penetrated through the sample and no flux was pinned within the sample. A linear dependence was expected, but a quadratic increase could not be explained. The test in the positive polarity created unreliability in the measurements. The results produced were not similar to the measurements observed for the negative polarity test. Additionally, when B_1 was reduced B_2 increased.

Due to the quadratic dependence between B_1 and B_2, followed by the unexpected behaviour in the positive polarity test, it was thought that there could be some magnetic hysteresis within the cage. The magnet could have been magnetised from previous tests and should be degaussed in between runs to remove any magnetic history. This lead to a second test on the Nb disk once the magnet had been degaussed to determine if there was any change in the results.

4.4.3.4 Niowave Nb disk - Test 2

The magnet was degaussed by ramping the current up to the maximum value of the previous test in the opposite polarity. The current was reduced to 90 % and the polarity was reversed. This was repeated until the minimum step of the power supply was reached. After the magnet had been degaussed the cage was removed from the LHe bath to warm the sample above T_c to expel any flux that could be trapped. The cage was then re-submerged into the LHe, and left until both thermometers read 4.2 K. The system was left another 2 minutes to ensure thermal equilibrium. The same method as the previous section was used to test the Nb, increasing and decreasing the current in the negative polarity, repeating in the positive polarity and finally repeating in the negative polarity a final time. The only difference between the 2 tests was that the second test increased the current up to 15 A, and therefore should produce an increased B_1. The results are shown in Fig. 4.18.

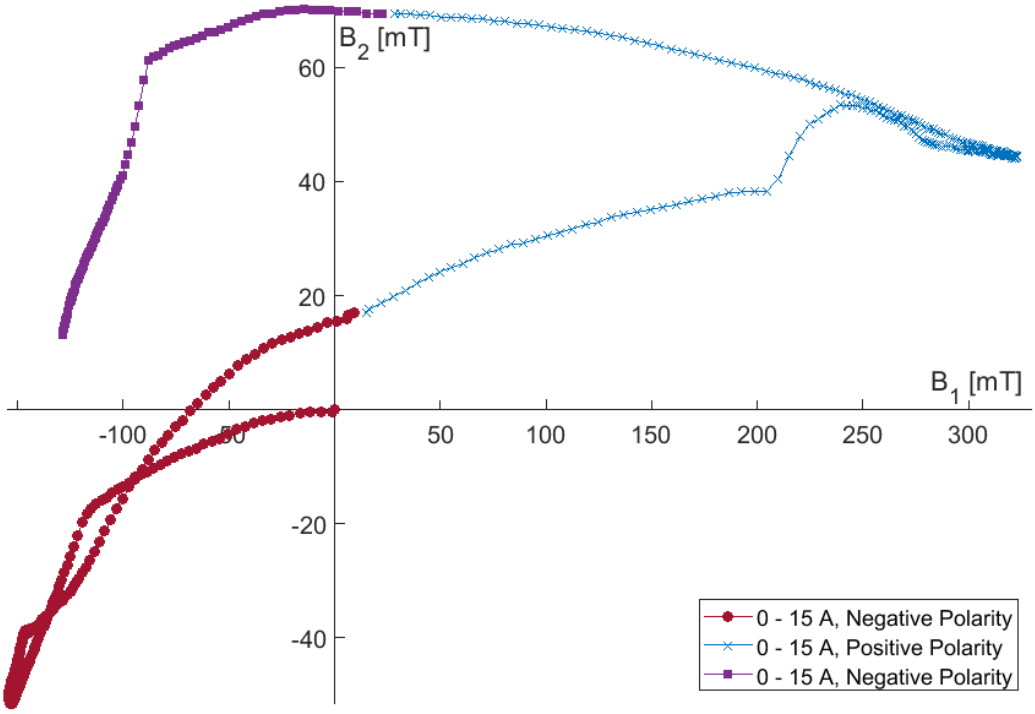

Figure 4.18: The penetrated field (B_2) as a function of applied field (B_1) post demagnetisation for a bulk Nb sample.

The results produced during the second test confirmed magnetisation within the system. Initially, B_1 and B_2 begin at 0 mT. As in the previous test, increasing B_1 created an exponential increase in B_2, which was followed by a linear increase. The maximum B_1 was 153 mT, similar to the previous test even though the maximum

current had been increased. Decreasing B_1 reduced B_2, however B_2 became positive and increased much more than the remanence field ($B_1 \approx 9.3\,mT$, $B_2 \approx 17.1\,mT$).

The test was repeated in the positive polarity. Ramping the current caused B_2 to increase with B_1, with a sharp increase in B_2 at 210 mT. However, B_2 then decreased, which cannot be explained. It would be expected for B_2 to continue to increase with B_1. As B_1 continued to increase up to its maximum, B_2 continued to decrease. The maximum B_1 reached was 322 mT, which was larger than in the negative polarity. As B_1 was reduced back to 0, it can be seen that B_2 increased to a much greater value than the previous test. After the positive polarity test the remanence fields became: $B_1 \approx 28.4\,mT$, $B_2 \approx 69.9\,mT$. Increasing B_2 determined that there was some magnetisation present within the cage or cryostat which created errors in the measurements.

Finally, the test in the negative polarity was repeated. The B_2 changed a small amount as B_1 was increased, followed by a sharp increase in B_2, which looked as if B had broke from one side of the sample through to the other. Figure 4.18 shows that the corresponding B_1 is not the same for the possible B_{fp} for both negative polarities, and the maximum B_1 for both negative polarities are also not the same. It was determined that something had been magnetised within the system. Due to the length of time it took to run the experiment, there was not enough LHe left to perform another test.

4.4.3.5 Summary

Before another test was performed, a hand-held Hall probe sensor was used to determine if there was any magnetisation around the cage at room temperature, or if it was only present whilst the superconductor was in the Meissner state. Moving the sensor around the cage determined 3 bolts were strongly magnetised due to being made of steel, and were disrupting the measurements. One of the bolts held the Cu cylinder on which the sample was situated (inside the spring in the cage in Fig 4.11), and 2 bolts held the magnet in place and were inserted into the removable poles. These bolts were replaced by brass components to remove as much magnetisation as possible. Although the cage did not seem to be magnetised, the cage was magnetic, which was determined by placing a permanent magnet near the cage. Nothing could be done quickly or easily to fix this. For future tests the cage was remade out of Cu to ensure the only magnetic parts in the system is the C-shaped dipole magnet, which was later performed by the laboratory technician, Liam Smith.

Another test day was planned using LHe. Due to the amount of LHe that was used to cool the system (and the cost of LHe), it was decided that the system should be pre-cooled with liquid N (LN_2). However, LN_2 was still present within the system when the LHe was injected, the LN_2 froze, and burned off more LHe and also limited

the minimum T=5 K in which the experiment could be operated. The frozen N did not allow the system to remain in thermal equilibrium, and more LHe boiled off to try and keep the system at 4.2 K. The liquid in the Dewar had to be removed, including the solid N, before more LHe could be injected to cool the system. This only allowed one more result to be obtained, which was not reliable due to the magnetic cage.

After the 2 days of running the facility as a wet system, followed by complications due to the magnetic history of the facility, it was decided to design a new, dry cryogenic system. The decision was made as the wet cryogenic system could only be run by supervisors who had been trained to use LHe, and not by myself due to the health and safety required whilst using liquid cryogens. In addition, the cost of LHe at the time of these experiments cost approximately £1000 for every 60 L, and if the LHe was not finished by the end of the day there would not be enough left for the following day such that it would be wasted. Hence, a new facility was designed to be cryogen free to ensure the system could be operated at any time, whilst not requiring extra training to use the facility.

As there was trouble with B_1 producing producing magnetisation, the facility was designed such that the only magnetic component in the facility was the magnet, to ensure that in the possibility of a large magnetic field no components would become magnetised.

4.5 Conduction cooled MFP facility

4.5.1 Design

After the field penetration method had been verified to somewhat work in the LHe system, it was decided that a new facility should be built mounted directly onto a cold head. It was decided to move to a dry system due to the rising price of LHe would cause the experiment to become extremely expensive without a He recovery line. A LHe based facility could also only be run by someone who had undergone proper liquid cryogen safety training, causing further disruption to others work.

The cold head used is a Sumitomo RDK-408D2 had been procured specifically for this experiment, and had a cooling capacity of 1 W on stage 2 at 4.2 K. After some quick heat load calculations, it was determined that an overestimation of the amount of component wires would still produce a lower heat load than the cooling capacity of the cold head. A CAD drawing of the cold head was made in Solid Edge 2019 to ensure all the parts would fit together before they were fabricated.

The design was started using spare parts that had already been procured and not used, such as a vacuum chamber that would already fit onto the cold head, and a second magnet which was made for the VTI. When the vacuum can was attached to the cold head, it was found that it reached stage 1, shown in Fig. 4.19. An adapter

Figure 4.19: The vacuum can was the same height as stage 1 of the cold head.

had to be bought so that a stage 1 plate could be made large enough to bolt on components. An extender was also designed to enable sufficient space between the vacuum can and the plate, shown in Fig. 4.20 by the Cu ring placed on stage 1. This extender was designed for ease when attaching components onto the plate and to ensure the wires could reach the plate without causing a thermal short by touching the vacuum can. Thus the distance between T_{room} and the stage 1 plate remained large, which reduced the static heat load onto stage 1.

Due to the system moving from a gas cooled experiment to a conduction cooled experiment, a new approach was required to determine how/where components should be placed for efficient cooling. Due to being designed from scratch, a few new components were also designed to make the operation of the facility easier. The magnet consisted of a LTS solenoid, so LTS to HTS joins and HTS to normal conducting joins would have to be made to allow power to be applied to the electromagnet.

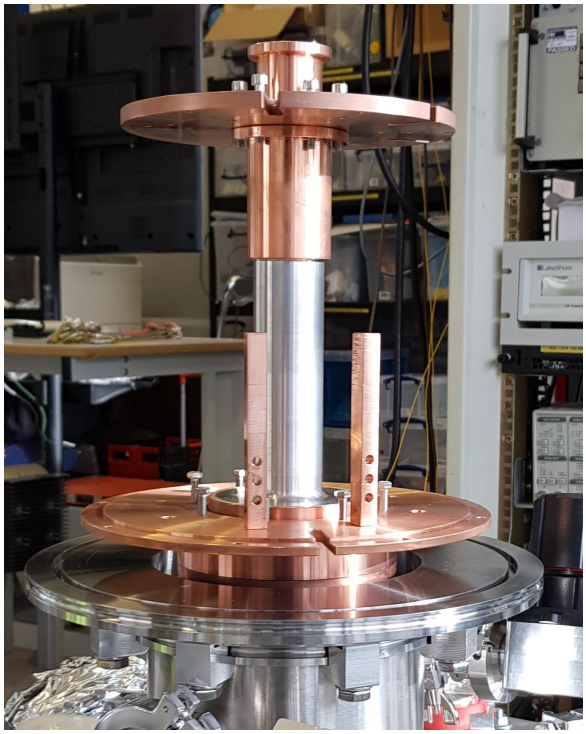

Figure 4.20: Once all the OFHC Cu components were finished, a trial build was done to ensure everything fit together and no further mechanical work was needed.

4.5.1.1 Stage 1

The stage 1 plate was designed to allow 2 Cu bars to be bolted directly onto the plate, seperated by a layer of Kapton tape to allow good thermal conduction whilst the bars remained electrically isolated from the plate, and therefore each other. The plate had 4 countersunk holes designed to hold ceramic screw insulators which ensured the bolts attached to the bars were also electrically isolated.

I travelled to the University of Manchester to take inspiration from some of their cryostat designs, to design my facility to be more operator friendly. One technique of theirs from which inspiration was taken was a 'breakout board'. A breakout board is a standard PCB with a 51 pin D-sub connector (or any amount of pins) with a 1 to 1 connection. The breakout board made at Daresbury can be seen in Fig. 4.21. Every wire can be connected from the external feed through to the stage 1 plate, as this generates a negligible amount of heating compared to the cooling capacity of the first stage, and does not affect the temperature of the system. This allows a rapid change of components when required. Thus, when making a change, the only wiring that needs to be done is wiring the component itself to plug into the board, and the wiring from the controller to the external feed through.

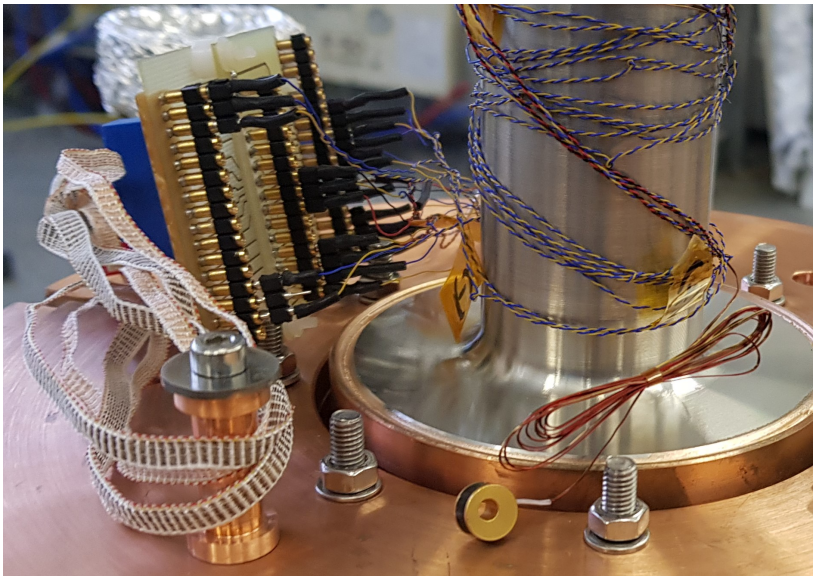

Figure 4.21: The breakout board with come components plugged in.

4.5.1.2 Stage 2

Due to the system being conduction cooled the superconducting wires required a physical connection to be thermalised. A large Cu bobbin was designed such that the LTS wire could be wrapped around for thermalisation, similar to wrapping wires for components around small Cu bobbins. Many superconducting wires have a minimum bend radius, which was also our case, so the bobbin was designed to be larger than the minimum bend radius, as the bobbin and LTS wire would contract as the temperature was reduced. The LTS wire was indium brazed to HTS ribbon which is shown in Section 4.5.2.1, and thermalised using Cu bars bolted to stage 2. To ensure there was not an electrical short, Kapton tape was used to insulate the Cu bars from stage 2, and heat shrink tubing was used to isolate the bolts.

Smaller Cu bobbins were also used to ensure all the wires on stage 2 would be thermalised, and are shown on the left in Fig. 4.22. One resistor is placed either side of the magnet shown in Fig. 4.22 which allows the temperature of the system to be controlled, either for a B_{fp} test, to warm the sample up to release any trapped flux, or to warm the facility to room temperature to change the sample.

Initially, a thermometer was taped onto each sample to determine the sample temperature using Al tape. However it was determined after a couple of tests that it is much more reliable to place a thermometer onto the sample and compress them together using a brass strip as shown in Fig. 4.22. Initially, a silicon diode thermometer was used to measure the temperature of the sample, which was later changed to a Lakeshore Cernox CX-1050-CU-HT-1.4L due to having an accurate

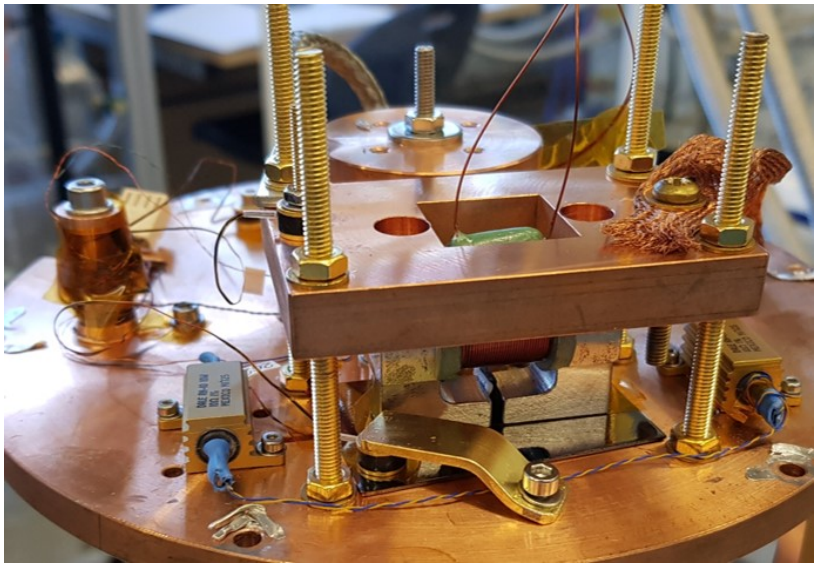

Figure 4.22: A standard set up of a sample in the magnetic field penetration experiment. The sample is Nb on a Cu substrate deposited as part of the ARIES collaboration.

calibration curve and reduced error at low temperature. Silicon diode thermometers were placed onto the Cu block holding the magnet, and onto the stage 2 plate, however these temperatures were not required to be known with great accuracy.

4.5.1.3 Thermal radiation shields

The new system was designed to have 2 thermal radiation shields made out of OFHC Cu to reduce the heat load on the system. The thermal radiation shield on stage 1 was used to reduce the minimum temperature the system could reach by ensuring no 300 K photons would strike the stage 2 plate, thus producing an increased heat load compared to photons from a 40 K radiation shield. A second radiation shield attached to stage 2 was made to intercept any photons with from a T greater than then sample T from striking the sample during the test to ensure more reliable results. I.e. - the sample will only be struck by photons emitted from components of a similar T. Both thermal radiation shields were wrapped in MLI to further reduce the heat load.

4.5.1.4 Magnet

Due to the problems that appeared whilst testing the VTI, simulations were performed with variations of the magnet. Simulations confirmed that the long steel bolts directed the B such that it would leak around the sample, confirming what had been found

experimentally. In addition, simulations showed that B_1 was reduced when the bolts that hold the yoke together are non-ferrite due to a reduction in the cross sectional area of the magnet. It was decided to use short Fe bolts that are close to flush with the top of the magnet. These bolts increased the maximum B the magnet could produce, whilst reducing the amount of B that would leak around the sample. A Cu block was used to hold and thermalise the magnet to ensure thermal stability. The Cu block had 4 guide rods to ensure the magnet would twist or change position between each test. Initially, these guide rods were made out of G10, a thermal insulator made out of epoxy. After a couple of tests these rods became worn and broke as the epoxy was brittle. The rods were then replaced with long Brass bolts, as Brass is non-magnetic, more durable and aided in cooling the Cu block. Two Cu braids were also attached to the magnet holder to thermalise the magnet to stage 2.

4.5.2 Complications

Due to unforeseen circumstances, some of the parts that were machined took longer than expected, delaying the start of the experiment. Both thermal radiation shields were at University of Manchester to be silver soldered, and were delayed due to COVID-19. All the other parts of the system were finished before the thermal radiation shields were returned. To try and start the experiment different, simple thermal radiation shields were tested to try and reduce the system to a low enough temperature for testing. The first attempt consisted of Al studding and MLI which did not reach a low enough temperature, so 2 crude thermal radiation shields were made from Al, using tin snips and bolts, which allowed the first successful cool down of the facility.

Similar to the VTI, the LTS to HTS to NC joins were intended to be made at RAL. Due to the pandemic, many places closed. The group who intended to perform the SC joins were delayed for their regular project and could not perform the joins. It was determined that the system should be returned to Daresbury laboratory where the SC joins would be made in house.

4.5.2.1 Superconducting joins

There was no experience in making SC joins at Daresbury laboratory, with no specialised equipment. It was determined the best way to perform the task was to machine Cu blocks with 'trenches' in which the SC wires would be joined. The Cu blocks were made as long as possible so the joins between the SC leads could also be made as long as possible. Increasing the contact area between the 2 superconductors reduced the contact resistance and thus any localised heating. The Cu blocks were placed on a hot plate, the In and SC wires were placed into the trenches, with the cover of the trench placed on top. Indium was used as it is a soft metal with good thermal

conductivity and low electrical resistivity, ensuring no thermal gradient between the SC leads and the Cu bar, whilst also reducing the resistance. Additionally, if SC wire is heated excessively, it can break and lose its superconductivity. Thus, In was used due to having a low melting point of 156.6 °C [117].

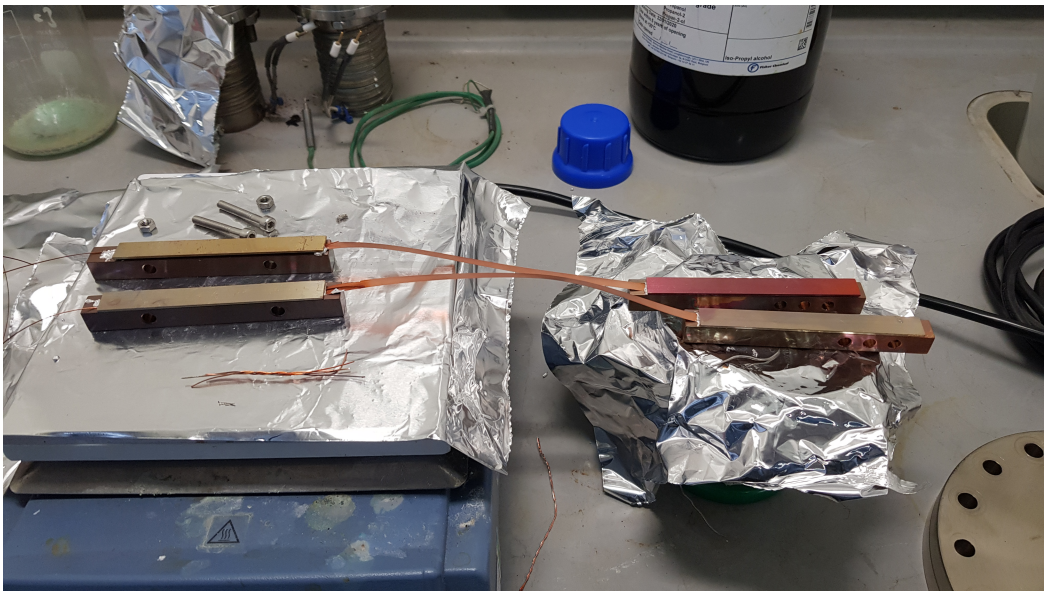

Figure 4.23: The Cu bars which show the joins between the HTS ribbon and LTS wire (left) on the hot plate, and the HTS ribbon to the Cu bar (right).

The Cu bars were slowly heated by stepping up the temperature of the hot plate until the In melted. When the In became molten, the Cu cover slotted into the trench compressing the LTS wire and the HTS ribbon together, and the HTS ribbon onto the Cu block. Weights were then placed on the surface of the Cu blocks to ensure the Cu covers were sufficiently compressed, and remained there as the Cu blocks were left to cool naturally to T_{room} to allow the In to solidify in place. Once the bars were at T_{room}, the SC circuit is presented in Fig. 4.23, with the magnet and LTS wires to the left of the image.

4.5.3 Operation of the facility

The initial aim was to design a system that allowed a fast sample turn around. However, the VTI displayed that this was difficult whilst still ensuring the sample cooled to a low enough T for testing. Unlike the VTI, the cryostat was more inconvenient, as the sample could not be removed from a cold system for a quick changeover, with only the experimental area required to be heated and cooled. Instead, the whole system had to reach T_{room} for a sample change over.

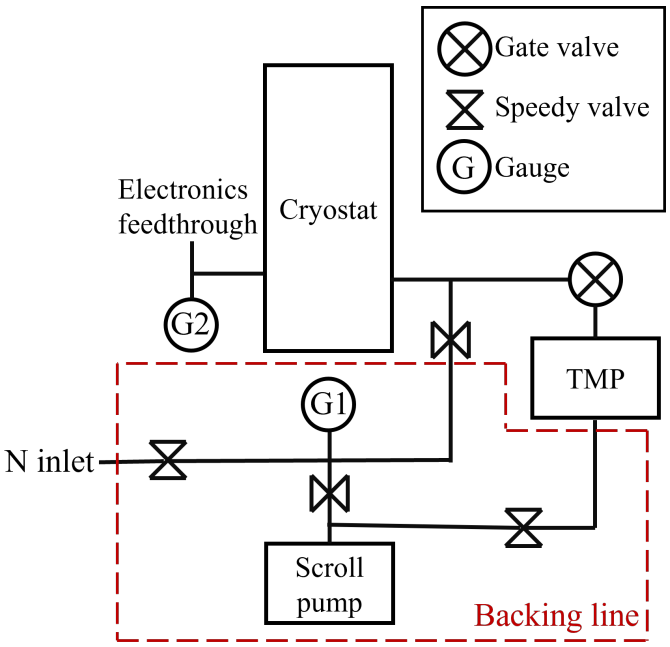

Figure 4.24: A schematic of the vacuum system for the conduction cooled MFPE.

It takes approximately 1 hour to change a sample over. First the facility would have to be vented with N to be removed from vacuum before the steel vacuum and both thermal radiation shields can be removed to change the sample. The components must be re-attached to the system and placed back under vacuum. Whilst the sample is changed over, the backing line (shown in Fig. 4.24) to the turbo-molecular pump (TMP) (Agilent TwisTorr 84 FS) and the vacuum system is left under vacuum provided by the scroll pump (initially an Agilent scroll pump which broke within a couple of weeks, and it was replaced by an Edwards nXDS10i), which produced a pressure of 1×10^{-3} mbar. Once the system was closed, the backing line to the TMP is closed off with a valve, and the cryostat is opened to the scroll pump using second valve. The backing line of the TMP can be opened when the backing line pressure is below 1×10^{-1} mbar, which typically took less than 5 minutes. The system is generally pumped down to 1×10^{-2} mbar in $\approx$ 30 minutes. Once the pressure of the main volume (i.e. the cryostat) reached low 1×10^{-2}/high 1×10^{-3} mbar, the scroll pump is closed to the main volume using a valve, and the valve connecting the TMP to the main volume is opened to further reduce the pressure.

It took approximately 5 hours to pump the main volume down to a pressure of $\approx 1 \times 10^{-5}$ mbar before the compressor (Sumitomo cryogenics F-50) was started to begin cooling the system. Generally, it took approximately 5 hours for the system to cool from T_{room} down to the minimum T $\approx$2.5 K. The Stage 1 final temperature is

≈25 K. The sample temperature can be varied in the range 2 K≤T≤30 K using the heaters placed either side of the sample, which are controlled using a proportional-integral-differential (PID) loop from the Lakeshore temperature controller, which is sufficiently wide for studying both Nb and A15 SC materials. Whilst the temperature range is wider than the LTS solenoid, a small current can still be passed through the wire without causing damage to the wire. Especially as the thermal conductivity of the Cu component of the LTS wire will have an increased thermal conductivity. No more than 2 A is applied to the LTS solenoid above its T_c, which is ≈10 K.

The accuracy of the temperature reading is defined by the type of thermometer used. The error for a Cernox is ±5 mK and ±0.25 K for silicon diodes from the calibration curves provided from the manufacturer. Silicon diodes were the only thermometer used at the beginning of the tests due to being cheap with a standard calibration curve, except one PT100 thermometer which was chosen as accuracy of the stage 1 was not required during testing and only when close to T_{room} to allow the facility to be safely opened. Due to the size of the error, the silicon diode thermometer placed on the sample was replaced by a Cernox for a greater accuracy in the temperature measurements, and calibrated using a calibration curve provided by Lakeshore. Whilst at set T, there is still a fluctuation in the T due to the refrigeration cycle of the compressor, which has a frequency of 1 Hz. The fluctuation produced an error in the measurements, as the PID control cannot completely remove the temperature fluctuation. The standard deviation of the temperature fluctuation during measurements is taken in order to quantify the error in the sample temperature during fixed temperature measurements, which was found to not exceed 15 mK in the final configuration of the facility.

4.5.3.1 Automation

One limitation with the VTI was the time limit with LHe, and during initial tests using the cold head it was determined that the system should be automated. Automation allowed the facility to be controlled remotely, allowing the compressor to be controlled via the PC, thus reducing the amount of electricity used to run the system. Automating the system also allows the number of measurements to be increased, thus increasing the accuracy of the measurements. The facility was fully automated using a pre-defined procedure in LabVIEW, which controls:

- Set fixed temperatures points to perform the measurements.
- The applied current to the magnet to generate B_1.
- The step size of the applied I, and thus the corresponding step size in B_1.
- Whether the magnet should be demagnetised between each run.
- The temperature to warm the sample above to release any trapped flux.

The amount of set temperature measurements and the maximum B required defines the length of time required to perform a full temperature sweep. A full test can range between 24 hours and a few days. The Hall probe sensors are recorded by a USBDAQ controller from Arepoc, which records the voltage of the Hall probe sensors using a four wire measurement. A data sheet was provided with the sensors which give the sensitivity of the Hall probes at 297, 77 and 4.2 K. The sensitivity used for the measurements was the sensitivity at 4.2 K, as the sensitivity only changed a small amount between 77 and 4.2 K, the measurements around 10 K will have a negligible affect on the results. The data sheet also contained an offset voltage for each Hall probe, however this was re-measured once the Hall probe sensors had been integrated with the system.

4.5.3.2 Testing cycle

A typical test cycle for the MFPE for the conduction cooled system consists of:

1. Zero field cool down to the minimum T of the system (≈2.5 K) - No heaters are used.
2. The applied current is stepped up by a predefined step size defined by the operator, which in turn produces a corresponding B_1, up to a maximum current which should correspond to a $B_1 > B_{fp}$.
3. The current is reduced to 0 A and no measurements are recorded.
4. The system is de-gaussed if chosen by the user.
5. The system is heated to a pre-defined T chosen by the user, where $T > T_c$ so the sample transitions out of the Meissner state to release any trapped flux.
6. The sample T is held within 0.05 K for 15 minutes to ensure the system/sample is in thermal equilibrium, and ensure all flux has been expelled. If the T of the sample falls out of range, the timer restarts when it is back within range.
7. The sample undergoes another ZFC to the next set T point, and is again held within 0.05 K for 15 minutes to ensure the system is in thermal equilibrium.
8. Points 2 - 7 are repeated until all the pre-defined temperature set points have been tested.
9. Once all set temperatures have been tested, the program turns the compressor off, the heaters are turned on and set to 280 K, and the system is left to warm up under vacuum.

4.6 Commissioning the conduction cooled MFPF

4.6.1 Magnet testing

Similar to the VTI, both B_1 and B_2 are measured by Arepoc Hall probe sensors, HHP-NP and HHP-NA for Hall probe 1 and 2 respectively, shown in Fig. 4.1. The error for the Hall probes are ±2.68 mT and ±7.00 mT for HP1 and HP2 [118], [119]. A second set of sensors were also used after the first pair broke, which had an error of ±5.03 mT and ±4.95 mT for HP1 and HP2 respectively [120], [121].

The SC magnet testing produced $B_1 \approx 144$ mT at 1 A, which was similar what the team at RAL found when they tested the magnet in the NC state, and also similar to the simulated field. An external, hand held Hall probe sensor was used to measure B without a SC sample present, which determined a perpendicular component of B (B_y) had a maximum of 46 mT under one of the poles. B_1 can be described as ≈63 % parallel to a NC sample surface. In the presence of a thick superconductor, the superconductor behaves as a magnetic mirror. Thus the B_y components are cancelled on the surface of the superconductor whilst in the Meissner state, and B is only parallel to the sample surface.

To determine the maximum B that can be applied by the magnet, the current was slowly stepped up and B_1 was measured. The test was performed at 2.5 K, and the maximum applied current was 8 A, which generated a B_1 of 612 mT. Whilst I=1 A generated the expected B_1, the maximum field was lower than produced in the simulations, which indicated that the magnet is could have become saturated, or the permeability of the magnet had reduced due to cooling. This was not the maximum current that could be applied, but the large B_1 indicated that a larger B was not required, and would also be limited due to the magnet becoming saturated.

4.6.2 Cool downs

To get the facility running as soon as possible, Al thermal radiation shields (TRS's) were made in house. The Al was 2 mm thick, and allowed the system to reach low temperatures which allowed the facility to begin testing samples. Once the TRS's out of OFHC Cu were finished, they were placed into the system to increase the thermal conductivity. The final Cu TRS's wrapped in MLI are shown in Fig. 4.25. Finally, a comparison of the final temperature of the system has been made for the Cu radiation shields with and without MLI, shown in Table 4.2.

A few things should be noted; These measurements were performed using Silicon diode sensors (error of ±0.25 K [122]), and the thermometer on the samples were held on using tape. The aim was to try and keep the conditions for each test the same to allow a comparison to be made between each set up. However, the TRS's were not bolted down using the same torque, which can change the thermal contact between

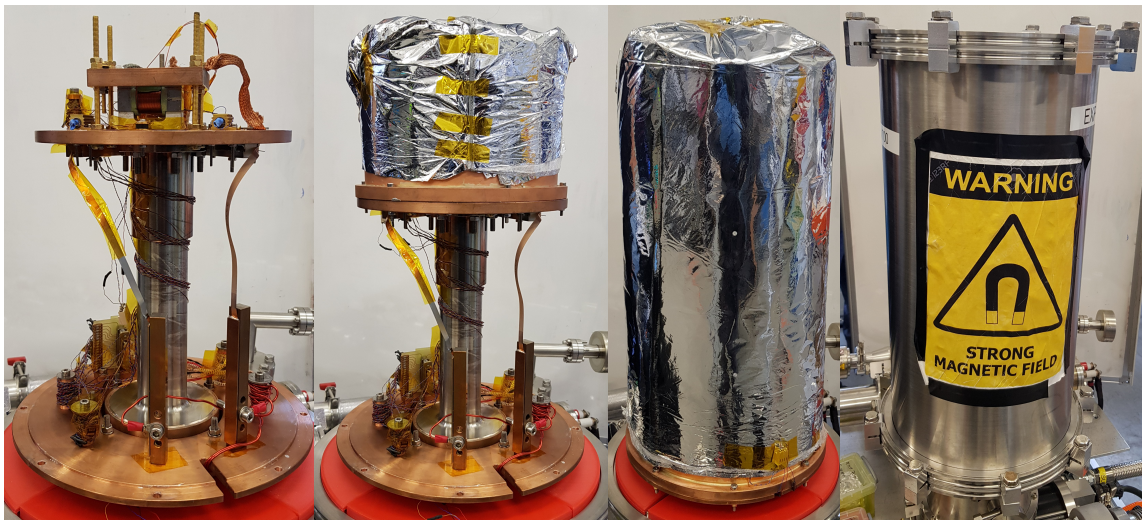

(a) (b) (c) (d)

Figure 4.25: The layout of the field penetration system: (a) shows the system open, (b) shows the stage 2 shield attached, (c) shows the stage 1 shield attached to the system and (d) shows the facility fully closed by the stainless steel vacuum can.

the plate and the TRS. The Cu TRS's had a Cu ring which was used to bolt the TRS to the plate, where as the Al TRS had small tabs which were used to connect the shield to the plate, limiting the thermal conductivity. Finally, a comparison between the stage 1 TRS temperature has not been made, as the thermometer is a PT100, which has a lower range of 28 K. All three variations of the stage 1 TRS's read 28 K once cold, which indicating that the top of the stage 1 TRS's temperature is $28 \geq T \geq$ stage 1 plate.

A typical cool down of the cryostat with Al TRS's is shown in Fig. 4.26. Stage 1 cools much faster that stage 2, and the stage 1 TRS shows thermal lag as the heat is slowly removed, due to the thermometer reading the temperature at the top of the shield, at a distance away from the cold source. Stage 2 (and all the components attached to stage 2) take much longer to cool down. As stage 2 reaches a comparable temperature to stage 1, the T rapidly reduces to a minimum.

A comparison between the three TRS's are shown in Table 4.2. The errors in the temperature in Table 4.2 do not include the error in the silicon diodes as the error in the diodes greatly outweigh the fluctuation error, and would obscure the temperature fluctuation. All three versions of the stage 1 TRS cooled to below 28 K, and due to the type of thermometer used (PT100), no comparison can be made as the temperature is too low for a reading and it is outside the range of this thermometer.

Replacing the Al TRS with Cu made some noticeable differences. For example,

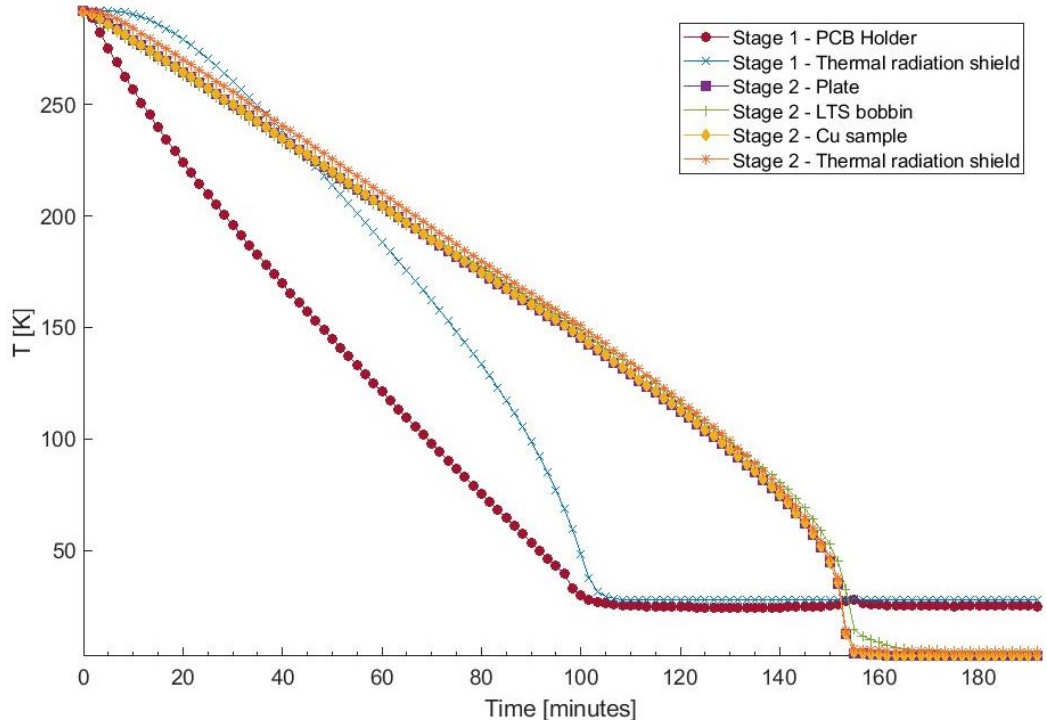

Figure 4.26: The temperature of the cryostat with Al thermal radiation shields during the cooling process.

Table 4.2: A table comparing the average minimum temperature for different thermal radiation shields, the time taken to cool the system to the minimum temperature and the standard deviation of T_{avg} once the system has reached an equilibrium at the minimum T.

	T_{avg} [K]			**Cooling time [minutes]**	
TRS material	Stage 1 PCB holder	Stage 2 plate	Stage 2 TRS	Stage 1 TRS	Stage 2 TRS
Al	25.28 ± 0.05	2.81 ± 0.03	4.61 ± 0.12	110	155
OFHC Cu	25.44 ± 0.07	2.93 ± 0.03	2.41 ± 0.04	150	216
OFHC Cu + MLI	25.23 ± 0.06	2.86 ± 0.11	2.55 ± 0.15	134	200

it took ≈1 hour longer to cool the Cu TRS's, due to an increased thermal mass. Changing the TRS's to Cu did not improve the minimum temperature of the stage 1 PCB holder or the stage 2 plate. The stage 2 TRS had a reduction in the minimum temperature by 2 K, and a reduction in the temperature fluctuation from 0.12 to 0.04 K. The reduction in T is due to 2 reasons; 1) a greater thermal contact between

the different parts of the TRS, and 2) a greater contact between the TRS and the stage 2 plate, due to the TRS having a full ring (rather than small tabs) such that more torque could be applied to the TRS which increased the contact between the TRS and the stage 2 plate. The 3 parts of the Cu shield were silver soldered together which created good thermal contact between the adjacent parts. This allowed the heat to flow through the shield to the stage 2 plate, where as the Al shield was only bolted together, thus limiting the removal of the heat due to a small contact area. The reduction in the fluctuation of the stage 2 TRS T is due to the increased thermal inertia of the Cu shield due to having a greater mass.

Table 4.3: Typical minimum temperatures of the system whilst in equilibrium for the final set up of the facility. T_{std} is the temperature fluctuation at each position in the system, and ΔT is the total error of the temperature due to the fluctuation and the error in the thermometer.

Thermometer placement	$\mathbf{T_{avg}}$ **[K]**	$\mathbf{T_{std}}$ **[K]**	$\mathbf{\Delta T}$ **[K]**
Stage 1 TRS	'28'	-	-
Stage 1 PCB holder	25.123	0.045	0.254
Stage 2 TRS	2.366	0.039	0.253
Stage 2 Magnet holder	2.597	0.002	0.250
Stage 2 Sample	2.643	0.002	0.005

Adding the MLI to the Cu shields did not significantly decrease the minimum T of the system, or the thermal stability of stage 2. This is likely due to the TRS not being attached onto the stage 2 plate with a similar amount torque. To perform a reliable measurement between these set ups, a torque wrench should be used to ensure the TRS's are always bolted down with the same amount of force applied. The minimum T and T stability measurements were repeated using the final set up of the facility, which resulted in Table 4.3. It should be noted that the final set up of the system was using a Cernox thermometer, producing the much lower error on the sample shown in Table 4.3.

4.6.3 Sample purity

During the commissioning process, multiple samples were procured from Goodfellows Cambridge Ltd and used to qualify the MFPF, which are shown over the remainder of this chapter and the next. The samples were bought due to having a high purity of 99.9 % and being a specified size. However, the samples still contained impurities which are shown in Tables 4.4 and 4.5 for the Pb and Nb samples respectively.

The Pb sample has an extremely low impurity content of 71 ppm. This is not the case for the Nb foils. There are a greater number of impurity elements (14) reported

Table 4.4: The impurities of the 10 µm Pb samples from Goodfellows Cambridge Ltd in parts per million (ppm).

Al	Au	B	Sn	Cd	Ca	Cr	Mg	Ag	Bi	Cu	Na	Fe	Se
1	2	1	8	1	15	8	1	1	4	25	2	1	1

Table 4.5: The impurities of the Nb foils from Goodfellows Cambridge Ltd taken from the Goodfellows website, and their relevant resistivity, r_i, from Ref. [13].

	Impurity content [ppm]		
Impurity	Nb (1-10 µm)	Nb(50-100 µm)	r_i
B	<10	-	-
C	25	50	4380
W	<100		262000-721000
Cu	<5	-	-
H	<10	5	2640
Ni	<5		-
Fe	30	200	-
Mo	10	-	717000
N	20	50	4230
O	100	100	5580
Ti	<10	30	53700
Si	100	-	-
Ta	500	2000	114000
Zr	<10	-	102000-239000

for the Nb samples between 1-10 µm samples, with a total number of impurities as large as 935 ppm. On the other hand, the thicker samples with a 50-100 µm have less reported elements (7), but have a much larger impurity content (2435).

It is well documented that the impurity content of Nb alters the residual resistivity ratio (RRR), which is an indicator on the quality of Nb. Typical resistivity of high gradient Nb cavities is $\geq$300, where as reactor grade Nb typically has RRR$\approx$30. The RRR can be calculated using Eqn. 4.3 from Ref. [123], where f_i is the content of impurity i and r_i is the relevant resistivity.

$$RRR = \left(\Sigma f_i / r_i\right)^{-1} \tag{4.3}$$

Using Eqn 4.3 the RRR was calculated for the Nb foils. The Nb foils with a thickness between 1-10 µm produced a calculated RRR between 30-34 depending on the whether the maximum or minimum impurity content was used for certain elements. The Nb foils with a 50-100 µm had much less impurities listed than the

thinner samples, but had a much greater impurity content, such that the calculated RRR was found to be 22. Thus, although the Nb is of high purity, the known impurities drastically reduce the quality of the samples. The 50-100 µm thick Nb foils also underwent heat treatment after production, the exact details not shared.

4.7 Raw Data

To determine how the data obtained by the MFPF should look, it was determined to use a Type I superconductor. Type I superconductors do not have an intermediate state, and the transition between the Meissner state and the normal conducting state should be sharp, thus it is clear when B_1 has broken through the sample to help define a method to determine B_{fp}. It should be noted that B_{fp} is not the same as the lower critical field, B_{c1}, as vortices can enter and leave from the same side as the sample if the sample is thick enough. A sharp transition was beneficial such that multiple data analysis techniques could be tested to determine the most reliable way to extract B_{fp}. A Pb foil (10 µm thick with a cross section of $50\times50\,mm^2$) was bought from Goodfellow Cambridge Ltd to help commission the experiment. Additionally, testing a thin Type I superconductor allowed the sample size to be reduced easily to determine how the sample size affected both B_{fp} (described in the next section) and the amount of magnetic field that would leak around the sample.

The sample was tested as delivered, at the original size of $50\times50\,mm^2$ with no treatments performed on the sample before being placed in the MFPF. The sample was placed in between 2 thin pieces of brass - one square $50\times50\,mm^2$ between the Pb and the stage 2 plate, and one $10\times40\,mm^2$ rectangle between the sample and the magnet. The brass spacers were to limit the damage that could be produced on the Pb sample during each run. It should be noted that the brass spacer between the sample and the magnet reduces B on the sample surface, as shown in Table 4.1, therefore the local B (B_{local}) is not necessarily the same as B_1. All results that are reported use B_1 as it is a comparison between each test. The Pb sample was tested using the method described in Section 4.5.3.2, and the sample was heated to 10 K after each test to ensure any trapped flux was released from the sample. The raw data for the $50\times50\,mm^2$ is shown in Fig. 4.27.

It was initially thought that the superconductor would completely screen B_1. Figure 4.27 shows that this is not the case, as B_2 initially increases linearly with B_1, labelled B_1K_2, and indicates that not all the B is screened by the superconductor. A second straight line can be seen in Fig. 4.27, labelled as B_1K_1, which is $B_1(B_2)$ in the normal conducting regime. Thus, the relationship depends on the distance between both Hall probe sensors (K_1). This is the normal conducting line, which was found for this sample configuration by finding the relationship between B_2 and B_1 at $T = 8\,K$, as the T_c of Pb=7.2 K [33] and the sample would be normal conducting.

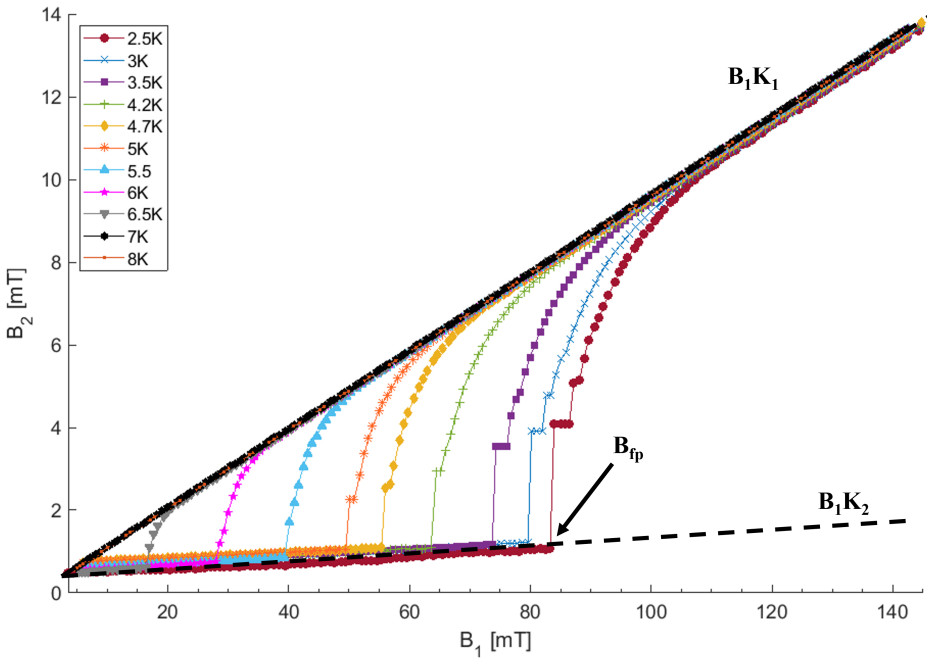

Figure 4.27: The raw data produced by the conduction cooled MFPF with a 10 µm thick Pb sample with a $50 \times 50\,\mathrm{mm}^2$ surface area. Here B_1 is measured by HP1 and B_2 is measured by HP2.

Between B_1K_1 and B_1K_2, B_{fp} can be seen. As B_1 is increased, there is a rapid change in B_2 when the field breaks from one side of the sample to the other, which indicates B_{fp}. The sharp breakthrough is intrinsic of a Type I superconductor due to having no intermediate state; the sample is either in the Meissner state or the normal conducting state. Once the field has broke through the sample, $B_2(B_1)$ increases with a linear trend and matches the same gradient as the tests performed above T_c, which shows that the Pb sample is normal conducting. Furthermore, B_2 does not immediately jump from B_1K_2 to B_1K_1, and there is a short but gradual change. As B_1 is localised to a small area on the surface of the sample, it is expected that an island of normal conducting volume expands from the centre of the sample. Thus, the superconducting volume of the sample would decrease as B_1 is increased, until all the field has penetrated through the sample. In addition, the higher the temperature, the less pronounced transition for B_{fp}. This is due to the B_2/B_1 ratio becoming smaller.

4.7.1 Defining B_{fp}

Multiple analysis methods were generated and tested to try and extract the exact point of B_{fp}. The value of B_{fp} was found using various analysis methods and compared to the 'obvious' B_{fp} shown in the raw data for the $50\times50\,mm^2$ Pb foil to ensure the 'correct' point was found.

4.7.1.1 Method 1 - Normalisation of B_1K_2

The first tests produced a linear B_1K_2. It was logical to determine B_{fp} by normalising B_1K_2 to 1, to represent the superconducting volume ratio (for this section, R). For a given position of the magnet with respect to the sample plate, the B_2 measured in the absence of a superconducting sample is defined by the parameter $K_1 = B_2/B_1$. The same is also true for a superconducting sample in a magnetic field greater than B_{c2}. The superconducting state of an infinitely large sample can be described with a superconducting ratio, R:

$$R_\infty = 1 - \frac{B_2}{B_1 K_1} \tag{4.4}$$

When B_2 is screened by an infinitely large sample, R will remain 1 until B_{fp}, where R will reduce due to B breaking through the sample. Due to the magnetic field leaking around a sample with a finite size, (B_1K_2), must then be accounted for, such that Eqn. 4.4 becomes:

$$R = 1 - \frac{B_2 - B_1 K_2}{B_1 K_1} = 1 + \frac{K_2}{K_1} - \frac{B_2}{B_1 K_1} \tag{4.5}$$

The results shown in Fig. 4.27 have been analysed with Eq. 4.5 and are shown in Fig. 4.28. Theoretically, Eq. 4.5 should produce $R = 1$ for any sample in the Meissner state. However, it can be seen experimentally that at low B_1 the normalisation curve does not always produce $R = 1$ due to the large relative error in HP2 compared to the measured B_2. The error in B_2 due to HP2 must be accounted for during this process, and this can vary for each run. There are two possible causes for this:

- A remanence field exists within the magnet after each run. The maximum residual magnetisation after degaussing being $B_1 \leq \pm5\,mT$.
- The error of HP2 produced is $\Delta\ B_2 = 0.7\,mT$.

For larger B_1 the plateau for $R = 1$ is clearly present, followed by a sharp transition. The points just before the sharp transition are used to normalise the curve.

Using this method, B_{fp} is defined as the B_1 where R has reduced to $R = 0.99$. The error in B_{fp} is $\leq \pm1\,mT$ for $B_1 \leq 100\,mT$ and $\approx \pm2\,mT$ for $B_1 = 10\,mT$ depending on the step size of B_1 due to the applied current.

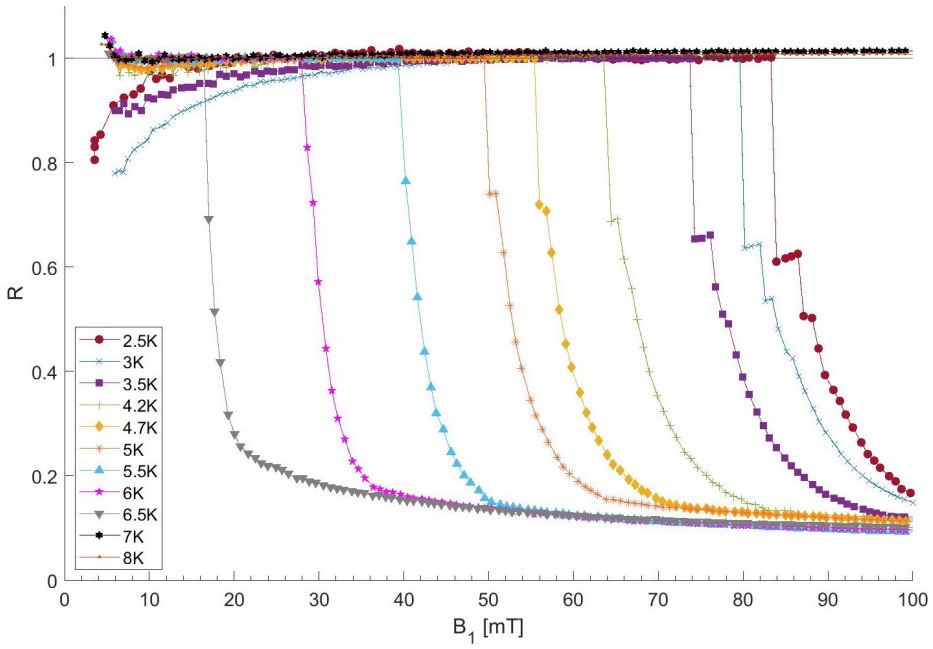

Figure 4.28: The data for 10 µm thick Pb with a cross section of $50\times50\,\mathrm{mm}^2$ once the Meissner state has been normalised to have a superconducting ratio of 1 using Equation 4.5.

In further tests the sample size was reduced, which is reported in Section 4.9. As the sample size was reduced, B_1K_2 did not remain linear, and in turn the ratio method became much more difficult. The section of B_1K_2 which is normalised to 1 can be changed. For example, the section just before the sharp increase in B_2 for the 50 mm disk shown in Fig. 4.36. Whilst this does allow B_{fp} to be found for samples with a sharp transition, this cannot be performed for smaller samples where the transition is not as distinct, or for T close to T_c. This method included an input from an operator, which can also skew the results. Thus a new method should be used to determine B_{fp} which could be done without a human input.

4.7.1.2 Method 2 - Second derivative

Another method was developed to define B_{fp} in cases where the transition for B_{fp} is not as sharp, and therefore not as clear. This method required to be a robust numerical algorithm that could be programmed for automated data analysis, and therefore could not produce skewed data due to an operator.

The raw data could be analysed using the second derivative of $B_2(B_1)$. The second derivative of B_2 is 0 for both the Meissner state and the normal conducting state, i.e

K_2 and K_1 respectively as they both produce a linear trend. The B_{fp} corresponds to the largest increase in d^2B_2/dB_1^2, as the flux from one side of the sample abruptly breaks through the sample. The numerical definition of the second derivative for three unevenly spaced points is defined as:

$$\frac{d^2y}{dx^2} = \frac{\left(\frac{y_{n+1}-y_n}{x_{n+1}-x_n}\right) - \left(\frac{y_n-y_{n-1}}{x_n-x_{n-1}}\right)}{\left(\frac{x_{n+1}-x_{n-1}}{2}\right)} \tag{4.6}$$

Equation 4.6 is performed using the 'gradient' function twice in MATLAB [124], and is referred to as $d^2(B_2)/d(B_1)^2$. The results shown in Fig. 4.27 have been analysed with Eqn. 4.6 and are shown in Fig. 4.29.

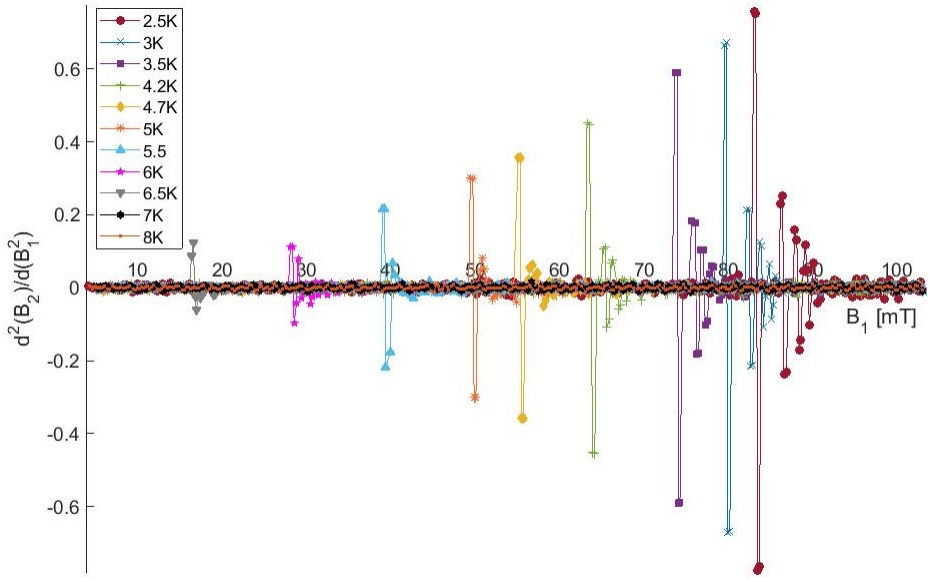

Figure 4.29: The rate of change of B_2 as a function of B_1 for the 10 µm thick Pb ($50\times50\,mm^2$ sample).

For each temperature the dependence of the second derivative as function of B_1 can be described as the following: Initially $d^2(B_2)/d(B_1)^2$ is ≈0 (in theory it should be exactly 0), followed by a series of peaks. The first peak corresponds to the sharp transition in B_2 shown in Fig 4.27, with the following smaller peaks corresponding to the steps towards the B_1K_1 line. The largest peak in $d^2(B_2)/d(B_1)^2$ corresponds to B_{fp} due to ithe most abrupt change in B_2 as a function of B_1.

Smoothing noisy data

The second derivative method is a highly sensitive analysis tool. The data produced by this method can also be extremely noisy, thus it is sometimes difficult to define B_{fp} from the noise. To try and limit this problem a robust linear regression procedure is performed on B_2 to remove noise from the experimental data. The regression weights are calculated for each point using Eqn. 4.7 using the MATLAB function [125].

$$w_i = \left(1 - \left|\frac{x - x_i}{d(x)}\right|^3\right)^3 \tag{4.7}$$

Where x is the predicted value associated with the the value to be smoothed, x_i are the values surrounding the point being smoothed (and the amount are chosen by the operator), and d(x) is the distance along the abscissa from x to the most distant predicted value within the span [125]. Points which have the largest w_i have the most influence on the fit. The 'rlowess' function is used in MATLAB [125], a weighted least squares regression is performed using a first degree polynomial. The smoothed value is given by the weighted regression at the predicted value.

Whilst the linear regression smoothes the raw data, there is still a possibility of outliers within the raw data that can produce a false B_{fp}. To eliminate the effect of these points, a robust local regression can be used. The residuals are calculated the same way as the non-robust smoothing mentioned previously, and the robust weights are then calculated given by the bisquare function in Eqn. 4.8:

$$\begin{aligned} &w_i = (1 - (r_i/6MAD)^2)^2),\ |r_i| < 6MAD \\ &w_i = 0,\ |r_i| \geq 6MAD \end{aligned} \tag{4.8}$$

Where r_i is the residual of the i^{th} data point produced by the smoothing procedure, w_i are the robust weights and MAD is the 'median absolute deviation', a measure of how spread out the residuals are, given by $MAD = median(|r|)$. If $r_i \geq 6MAD$, the associated data is excluded from the smoothing calculation. The data is smoothed again using the robust weights, and the final smoothed value is calculated using the local regression and robust weight. This process is repeated for a total of 5 times using the 'rlowess' function in MATLAB described in [125]. The function was chosen due to being more resistant against outlying points, thus eliminating some of the noise that can be present within the data. The second derivative method with an additional smoothing step (Eqn. 4.8) is required for the data where the largest peak (and thus B_{fp}) is difficult to separate from the noise, such that it is difficult to determine B_{fp}. Both Eqn. 4.6 and 4.8 are included in the data analysis procedure wrote in MATLAB. If the window parameter is set to 1 by the operator, the smoothing function described

above is effectively not used, in all other cases where the window > 1, smoothing is performed on the raw B_2 data, before the second derivative method is performed.

4.7.1.3 Method 3 - Standard deviation of B_1K_2

For results that are too noisy or without a clear step indicating B_{fp}, a final method was used to determine B_{fp}. The chosen method has been presented by Roy et al. [99]. This method uses the standard deviation of B_1K_2 to define a limit for B_{fp}, and can be used for every data set independent of the noise level. The B_1K_2 slope is removed, such that $B_3 = B_2 - B_1K_2$, and the standard deviation is found on B_3. The value chosen for B_{fp} is the last point within the standard deviation of B_3, with an example shown in Fig. 4.30. This method consists of limitations such as requiring an operator input to define the start and end point of B_1K_2 and the standard deviation. If the start and end points are not chosen correctly due to human error, the true B_{fp} can be missed or altered.

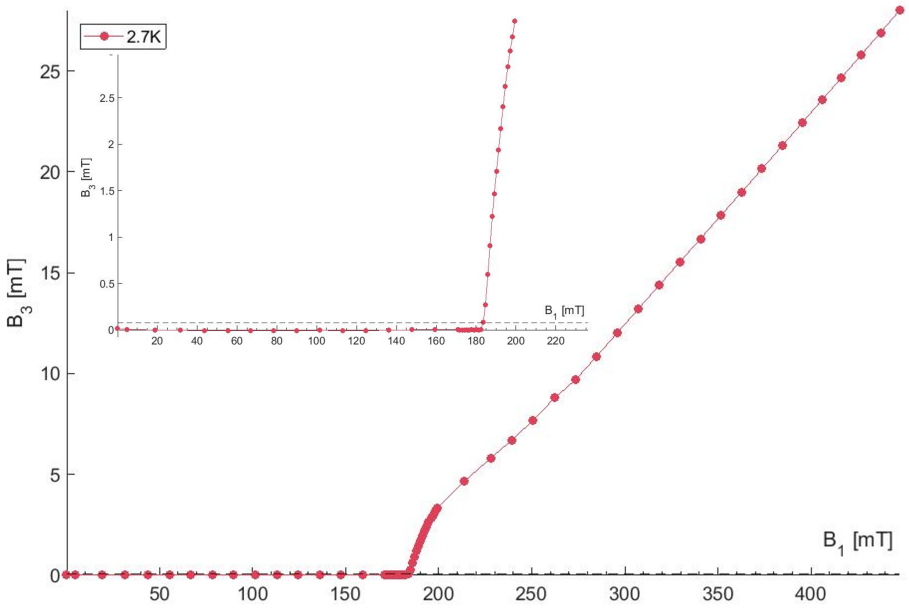

Figure 4.30: An example of the standard deviation method to extract B_{fp} for a 10 µm Nb film on Cu, with an inset to show where B_{fp} would be taken.

4.7.1.4 Error in the field of full flux penetration

Each method finds a single point, from which the error is defined. The difference between B_{fp} and the points before (B_{lower}) and after(B_{upper}), are averaged. The error in the Hall probe sensor HP1 is also then included, with the full error analysis shown

in Eqn. 4.9. The majority of these tests a Hall probe was used which had a 2.68 mT error [118], however some tests were performed with Hall probes with an error of 5.03 mT[120] which increases the error on the measurements.

$$\Delta B_{fp} = \sqrt{\left(\frac{(B_{fp} - B_{lower}) + (B_{upper} - B_{fp})}{2}\right)^2 + 2.68^2} \tag{4.9}$$

In most tests the step increase in B_1 is less than that in the error in HP1, such that the total $\Delta B_{fp} \approx$ the error in the Hall probe, either 2.68 mT or 5.03 mT. If the step size in B_1 is increased, then the error is dominated by the step size. All measured values of B_{fp}(T) are reported as the error produced by Eqn. 4.9, where as any extrapolated values are reported using the standard error of the data set. The produced standard error is the random error in the measurements. The random error (shown in Section 4.8) is further included in the errors for the measured data points.

4.8 Repeatability studies

Once the MFPF was operational, the reliability of the results had to be determined. To do so, 2 Nb samples were procured from Goodfellow Cambridge Ltd with a thickness of 50 and 100 µm to ensure that the B_{fp} would produce a sharp transition, whilst also being thick enough that multiple tests would not damage the sample. The samples were chosen to be $50 \times 50\,mm^2$ to ensure that the B leaking around the sample was minimal. Both samples had heat treatment as stated by Goodfellow Cambridge Ltd, however the maximum temperature or duration of the annealing was not clarified, and was not shared due to being proprietary [126]. To understand the quality of the samples the impurity content stated by Goodfellows was used with the method and weightings shown in Ref. [123] with calculations shown in Section 4.6.3, that determined that the 2 samples shown in this section had a RRR=22. Thus these samples are not of high purity in terms of SRF applications.

Both samples were tested in the MFPF at the same temperature set points, and after the first initial cool down, the system was left to warm for a few hours before cooling restarted. The facility/sample never left cryogenic conditions. After each cycle the facility was left to reach an equilibrium before the measurements were repeated.

The 50 µm sample was tested twice before the sample was removed, and the 100 µm sample was tested 3 times before the sample was removed.

4.8.1 Raw data

An example of the raw data for the 100 µm (Test 2) sample is shown in Fig. 4.31. Similar to the Pb sample, a sharp transition is observed for T≤5.5 K, where as

for T>5.5 K there is a more gradual transition. For set temperature points where T≤5.5 K, following the transition there is a plateau in B_2, where $B_2(B_1)$ does not increase as if B had broken through the SC. The plateau indicates that the vortices have become trapped within the Nb, such that the B does not freely pass through the SC. The trapped vortices have to be de-pinned before the B will travel through the sample. Increasing B_1 increases the force applied on the trapped flux, until the force is greater than the pinning force. Once B_1 has been increased sufficiently and the trapped flux has been de-pinned, B_2 begins increasing as expected.

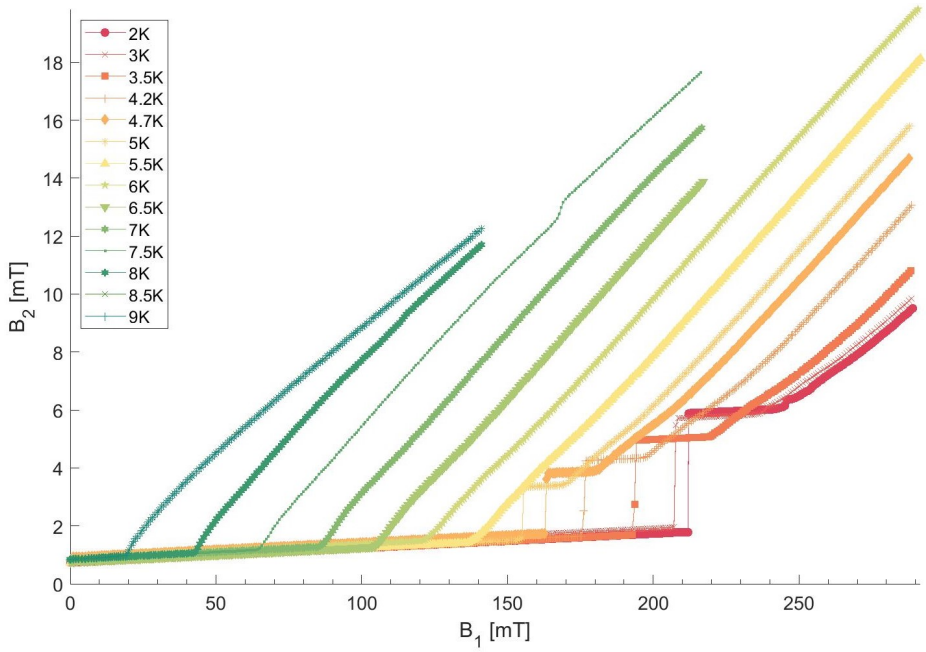

Figure 4.31: The raw data for the first test of the 100 µm Nb sample.

Both samples were analysed using the three methods presented in Section 4.7, with the results shown in Table 4.6 and Figs. 4.32 and 4.33. Table 4.6 shows the extrapolated $B_{fp}(0\,K)$ that is found using the whole data set with the standard error, whilst also comparing the measured data for $B_{fp}(4.2\,K)$ that still contains a transition over a single large jump, and the data at $B_{fp}(6\,K)$ that produces a transition over multiple smaller points.

4.8.2 Discussion

Both the 50 and the 100 µm sample were tested multiple times and analysed using the 3 different methods presented in Section 4.7. A comparison of the 3 different methods are shown in Fig. 4.34 for the 100 µm Nb sample. This shows that there

Table 4.6: A table showing the differences in B_{fp} for each method for extrapolated values at 0 K, and the measured values at 4.2 and 6 K. Errors for $B_{fp}(0\,K)$ are the standard error of the data, where as all other values have been determined in the step size and error in the Hall probe, shown in Section 4.7.1.4.

	B_{fp}(0 K) [mT]		
50 Microns	Normalisation method	2nd derivative	standard deviation
Test 1	408.72±5.39	411.75±6.11	408.97±5.68
Test 2	409.21±5.06	412.64±5.10	410.22±5.19
100 Microns			
Test 1	230.80±1.55	230.25±1.48	230.95±1.68
Test 2	230.46±1.82	229.81±1.90	229.66±1.94
Test 3	232.08±1.58	231.41±1.49	231.29±1.54
	B_{fp}(4.2 K) [mT]		
50 Microns	Normalisation method	2nd derivative	standard deviation
Test 1	331.98±5.03	331.94±5.06	331.94±5.06
Test 2	329.90±5.03	329.31±5.08	329.91±5.03
100 Microns			
Test 1	175.76±5.05	175.47±5.08	175.47±5.08
Test 2	176.19±5.04	176.08±5.09	176.08±5.09
Test 3	176.00±5.04	175.88±5.07	175.88±5.07
	B_{fp}(6 K) [mT]		
50 Microns	Normalisation method	2nd derivative	standard deviation
Test 1	180.52±5.04	180.36±5.09	180.36±5.09
Test 2	178.82±5.04	178.70±5.09	178.70±5.09
100 Microns			
Test 1	105.86±5.18	104.87±5.08	104.29±5.08
Test 2	105.48±5.12	105.39±5.08	103.93±5.09
Test 3	104.74±5.13	103.36±5.09	103.36±5.09

is no difference between the B_{fp} across the 3 different methods for each T. The main difference between the methods (and therefore the results) is that the second derivative does not require a any mathematical expression to be found over a window of points, and therefore allows B_{fp} values to be extracted where the K_2 line is small, such as for $T \rightarrow T_c$. The second derivative method also requires no operator input to determine the end of a window that can skew the data for less abrupt B_{fp} transitions, and is the fastest method to analyse the data, thus it was decided to be used as the main analysis method where possible. This does not discredit the other methods, as these can be used for samples that behave differently (i.e.- the absence of a sharp transition).

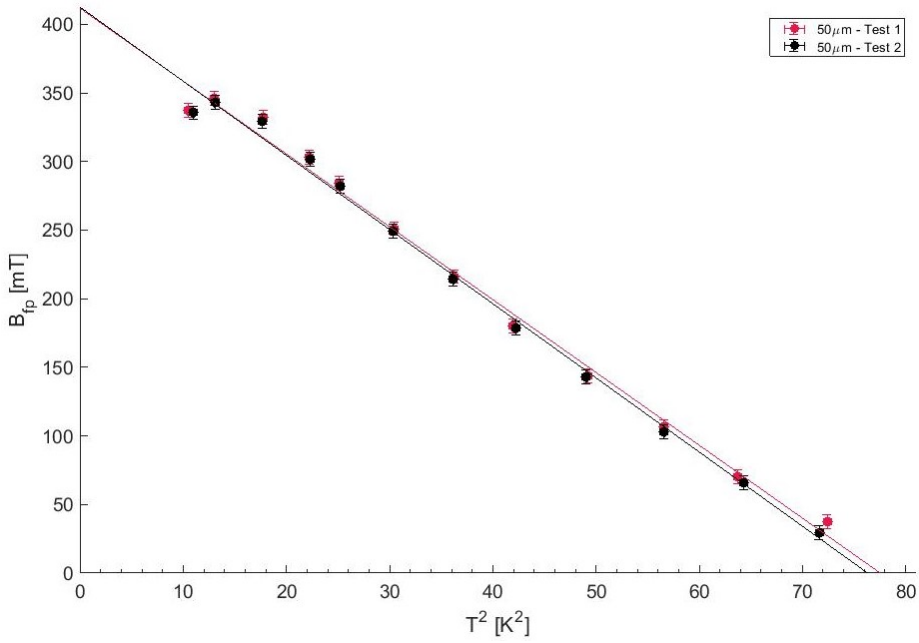

Figure 4.32: A comparison of B_{fp} as a function of T^2 found using the second derivative method for the 50 µm thick Nb sample.

It can be seen from Figs. 4.32 and 4.33 that tests for both the 50 µm and the 100 µm agree with each other respectively. This shows for samples tested in the same area, for multiple thermal cycles, over a range of temperatures that the results are consistent, and the MFPF produced a repeatable result. Additionally, at least for the thicker samples, it shows that repeated thermal cycles under the same conditions does not affect the results by damaging the samples.

One unexpected result is that the 50 µm sample has a larger B_{fp} than the 100 µm sample, which can be seen by comparing the data in Figs. 4.32 and 4.33, and in Table 4.6. Section 4.6 shows that these 2 samples have an extremely low RRR value (RRR≈22), which is one explanation as to why the 100 µm thick foil has a reduced B_{fp} in comparison to the 50 µm foil. Another possibility is that both foils were heat treated in different ways. During a private communication with the company [126], they stated that all heat treatments are performed in a vacuum furnace, however "*Typically, Niobium foil is annealed at* 850 *and* 1300 °C*, with the exact temperature and time depending on material form and thickness. I am afraid detailed info would be proprietary*". From the results, it is possible that both samples did not receive the same treatment, and would explain the difference in B_{fp}.

Figure 4.31 indicates that for the second test of the 100 µm sample, vortices were pinned within the sample after B_{fp}, indicated by the plateau immediately after B_{fp}.

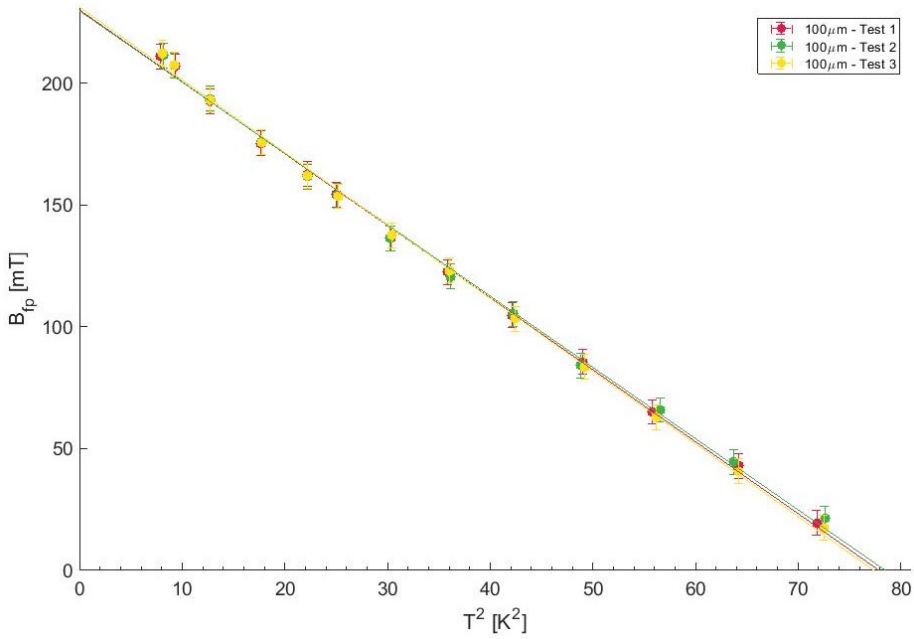

Figure 4.33: A comparison of B_{fp} as a function of T^2 found using the second derivative method for the 100 µm thick Nb sample.

This is also the present for the 50 µm sample. One explanation is that the higher B_{fp} in the 50 µm sample is due to flux being pinned within the sample, either the surface or the bulk, and thus a greater force is required to de-pin the vortices, thus delaying B_{fp}. It could be determined that the increase is only due to the pinning within the sample. Additionally, melting Nb and letting it re-crystallize increases the RRR of the Nb [123]. As the heat treatment for these samples is unknown, there is a possibility that these samples had different heat treatments that affect the behaviour.

The repeated measurements allowed the random error of the facility to be determined. All measurements were combined to calculate the random error of the system without moving a sample. The data was extrapolated to 0 K for B_{fp} and the standard error, which allowed the error to be calculated as a percentage. This is shown for each method in Table 4.7. Each method used produced a similar B_{fp} for each sample, with a similar standard error, and thus a similar % error. This indicates that the chosen method does not create a large difference in interpreting the results for these samples.

The largest error produced was for the 50 µm sample using either the normalisation method or the second derivative method, with a random error 0.94 %. The 100 µm sample had a smaller error, with a maximum of 0.42 % for the standard deviation method. Table 4.7 shows that the 50 µm sample had a larger error than that of the

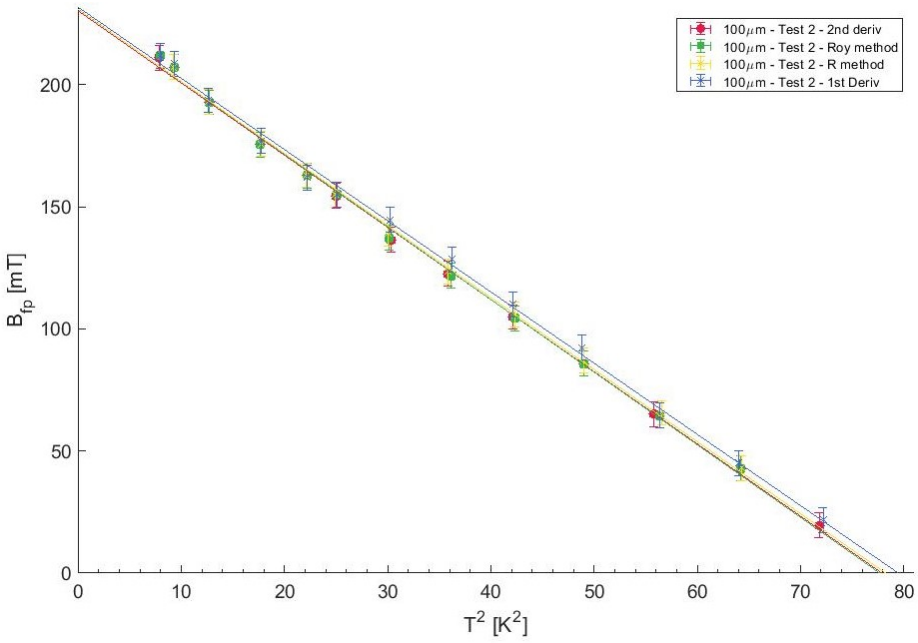

Figure 4.34: A comparison of $B_{fp}(T)$ for the three different methods to extract B_{fp} for the second test of the 100 µm sample.

Table 4.7: A table showing $B_{fp}(0\,K)$, the equivalent standard error and the error as a percentage for all three methods for only repeated measurements.

50 Microns	**B_{fp}(0 K)** [mT]	**Standard error**(0 K) [mT]	% **error**
Normalisation method	408.96	3.59	0.94
2nd deriv	412.19	3.87	0.94
Standard deviation	409.58	3.59	0.88
100 Microns			
Normalisation method	231.11	0.92	0.40
2nd deriv	230.49	0.91	0.39
Standard deviation	230.61	0.96	0.42

100 µm sample, a maximum of 0.94 % to 0.42 % respectively. Thus, the maximum error for repeated thermal cycles is 0.9 % of the measured value.

4.8.3 Alignment studies

Further measurements were performed on the 50 and the 100 µm sample, in which the samples were removed and re-inserted to the MFPF. By removing and re-inserting the samples, a different area of the foil was present in the localised magnetic field.

It is expected that a sample with perfect homogeneity would show no change in the results. In the real world it is unlikely that the samples are perfectly homogeneous, and that moving the samples would alter the results.

The $B_{fp}(0\,K)$ were found to be 453.0±8.2 mT and 226.0±3.3 mT for the 50 and 100 µm samples respectively. The 50 µm sample showed an increase of ≈42 mT compared to the previous tests, where as the 100 µm sample saw a reduction by ≈4 mT. Thus, the 50 µm foil produced a deviation of ≈10 % due to moving the sample, where as the 100 µm foil had ≈2 % deviation compared to the previous measurements. This indicates that the alignment and area of the sample that is tested can effect the results. One possibility for the change in B_{fp} is the homogeneity of the sample. For a 'high quality', homogeneous sample it would be expected that there should be little to no variation for different areas of the surface. The three methods to extract B_{fp} were compared for all measurements of the 50 and 100 µm samples, including the tests performed once the samples had been moved and replaced. The results for all tests combined are shown in Table 4.8.

Table 4.8: A table showing $B_{fp}(0\,K)$, the equivalent standard error and the error as a percentage for all three methods for all measurements of the 50 and 100 µm samples after the samples had been removed and re-inserted into the MFPE.

50 Microns	**$B_{fp}(0\,K)$** [mT]	**Standard error$(0\,K)$** [mT]	% **error**
Normalisation method	421.82	4.84	1.15
2nd deriv	425.41	5.03	1.18
Standard deviation	421.98	4.89	1.16
100 Microns			
Normalisation method	229.27	1.58	0.69
2nd deriv	229.35	1.48	0.65
Standard deviation	229.27	1.60	0.70

Similar to the initial results, all methods produced a similar $B_{fp}(0\,K)$, with a similar % error for each method. The 50 µm sample produced a larger % error compared to the 100 µm sample, similar to the repeatability measurements in the previous section. The largest % error was 1.18 % for the 50 µm sample analysed using the second derivative method. The average $B_{fp}(0\,K)$ increased for the 50 µm once the sample had been moved was included. The led to an increase between 3-3.2 %. Similarly, including the results after the 100 µm foil had moved with the repeatability measurements produced a reduction in the average $B_{fp}(0\,K)$ between 0.5-0.8 %.

4.8.4 Discussion

Two samples were used to determine the repeatability of measurements produced by the MFPF. The maximum error produced by repeated thermal cycles was found to be 0.9 % of the measured value. The random error is included in the error bar for all measured values, however it is not included in extrapolated $B_{fp}(0\,K)$ to allow the scattering in the results to be observed.

Removing and replacing the sample into the facility produced a maximum deviation from the previous measurements by ≈10 % for the 50 µm foil, where as the 100 µm foil deviated by 2 %. Including these measurements with those from the reliability study in the previous section altered the average $B_{fp}(0\,K)$ by a maximum of 3.2 % for the 50 µm sample, where as the 100 µm sample produced a change in the average $B_{fp}(0\,K)$ of 0.8 %.

Including these results where the sample was moved with the reliability measurements increased the maximum error from 0.9 % to 1.2 % (both for the 50 µm sample). This is due to only 1 measurement being performed after the sample was moved. One possibility for the change in B_{fp} is the in-homogeneity of the samples as a different area was tested. Future work should include testing over multiple areas of a sample to determine how B_{fp} changes for different areas. It is expected for a high quality sample that B_{fp} would change very little with each tested area.

The results for both the 50 and the 100 µm sample produced B_{fp} values larger than the theoretical B_{c1} for Nb. This is likely due to the large number of pinning sites within the Nb foil, increasing the amount of trapped flux within the film due to the low RRR of the material. These results further increase the need to investigate how the number of pinning sites affect B_{fp}. This is also relevant to sputtered films for SRF technology. One method to investigate this is to cold work bulk Nb to varying degrees to produce a varying number of pinning sites, or test multiple samples with varying RRR values.

4.9 The effect due to geometry

4.9.1 Type I - Pb

The initial results that the MFPF produced determined that some B had leaked around the sample, shown in Fig. 4.27 due to HP2 measuring a non-zero B_2. The Pb sample (the same from Section 4.7) was thin, and easy to cut. The sample was also soft such that great care had to be taken when the sample was cut to ensure it did not rip or become damaged whilst the sample size was reduced. This was also a concern when placing the thermometer on the sample. The thermometer was placed on the edge of the sample for large sample sizes where it was un-avoidable, and placed on the

brass plate for small sample sizes, to ensure the Pb was not damaged. It was expected than removing material from the sample would increase the amount of B that would leak around the sample, thus producing an increased K_2. After each test some Pb was removed or the sample was rotated, shown in Fig. 4.35, which corresponds to Table 4.9. Thus, the same sample was repeatedly tested.

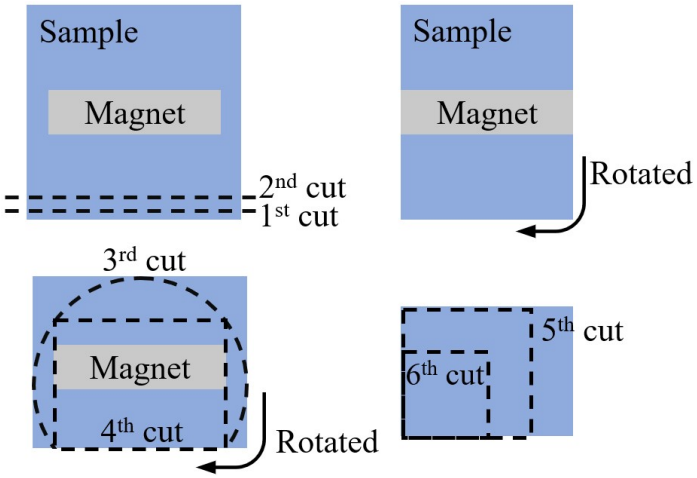

Figure 4.35: The order and orientation the Pb sample was cut for each test. The magnet has been removed from the 5th and 6th cut for clarity. The centre of the samples were placed in the centre of the gap to ensure a uniform B over the sample.

Table 4.9: The Pb sample sizes and geometry, and the order they were performed in, with the dimensions correlated to Fig. 4.1b

Run	**Length (x axis) [mm]**	**Width (z axis) [mm]**
Original	50	50
1st cut	50	45
2nd cut	50	40
Rotation	40	50
3rd cut	50 mm Disk	
4th cut	40	30
5th cut	30	30
6th cut	20	20

4.9.1.1 Magnetic field leakage, K_2

The Pb foil was tested at a range of temperatures for each sample size. Typical data for each sample size measured at 3.5 K is shown in Fig. 4.36. It should be noted that B_2 has been normalised due to a change in offset voltage within the error of HP2.

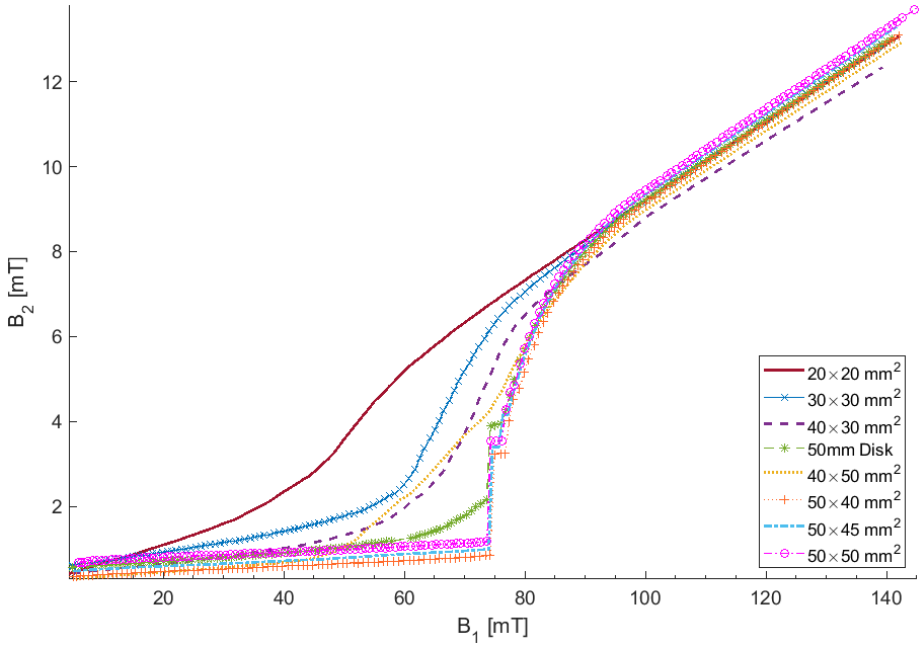

Figure 4.36: The raw data produced by the 10 µm thick Pb sample size at 3.5 K. The sample size is denoted as length×width. The length corresponds to B_x (perpendicular to the dipole faces) and the width corresponds to B_z (parallel to the dipole faces).

Figure 4.36 clearly shows that as the sample size is decreased, B_1K_2 is increased. For samples with a length of 50 mm it can be seen that B_1K_2 increases linearly and produces a very similar value, indicating that the variation of the sample width had little to no affect when the width $\geq$40 mm. When the Pb foil was cut into a disk, B_1K_2 was similar at low B_1, but begins to increase quadratically as $B_1 \rightarrow B_{fp}$. However, the B_{fp} is still a clear sharp transition with a step transition. For samples with an area $\leq 40 \times 30\,mm^2$, B_1K_2 is much larger and begins to obscure B_{fp}.

The K_2 value is $\approx$ 0.5 of the normal conducting gradient, K_1 ($K_1 \approx 0.0945$), for the $20\times20\,mm^2$ sample, thus making B_{fp} difficult to extract from the raw data. A comparison of K_2 has been made between experimental and simulation values, shown in Fig. 4.7. The simulations were performed using low μ values, such that the K_2 values will be slightly greater than the experimental measurements. This is because B is present within the sample in the simulation, whilst B is 0 inside a thick

Table 4.10: The data from the field of full flux penetration for the Pb samples size (denoted by length×width), geometry, $B_{fp}(0\,K)$ and T_c. Both $B_{fp}(0\,K)$ and T_c are extracted using the linear B_{fp} as a function of T^2.

Area [mm^2]	**K_2[10^{-3}]**	**$B_{fp}(0\,K)$ [mT]**	**T_c[K]**	**$B_{fp}(0\,K)$ [mT]**	**T_c [K]**
		Normalisation		**$d^2(B_2)/d(B_1)^2$**	
50 × 50	7.6 ± 0.9	96.0 ± 0.2	7.10 ± 0.01	96.7 ± 0.2	7.16 ± 0.01
50 × 45	8.3 ± 1.4	94.9 ± 0.6	7.15 ± 0.02	96.0 ± 0.6	7.19 ± 0.02
50 × 40	7.5 ± 0.8	95.7 ± 0.3	7.21 ± 0.01	96.6 ± 0.5	7.23 ± 0.02
40 × 50	11.0 ± 1.0	98.9 ± 1.0	7.14 ± 0.04	101.8 ± 1.38	7.12 ± 0.05
50 mm Disk	11.0 ± 2.0	95.4 ± 0.3	7.15 ± 0.01	96.3 ± 0.2	7.17 ± 0.01
40 × 30	17.5 ± 1.3	89.3 ± 0.9	7.12 ± 0.03	89.9 ± 0.8	7.16 ± 0.04
30 × 30	24.1 ± 1.2	76.9 ± 0.7	7.08 ± 0.03	84.4 ± 1.8	7.08 ± 0.08
20 × 20	47.3 ± 4.0	60.8 ± 0.6	6.98 ± 0.03	57.5 ± 1.5	7.28 ± 0.10

superconductor. Both experimental and simulated results show a similar trend for various sample sizes. To ensure reliable measurements and a distinct B_{fp}, the sample size should be kept as large as possible.

4.9.1.2 The effect of geometry on B_{fp}

As shown in the previous section, reducing the sample surface area increased K_2. Logically, as more B travels around the sample, it could be possible that flux enhancements are created at the edge of the sample, thus reducing B_{fp}. Investigating the effect of sample size allowed a comparison between the analysis methods to accurately determine B_{fp}. A Type I superconductor was necessary such that B_{fp} would be a sharp transition, and to ensure no mixed state was produced which could create ambiguity in the measurements.

Each sample that had a total length of 50 mm had a sudden, sharp transition with a rapid increase in B_2, which indicated that B had abruptly penetrated through the sample. A reduction in sample size caused B_{fp} to start becoming obscured, shown in Fig. 4.36. Both Method 1 and 3 rely on B_1K_2 being linear. This was not always the case, such as for the 50 mm diameter disk test. Thus, it was decided that the second derivative method (Section 4.7, method 2) was the best analysis tool to extract B_{fp}.

It was determined that B_{fp} produced a linear trend with T^2, such that:

$$B_{fp}(T) = B_{fp}(0\,K)(1 - (T/T_c)^2) \tag{4.10}$$

Thus B_{fp} produced a similar relationship to B_{eq} as a function of T^2, also shown in Chapter 3. Assuming a linear trend, the line of best fit was extrapolated to 0 K

to determine $B_{fp}(0\,K)$, and also to B_{fp}=0 mT to determine $T_c(0\,mT)$. A comparison between Method 1 and 2 are shown in Table 4.10 for $B_{fp}(0\,K)$. The linear trend of $B_{fp}(T^2)$ for the 50×50 mm^2 sample produced a R^2=0.999 879, indicating a good linear correlation between B_{fp} and T^2. Additionally, the p-value for the 50×50 mm^2 sample was 5.7×10^{-15} indicating B_{fp} had a statistically significant trend with T^2. There is no comparison for Method 3 as it had not been utilised at this time, however the results would be very similar to method 1.

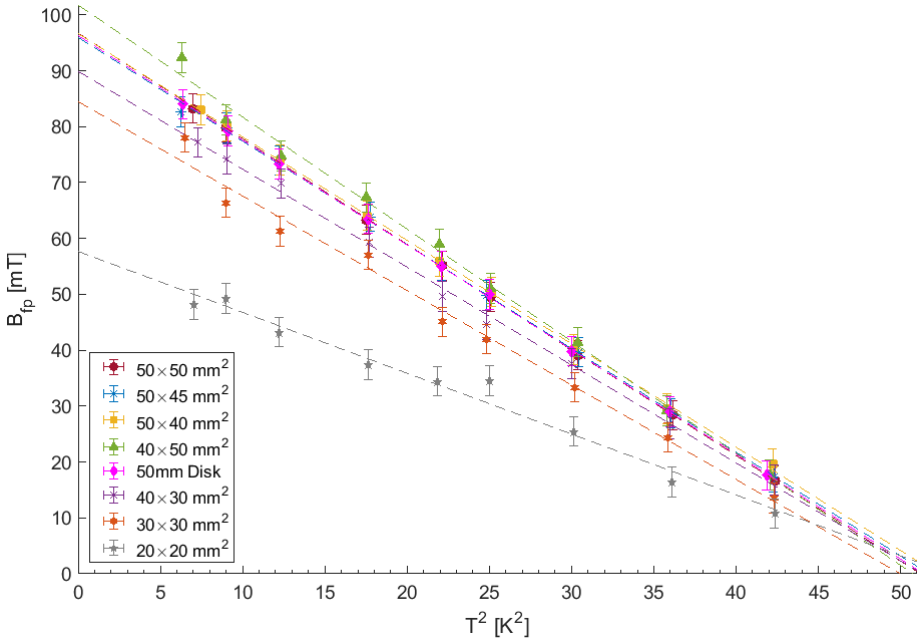

Figure 4.37: The B_{fp} found using the second derivative method as a function of T^2 for varying sample sizes of Pb, assuming a linear fitting. Sample size is denoted as length×width

.

The obtained B_{fp} for the Pb sample for varying sizes are shown in Figure 4.37 as a function of T^2. One can see that the results are comparable for samples with a length >40 mm. The width is slightly less critical than the length, provided the width >30 mm. However, there were no samples with a small width and a large length. The data shown for $B_{fp}(T^2)$ in Fig. 4.37 has been fitted using a linear trend. The results for $B_{fp}(0\,K)$ and $T_c(0\,mT)$ for each sample size have been determined for the multiple sizes of the Pb sample and are shown in Table 4.10 and Fig.4.38.

Figure 4.38 shows that $B_{fp}(0\,K)$ can vary for different sample sizes (using the second derivative method to determine B_{fp}) by comparing varying sample sizes. Table 4.10 shows $B_{fp}(0\,K)$ and T_c found by assuming a linear T^2 dependence and

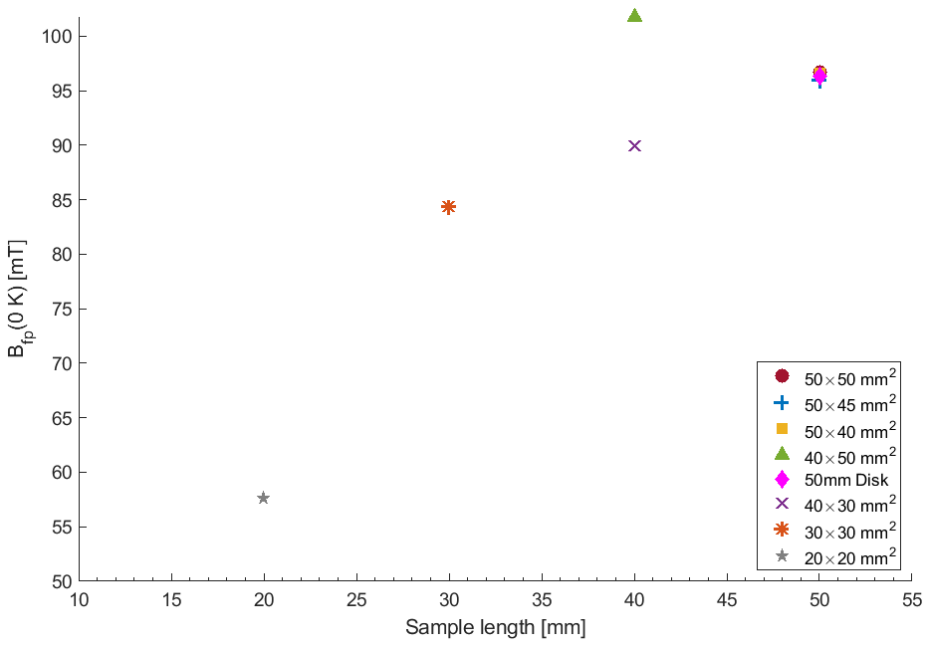

Figure 4.38: B_{fp} as a function of Pb sample length.

extrapolating to 0 K and 0 mT respectively. Reducing the surface area of the sample led to reduced R^2 values in $B_{fp}(T^2)$, indicating an increased error in determining B_{fp}. This is shown in Table 4.10 with the smaller samples producing an increased error.

The $B_{fp}(0\,K)$ is larger than the expected $B_c(0\,K)$ for Pb (95 mT compared to 80 mT [33]) which lead to the effect of thickness to be investigated, to determine the effect of sample thickness on B_{fp}. It is expected that B decreases over distance, such that B on the sample surface is ≈15 % lower than measured in the dipole gap, thus $B_{fp}(0\,K)$≈82 mT, which is similar to that of the $B_c(0\,K)$ for Pb (80 mT) found by Chanin [33]. Furthermore, $B_{fp}(4.2\,K)$=63.5-64.1 mT, which is 10 mT higher than the $B_c(4.2\,K)$=54.5 mT of Pb [33]. Applying the expected field reduction due to the increased distance between the sample surface and the magnet centre produces $B_{fp}(4.2\,K)$=54.0-54.5 mT, and agrees with that of theoretical values for Pb.

For samples with a length of 50 mm, B_{fp} is similar for different widths, shown in Fig. 4.39. The reduction in the sample length produced inconsistency in B_{fp}. For example, the reduction in sample length from 50×50 mm^2 to 40×30 mm^2 caused B_{fp} to reduce from 96.7 mT to 89.9 mT, found using the second derivative method. Further decreasing the length continued to reduce B_{fp}, shown in Figs. 4.38 and 4.39, and Table 4.10. Additionally, Table 4.10 shows that the normalisation method produces a greater deviation in both B_{fp} and T_c compared to the second derivative method.

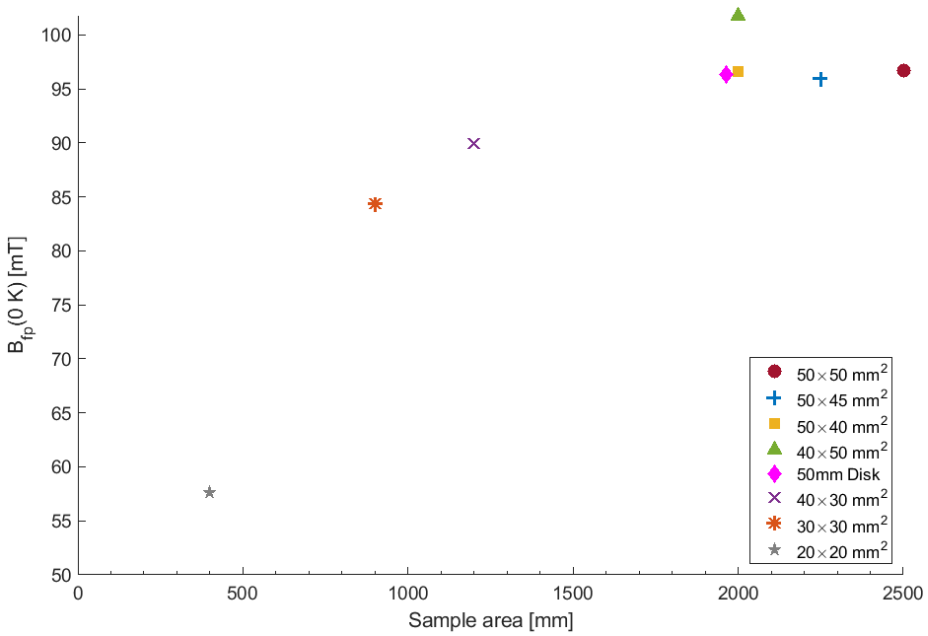

Figure 4.39: B_{fp} as a function of the area of the Pb sample. The sample sizes denoted as length×width.

4.9.2 Type II - Nb

Due to variation in B_{fp} for a Type I SC, it was beneficial to also test a type II SC using the same method. This was to determine if the B_{fp} could still be accurately determined using $d^2(B_2)/d(B_1)^2$ for Type II superconductors, or if flux enhancements at the edges would allow early penetration of vortices, thus obscuring B_{fp}.

The chosen sample was a thick Nb film, which was deposited at Daresbury Laboratory as part of the ARIES collaboration's investigation on the effect of polishing Cu substrates on the superconducting properties of Nb films. The deposition parameters are shown later in Section 5.1.3. The sample size at the time of deposition was 53×53 mm^2 and was 10 µm thick on a 1 mm thick Cu disk, from which smaller samples were taken to be tested in a VSM and for SEM imaging, leaving the remaining sample size to be 53×35 mm^2. The sample was placed 'parallel' to the magnet, as shown in Fig. 4.40a.

As the sample was a thick metal, it had to be cut using wire erosion by the workshop and could not be done by hand without risking damage to the film. The sample was cut to produce two smaller samples; 30×30 mm^2 and a 20×20 mm^2. Both of these samples were placed either parallel or on a 45° offset (labelled perpendicular for ease) with respect to the magnet, shown in Figs. 4.40b and 4.40c. Only the

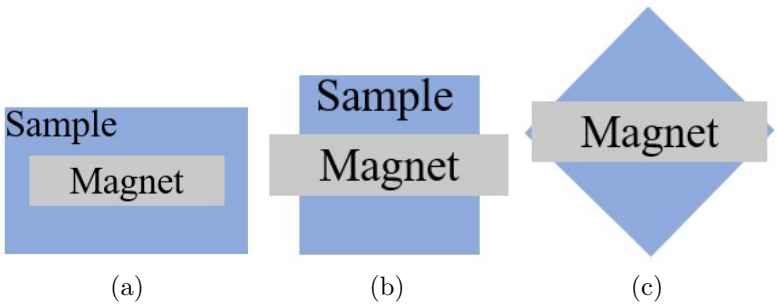

Figure 4.40: The position of the ARIES samples in relation to the magnet: (a) full size ARIES sample of $53\times35\,\mathrm{mm}^2$, (b) reduced sample size of $30\times30\,\mathrm{mm}^2$ 'parallel' to the magnet, and (c) reduced sample size of $30\times30\,\mathrm{mm}^2$ with an offset to the magnet, and thus labelled as 'perpendicular' to the magnet.

smaller samples were tested using the technique described in section 4.5.3, as the $53\times35\,\mathrm{mm}^2$ sample was measured before the system had been automated, and was therefore done manually by changing the temperature set points on the controller. This led to less points being taken to speed up the testing process. In addition to this, the $53\times35\,\mathrm{mm}^2$ sample was also tested using a silicon diode thermometer, which has an error of 0.25 K, and a Cernox thermometer was installed in the system whilst the sample size was reduced, hence the error in T was reduced to 5 mK.

4.9.2.1 Magnetic field leakage, K_2

Figure 4.41 shows the raw data for the 3 sample sizes in different orientations, which also show some interesting artefacts. There is a sudden decrease in B_1 (and thus B_2), which are present for the $30\times30\,\mathrm{mm}^2$ and the $20\times20\,\mathrm{mm}^2$ samples in the parallel orientation. The most reasonable explanation for this is the superconducting power supply read a small resistance and thus reduced the current applied to the magnet to avoid causing damage to superconductors. The cause for this is unknown as the magnet $T<T_c$ and no resistance should exist due to being in the superconducting state. In addition, if the magnet was quenching, then the features should occur at a similar B_1 for each temperature.

Similar to the Pb sample, there is a greater K_2 for the smaller samples, thus indicating more B had leaked around the sample. The results for K_2 are shown in Table 4.11, and are comparable to that of similar sizes for the Pb sample. The main source of error which produced small fluctuations in the values of K_2 would be due to the position of the sample. The aim was to place the centre of the samples in the centre of the poles, however there was no method to determine 'centre' other than by eye. Thus the sample may not have been placed exactly in the centre of the pole gap.

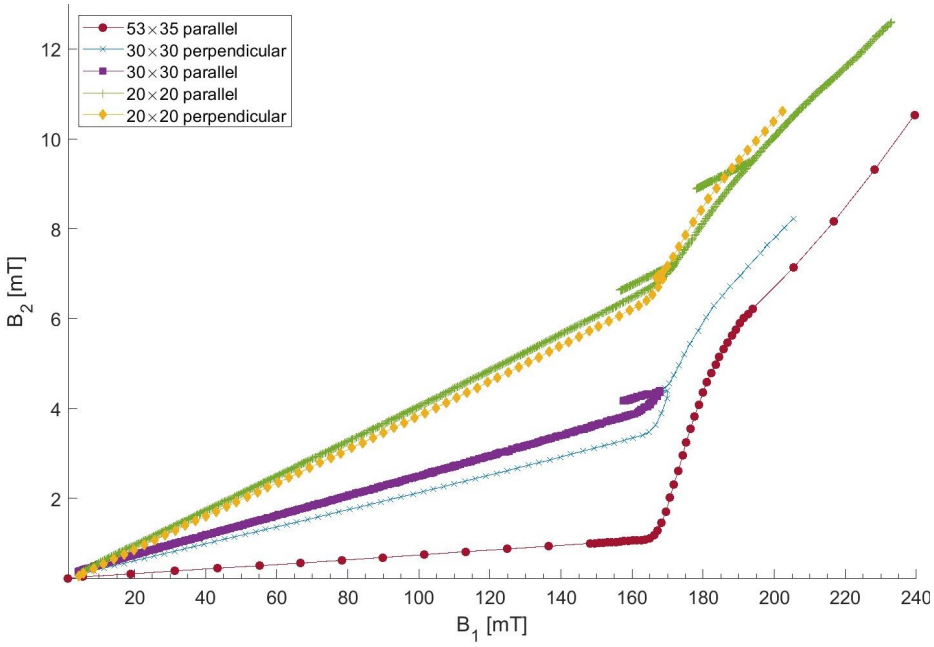

Figure 4.41: A comparison of $B_2(B_1)$ for different sample size and orientation of a Type II superconductor at 4.2 K.

Table 4.11: The $B_{fp}(0\,K)$ and T_c for a 10 µm thick Nb sample deposited at Daresbury Laboratory, found by using a linear relationship in B_{fp} as a function of T^2 extracted using the second derivative method. The sample size is written as length×width.

Size [mm^2]	**Orientation**	$\mathbf{K_2}$ [$\mathbf{10^{-3}}$]	$\mathbf{B_{fp}}(0\,K)$ [mT]	$\mathbf{T_c}$ [K]
20×20	Parallel	40.2 ± 1.9	205.5 ± 6.4	9.69 ± 0.17
20×20	Perpendicular	38.8 ± 1.5	208.58 ± 2.8	9.83 ± 0.08
30×30	Parallel	22.7 ± 0.9	188.0 ± 3.2	10.11 ± 0.12
30×30	Perpendicular	20.2 ± 1.7	209.4 ± 2.5	9.60 ± 0.06
53×35	Parallel	5.3 ± 0.09	205.0 ± 1.7	9.29 ± 0.07

Comparing the same sample size in both perpendicular and parallel orientation indicated that more B leaks around the sample whilst in the parallel orientation. This further solidified that the length of the sample is key in reducing B_1K_2. Finally, the increased length of the 53×35 mm^2 produced a slightly smaller K_2 than for the 50×50 mm^2 Pb sample.

Table 4.12: The $B_{fp}(0\,K)$ and T_c for a 10 µm thick Nb sample deposited at Daresbury Laboratory, found by using a linear relationship in B_{fp} as a function of T^2 extracted using method 3. The sample size is written as length×width.

Size [mm^2]	**Orientation**	**B_{fp}**(0 K) [mT]	**T_c** [K]
20×20	Parallel	204.1 ± 2.2	9.81 ± 0.48
20×20	Perpendicular	200.5 ± 2.4	9.78 ± 0.54
30×30	Parallel	199.4 ± 0.6	9.86 ± 0.12
30×30	Perpendicular	203.0 ± 3.3	9.34 ± 0.70
53×35	Parallel	201.9 ± 2.1	9.27 ± 0.61

4.9.2.2 The effect of geometry on B_{fp}

Using both the $d^2(B_2)/d(B_1)^2$ method and method 3, B_{fp} was extracted and compared for each sample size and orientation, shown in Tables 4.11 and 4.12 for each method respectively. The $B_{fp}(T^2)$ is shown for each method in Fig. 4.42.

Using the $d^2(B_2)/d(B_1)^2$ method to analyse the data produced some deviation at each set T, shown in Fig. 4.42a, where as using method 3 produced 2 similar trends shown in Fig. 4.42b. These deviations were not shown in the Pb sample. However, unlike the Pb sample, the Nb sample was tested at different locations across the sample surface, where as the Pb sample was repeatedly tested at a similar location on the sample surface. Furthermore, the Nb sample was deposited and may not be a uniform film, which could also alter the results. Lead is a Type I and not a Type II superconductor which can also explain the difference in the results. Compared to the original 53×35 mm^2 sample, the reduction in sample size produced a deviation in $B_{fp}(0\,K)$ from 91.7-102.1 % for the second derivative method and 98.8-101.1 % for method 3. Both analysis techniques showed that the lowest value of $B_{fp}(0\,K)$ produced was by the 30×30 mm^2 sample.

It was also possible to extract B_{fp} for the 20×20 mm^2, whilst still producing a similar B_{fp} to the films with a larger surface area, which could not be performed for the Pb sample. One theory for this is that B_{fp} is much greater for the Nb sample. Thus, when B has penetrated though the sample the $d^2(B_2)/d(B_1)^2$ is larger than for Pb. I.e.- The B_2/B_1 is larger for the Nb, and B_{fp} is more likely to stand out from the background noise and leakage magnetic field. However, it could also be due to the Pb sample becoming damaged over time due to being a thin foil and repeatedly handled introducing damage to the foil, where as the Nb film was attached to a substrate that allowed the film to remain rigid, and not become damaged.

Although the $d^2(B_2)/d(B_1)^2$ method can be easily used for samples with a sharp transition, these results indicate that if the data does not produce a step transition (i.e a single point increase in B_2), B_{fp} can be misreported. This is clearly indicated

by the increased range in $B_{fp}(0\,K)$ shown in Table 4.11. Using method 3 reduced this deviation compared to the original uncut sample, and produced similar values for $B_{fp}(0\,K)$ that are within error for each sample.

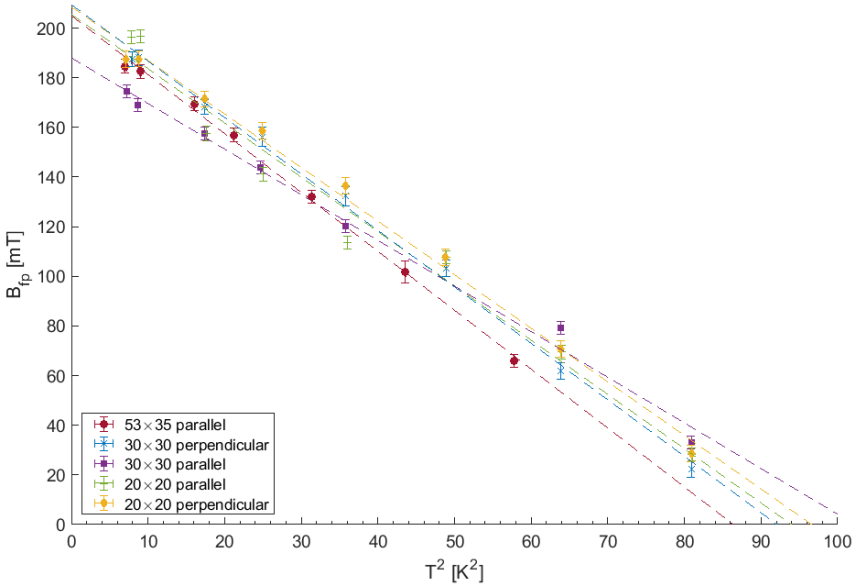

(a)

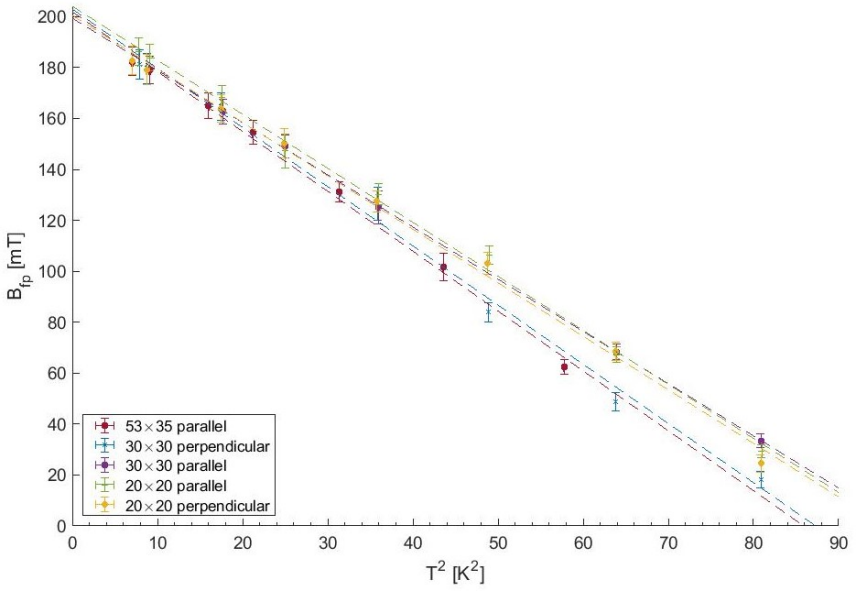

(b)

Figure 4.42: B_{fp} found using second derivative (4.42a) and method 3 (4.42b) as a function of T^2 for a Nb sample of various sizes deposited at Daresbury Laboratory.

4.10 Dealing with flux jumps

In the next section (Section 4.11), an investigation on the effect of thickness is presented for multiple Nb samples. The samples are Nb foils, procured from Goodfellow Cambridge Ltd, with thickness' of 1, 3, 5 and 10 µm. It was found in testing that some samples experienced flux jumps at certain T's. Flux jumps are defined as a small increase in B_2, occurring at a B_1 lower than the defined B_{fp}. The jump in B_2 is smaller than that of the B_{fp} jump, it is not considered to be B_{fp}. The samples that produced clear flux jumps were the 5 µm sample tested by itself and with spacers, and the 10 µm sample tested by itself. An example data set with flux jumps is shown in Fig. 4.43.

Flux jumps indicate that the T run is not viable. The flux jumps prior to B_{fp} imply that flux was trapped within the foil during the cool down, and the foil was not in the Meissner state, but the mixed state. Increasing B_1 increases the force applied to the trapped flux. Eventually, the force becomes large enough to de-pin the vortice and push it through the foil. This is the indicated flux jump. This means the flux has already entered the foil and we are not witnessing the B entering and then breaking through the sample, but only breaking through the sample as the B is already in the volume. Additionally, the force acting on the flux lines on the foil surface is reduced, and such that B_{fp} is not reliable. A comparison has been made comparing $B_{fp}(T^2)$ for with and without the flux jumps, shown in Fig. 4.44.

A summary of the effect of the flux jumps is shown in Table 4.13. For the 10 µm sample, the removal of the T runs with flux jumps increases the $B_{fp}(0\,K)$. However, this is not always the case. The 5 µm samples had both an increase and decrease in B_{fp} due to the removal of the flux jumps for the 2 brass plates and single brass plate respectively. For all future results, the data that includes flux jumps prior to B_{fp} has been removed.

Table 4.13: The $B_{fp}(0\,K)$ for the 5 and 10 µm samples with and without the measurements with flux jumps.

	$\mathbf{B_{fp}}(0\,K)$ [mT]	
Sample	**All points**	**Flux jumps removed**
5 µm 2 Brass plates	263.35 ± 9.26	300.12 ± 8.66
5 µm Single Brass plate	228.57 ± 6.95	219.47 ± 3.38
10 µm Single Brass plate	369.79 ± 9.87	385.29 ± 6.53

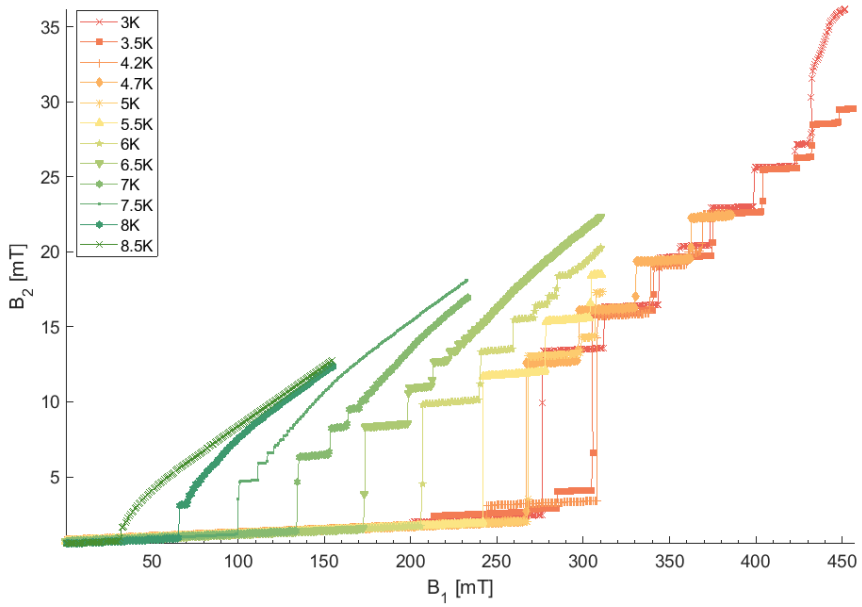

(a)

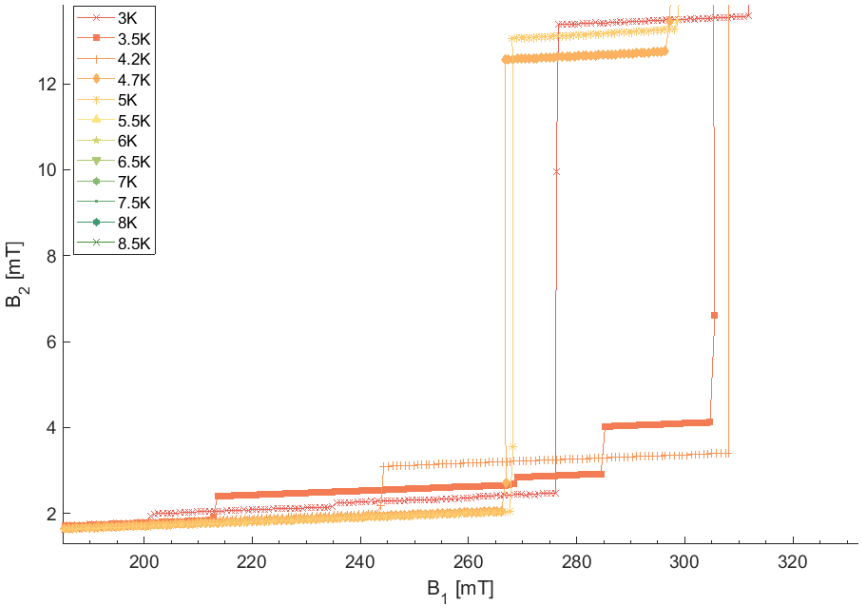

(b)

Figure 4.43: The raw data for the 10 µm thick Nb foil with only a brass strip under the sample. The entire data set is shown in 4.43a and the T's where pinning occurs is shown in 4.43b.

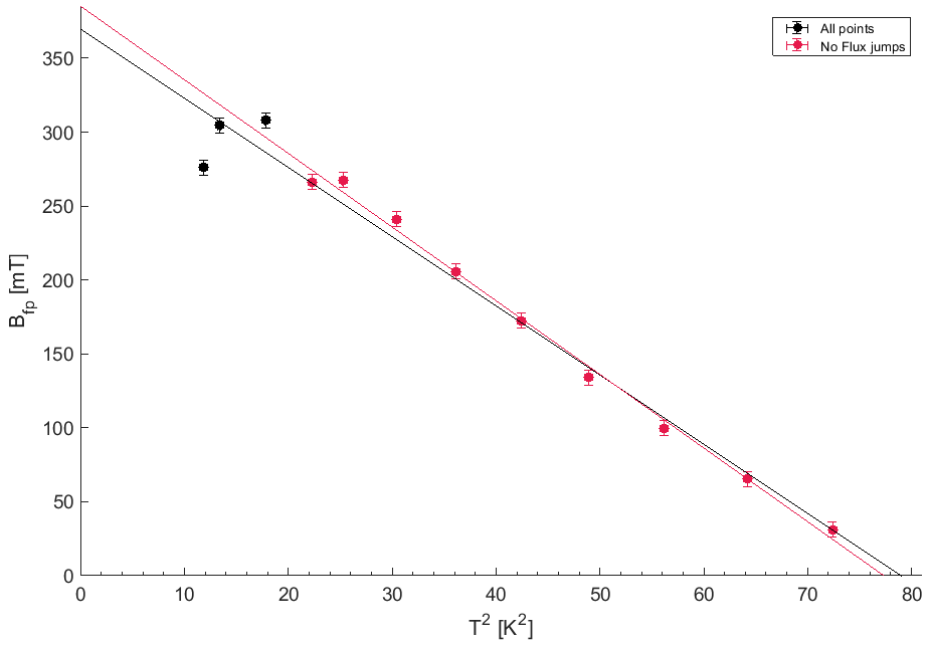

Figure 4.44: The $B_{fp}(T^2)$ for the 10 µm thick Nb foil, with and without flux jumps.

4.11 The effect of thickness

The material of choice for SRF cavities is bulk Nb and has already been extensively studied. Type II superconductors can split into NC/SC regions making it difficult to determine B_{fp}. The vortices can enter one side of the sample and leave from the same side of the sample provided the sample is thick enough, consequently not being detected by HP2. This behaviour is intrinsic of Type II superconductors as it is favourable to split into NC/SC regions. Increasing the thickness of the Type II SC's increase the distance in which the vortices have to travel to fully penetrate through the sample. Thus, a greater force would have to act on the flux lines to push the vortices through the superconductor that is expelling the B, thus it would be expected that B_{fp} would increase with the thickness, d, of the SC material, possibly such that B_{fp} could be larger than the expected values of B_{c1} as seen by the team at ODU [110].

There were two aims for this experiment. Firstly, to determine how the effect of thickness affects B_{fp}. Secondly, to determine if a normal component of the B field was present during testing, and to determine if a normal component was the cause of B_1K_2. If a normal component of B was present on the surface of a SC sample due to the fringing fields of the dipoles, B_1K_2 would be increased due to vortices penetrating through the sample at a low B, which would then look like B was leaking around the sample. To determine if any normal component existed within the experimental set up and produced B_1K_2, SC samples with varying thickness were used. Samples with

less SC material would produce a greater B_1K_2 as the normal component would break through the sample earlier. To determine if B_1K_2 was due to the normal component of B, all other factors other than the thickness had to be kept consistent such as the cross sectional area of the sample, deposition temperature, method etc.

To conduct this experiment, Nb foils were procured from Goodfellow Cambridge Ltd with thickness of 1, 3, 5 and 10 µm. These samples were determined to have a RRR≈30-34 from the impurity content (Section 4.6), and were not heat treated. Thus, they cannot be compared to the samples shown in Section 4.8. Additionally, Goodfellows Cambridge Ltd stated "*When the foil thickness surpasses* 0.05 mm *these foils become naturally denser*". Thus, this study on thickness cannot be extrapolated for thicker, bulk samples, such as those presented in Section 4.8 previously.

Each sample had a surface area of $50\times50\,\mathrm{mm}^2$ to ensure that B_1K_2 was minimal to increase the reliability of the tests. Each test consisted of a range of temperatures, from ≈2.6 K up to 9 K in 0.5 K steps. A brass plate was always placed under the sample to ensure the foils did not tear during testing, including mounting and replacing the samples, or catching on the plate or the Hall probe underneath where the sample was mounted. Tests were also performed with a Brass plate above and below the foils to determine if the cool down of the facility caused damage to the samples, or pinched the foils. Damage to the foils would reduce the B_{fp} permanently, however the foils being pinched would produce unknown B field enhancements that would reduce B_{fp} that could look like damage, but be recovered in a future test.

4.11.1 Raw data

An example of the raw data for the 3 µm sample can be seen in Fig. 4.45. Similar to both the Pb foil and the Nb samples in Sections 4.8 and 4.9.2, B_2 increases slowly as B_1 is increased, until a rapid increase in B_2 indicating that the flux has suddenly broke through the foil. Thus, the second derivative method could be used to determine B_{fp}.

After the B field had broken through, B_2 almost plateaus, followed by a series of smaller jumps in B_2 as B_1 continues to increase. This could be due to trapped flux, or the normal conducting area through the sample increasing, however this behaviour was also seen in the thicker Nb samples shown in Section 4.8. Furthermore, this behaviour was seen for all foils tested in this investigation, including when a brass strip seperated the foil and the magnet.

4.11.1.1 The effect of thickness on K_2

The gradient of B_1K_2 was determined for each foil, and ranges between 5.6×10^{-3} to 28.5×10^{-3}, with the values shown in Fig. 4.46. The errors are the standard deviation in the values for K_2 for each T run. The values for K_2 are similar to those

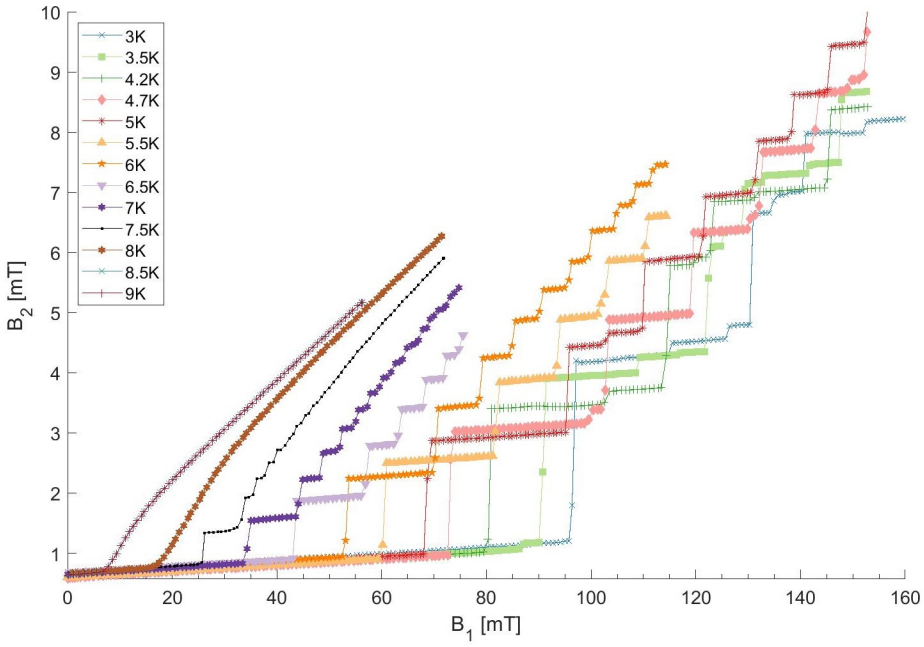

Figure 4.45: The raw data for the 3 µm Nb foil held between 2 Brass plates.

for the Pb sample (K_2=7.6 × 10^{-3}±0.9 × 10^{-3}), with some variation, likely due to the installation of the foils in slightly different locations.

However, K_2 has a similar magnitude for varying thickness of the Nb foils. It can be concluded that there is no normal component of B on the surface of the sample that is creating the B_1K_2 slope. This should be investigated further, with a greater range in superconducting sample depth, where all samples have been produced with the same treatment. Investigating a greater number of sample thickness' also allows a relation to be produced for $B_{fp}(d)$, which might be comparable to other superconducting materials. In addition, a greater number of sample d's allow extrapolation of B_{fp} to $d \approx \lambda_L$ to determine accurate critical magnetic fields that are independent of sample d, similar to the work presented by Senevirathne et al. [110].

4.11.2 The effect of thickness on B_{fp}

The Nb samples with varying thickness were analysed using only the second derivative method (method 2) due to producing sharp transitions. The raw data for the 3 µm Nb foil in between 2 Brass plates is shown in Fig. 4.45, with the corresponding second derivative data shown in Fig. 4.47. The flux jumps shown in Fig. 4.45 produce multiple peaks in the second derivative method, however the repeated jumps are all after B_{fp} and smaller than the B_{fp} jump. The B_{fp} is always the largest increase in $d^2(B_2)/d(B_1{}^2)$. This is due to the gradient of flux over the sample thickness being

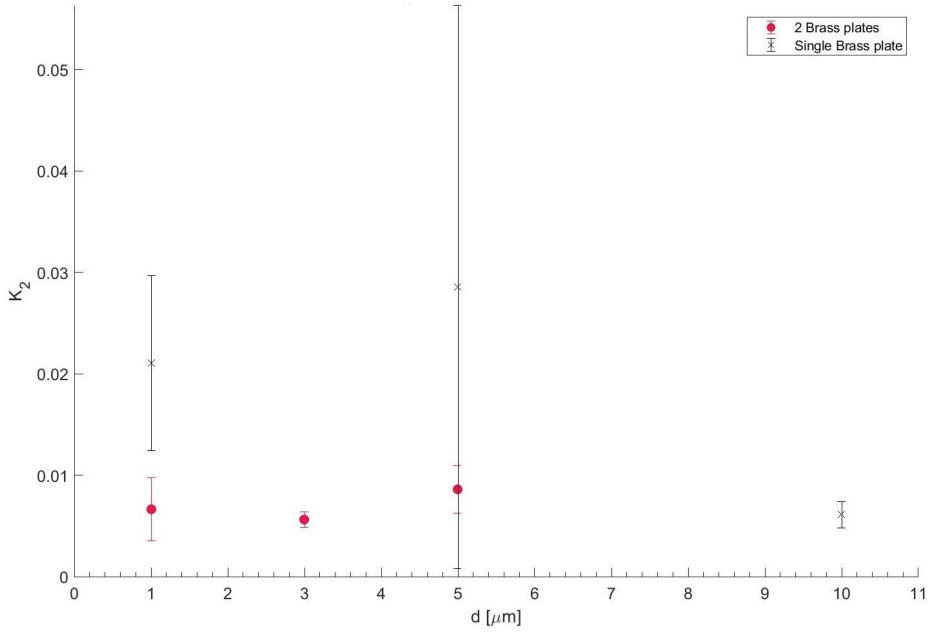

Figure 4.46: The gradient of the magnetic field leakage (K_2) for the Nb foils.

the largest as it penetrates through the sample. There are more peaks in the results for the Nb foil than for the Pb sample, which further re-enforces that the jumps are both flux jumps between pinning sites, and an expansion of the NC area of the foil. This behaviour is similar to what has been shown in Section 4.8 for thicker samples used in the reliability studies.

Figure 4.48 shows B_{fp} as a function of T. The values for B_{fp} are linear as previously seen in the Pb sample, with some fluctuations. These fluctuations could be due to the low RRR of the sample, such that a greater force was required to displace the trapped flux from the pinning site. Similarly, the foils had not been treated such the surface could be rough, producing flux enhancements, or the foils could have become pinched in the cool down which would also produce a flux enhancement.

The $B_{fp}(0\,K)$ was been extracted from the $B_{fp}(T^2)$ using a linear fit, which produced a range in B_{fp} from 46.58 - 385.29 mT, with all the values shown in Table 4.14 and Fig. 4.49. This range covers all of the expected critical fields for Nb [18], [34]. There should be little to no error in the extraction of B_{fp} as the transitions are sharp, with the main variation shown in Section 4.8 shown by testing different areas on a sample. Additionally, measurements where a flux jump was observed prior to B_{fp} have been removed. As shown in Section 4.8.3, the area that is tested of a sample can produce a large difference in results. Thus, the B_{fp} being different for measurements with a single or two brass plates is due to testing a different area of the sample when the brass plates were added or removed.

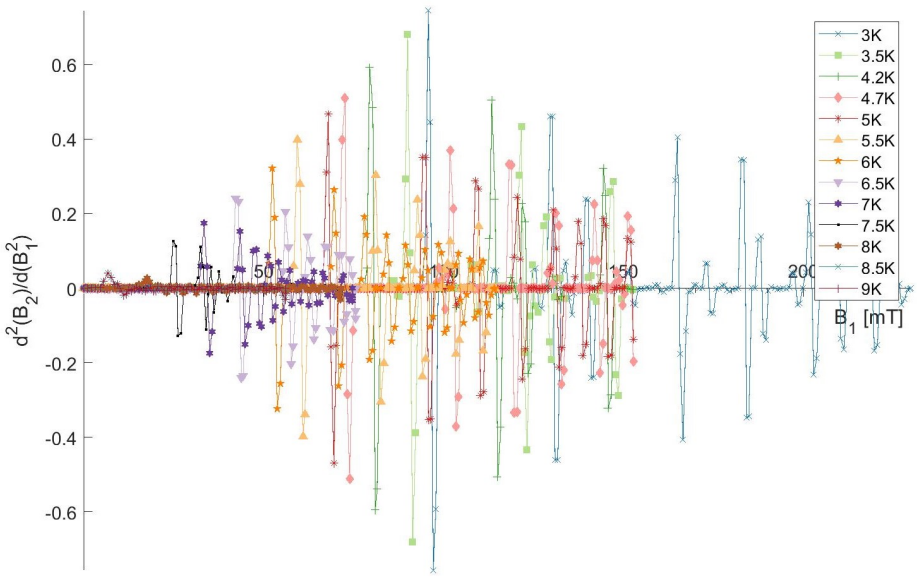

Figure 4.47: The rate of change of B_2 as a function of B_1 for the 3 µm Nb foil, corresponding to Fig. 4.45

The change in B_{fp} with sample thickness enforces that the B field must be present within the foils without fully penetrating to the opposing side. Samples with a smaller thickness have a reduced $B_{fp}(0\,K)$ compared to the the samples with a greater thickness. This is intuitive as there is a greater SC volume which B_{app} has to break through to indicate $B_{fp}(0\,K)$.

Table 4.14: The extracted values of $B_{fp}(0\,K)$ using a linear fit of $B_{fp}(T^2)$.

	$\mathbf{B_{fp}}(0\,K)$[mT]	
Sample thickness [µm]	Single Brass plate	Two Brass plates
1	55.20±2.28	46.58±0.81
3	N/A	104.49±1.79
5	219.47±3.38	300.12±8.64
10	385.29±6.53	N/A

The $B_{fp}(0\,K)$ is plotted as a function of sample thickness in Fig. 4.49. Assuming a linear dependence of $B_{fp}(d)$ is consistent with the Bean critical state model, with some small error. It can be seen that the points are scattered, and do not follow a perfect linear relationship. The scattering is expected as they are 4 different samples, and not one sample with varying thickness. Thus, the samples may have different impurity content, grain boundaries or history, which can effect B_{c1} and J_c values.

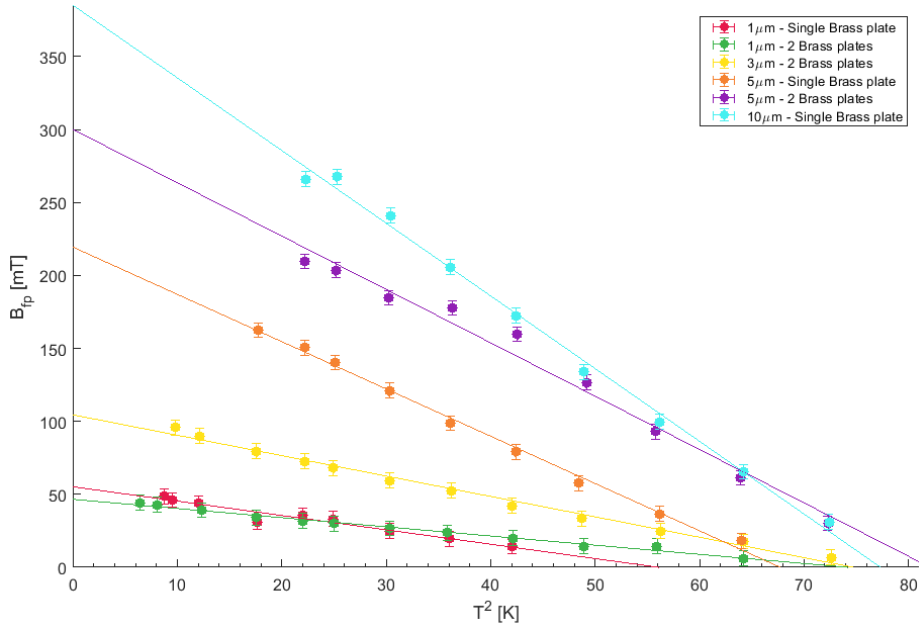

Figure 4.48: $B_{fp}(T^2)$ (found using the second derivative method) for the Nb foils with varying thickness and set up.

Extrapolating the data to d=0 µm, the $B_{fp}(0\,K)$ was found to be 21.24 mT. This value is much lower than $B_{c1}(0\,K)$ (174.0 mT [42]). This was not expected, as it was expected that $B_{fp}(0\,K, d=0)=B_{c1}(0\,K)$. This could be due to the quality of the foil, as the foils were not annealed and flux pinning could be affecting B_{fp}. Additionally, these effects could be due to stray fields producing edge effects, which are more pronounced on thinner samples. Nonetheless, the J_c can be extracted from the Nb films. The B_1 at which B_2 indicates B_{fp} can be wrote as [110]:

$$B_{fp}(d) = B_{fp}(0\,\mu m) + \mu_0 J_c d \tag{4.11}$$

Which can be rearranged to determine J_c. Attempting to use the $B_{fp}(0\,K, d=0)$ produced values show in Table 4.15, with an example for the 1 µm thick film:

$$J_c = \frac{B_{fp}(d) - B_{fp}(0\,\mu m)}{\mu_0 d}\frac{T \cdot s \cdot A}{m^2 \cdot kg} = \frac{(55.20 - 21.24)/1000}{4\pi E - 7 \cdot 1E - 6} = 2.7 \times 10^{10}\,A\,m^{-2}$$

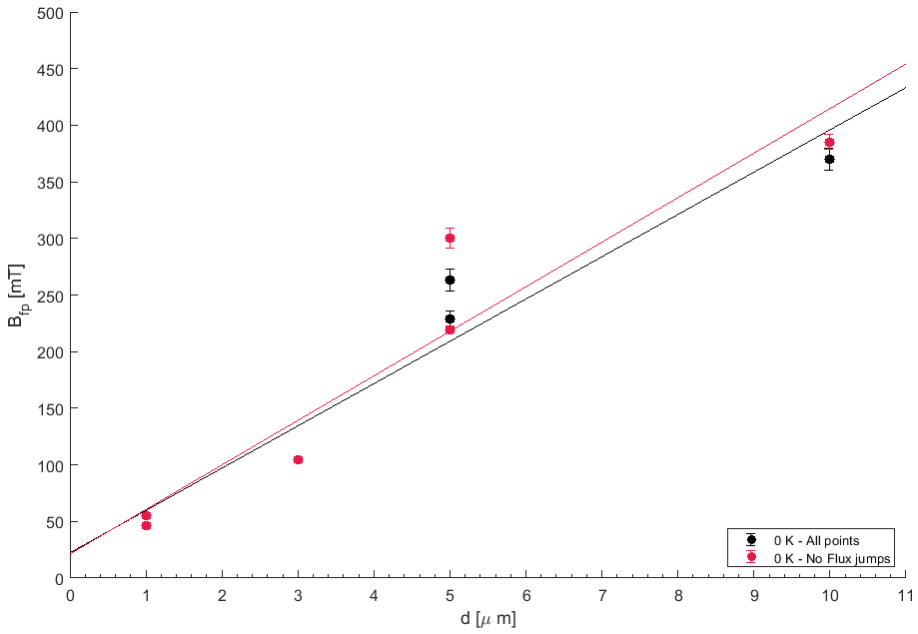

Figure 4.49: $B_{fp}(d)$ for the Nb foils with varying thickness and set up.

Table 4.15: The $J_c(0\,K)$ of the Nb foils found using Eqn. 4.11.

	$J_c(0\,K)$ [$A\,m^{-2}$]	
d [µm]	1 Brass plate	2 Brass plates
1	2.7×10^{10}	2.0×10^{10}
3	-	2.2×10^{10}
5	3.2×10^{10}	4.4×10^{10}
10	2.9×10^{10}	-

However, the results of J_c found in Table 4.15 depend on the samples used to fit the data, and can be skewed if the tested samples were not high purity, contained defects or produced flux pinning etc. As it was already found that $B_{fp}(0\,K, d=0)$ did not produce a similar value for $B_{c1}(0\,K)$, the $B_{fp}(0\,K, d=0)$ should not be used to calculate the J_c. Thus, the same method was used as shown in Eqn. 4.11 but by using the theoretical B_{c1} rather than $B_{fp}(d=0\,µm)$, and using the absolute value. This leads to the results shown in Table 4.16.

Table 4.16: The $J_c(0\,K)$ of the Nb foils found using Eqn. 4.11 whilst using the literature value for B_{c1} (174 mT [34]).

	$J_c(0\,K)$ [$A\,m^{-2}$]	
d [µm]	1 Brass plate	2 Brass plates
1	9.4×10^{10}	1.0×10^{11}
3	-	1.8×10^{10}
5	7.4×10^{9}	2.0×10^{10}
10	1.7×10^{10}	-

Both methods produced a J_c on the order of ($10^{10}\,A\,m^{-2}$), which is on the same order of magnitude as what was found for low RRR Nb (≈40) $J_c(4.2\,K)$ [101], and similar to what was found for low RRR (≈50), single crystal Nb (J_c=$5 \times 10^{10}\,A\,m^{-2}$)[127]. Tthe J_c values shown in Table 4.16 indicate that the J_c of the foils varies and it is not the same for each foil. It is expected that the individual B_{c1} values for each foil also vary, which cannot be assumed for different samples.

The $B_{fp}(0\,µm)$ measured by the conduction cooled MFPF is lower than what was determined using the solenoid at Old Dominion University (ODU) (≈ 132.5 mT at 4.35 K), the J_c is two orders of magnitude larger than the J_c found at ODU for Nb [110]. This could be due to a number of reasons, such as the foils tested in the MFPF were on the order of µm, where as the smallest sample tested in the ODU facility was 125 µm. The foils are prone to pinning effects within the sample due to the large impurity content, especially as they had not been annealed. Another possibility is the orientation of B_{app}. In theNC state, the B_{app} produced by the MFPF is still close to parallel, remaining parallel as it passes through the foil. On the other hand, the facility at ODU produces a B_{app} perpendicular to the sample whilst in the NC regime, such that when the B enters the superconductor, it very rapidly breaks through the sample, thus pinning has less of an effect on their B_{fp}. No comparison can be made to the bulk Nb tested as the RRR is not reported, however the team at ODU calculated J_c to be $10^8\,A\,m^{-2}$, which is comparable to cavity grade Nb with flux pinning. Thus, the quality of samples differ greatly between both tests.

The B_{fp} for low RRR samples is much larger for low RRR materials than for high purity materials. The RRR of a sample can depend on the sample thickness [128], [129] as well as the impurity content [130]. Typically, thin film (on the order of µm) coatings for SRF applications typically have lower RRR than ingot Nb. Thin film Nb typically has a RRR on the order of 10-100 [131]–[135], where as bulk Nb for SRF cavities is typically 300-400 [131]. A single measurement of a low RRR sample is indistinguishable from a single measurement from a high RRR sample for a finite thickness. To mitigate this, multiple thickness' should be tested of each sample to determine the J_c and B_{fp} to allow a comparison. Similarly, a bi-polar power supply

could be used to determine the quantity of trapped B within a sample by performing hysteresis loops by reversing the polarity.

For further investigation into the effect of thickness, one sample should be tested and the thickness slowly reduced, to try and determine a full range of the effect of thickness with a parallel B_{app}. Additionally, this sample should be of high quality to reduce the effect produced by other factors.

4.12 Summary

A magnetic field penetration experiment has been designed and built at Daresbury Laboratory that uses a ferrite C-shaped magnet to apply a DC B parallel to a superconducting sample, from one side of a sample to the other. The B is generated by LTS solenoid.

The aim was to produce a fast sample turn around to allow the optimization of deposition parameters. Two facilities were designed to house the experiment; a VTI which was designed to use a gas as a heat exchange to a cold head, and a conduction cooled facility in which a sample is mounted directly onto a cold head. The lowest T the sample area reached on the VTI in the gas system was 7.5 K which was not low enough T to perform adequate testing for materials intended for SRF applications. To determine if the experiment would work as intended the VTI was tested using LHe. A couple of tests were performed using this configuration. The results produced a B lower than the simulated values, and the magnitude was not the same in both polarities. Experimental results produced determined there were large amounts of magnetic materials present within the facility.

Due to the LHe system not having a recovery line, the high price of LHe and magnetisation present within the VTI, it was decided that a new facility should be designed. The conduction cooled MFPF was designed using the experience of previous tests. The facility was designed to be conduction cooled such that the time taken for each experiment was not an issue, whilst reducing the amount of LHe used.

The conduction cooled MFPF was tested using Al and Cu thermal radiation shields, which determined that the Cu thermal radiation shields took longer to cool down due to the larger thermal mass. However, the increased thermal inertia also improved the T stability. Thus, the facility allowed the magnet to be tested at low T. The maximum applied B that was generated was $\approx$600 mT at 8 A, which is slightly lower than the simulated values which is most likely due to the saturation of the magnet. The B is still large enough for testing materials for SRF applications. The conduction cooled facility was the system that produced all further results presented, using the method stated in Section 4.5.3. Some samples were tested before the facility was upgraded to be automated, however the testing method remained the same and was performed manually.

It is intuitive that a sample must be larger than the gap present in the magnet or else B would not be localised to the sample surface. Systematic tests were performed using a 10 µm thick Pb foil to determine the effect of sample size. Results determined that the smaller a sample size becomes, the greater K_2 becomes, which can obscure B_{fp}, and for even smaller samples reduce B_{fp}. This could be due to either edge effects, where unknown flux enhancements have been produced, or due to the fact B is also being applied from the opposing side (the same side as HP2). To ensure a reliable B_{fp} (and thus $B_{fp}(0\,K)$ and $T_c(0\,mT)$) the samples should remain as large as possible. The minimum sample size that can be tested whilst a B_{fp} can be extracted is $30\times30\,mm^2$, however there can be a deviation from what is expected to be the 'true' value by up to 10 %. Samples with an area greater than $40\times40\,mm^2$ can be compared directly to each other, where as smaller samples must be directly compared to similar sizes. Care must be taken when comparing samples of different sizes.

Additionally to the Pb sample, a sputtered Nb sample was used to investigate the effect of sample size and geometry. Due to the sample being deposited onto a Cu substrate and could not be easily reduced in size, the sample was only tested at 3 different sizes with different orientations to the magnet. The K_2 values are similar to those produced in the tests from the Pb samples for a similar size. It was observed experimentally that when samples were placed at a 45° angle to the poles, the K_2 value decreased slightly. The B_{fp} varied from 188.0-209.4 mT. The three samples were different, hence the film may have not been uniform, thus affecting the results. Contrary to the Pb sample, the B_{fp} could still be extracted for the $20\times20\,mm^2$ Nb sample. This concludes that accurate B_{fp} values can still be determined for small samples. The difference between the two samples is that the Nb samples have a larger B_{fp}. Thus, the ratio of B_2/B_1 has a greater change pre to post B_{fp}, thus producing a more pronounced transition when B has penetrated from one side of the sample to the other.

To determine the random error of the facility, two samples were bought from Goodfellows Cambridge Ltd. with a thickness of 50 and 100 µm. These samples were placed in the MFPF and underwent multiple tests and thermal cycles without the samples being removed. The largest error produced was 0.9 % for the 50 µm sample using both the normalisation and second derivative method to extract B_{fp}. The samples were then removed and re-inserted into the MFPF, which increased the error up to a maximum of 1.2 %, once again for the 50 µm foil. Although the error increased, this could be due to the samples low RRR and in-homogeneity, such that the random error of the system is reported as 0.9 %.

The purpose of the MFPF is to measure superconducting thin films for SRF applications, typically on the order of microns, which often have low RRR. It was therefore relevant to determine how the effect of thickness effects B_{fp} for samples with low RRR. To do so, four Nb foils with thickness' of 1, 3, 5 and 10 µm were procured

from Goodfellows Cambridge Ltd. to investigate the effect of sample thickness on B_{fp}. It was estimated that these samples have a low RRR, between 30-34. The K_2 value was similar for each sample, such that it can be deducted that B_1K_2 is not produced by a normal component present within the system. Additionally, the K_2 values for the Nb foils are comparable to that produced by the Pb sample in an earlier experiment.

Using the foils of varying d, the B_{fp} independent of thickness was found, and was lower than that of B_{c1}. This could be due to a number of possibilities, such as flux pinning within the sample due to defects and impurities (and thus a RRR value of reactor grade Nb), the foils had not being annealed. The most likely explanation is due to the high impurity content of the samples (hence the low RRR), causes the B field to be pinned within the foils. This was also seen for the 5 and 10 µm samples both prior to B_{fp}, and can also be seen by plateaus after B_{fp} for all samples. Similarly, edge effects could be present on the sample that are currently unable to be detected. Future work should include adding flux gates at sample edges to determine if edge effects are present and the magnitude of them.

Comparing the $B_{fp}(d)$ to $B_{fp}(0\,\mu m)$ allowed J_c to be determined for the surface layer, which was found to be $\approx 2.7 \times 10^{10}\,A\,m^{-2}$, which is two orders of magnitude higher than what was found by the field penetration experiment at ODU using a solenoid. One possibility is that the difference could be due to the difference in B orientation. Although B is forced to be parallel across the surface of a superconductor in the Meissner state, perpendicular components are present whilst a sample is in the normal conducting state, including the B fully penetrating through the sample once the B has entered the sample. Thus, normal components could be present on the sample, thus reducing the response in J_c to the applied B.

Although it would have been beneficial to be able to extract B_{c1} using the MFPF, this was not the aim of the facility. The facility was designed to compare measurements between samples, and to gain a relative measurement between samples of similar size or thickness. It is clear that samples can produce a large difference in B_{fp}, depending on the qualities of the samples.

For given samples of finite thickness, B_{fp} cannot be compared unless the J_c is also known. To obtain J_c, multiple thickness' of the same sample must be measured. Once both B_{fp} and J_c are known, a clear comparison can be made.

However, it is likely the difference in the samples, as a high purity sample was used at ODU. This implies that the MFPF is sensitive to impurity content of samples, and also flux jumps. This is confirmed by both the raw measurements and also by investigating the J_c.

Chapter 5

Magnetic Field Penetration Facility Results

5.1 The effect of thickness of sputtered films

The material of choice for SRF cavities is bulk Nb. One alternative to bulk Nb is Nb films deposited onto Cu substrates. The Cu substrate produces a greater thermal conductivity between the RF surface and the LHe bath, whilst only a small amount of Nb is required to fully screen the RF. Sputtered films also have limitations, such as the deposited film being altered by the substrate surface, and that the films usually have much larger pinning than what is usually found for bulk Nb.

The effect of thickness has already been presented in Section 4.11 for foils produced by Goodfellow Cambridge Ltd. Sputtered films are expected to behave differently to Nb foils of a single material - i.e, not on a substrate consisting of a different material, which in turn alters the structure of the Nb, and therefore the performance of the film [136]. As sputtered films (at least throughout this thesis) are predominantly on Cu, the films cannot be annealed to high temperatures to remove pinning present in the film. Typically sputtered Nb films produce a low RRR (10-100) and the RRR is known to increase with sample thickness [131]–[135]). Thus, the high impurity content of the foils and structure of the Nb films should produce different results due to the different fabrication methods.

5.1.1 Sample preparation

To investigate the effect of thickness on the measurements produced by the MFPF, three Nb samples were deposited on Cu disks at Daresbury laboratory using DC magnetron sputtering. The deposition facility consisted of two chambers, a deposition and a load lock chamber. The load lock chamber could contain up to 7 samples at

once, thus multiple depositions could be performed without samples requiring to be removed. This ensured that the same internal conditions were kept for each deposition. To ensure the system was free from contaminants, the facility was baked to 150 °C for 4 days before depositions began. A base pressure of 5×10^{-10} mbar was reached after the system had cooled back to T_{room}.

After all the samples were deposited, new substrates were inserted and only the load lock vacuum chamber has to be baked again. The process gas was injected into the deposition chamber by separate MKS 1179A12CS1BVB mass flow controllers, calibrated for krypton. The mass flow controllers have a flow range up to 100 sccm and were controlled by MKS Type 250B and MKS Model 247C control units. Pressure during deposition was typically 10^{-3} mbar and was adjusted by the flow rate through the mass flow controller, with a constant pumping speed, until the desired pressure was read from the Baratron. The deposition chamber had four 3 inch concentric magnetrons which can be configured both in balance and unbalanced conditions. The vacuum in both chambers were provided by a TMP and a scroll pump for backing. The power supply used in this experiment was Advance Energy pinnacle plus with DC pulse mode.

Table 5.1: Nb deposition parameters set to produce the Nb film on Cu disks.

Parameter	**Value**
Substrate heated	650 °C for 12 hours
Base pressure at 650 °C on a substrate	$<10 \times 10^{-8}$ mbar
Deposition temperature	650 °C
Power supply	DC MS
Current density	1.11, 1.12, 1.26 A
Voltage	358, 354, 317 V
Target power	$\approx$ 400 W
Discharge gas	Kr
Discharge gas pressure	$<1.5 \times 10^{-3}$ mbar
Target-substrate distance	10 cm
Substrate rotation	4 rpm
Deposition time	2, 6 and 10 hours
Deposition rate	11.2, 9.9 and 8.4 nm/ min
Nb film thickness	1.3, 3.6 and 5.1 µm

To reduce any possible variations between the samples, all three samples were deposited using a planar DC magnetron with the same deposition conditions and parameters, and were deposited consecutively without changing the vacuum conditions. The only variation between samples was the time taken for each

deposition, which altered the thickness of the Nb samples. The films were grown at 650 °C to reduce dislocation density and produce a film density similar to that of bulk Nb. Due to the high temperature deposition, the Cu substrate is also annealed leading to the growth of large Nb grains, ≈ tens of µm. The oxide layer is completely dissolved in the Cu at this T, and the Nb grains are influenced by the crystal orientation of the underlying Cu substrate. The deposition parameters are shown in Table 5.1. Cross sectional measurements were performed by electron back scattered diffraction (EBSD) by Dr. Francis Lockwood, and display grain growth perpendicular to substrate surface, and the film growth has a randomly oriented structure, that is slightly textured in the 110 orientation [2]. The lattice parameter was calculated from grazing angle X-ray diffraction to be 3.295 Å, which is similar to that of bulk Nb [2].

5.1.2 Raw Data

Three Nb samples were deposited on 50 mm diameter and 2 mm thick Cu disks, with thickness' of 1.3, 3.6 and 5.1 µm by DC magnetron sputtering. A typical data set is shown in Fig. 5.1 for the 3.6 µm Nb sample. Initially $B_2 = B_1K_2$, since $K_2>0$ there is B on the opposing side of the sample. Initially, $B_2(B_1)$ is linear. As B_1 is increased, $B_2(B_1)$ deviates away from the linear trend, which indicated that the magnetic field has penetrated through the sample. Unlike the samples shown previously (both Pb and Nb) there is no sharp, abrupt increase in B_2 to indicate B_{fp}. Instead, the change in B_2 was more gradual, thus making B_{fp} harder to determine using the second derivative method. Thus, the deviation away from B_1K_2 was used to determine B_{fp} - Method 3 from Section 4.7. One theory for the gradual transition is that B did not penetrate through the sample all at once, but in the form of individual vortices. As each fluxoid breaks through to the opposing side of the sample, B_2 increases slightly, thus making it hard to distinguish B_{fp} from background noise. Additionally, this could also be due to the Nb not having a large B_{fp}, thus the ratio between B_2/B_1 is reduced when compared to the deposited Nb sample in Section 4.9.2.

As B_1 is increased such that $B_1 \gg B_{fp}$ for each temperature run, $B_2(B_1)$ approaches B_1K_1, but never reaches the limit within the range of the applied B_1 as seen for the Pb sample. One assumption is that although B has broken from one side of the sample to the other, the sample is in the Abrikosov state with vortices present within the sample. Thus, only a fraction of the B fully penetrates through the sample, and the remaining B is still screened. This would be intrinsic for Type II superconductors, which explains why this was not observed for the Pb sample. Another possibility is it could also be an effect of geometry due to the samples being disks, as a similar looking curve (before B_{fp}) was found for the Pb sample, shown in Fig. 4.36.

It should be noted that both the 1.3 and 3.6 µm run were performed using silicon diode thermometers using the standard factory calibration curve, thus there

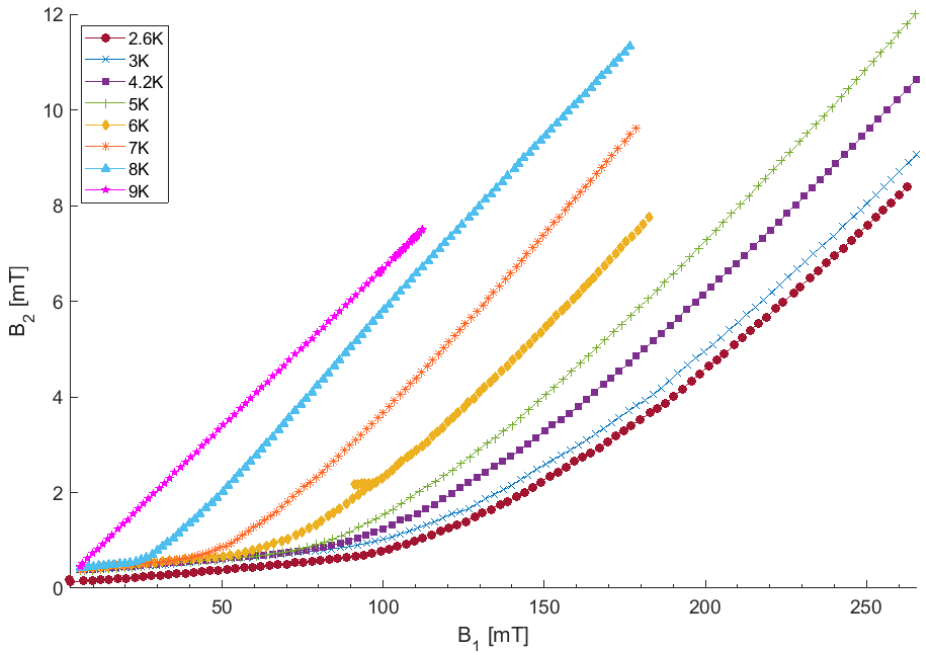

Figure 5.1: The raw data for 3.6 µm of Nb on a Cu disk with a diameter of 50 mm.

is an increased error in the temperature readings of ±0.25 K due to no CERNOX thermometer being available at the time.

5.1.2.1 The effect of thickness on K_2

Once again the gradient K_2 was determined for the three samples, and ranges from 6.0×10^{-3} to 7.1×10^{-3}, shown in Table 5.2. These values for K_2 are lower than that for the Pb sample (K_2=11.0×10^{-3}). Possible reasons for this include:

- The Pb sample had a spacer between the sample and magnet, unlike the Nb samples. Thus the flux was not forced into the surface of the Pb and can flow over and around the sample.
- The position of the samples were not exactly the same due to human error.

The K_2 has a similar magnitude for varying thickness' of Nb. It can be concluded that there is no normal component of B was produced on the surface of the sample under the poles, creating the B_1K_2 slope, similar to what was found for the Nb foils in Section 4.11. In conclusion, the B_1K_2 does not depend on the material of the sample, only on the geometry. Further investigations should be performed to produce a relation for different B_{fp} as a function of sputtered sample thickness', which might

be comparable to other superconducting materials. In addition, a greater number of sample thickness' allows extrapolation of B_{fp} to d$\approx \lambda_L$ to determine accurate critical magnetic fields that are independent of sample thickness [110], and also to determine if the behaviour on B_1K_2 varies from very thin samples to very thick samples.

Table 5.2: The extracted data from $B_{fp}(T^2)$ using both a linear trend and the second derivative method to produce $B_{fp}(0\,K)$ and $T_c(0\,mT)$), and the film thickness found by EBSD performed by Dr. Francis Lockwood.

Sample	**Film thickness** [µm]	$\mathbf{K_2}$ $[\mathbf{10^{-3}}]$	$\mathbf{B_{fp}}(0\,K)$ [mT]	$\mathbf{T_c}$ [K]	$\mathbf{B_{fp}}(0\,K)$ [mT]	$\mathbf{T_c}$[K]
			Method 3		$\boldsymbol{d^2(B_2)/d(B_1)^2}$	
Nb-1	1.34 ± 0.18	6.3 ± 0.3	54.6 ± 1.6	10.15 ± 0.42	127.1 ± 6.8	8.79 ± 0.24
Nb-2	3.58 ± 0.08	6.0 ± 0.2	104.1 ± 0.8	9.04 ± 0.21	142.9 ± 3.0	9.10 ± 0.15
Nb-3	5.06 ± 0.04	7.1 ± 0.4	126.6 ± 1.0	9.09 ± 0.26	157.8 ± 1.6	8.96 ± 0.06

5.1.3 The effect of thickness on B_{fp}

The Nb samples were analysed using both the standard deviation method and the second derivative to determine B_{fp}, with an example shown for 1 temperature cycle in Figs. 5.2a and 5.2b respectively for the 3.6 µm thick sample. Unlike the Nb and Pb foils tested in the previous section, the sputtered films did not produce a sharp, step transition and the data was noisy. As the second derivative method is highly sensitive, the noisy data can produce an illogical B_{fp} such that it can be misreported. Whilst the second derivative has been shown to show no discrepancy in the results, method 3 from Section 4.7 was chosen for the analysis to allow a comparison. The B_{fp} is different for each analysis technique, as they are reporting different behaviour. The second derivative reports the largest change in B_2/B_1, where as the standard deviation method reports a B_{fp} that differs from the B_1K_2 slope. The $B_{fp}(0\,K)$ for each method is shown in Table 5.2, as well as $B_{fp}(T)$ shown for each method in Fig 5.3.

Figure 5.2b shows that the values for B_{fp} for the 1.3 µm sample are not within error of the line of best fit. This indicates that either the extraction of B_{fp} is not correct, or the line of best fit is incorrect. However, as shown in Fig. 5.2a and Table 5.2, using the simple standard deviation method produced very different values. This indicates that the second derivative method is not reliable for samples that do not produce a sharp step transition.

The B_{fp} was obtained by finding the last point within the standard deviation of the B_1K_2 slope. The results for the three Nb samples are shown in Fig. 5.3a as a function of T^2, fit using a linear expression. Samples with a smaller thickness produce

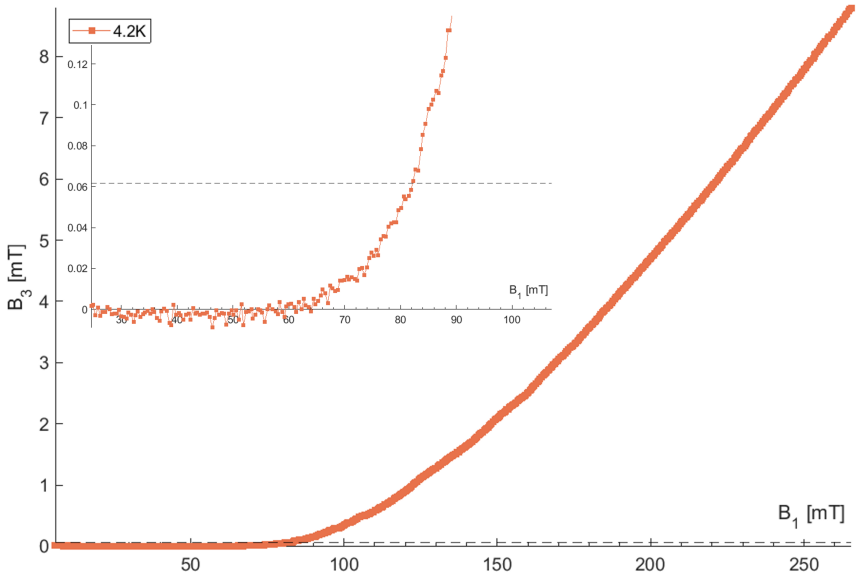

(a)

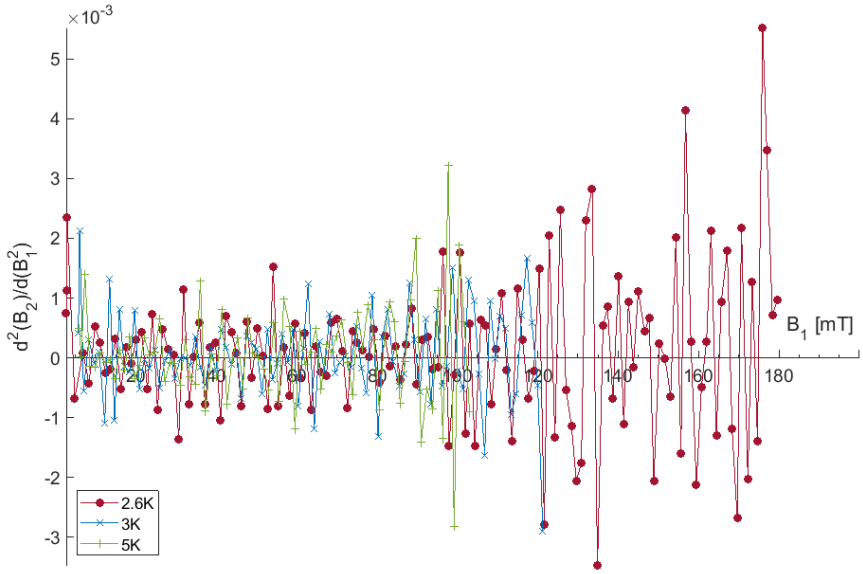

(b)

Figure 5.2: Examples of the analysis techniques using method 3 (5.2a) and the second derivative (5.2b) method.

a reduced B_{fp}. This is intuitive as there is a greater superconducting volume for B_1 to break through to indicate B_{fp}. This is the same conclusion as to what was found for the Nb foils in section 4.11.

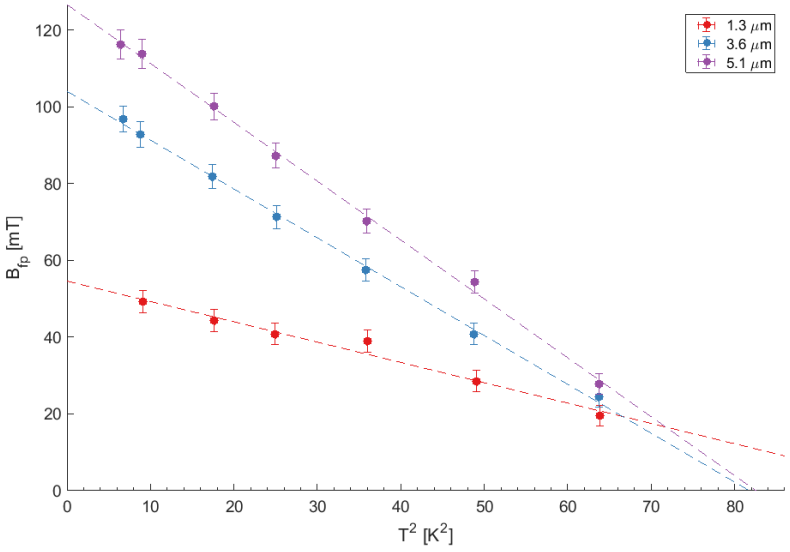

(a)

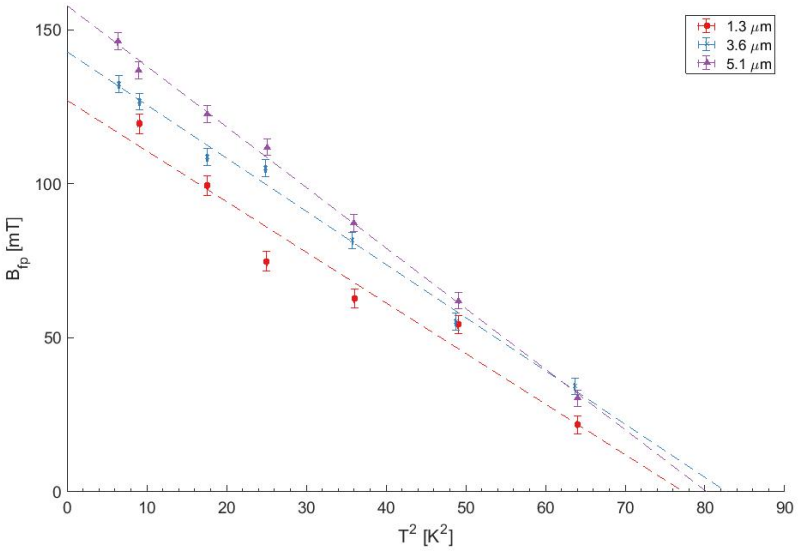

(b)

Figure 5.3: B_{fp} found using method 3 (5.3a) and the second derivative (5.3b) as a function of T^2 for the three Nb samples of varying thickness deposited at Daresbury Laboratory.

A comparison of $B_{fp}(0\,K)$ and $T_c(0\,mT)$ are shown in Table 5.2. The $B_{fp}(0\,K)$ ranges between 54.6±1.6 - 126.6±1.0 mT for the 1.3 µm and 5.1 µm respectively using

method 3, where as the second derivative produces 127.1±6.8 - 157.8±1.6 mT for the 1.3 µm and 5.1 µm respectively. The increased standard error obtained for the values found using the second derivative indicates that due to the gradual transition, the B_{fp} is incorrect. This further implies that the second derivative method is only reliable when the samples have a sharp transition in the form of a step.

The results for the 1.3 µm and 3.6 µm obtained using method 3 are similar to the results found for the Nb foils from Goodfellows ltd of a similar thickness; 54.6 mT for the 1 µm sputtered film compared to 55.2 mT for the foil with the same thickness. Similarly, the 3 µm sputtered film produced a $B_{fp}(0\,K)$=104.05 mT, whilst the Goodfellows foil produced B_{fp}=104.49 mT. Although the sample thickness' are not identical, the results are close enough to be considered a good comparison with low RRR foils. This is expected as the sputtered films are likely to also have a low RRR. However, as the samples reached 5 µm the B_{fp} began to diverge significantly - 126.6 mT for the sputtered film compared to the 219.5 mT found for the foil.

Similar to the Nb foils from Goodfellows, the $B_{fp}(0\,K)$ is lower than the expected critical fields for Nb [18], [34]. This could be due to a number of reasons such as:

- An error in extracting B_{fp}.
- The samples are not high quality as typical for sputtered films, and could contain grain boundaries.
- The surface of the Nb has not been treated post deposition, and could be rough. Thus, flux enhancements could exist on the surface allowing early flux entry.
- Possible flux enhancements at the edges of the sample.

The $B_{fp}(0\,K)$ is plotted as a function of sample thickness in Fig. 5.4, assuming a linear dependence of $B_{fp}(d)$ to be consistent with the Bean critical state model. Extrapolating the data to d=0 µm, the $B_{fp}(0\,K)$ independent of thickness was found to be 31.2±6.4 mT. This is lower than $B_{c1}(0\,K)$ (173.0 mT [34], [42]).

This could be due to the extremely thin regime which the samples were deposited. I.e.- <6 µm, the fact the Cu substrates were not polished prior to deposition, or impurities/dislocations present within the film.

Nonetheless, the critical current can be estimated from the Nb films. Similar to Section 4.11, the theoretical B_{c1} was used to determine the critical current using Eqn. 4.11 for the sputtered films at 0 K. The results are shown in Table 5.3.

The results show that J_c is comparable to that of low RRR Nb [101], [127], with a $J_c \approx 10^{10}\,A\,m^{-2}$ at the surface. Results from Dhavale et al [101] indicated that the large J_c is due to material inhomogeneities dominating the pinning mechanism, in their case O and H precipitates near the surface. This was also the conclusion obtained by Das Gupta. Measurements at Oak Ridge National laboratory on single crystal high RRR (≈5000) produced a J_c=$10^7\,A\,m^{-2}$.

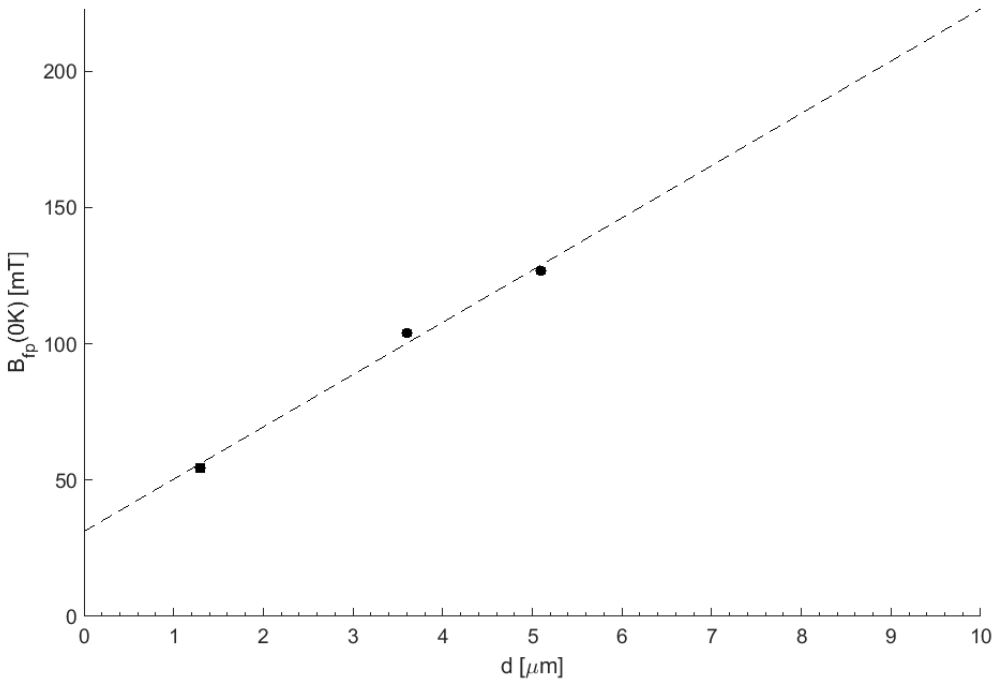

Figure 5.4: The $B_{fp}(0\,K)$ found using method 3 as a function of sample thickness.

Table 5.3: The calculated J_c for sputtered Nb films, found using Eqn. 4.11.

Sample	**d** [µm]	$\mathbf{J_c}(0\,K)$ [$A\,m^{-2}$]
Nb-1	1.34 ± 0.18	7.2×10^{10}
Nb-2	3.58 ± 0.08	4.2×10^{10}
Nb-3	5.06 ± 0.04	2.8×10^{10}

Whilst the $B_{fp}(0\,\mu m)$ measured by the conduction cooled MFPF is lower than expected, the estimated J_c is large. It is expected that the main cause of this discrepancy is the quality and thickness of the Nb used. The sputtered films produced a $B_{fp}(4.2\,K)$=44.3, 81.9 and 100.1 mT for the Nb-1,2 and 3 respectively. These are similar to what was presented by ODU using a solenoid system for Nb on fine grain Cu and Nb on Sapphire on a similar thickness scale [137].

There are multiple differences that will have produced an effect on the results, with the most influential being the sample thickness and quality, which can vary depending on the deposition institute. For a greater understanding of the effect of thickness on B_{fp}, more samples should be deposited and tested with increased thickness than those presented here. For example, extending the sample thickness to 10, 50 and 100 µm should be the performed to determine how the films differ from the procured foils.

Similar to $B_{fp}(0\,K)$, the T_c values also vary for each sample thickness and for the analysis method used. The values of T_c ranged between 9.04 - 10.15 K, which is a large range for 3 identical samples. The thicker the samples became, the closer the T_c became to the theoretical value for Nb. Increasing the thickness increases RRR, which is possibly reflected in the T_c of the samples. This should also be further investigated as a function of sample thickness, to compare to well known high RRR Nb.

Deposited samples will all vary due to quality or thickness. Thus, these Nb films are a good baseline to compare samples of a similar thickness by comparing to the line of best fit for $B_{fp}(d)$. If the results lie above the line of best fit, the samples are better than the samples tested within this section, and vice versa for samples of poor quality. Due to the limited thickness of samples tested, this can only be compared within the range of these samples.

5.1.4 The effect of polishing Cu substrates

One alternative for SRF cavities is to use Nb deposited onto a Cu cavity. Only surface layers of Nb affect the affect the RF performance, thus only a small amount of Nb is required for a full cavity, thus reducing the cost to fabricate a cavity as Cu is cheaper than Nb. Additionally, Cu also has an increased thermal conductivity compared to Nb, such that heat generated in the Nb is more easily conducted to the LHe bath, which make thin film Nb cavities more resistant to multipacting and field emission [39]. Depositing Nb thin films also mitigate impurities being present within the Nb from machining, or present within the Nb which are then uncovered by etching, which can act as pinning centers for flux [39]. Whilst the impurities can be removed from the Nb, this further increases the fabrication cost of the cavity.

Depositing Nb on Cu consists of limitations. One of which is that the Nb film replicates that of the Cu substrate, which in turn affects the superconducting properties of the Nb [136]. To ensure a high quality Nb film is deposited, the Cu substrate must first be treated. Work package 15 of the H2020 ARIES collaboration investigated the effect of surface treatment on Cu substrates on the deposition of Nb thin films. Both the superconducting and physical properties were examined to determine what affect the substrate polishing produced on the Nb.

5.1.4.1 Sample preparation

All the substrates were cut from 2 mm thick OFHC Cu, with a surface area of $53\times53\,mm^2$ [81]. As the condition of the substrate surface influences the growth of the thin film, each sample was polished prior to deposition. The polishing methods include: mechanical polishing (Tumbling), chemical polishing (using a SUBU solution, further referred to as SUBU), electrical polishing (EP), or a combination of EP and SUBU [81]. Chemical polishing was performed on 25 samples at CERN, whilst another

25 samples were sent to INFN LNL which were split into 4 batches to undergo the various other polishing methods [81].

The substrates were sent to one of three institutes once they were polished; INFN LNL, the University of Siegen and STFC Daresbury Laboratory for film deposition. Each system was heated to 650 °C for varying amounts of time prior to deposition, before the Nb films were deposited by DC magnetron sputtering at 650 °C [81]. The Nb deposited at STFC were sputtered with 1.5 mbar of Kr, whilst both the University of Siegen and INFN LNL both used Ar, with all three institutes having using different pressures. Both STFC and INFN had a 10 cm distance between the target and the substrate, whilst Siegen had 6 cm. The largest difference between all three facilities was the deposition time and rate. The films deposited at the University of Siegen and INFN LNL both deposited for 20 minutes with a deposition rate of 150 nm, whilst the films deposited at STFC were deposited for 480 minutes with a deposition rate of 7 nm whilst rotating at 4 revolutions per minute.

The films deposited at Siegen and INFN LNL resulted in a thickness of 3 µm, whilst the samples deposited at STFC resulted in a thickness of 10 µm. The sample names, substrate treatment, deposition institute and sample thickness are shown in Table 5.4.

Table 5.4: A table summarising the sample names, polishing technique, deposition institute and film thickness for the investigations of micrometer thick Nb.

Name	**Substrate treatment**	**Deposition institute**	**d [μm]**
C7	SUBU CERN	STFC	10
L13	EP	STFC	10
L18	EP + SUBU	STFC	10
L19	SUBU INFN	STFC	10
C1	SUBU CERN	Siegen	3
L1	SUBU INFN	Siegen	3
L9	Tumbling	Siegen	3
L10	EP	Siegen	3
L23	EP + SUBU	Siegen	3
C10	SUBU CERN	INFN	3
L8	Tumbling	INFN	3
L16	EP + SUBU	INFN	3
L20	SUBU INFN	INFN	3
L21	EP	INFN	3

The samples were then cut for analysis of the superconducting properties by a VSM and the growth of the films by scanning electron microscopy (SEM) and atomic force

microscopy (AFM). Thus, the final sample size was $\approx 53\times35\,\mathrm{mm}^2$. Some samples had more material removed for further tests, resulting in a sample size of $30\times30\,\mathrm{mm}^2$.

These samples were then tested using the MFPF to determine if there was any correlation between the MFPF designed at Daresbury Laboratory and a VSM, whilst also investigating the effect of substrate polishing on the superconducting properties.

5.1.4.2 Raw Data

The micrometer thick Nb films were ready to be tested before the system had become automated, such that the system had to be controlled manually. To minimise the amount of time taken for each set T test (to increase the speed of measurements) a high point density was only used close to the point of B_{fp}. Otherwise, a low point density was used. This allowed each sample to be completed in one day of testing. Nonetheless, the increased size of the steps in B_1 also increased the error in B_{fp}, as mentioned in Section 4.7.1.4. These tests were performed before the installation of the Cernox thermometer, such that the error in the T measurements were 0.25 K. The method in testing the samples remained similar to the method presented in Section 4.5.3. All the samples in Table 5.4 were tested in the MFPF except except sample 'L21' which had been used by another institute for further testing, and the films deposited by INFN LNL had undergone laser treatment prior to being tested in the MFPF.

The raw data from each sample looked similar to the raw data presented in Fig. 5.5 for sample 'C7', which are similar to the results shown for Nb earlier. There is an initial linear increase in B_1K_2 which was the same for each temperature run, followed by an increase in B_2 away from the B_1K_2 line indicating a relatively clear B_{fp}. Further increasing B_1 did not reach B_1K_1. Although some samples produced a sharp transition such that the second derivative could be used to analyse the data, some samples did not. For consistency, the standard deviation method was used and the last point within the standard error of B_1K_2 is the reported B_{fp}. This produced a consistent linear trend for B_{fp} as a function of T^2. The results for each deposition institute are shown in Figs. 5.6, 5.7 and 5.8 for samples deposited at STFC, INFN LNL and the University of siegen respectively. Both $T_c(0\,\mathrm{mT})$ and $B_{fp}(0\,\mathrm{K})$ were extracted using a linear trend and compared for each sample, shown in Table 5.5.

Each sample produced a linear trend in $B_{fp}(T^2)$. Once again the line of best fit was extrapolated to $B_{fp}(0\,\mathrm{K})$ and $T_c(0\,\mathrm{mT})$. The values for T_c range from 7.68 - 9.63 K. The thermometer (silicon diode) had an error of $\pm0.25\,\mathrm{K}$, thus producing a larger error in the measurements compared to measurements performed with the Cernox thermometer, which had a smaller error.

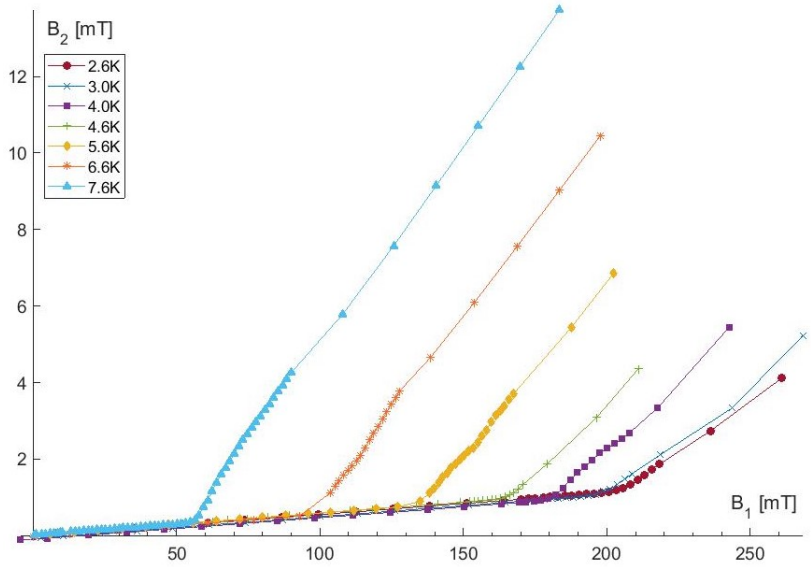

Figure 5.5: The raw data of the magnetic field penetration experiment for the penetrated field B_2 as a function of the applied field B_1 for C7 - 10 µm of Nb deposited by STFC on SUBU polished Cu by CERN.

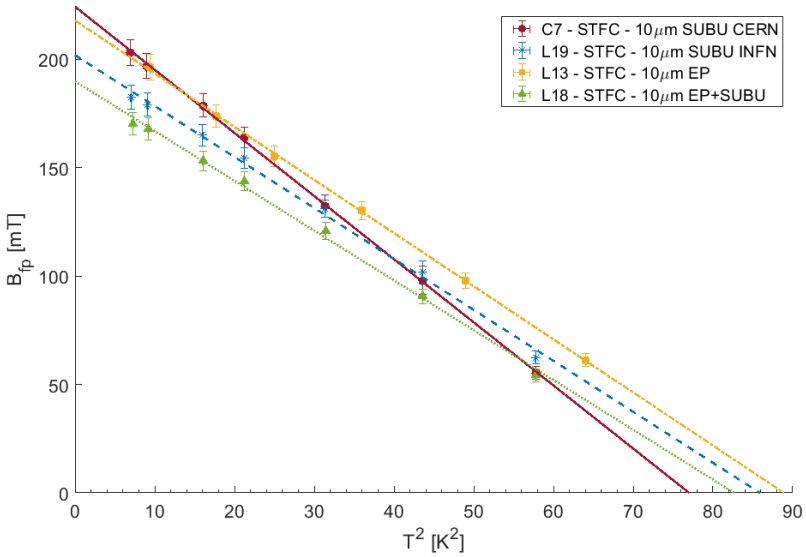

Figure 5.6: The $B_{fp}(T^2)$ for the samples deposited at STFC Daresbury laboratory with varying substrate treatments.

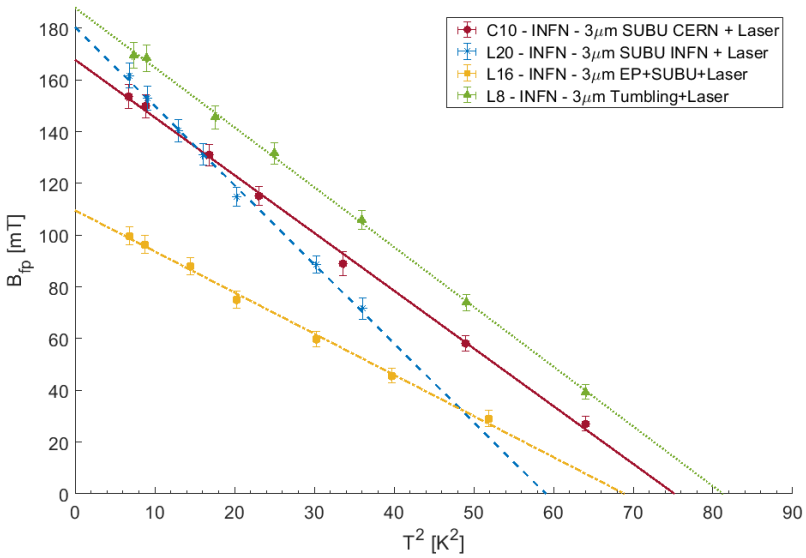

Figure 5.7: The $B_{fp}(T^2)$ for the samples deposited at INFN LNL with varying substrate treatments.

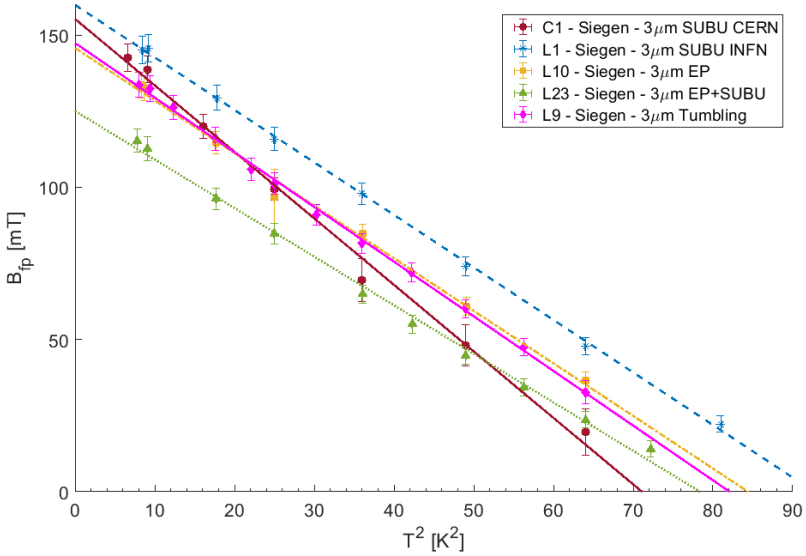

Figure 5.8: The $B_{fp}(T^2)$ for the samples deposited at the University of Siegen with varying substrate treatments.

5.1.4.3 Discussion

Whilst all the substrates underwent the same polishing, and the deposition parameters were the same, it can clearly be seen that there is variation between the samples

Table 5.5: Both $B_{fp}(0\,K)$ and $T_c(0\,mT)$ extrapolated from $B_{fp}(T^2)$ using a linear dependence.

Name	**Substrate treatment**	**Deposition institute**	**B_{fp} (0 K) [mT]**	**T_c [K]**
C7	SUBU CERN	STFC	224.2 ± 0.8	8.78 ± 0.22
L13	EP	STFC	217.9 ± 1.0	9.43 ± 0.24
L18	EP + SUBU	STFC	189.9 ± 1.8	9.09 ± 0.51
L19	SUBU INFN	STFC	201.9 ± 2.1	9.27 ± 0.61
C1	SUBU CERN	Siegen	155.3 ± 2.8	8.43 ± 0.66
L1	SUBU INFN	Siegen	159.9 ± 0.9	9.63 ± 0.20
L9	Tumbling	Siegen	147.4 ± 0.76	9.06 ± 0.19
L10	EP	Siegen	145.7 ± 0.8	9.19 ± 0.23
L23	EP + SUBU	Siegen	125.1 ± 1.6	9.19 ± 0.23
C10	SUBU CERN + LT	INFN	167.8 ± 1.5	8.67 ± 0.37
L8	Tumbling + LT	INFN	187.9 ± 1.0	9.01 ± 0.25
L16	EP + SUBU + LT	INFN	109.6 ± 1.24	8.3 ± 0.35
L20	SUBU INFN + LT	INFN	180.39 ± 1.57	7.68 ± 0.57

depending on the deposition institute and the polishing method. Although the aim was to produce a comparison between the samples, this was not possible due to the samples not being the same thickness or having further treatment post deposition. Some deviation in the linear dependence of $B_{fp}(T^2)$ is present. One possibility for this is flux getting pinned within the sample during cool down, due to a remanence field being present within the magnet, causing some discrepancy between the results.

The samples that produced the consistently largest B_{fp} were the samples deposited at STFC, which was expected due to the samples having an increased thickness compared to the other institutes. Samples produced by Siegen also produced a consistent B_{fp}, with a range in $B_{fp}(0\,K)$=125.1-159.9 mT.

Some of the samples deposited it INFN LNL produce similar values to $B_{fp}(0\,K)$ to the films deposited at Siegen. The outlier for INFN LNL was the sample with the lowest B_{fp} for any institute. The samples from INFN LNL had also undergone laser treatment after the deposition which could have affected the results, which had not performed on the samples from Siegen at this stage.

Due to the system not being automated, the samples were not tested at exactly the same temperature. Thus to allow comparison the $B_{fp}(0\,K)$ and T_c were extracted using a linear dependence of $B_{fp}(T^2)$, and are shown in Table 5.5. Comparing $B_{fp}(0\,K)$ allows a comparison for the polishing technique within each institution to identify any trends between the results, which are shown in Table 5.6.

The best performing samples from Siegen and STFC had the Cu substrate polished by chemical polishing by INFN and CERN for each institute respectively. Calculating the J_c using the same method as Eqn. 4.11 produces J_c=$3.5 \times 10^9\,A\,m^{-2}$ and $4.1 \times 10^9\,A\,m^{-2}$ for the sample deposited at Siegen and STFC respectively. Due to

Table 5.6: The $B_{fp}(0\,K)$ in descending order for micrometer thick Nb films produced by the MFPF for substrates polished by various techniques. LT stands for post deposition laser treatment.

STFC	**Siegen**	**INFN**
SUBU CERN	SUBU INFN	
EP	SUBU CERN	Tumbling + LT
SUBU INFN	Tumbling	SUBU INFN + LT
	EP	SUBU CERN + LT
EP + SUBU	EP + SUBU	EP + SUBU + LT

the lower J_c of the film, it would be expected that the sample deposited at Siegen is of higher quality, which is un-expected due to the lower B_{fp} produced.

The EP sample deposited at STFC also produced a high $B_{fp}(0\,K)$, similar to that of the of the SUBU CERN. The Nb sample deposited at INFN onto EP Cu was the one sample not tested by the MFPF. It would be assumed that the EP sample would produce a large $B_{fp}(0\,K)$ for INFN LNL, similar to the other two institutes, and due to the EP technique was found by the ARIES collaboration to be the best pitting free technique [81] for the polishing methods that were investigated.

Films deposited on chemically polished Cu at both INFN and CERN produced a mid-range $B_{fp}(0\,K)$, if not the largest for each institute individually. As both Siegen and STFC had high $B_{fp}(0\,K)$ values for chemically polished Cu samples, it is expected that prior to laser treatment the chemically polished INFN samples would also have one of the largest $B_{fp}(0\,K)$. The difference between the SUBU CERN and SUBU INFN samples varied for each institute. I.e. - SUBU CERN outperforms SUBU INFN by $\approx$22 mT for Nb films deposited by STFC, where as the samples deposited at Siegen show that substrates polished by SUBU INFN outperform the sample deposited on the SUBU CERN polished substrate by $\approx$4 mT. Finally, samples deposited at INFN showed an increase of 13 mT, however the original effects of polishing could have been altered due to the post deposition laser treatment. The SUBU technique produced the lowest roughness (R_a) on substrates [81], and therefore will alter the growth of the Nb films on the substrate. Additionally, thicker samples (STFC) are expected to produce a greater increase in B_{fp} produced by polishing due to the different grain structure and a reduced RRR at an increased thickness.

The largest $B_{fp}(0\,K)$ produced by the samples deposited at INFN was on the Cu substrate polished by tumbling. The effect due to mechanical polishing could not be analysed, as the films deposited on tumbled substrates at INFN produced the largest B_{fp}, whilst the films deposited at the University of Siegen on the tumbled substrate produced a reduction in $B_{fp}(0\,K)$ of 14 mT. However, the sample from INFN had been laser treated which could have also affected the properties of the film until the

samples from Siegen had also been laser treated. No comparison could be made to the films from STFC as no sample was deposited on tumbled Cu substrate.

For all deposition institutes, the Cu substrates polished by the EP+SUBU technique produced the lowest $B_{fp}(0\,K)$. Thus, these samples would be expected to produce the worst samples for RF performance, whilst the individual components of the polishing technique (EP ***or*** SUBU) should produce better RF results in comparison. This claim is supported by 4 samples that were later deposited for QPR measurements, polished by EP and SUBU which are reported in Ref. [138]. However, the samples tested in the QPR were not the same samples tested in the MFPF so no direct comparison can be made. The samples were deposited at both the University of Siegen and STFC. The samples deposited at STFC produced a T_c close to the theoretical value, where as the Siegen samples had a slightly increased T_c. The results in the QPR concluded that the Nb films deposited on the Cu substrate polished by EP produced lower surface resistances for both institutes, which indicated a cleaner film deposition. One theory is that the reduced surface resistance is the cause of the increase of B_{fp} in the MFPF compared to other polishing techniques.

A rough comparison can be made between these samples and the samples in Section 5.1. Extrapolating the $B_{fp}(d)$ relation found in Fig. 5.4 to 3 and 10 µm produces an expected $B_{fp}(0\,K)$ = 93.5 and 238 mT respectively. All 3 µm samples deposited at INFN and Siegen are above 93.5 mT and can be considered better quality than those in Section 5.1. This can be explained by the fact the deposition process is different in each institute. The samples deposited at STFC all produced a lower $B_{fp}(0\,K)$ than predicted, with the EP and SUBU CERN polished substrates producing the closest values of $B_{fp}(0\,K)$=217.9 and 224.2 mT respectively. These values are much closer to the predicted values, which is expected as the deposition institute is the same.

The next step was to compare the results produced by the MFPF to those produced by the VSM at IEE in Bratislava. The hysteresis curves performed in the VSM are taken at 4.2 K only. Thus, to compare the MFPF to the VSM the B_{fp} had to be taken at 4.2 K, $B_{fp}(4.2\,K)$. For those samples that were not tested at 4.2 K, $B_{fp}(4.2\,K)$ was extrapolated using the linear dependence in $B_{fp}(T^2)$.

The VSM tested small samples of $\approx 2\times2\,mm^2$ cuboids. The samples were placed in a uniform B, and orientated as best as possible such that B was applied either parallel or perpendicular to the face of interest of the SC film. The samples underwent a ZFC before the initial magnetisation curve was measured with the same technique as reported in Chapter 3, however the B was ramped at a constant rate for the whole test. As the samples were flat and the geometrical constant was not known, the field of first flux entry (B_{en}) could not be corrected for the local B on the sample at which B entered the sample. The IEE reports B_{en} differently to in Chapter 3, hence the variable has been changed from the variable B_{vp} to be clear on the difference in analysis techniques. Instead, IEE report a 2 % deviation from the linear Meissner

slope. It should be noted that this 2 % deviation may be earlier than what looks like the obvious B_{en}, i.e, B_{en} is not necessarily where the rapid change in m occurs, but rather where the smooth deviation from the linear Meissner slope. Before these results are discussed further it should be noted again that B_{en} and B_{fp} are also not the same. Vibrating sample magnetometers measure the entire SC volume within the system, and B_{en} is the field of first flux entry which decreases the SC volume. On the other hand, B_{fp} is the field of first ***full*** flux penetration, when B has penetrated from one side of the sample to the other, and not when it first enters the sample. For thick samples B can enter the SC sample and leave the same side that B is applied which therefore cannot be detected in the MFPF.

The B_{en} for both the perpendicular and parallel field for the VSM are compared to B_{fp} produced by the MFPF at 4.2 K for each deposition institute. Figure 5.9 shows the comparison between B_{en} and B_{fp} for samples deposited by STFC Daresbury laboratory. The comparison for the samples deposited at the University of Siegen and INFN are shown in Figs. 5.10 and 5.11 respectively. The $B_{fp}(4.2\,K)$ was determined by using the linear relation for $B_{fp}(T^2)$.

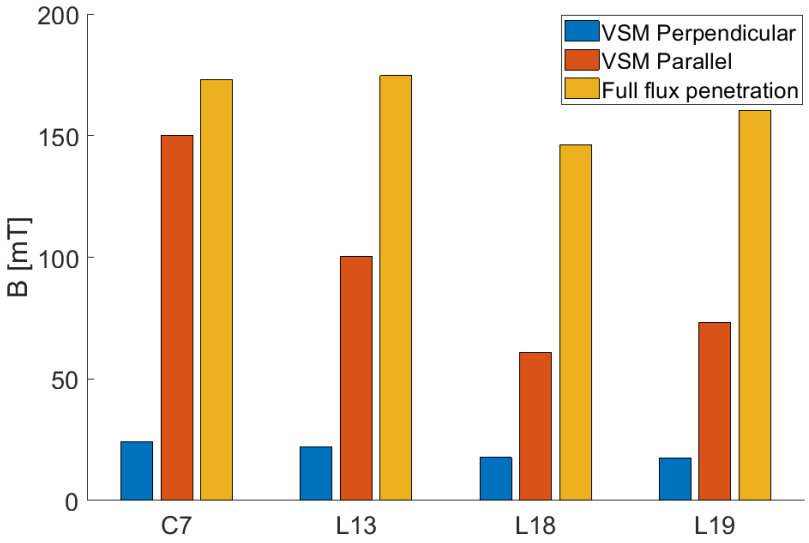

Figure 5.9: A comparison between B_{en} in the VSM at IEE and B_{fp} in the MFPF at Daresbury laboratory, performed at 4.2 K for Samples deposited at STFC Daresbury Laboratory.

It can be seen that B_{en} with a parallel B_{app} is similar to B_{fp} for sample C7. The B_{fp} varies ≈30 mT across the films deposited by STFC, where as B_{en} parallel varies from 61-150 mT. It is more observable for films deposited at Siegen and INFN in Figs. 5.10 and 5.11, B_{en} in the parallel orientation becomes somewhat comparable to B_{en} in the perpendicular orientation, whilst B_{fp} is similar for the films for each institution. This

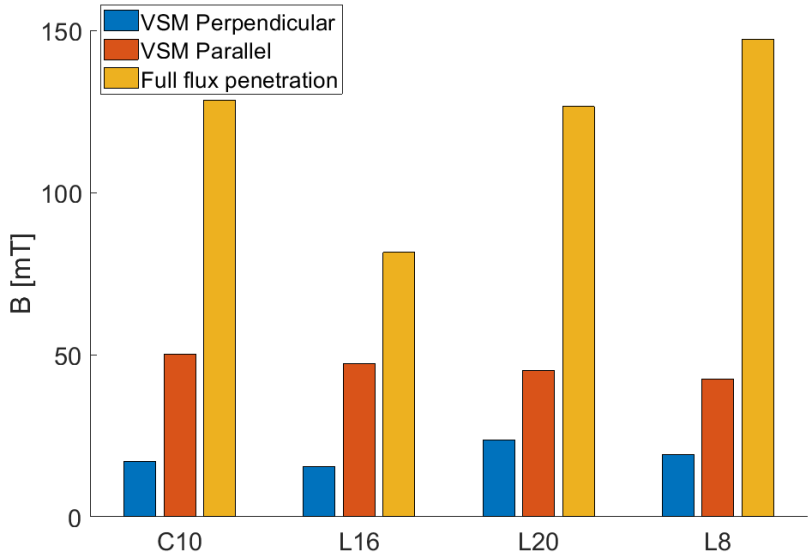

Figure 5.10: A comparison between B_{en} in the VSM at IEE and B_{fp} in the MFPF at Daresbury laboratory, performed at 4.2 K for samples deposited at INFN LNL.

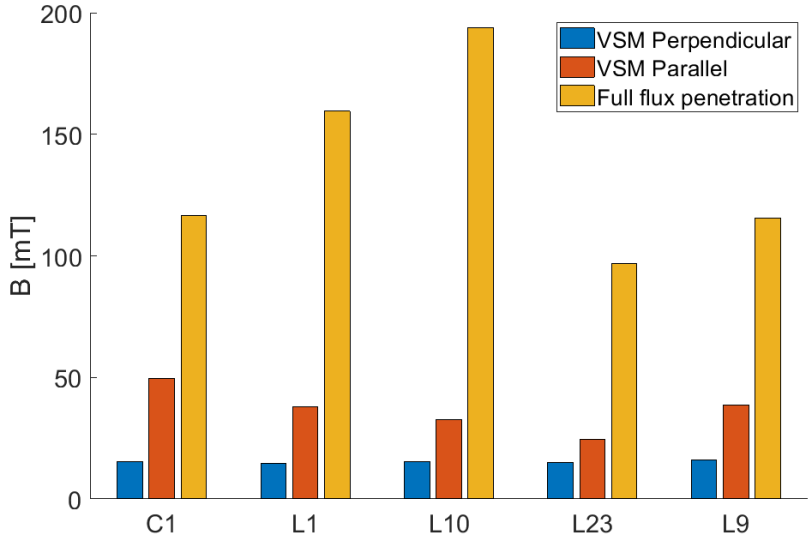

Figure 5.11: A comparison between B_{en} in the VSM at IEE and B_{fp} in the MFPF at Daresbury laboratory, performed at 4.2 K for samples deposited at the University of Siegen.

indicates that during the tests in the VSM the films were not perfectly aligned with the B in the parallel direction, in some cases more than others. Thus, a normal component of B was applied to the film surface that generated unknown flux enhancements which

could not be accounted for, producing a B_{en} lower than expected. These results were important, as the difference in the orientation of the sample in an B_{ext} shows that the orientation of the sample can drastically vary results. Finally, both the VSM and the MFPF did not measure the same part of the deposited film as the sample for the VSM was a cut out of the original sample, and hence the inhomogeneity of the film could have caused discrepancy in the results.

5.1.5 The effect of post deposition laser treatment on Nb thick films

The previous section concludes that the effect of polishing has an affect on the SC properties of micrometer thick Nb films, due to the films replicating the structure of the substrate. This is not ideal for large structures such as cavities, that then exhibit poor performance due to the time and cost to fabricate a full size or multi-cell cavity. However, it is possible that the SC performance can be regained post deposition, by altering the structure of the superconductor using post deposition laser treatment. The laser generates heat which is deposited into the SC film, rapidly annealing localised areas of the sample, which recrystallise into a desired structure upon cooling, whilst also significantly reducing the surface roughness of the film [87]. Thus, improving the SC properties of the film.

This technique has been performed on bulk Nb [85], [86], and micrometer thick Nb films [87]–[89]. Additionally, DC magnetometry tests on cut outs from the samples in the previous section had been performed on laser treated samples [90], [91]. The aim of this study was to determine if the SC properties of the Nb films could be recovered, or further improved using post deposition laser treatment.

5.1.5.1 Sample preparation

After the initial measurements were performed on the thin films deposited on polished Cu substrates (previous section), there was a possibility that the performance of the films could be improved by using laser treatment. The samples were sent to Riga technical university (RTU) where the films were irradiated using a Nd:YAG laser in an Ar atmosphere, with the parameters shown in Table 5.7.

It has been calculated in Ref. [87] that the parameters shown in Table 5.7 that the heat diffusion length is 0.38 µm within the Nb. However, during the annealing process the Nb thickness becomes non-uniform as film melts and re-crystallises. Thus, where the film is thin, the substrate can melt, known as subsurface heating [87].

All samples except the 'L19' sample (Cu substrate chemically polished by SUBU at INFN, Nb film deposited at STFC) did not undergo laser treatment due to the sample being cut down for the effect of geometry experiment in Section 4.9.2, and

Parameter	**Value**
Wavelength, λ	1.064 µm
Pulse duration, τ	6 ns
Intensity, I_v	70 MW cm^{-2}
Step	5 µm
Dose	66 J cm^{-2}
Frequency, ν	10 Hz
Beam diameter	3 mm

Table 5.7: The parameters of Nd:YAG laser used to irradiate the micrometer thick Nb films.

the films deposited at INFN were also not treated due to having already been laser treated. The cross sectional area of the films was not reduced between the effect of polishing results and laser treatment tests. All other measurements performed on these samples (such as surface analysis and VSM) were performed on a 2×2 mm^2 sample cut from the edge of the samples using wire erosion after the samples were tested in the MFPF facility.

The samples deposited at STFC are thicker than the samples deposited at the other two institutes, thus it is expected that B_{fp} will be greater than for thinner samples [139]. Between the effect of polishing tests and the laser treatment tests, the facility had been integrated with LABView and had become automated, which allowed remote operation of the MFPF. Thus a greater point density was used during each measurement which was kept constant to ensure B_{fp} was not missed. The step in T points was also reduced to increase the number of points taken. Thus the testing process of the samples followed the same process as described in Section 4.5.3.

5.1.5.2 Results

MFPF

To compare the results for pre and post laser treatment, it was determined that $B_{fp}(0\,K)$ should be used to compare results as the whole data set is used and therefore reduced the effect of outliers, allowing a more accurate comparison. Again, a linear relation for $B_{fp}(T^2)$ was used to determine $B_{fp}(0\,K)$ and $T_c(0\,mT)$, which are both shown in Table 5.8.

There was a small change in $B_{fp}(0\,K)$ for the samples deposited at STFC, with L13 having the largest change with a decrease in $B_{fp}(0\,K)$ by 6 %. Only sample L18 produced an increased $B_{fp}(0\,K)$ by 4.4 %, however this sample also had the lowest $B_{fp}(0\,K)$ as deposited. Prior to laser treatment the $B_{fp}(0\,K)$ ranged between 189.9-224.2 mT, which was reduced to 198.2-221.0 mT after laser treatment. This

Table 5.8: The $B_{fp}(0\,K)$ and T_c found by extrapolating $B_{fp}(T^2)$ using a linear dependence.

	Pre-Laser Treatment		**Post-Laser Treatment**		**Change due to laser treatment**	
	$B_{fp}(0\,K)$ [mT]	**T_c** [K]	**$B_{fp}(0\,K)$** [mT]	**T_c** [K]	**Δ $B_{fp}(0\,K)$** [mT]	**Δ $B_{fp}(0\,K)$** [%]
C7	224.2 ± 0.8	8.78 ± 0.22	221.0 ± 1.9	9.27 ± 0.42	-3.2	-1.4
L13	217.9 ± 1.0	9.43 ± 0.24	205.3 ± 2.3	9.11 ± 0.52	-12.6	-5.8
L18	189.9 ± 1.8	9.09 ± 0.51	198.2 ± 1.3	9.5 ± 0.29	+8.3	4.4
L19	201.9 ± 2.1	9.27 ± 0.61	-	-	-	-
C1	155.3 ± 2.8	8.43 ± 0.66	152.7 ± 1.8	9.17 ± 0.4	-2.6	-1.7
L1	159.9 ± 0.9	9.63 ± 0.20	150.0 ± 0.8	9.64 ± 0.19	-9.9	-6.2
L9	147.4 ± 0.76	9.06 ± 0.19	119.2 ± 1.7	9.03 ± 0.4	-28.2	-19.1
L10	145.7 ± 2.0	9.19 ± 0.50	123.7 ± 1.6	8.85 ± 0.35	-22.0	-15.1
L23	125.1 ± 1.6	9.19 ± 0.23	121.1 ± 2.0	8.99 ± 0.44	-4.0	-3.2
C10	167.8 ± 1.5	8.67 ± 0.37				
L8	187.9 ± 1.0	9.01 ± 0.25				
L16	109.6 ± 1.24	8.3 ± 0.35				
L20	180.39 ± 1.57	7.68 ± 0.57				

is likely due to the film surface becoming more homogeneous. Similar to pre-laser treatment the EP+SUBU sample (L18) produced the lowest $B_{fp}(0\,K)$ for the samples deposited at STFC that underwent laser treatment, although still produced an increase in B_{fp}, it was not as large as the other films deposited by STFC. The films at STFC did not see a consistent change for all samples, and the change was small for each sample. Thus the change in $B_{fp}(0\,K)$ could be attributed to a different sample area being tested tested before and after laser treatment.

None of the samples produced by the University of Siegen produced an increase in $B_{fp}(0\,K)$. Only 2 of these samples saw a reduction similar to that found in STFC (C1 and L23 had reductions of 2.6 mT and 4.0 mT respectively) which are low enough to consider the change in $B_{fp}(0\,K)$ to be due to testing a different sample area. The film deposited on the substrate polished by Tumbling (L9) produced the greatest deterioration (28.2 mT) for all the samples that were laser treated. Samples L1, L9 and L10 all deteriorated by amounts large enough to not be considered due to a change in sample area, such that the reduction is due to the laser treatment.

Comparing the films within each institute showed that the substrate polishing had no effect post laser deposition. The films deposited at STFC are still in the same order of descending $B_{fp}(0\,K)$ as they were prior to laser treatment, shown in Table 5.9. The range in $B_{fp}(0\,K)$ after laser treatment was reduced.

This is also similar for the films deposited at Siegen. The chemically polished

Table 5.9: The $B_{fp}(0\,K)$ for Nb films in descending order produced by the MFPF for various polishing techniques on Cu substrates for Nb thin films that had undergone laser treatment post deposition.

STFC	**Siegen**	**INFN**
SUBU CERN	SUBU CERN	Tumbling
EP	SUBU INFN	SUBU INFN
	EP	SUBU CERN
	EP + SUBU	
EP + SUBU	Tumbling	EP + SUBU

samples produce similar results, and the small may not be due to the laser treatment. The samples deposited at Siegen also produced a lower $B_{fp}(0\,K)$ values than for the films deposited at INFN that had also been witness to post deposition laser treatment. Both institutes deposited samples with a 3 µm thickness, and the Siegen samples produce a lower $B_{fp}(0\,K)$, indicating that there is still a difference in results due to the deposition institute. Although the samples have a similar thickness, after laser polishing it is clear that the substrate polishing has no effect. This is because the mechanically polished sample from INFN produces the largest $B_{fp}(0\,K)$ after laser treatment, where as the mechanically polished sample from Siegen was the sample with the largest reduction. It can be see that films deposited on chemically polished Cu by both INFN and Siegen were mid table results, i.e. not the best performing and not the worst performing. Once again, substrates polished by EP+SUBU produced the lowest $B_{fp}(0\,K)$ after laser treatment for each institute other than Siegen, where the EP+SUBU and Tumbled samples behave silmilarly.

The results indicate that the effect of substrate treatment has no effect on post deposition laser treatment. All samples saw a decrease by various amounts except 1 produced by STFC, which increased by 4.4 %. This increase cannot be attributed to the laser treatment as a different sample area could have been tested, and the increase is very little. As nearly all samples saw a decrease after laser treatment, it can be concluded that the laser treatment damaged the films. Comparing films with a similar thickness (from INFN and Siegen) do not show correlation in the effect of substrate polishing followed by laser treatment. To fully study this, the samples from INFN should be repeated and tested both before and after laser treatment to determine he effect laser treatment had on the films.

The next theory was that the effect of laser treatment could be dependant on the film thickness. In this case the effect would be similar for the samples deposited at INFN and Siegen, and samples deposited at STFC would also behave differently.

Sputtered Nb films are not perfectly flat. They consist of peaks where there is a greater thickness of Nb, known as hills, and areas where there is a reduction in

the Nb thickness known as a valley. As the heat from the laser is deposited into the Nb, the Nb on the 'hills' melt, and run into the 'valleys', thus reducing the surface roughness of the films [87]. As the SC films replicate the Cu substrate underneath, the when the hills of the Nb flow into the valleys, the thickness of the Nb is reduced at the original site of the hill. Thus, when the laser re-passes over the area of reduced Nb thickness, the heat of the irradiation is deposited into the substrate instead of the Nb. As Cu has a greater thermal conductivity than Nb, the Cu rapidly expands, generating stress on the film. Additionally, the Cu could melt and break through the thin Nb film, which is known as 'the lid effect' [140] or subsurface heating [141].

Thus, laser treatment is related to the sample thickness. A. Medvids et al. calculated using these parameters the heat should not be deposited more than 3 µm [87] into the surface of the sample. Thus, indicating why the lid effect and damage due to the sample is only witnessed in the samples deposited at Siegen, and not those at STFC. As the Nb films melt in the samples from Siegen, the films can become smaller than the heat deposition thickness for the Nb, and thus the Cu melts. On the other hand, the samples deposited at STFC do not show this due to the increased film thickness, as when the Nb has melted, the film still has a greater thickness than the heat deposition distance.

VSM

Similar to the investigation on polishing the Cu substrates, small samples were cut from the edges of the samples to undergo further analysis in both the VSM at IEE and also SEM to investigate the surface quality of the films. Post laser treatment the samples were only tested with the sample orientated parallel to B, with the method of testing was the same as the previous section. The raw data produced by IEE is shown in Fig. 5.12, and the perfect diamagnetic line is shown for samples C1, C7 and L13. Where the raw data deviates from the perfect Meissner state by 2 % shows the point at which B_{en} is taken. Thus, Fig. 5.12 shows that B_{en} is not always the rapid change of the magnetic moment, where it is expected that B has entered the sample.

It is also shown in Fig. 5.12 that for some samples (E.g. L13 and L18 for STFC and C1 and L9) that the B_{fp} is close to the 'obvious' entry into the samples in the VSM (not B_{en}). This could indicate that the samples are of low quality, and therefore have a reduced B_{c1}. This is not the case for all samples. As seen in the previous section, this could be due to the orientation of the samples within the VSM.

The magnetic moment varies for each sample due to the amount of SC material present in the sample. The 10 µm samples from STFC produce the greatest moment due to having the most material. The small variation of m can be explained by the samples not all being cut to the exact same size.

A summary of the results produced by the VSM post laser treatment are shown

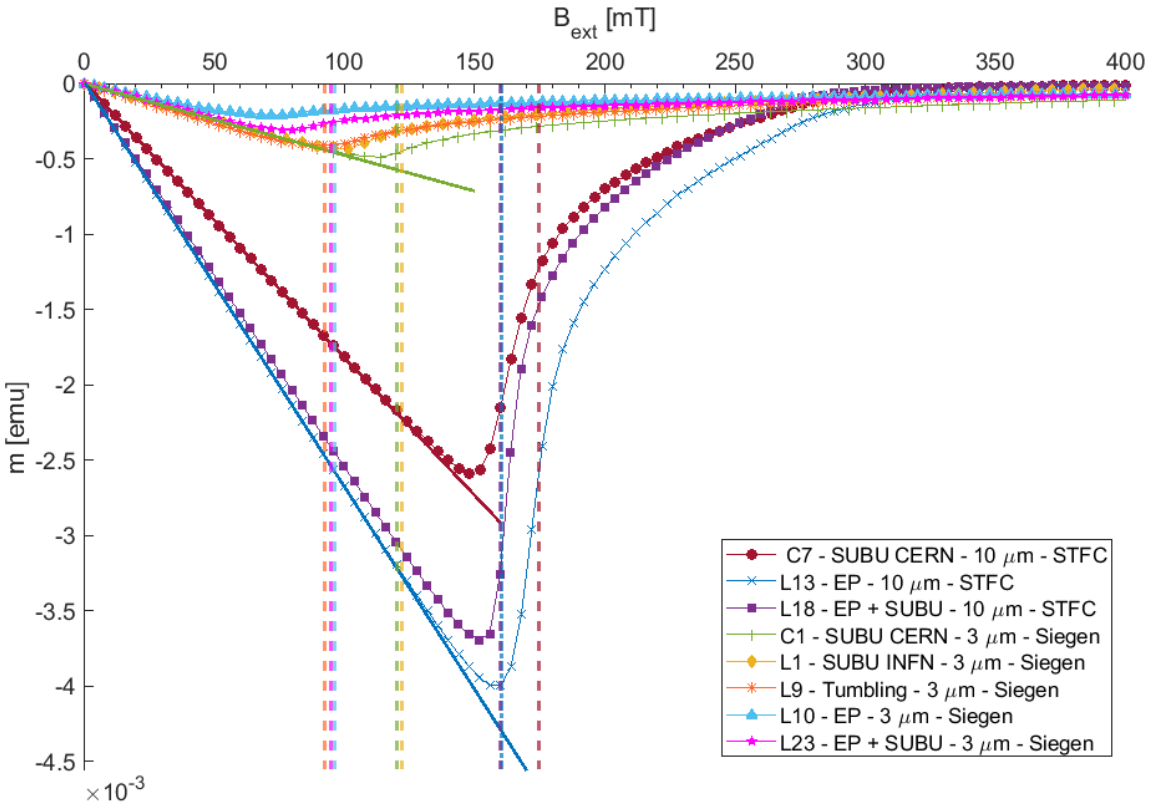

Figure 5.12: The initial magnetisation curve produced by the VSM at IEE for the laser treated Nb films, all performed at 4.2 K. The Meissner state line is shown for samples C1, C7 and L13. The vertical lines show the B_{fp} for the corresponding samples at 4.2 K.

in Table 5.10. The results for pre-laser treatment have already been presented in [6], [81], [82] and also the previous section, and are presented again to allow a comparison post laser treatment.

Table 5.10 shows that the VSM measured an increase in B_{en} for all but one film; C7, the Nb film deposited at STFC on a chemically polished Cu substrate. The largest increase in B_{en} was shown by L18, such that both L18 and L13 produce very similar B_{en} post laser treatment.

All the samples deposited at Siegen that also underwent laser treatment saw an increase in B_{en}. Sample L1 produced the largest increase in B_{en}=45 mT in the sample set, and both chemically polished samples (C1 and L1) post laser treatment produced a B_{en}=83.0 mT with the films orientated with the SC face parallel to B. Although the samples deposited at Siegen see an increase in B_{en}, the B_{en} is still lower than the samples deposited at STFC post deposition.

Table 5.10: The $B_{en}(4.2\,K)$ and $T_c(5\,mT)$ for micrometer thick Nb films on Cu substrates with varying polishing methods, followed by post deposition laser treatment on the Nb surface.

	Pre-Laser Treatment			**Post-Laser Treatment**			**Δ due to laser treatment**		
	$B_{en,perp}$ [mT]	**$B_{en,para}$ [mT]**	**$_c$ [K]**	**$B_{en,perp}$ [mT]**	**$B_{en,para}$ [mT]**	**T_c [K]**	**$B_{en,perp}$ [mT]**	**$B_{en,para}$ [mT]**	**ΔB_{en}** [%]
C7	24.1	150.1	9.35	-	139.0	9.23	-	-11.1	-7.4
L13	22.0	100.3	9.35	-	144.0	9.24	-	+43.7	43.6
L18	17.7	61.0	9.30	-	143.0	9.22	-	+82.0	134.4
L19	17.3	73.2	9.20	-	-	-	-	-	-
C1	15.5	49.6	9.50	-	83.0	9.28	-	+33.4	67.3
L1	14.5	38.0	9.60	-	83.0	9.27	-	+45.0	118.4
L9	16.0	38.6	9.38	-	59.0	9.30	-	+20.4	52.8
L10	15.5	32.7	9.38	-	37.0	9.16	-	+4.3	11.4
L23	15.0	24.5	9.38	-	43.0	9.14	-	+18.5	75.5
C10	12.0	-	9.37	17.0	50.2	-	+5.0		41.7
L8	18.0	-	9.48	19.1	42.5	-	+1.1	-	6.1
L16	14.0	-	9.37	15.5	47.2	-	+1.5	-	10.7
L20	20.0	-	9.58	23.7	45.0	-	+3.7	-	18.5
L21	18.0	-	9.28	18.8	45.2	-	+0.8	-	4.4

The films deposited at INFN were only tested with the SC face perpendicular to B, such that the change in B_{en} due to laser treatment could only be compared for the perpendicular field, and thus cannot be compared to the other institutes. Each film from INFN showed an increase in B_{en} in the B_{perp} configuration. The increase in B_{en} due to laser treatment was much smaller for the samples deposited at both Siegen and STFC, which is due to the samples being tested in a B_{perp}, thus the normal component of B entering the film much earlier.

The T_c was measured both before and after laser treatment, shown in Table 5.10. Laser treatment altered the T_c measurements closer to the theoretical values of T_c for Nb (9.25 K [34]). This could also be due to a change in the method used to measure T_c such as a change in the ramp rate of the T and an increase in the number of measured points.

5.1.5.3 Discussion

Of the original 14 µm thick Nb thin films deposited on polished Cu substrates, 9 films underwent laser treatment at Riga Technical University. The films that were laser treated were the remaining films that were not used for the geometry effect in Section 4.9.2 (L19) or the previously irradiated films deposited at INFN. The samples were tested pre and post laser treatment using the MFPF and a VSM to compare the results. Both techniques were used due to investigating different properties, and the VSM is a highly sensitive machine that helped to characterise the MFPF.

All but one sample produced a decrease in B_{fp} due to the laser treatment. The

small change in $B_{fp}(0\,K)$ in films produced by STFC are likely due a change in the area that was tested, where as the films produced by Siegen saw a large decrease. Thus, the only correlation is that the polishing technique does not have an effect on the post deposition laser treatment. The least performant samples were on Cu polished by EP+SUBU for each institute. It can be concluded that whilst the substrate must be polished to deposit a high quality film, and laser treatment can increase the $B_{fp}(0\,K)$ of the films, the results shown here can not correlate laser treatment to the technique used for polishing the substrate. Further work with a controlled set of samples may be able to bring further insight into these results.

The VSM at IEE tested samples with the SC films with B applied either in the parallel or perpendicular orientation, and observed an increase in B_{en} for all micrometer thick Nb samples due to laser treatment except sample C7 (SUBU polished Cu at CERN). Interestingly, C7 also produced the largest B_{en} in a parallel magnetic field pre-laser treatment. The deterioration in B_{en} could be due to multiple reasons, such as; the sample could have been damaged either due to laser treatment or due to being cut for small sample testing, the sample may have been placed on an angle such that B was no longer parallel to the sample surface inducing a reduced B_{en}. The other two films deposited at STFC saw large increases in B_{en}, of 43.7 mT and 82.0 mT for L13 and L18 respectively.

Unlike the MFPF, all the films deposited at Siegen show an increase in B_{en}. Thus, further investigation was required to determine the cause of the discrepancy. Both films deposited on SUBU polished Cu (L1 and C1) produced different increases in B_{en} due to laser treatment, which in turn led to both samples producing the same value for B_{en}, which was also the largest B_{en} for all the samples deposited at Siegen post laser treatment.

Whilst it is possible that the change in B_{en} could be due to laser treatment, the results also disagree with those produced by the MFPF. This could be due to the technical limitations that VSM's suffer in real world applications such as flux enhancements due to the samples being flat, or due to normal components being present (when the sample was in the B_{para} configuration, as the sample will not be installed perfectly parallel) on the film surface. These limitations could have been produced during the measurements pre-laser treatment (shown clearly in Fig. 5.11), and removed for the tests performed post laser treatment. This cannot be concluded post laser treatment as the samples were only tested in one configuration - B_{en} cannot be compared for both B_{para} and B_{perp} configuration. Additionally, these limitations could have been present on sample C7 post laser treatment, thus producing a reduced B_{en} compared to before the sample was laser treated.

All the samples deposited at INFN LNL all produced an increase in B_{en} in B_{perp}. It is assumed that an increase in B_{en} in B_{perp} would also produce an increase in B_{en} in the B_{para} configuration. The B_{en} values post laser treatment for the samples deposited

at INFN LNL are similar to the values produced by the films deposited at Siegen.

The films were investigated using a SEM after they had been tested in the VSM, to further investigate the effects produced by laser treatment. Images were also taken of both the film surface and along the edge of a small cut out to investigate the structure of the Nb post laser treatment. All SEM measurements were performed by Rastislav Ries at IEE.

The cross sectional images are shown in Fig. 5.13 for L18 deposited at STFC and L1 deposited at Siegen, for both before and after laser treatment. The images do not show any change of the grain structure due to laser treatment. The films deposited at STFC show what looks like a mix between the Nb and Cu at the boundary between the film and substrate in Fig. 5.13a. Post laser deposition shown in Fig. 5.13a shows that the mix between the film and the substrate has increased. This mixed boundary was not present for L1 deposited at Siegen, shown in Fig. 5.13c, and looks as if the Nb film is not in contact with the Cu substrate. The laser treatment did not produce this interface either. Instead, it can be observed that the Cu substrate has entered the Nb film in Fig. 5.13d, which could be interpreted as the lid effect [140].

The parameters of the laser are constant, thus the penetration depth of the laser is also constant. The heat deposited by the laser can vary for different areas of the sample, as the sample thickness' may not be homogeneous and initial surface roughness may also alter the penetration depth of the laser. The films deposited at STFC were 10 µm thick, thus 3 times thicker than the other samples. The heat of the laser could be deposited at the boundary between the Cu and the Nb, melting both, and possibly allowing them to mix, which is what looks to have happened for L18 deposited at STFC. Thus, the heat from the laser is most likely to have been deposited in the Nb film such that localised areas were annealed, thus reducing the surface roughness.

The cross section SEM images for the 3 µm films deposited at Siegen showed that the Cu substrate had melted, and the heat from the laser must have been deposited in the substrate. It could be determined that 3 µm thick samples were too thin for laser deposition using these parameters, such that the Nb was not annealed. As the heat was deposited either in the substrate or at the boundary, the substrate and film could mix, or possibly break through the SC film producing the the lid effect [140].

The surface of the films were probed using the SEM. Figure 5.14 shows that the Nb had been annealed, the cracks/grooves were reduced and large grains were produced.

On the other hand, the SEM observed that the films deposited at Siegen had become damaged during the laser treatment process. Figure 5.15 shows a comparison pre and post laser treatment. It can be seen that post laser treatment samples L1 and L10 produced cracks on the surface which were not present before.

If the heat produced by the laser was deposited in the Cu substrate and not the Nb. The thermal conductivity of Cu is greater than that of Nb, the Cu expanded

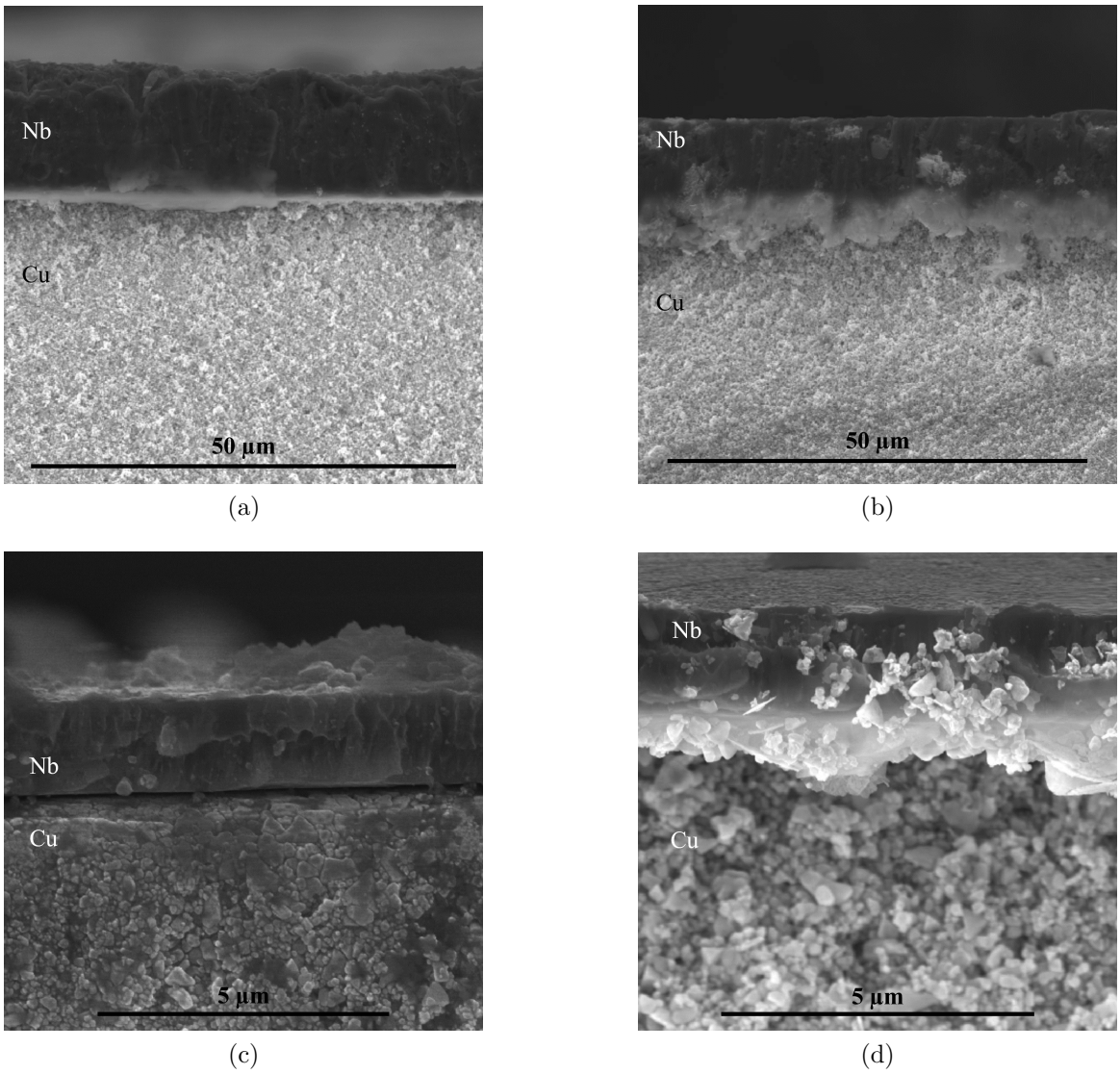

Figure 5.13: Cross sectional images taken by the SEM of samples L18 deposited at Daresbury laboratory (5.13a and 5.13b) and L1 deposited at the university of Siegen (5.13c and 5.13d). Images on the left are pre-laser treatment and images on the right are post laser treatment.

faster than the Nb film, thus generating stress between the film and substrate. The film is much thinner than the substrate, and becomes damaged. Additionally, the lid effect can clearly be seen for sample L10 in Fig. 5.15d, confirming what was observed in the cross sectional image.

It has previously been reported that post deposition laser treatment reduces the

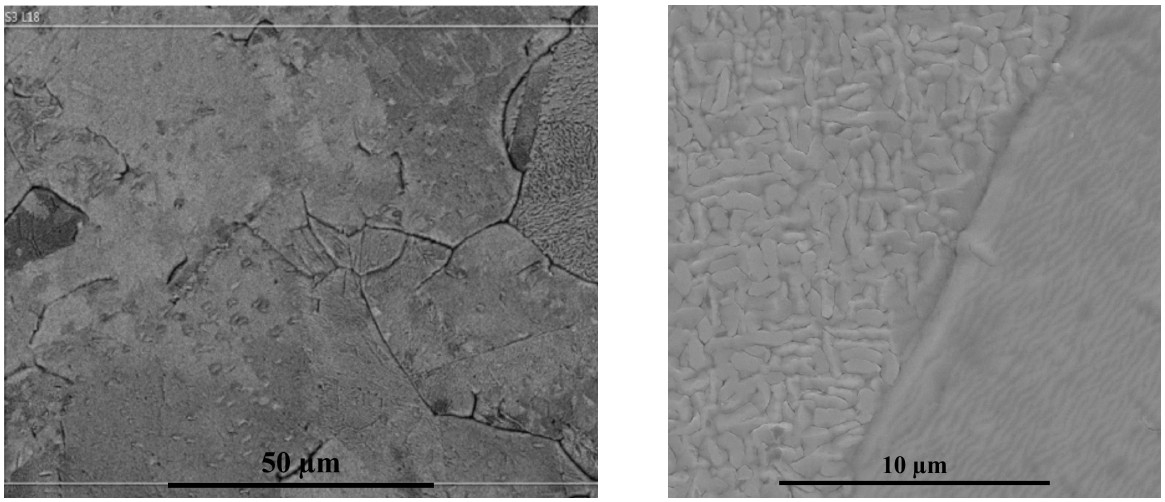

(a) (b)

Figure 5.14: Surface images of sample L18 deposited at STFC Daresbury Laboratory. The polished sample pre-laser treatment is shown in 5.14a, and post laser treatment is shown in 5.14b.

surface roughness of the film [82], with the maximum reduction in R_a from 25 nm down to 13 nm for sample L9. These measurements were performed on small samples cut from the initial $53 \times 53\,mm^2$ sample, hence the R_a is not the same as in Table 5.11. The results shown in Table 5.11 do not agree that laser treatment reduces the R_a of the films, as all the samples deposited at Siegen all show an increase in R_a.

The films deposited at STFC produced lower values for R_a than the films deposited at Siegen, except for C7 (SUBU polished Cu at CERN). Sample C7 produced the largest $B_{fp}(0\,K)$, it was also the film that witnessed a decrease in the VSM. The same sample used in the VSM was the same sample used to characterise R_a, thus it is possible that the low R_a produced the reduction in B_{en}, where as the MFPF measured a B_{fp} at a different area of the sample which could have had a different local R_a than the small sample. No correlation between B_{fp} and R_a could be made.

The surface characterisation produced an insight into the quality and structure of the micrometer thick Nb films. It is unlikely that the films were homogeneous, such that the area investigated by both the MFPF and the VSM/surface characterisation techniques are not the same. Additionally, the small samples could have become damaged during the cutting process to remove them from the original sample, thus changing the surface properties.

The 10 µm films deposited at STFC produced a small decrease in B_{fp} in the MFPF for all but one sample, that had a small increase. These cannot be claimed to be

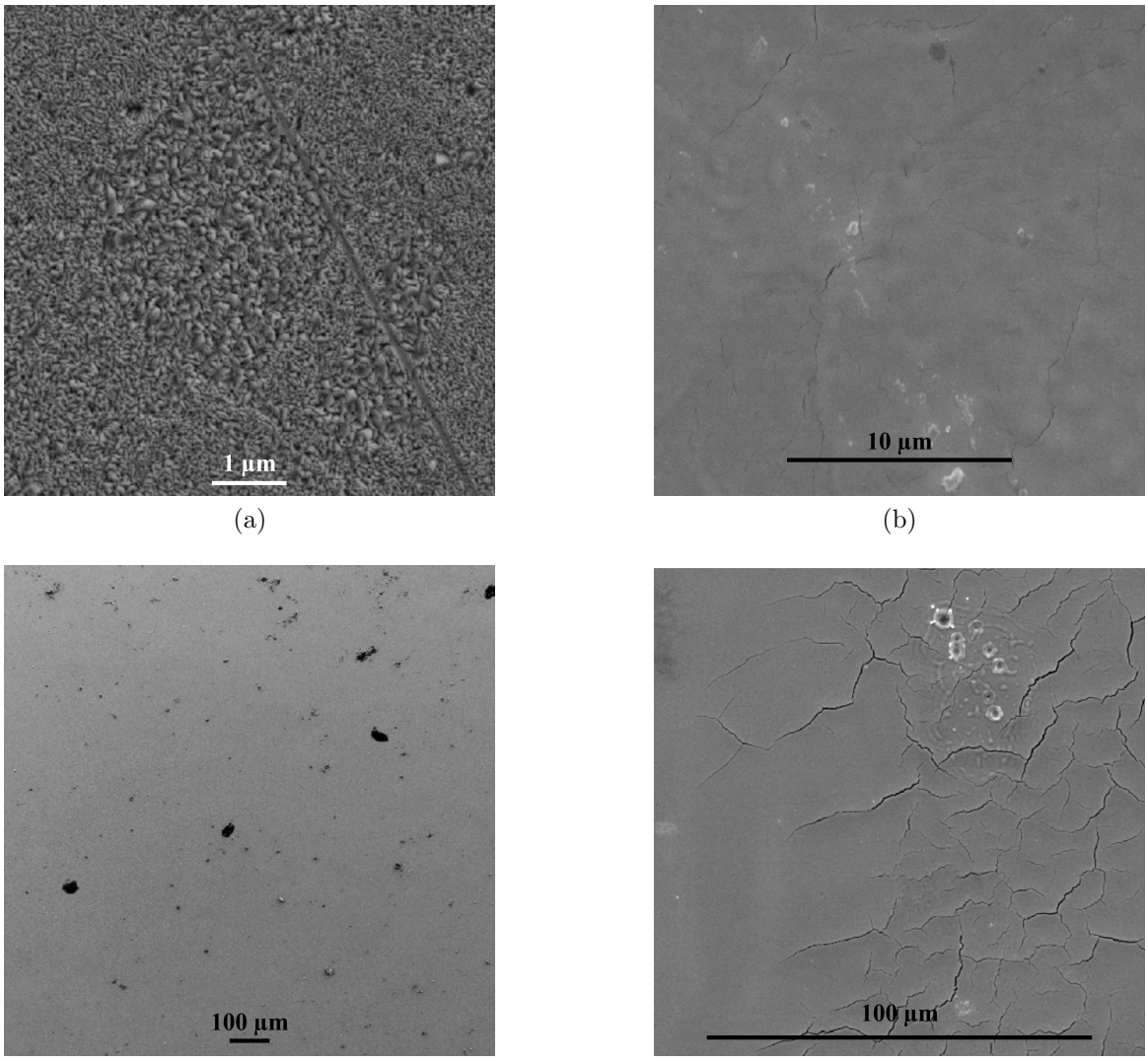

(a) (b)

(c) (d)

Figure 5.15: Surface images of samples L1 (5.15a and 5.15b) and L10 (5.15c and 5.15d) deposited at the University of Siegen. The polished samples pre-laser treatment are shown on the left, and post laser treatment are shown on the right.

directly caused by the laser treatment. However, all the 3 µm thick samples show a decrease in B_{fp}. One conclusion is that the effect of thickness is the main cause for the change in B_{fp}. To determine if the change in B_{fp} due to laser treatment is dependant on thickness, further studies should be performed where all samples are deposited by the same institute on substrates prepared by the same method, with the only the thickness varying between samples.

Table 5.11: The R_a(4.2 K) for each sample before and after laser treatment. The reported R_a is an average of three measurements across the film. Prior to laser treatment the measurements were performed at the deposition institute and are previously reported in [81], [82], where the measurements post laser treatment were performed at IEE by R. Ries.

Sample	**R_a Pre LT** [nm]	**R_a Post LT** [nm]
C7	-	38
L13	-	22.3
L18	-	19.3
L19	-	-
C1	21	36.4
L1	6.3	25.9
L9	18.3	40.4
L10	11.5	47.1
L23	14.2	32.9
C10	126.0	-
L8	207.0	-
L16	192.0	-
L20	197	-
L21	233.0	-

5.2 Alternative high T_c materials

One method to increase E_{acc} is to use superconductors with a T_c higher than that of Nb. The materials need to have a low resistivity in the NC state to minimise RF losses, a low κ_{GL} and a high T_c [39]. One material of interest is Nb_3Sn, which has a T_c of 18 K [35], that allows it to have a greater Q_0 at a wider T range compared to Nb [142]. Thus, less power is dissipated in the cavity walls such that accelerating cavities become more efficient. By increasing the operating T of the cavities the cryogenic losses can be reduced, as the refrigerator efficiency is increased from ≈20-30 % when T is increased from 2-4.2 K [143]. The increase in operating T has also allowed the possibility of using cryo-coolers to cool accelerating cavities [144], [145] as a low cost option to cool the systems.

The $B_{rf,crit}$ is limited by B_{sh}. Although Nb_3Sn has a B_{c1} lower than that of Nb (38 mT [35]), B_{sh} is much larger than that of Nb (440 mT compared to 240 mT), thus theoretically the E_{acc} can be increased from 57.1 MV m^{-1} (for Nb) to 104.8 MV m^{-1} (using Eqn. 2.40).

Both of these factors have produced an interest in alternative materials other than Nb for SRF applications. However, these materials also come with limitations. The

materials consist of multiple elements, and thus the stoichiometry of the samples must be correct to ensure the correct phase of the film is grown. If the correct phase is not grown, the superconductor will not perform as expected. Thus, it is beneficial to determine the correct deposition parameters by depositing small samples and investigating the properties before full size cavities are deposited.

It was of interest to test high T_c SC's that are strong Type II to investigate the behaviour in the MFPF. Initially, the aim was to determine if strong Type II SC's could be measured. Typically, high T_c SC's have a low B_{c1} that could be difficult to measure with the MFPF. It would be expected that the transition is different compared to Type I SC's, and more similar to that of Nb. As Nb is a weak Type II, it was also expected that strong Type II superconductors would have a different response, such as a more gradual transition in $B_2(B_1)$. Thus, it could be possible that the combination of a low B_{fp} and gradual transition could make determining B_{fp} difficult. Thus, the method to determine B_{fp} would have to be reviewed, depending on the response of the samples.

5.2.1 Micrometer thick Nb_3Sn

One limitation of Nb_3Sn is that many phases of Nb_3Sn exist, whilst the phase producing the highest T_c phase only occurring at $\approx$25 % atomic Sn content [35]. One deposition method which has been highly successful is physical vapor diffusion (PVD) [146]–[148] which allows to accurately control the phases of the Nb_3Sn, such that this PVD is used by several labs to investigate Nb_3Sn [5], [142], [149]. Depositing uniform, consistent stoichiometric Nb_3Sn films is still challenging due to the multiple phases. Thus, small sample deposition can be utilised to determine the optimal growth parameters before full size cavities are deposited.

Samples were deposited at STFC Daresbury laboratory before the facility was built, and have been previously reported in [5]. As the MFPF was not available at the time, such that the deposition parameters were not optimized between tests, thus no improvement in the superconducting properties was expected between samples.

5.2.1.1 Sample preparation

Multiple samples were deposited at STFC Daresbury laboratory using DC magnetron sputtering at 650 °C using a stoichiometric target. The samples were deposited for 3 hours, which produced a sample thickness' of 2.4 µm. The three samples that are presented here differ by one sample (Nb_3Sn (3)) having a voltage kick during deposition, and the substrates having different polishing treatments, summarised in Table 5.12.

Table 5.12: A summary of the Nb_3Sn samples.

Sample name	**Substrate treatment**	**Voltage kick** [V]
Nb_3Sn (1)	EP	0
Nb_3Sn (2)	Diamond turned	0
Nb_3Sn (3)	SUBU	80

5.2.1.2 Method

The samples were tested using the same method as described in Section 4.5.3. After each test the sample was heated to 20 K to remove any trapped flux that was present within the sample, as this is greater than the theoretical T_c of Nb_3Sn (18 K [35]). The tests were performed up to 16 K to investigate the samples at a wide range of temperatures. The $B_{c1}(0\,K)$ for Nb_3Sn is low compared to Nb (38 mT [93]), but has an large theoretical $B_c(0\,K) \approx 520\,mT$ [93]. Finally, the samples were deposited at the beginning of 2019, however were tested in the MFPF late 2021. The length of exposure in atmosphere could possibly affect the surface of the film, and therefore produce different results compared to shortly after deposition, and small samples had been cut from the edges such that the film could have been damaged and impurities could have been introduced.

5.2.1.3 Results

The Nb_3Sn did not produce a sharp transition in the raw data, with an example of the raw data for the samples shown in Fig. 5.16. Whilst this could be an artefact of Type II superconductors, some of the micrometer thick Nb reported in Section 5.1.3 showed a sharp transition as did the bought Nb in Section 4.11, thus indicating a clear B_{fp}. On the contrary, Nb is a weak Type II, where as Nb_3Sn is a strong Type II ($\kappa_{GL} \approx 0.8$ and 10.3 respectively), thus it is expected that $B_2(B_1)$ would behave differently. Due to the lack of a sharp transition by a step, these samples were analysed using both the second derivative method and method 3 from Section 4.7.

Although the tests were performed up to 16 K, Fig. 5.16 shows that B_{fp} becomes extremely small at T's ≥ 13 K, and cannot be accurately determined by either method. Simply, the raw data shows that the samples have a low T_c before any analysis was performed. A comparison between Nb_3Sn(1-3) are shown in Fig. 5.17, with the corresponding $B_{fp}(0\,K)$ and $T_c(0\,mT)$ shown in Table 5.13.

The K_2 was found for the 3 Nb_3Sn samples to be between 6.9-7.9 $\times 10^{-3}$ as shown in Table 5.13, which agrees with both the sputtered Nb samples and the Pb foil tested previously, indicating that there was no change in the magnitude of B leaking around the samples to effect the $B_{fp}(T)$ measurement. The small variation is likely due to human error in the placement of the samples under the magnet.

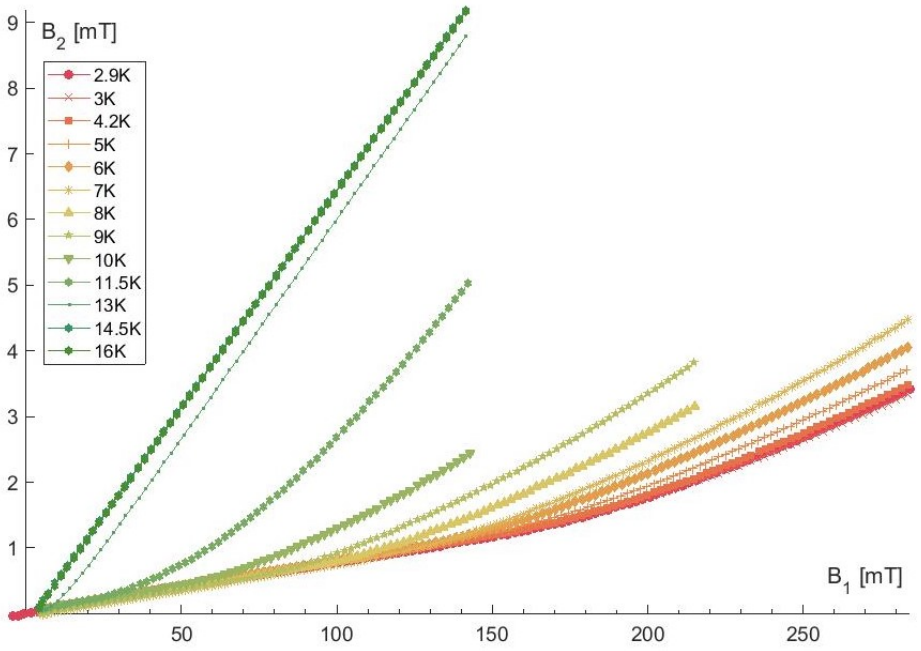

Figure 5.16: The raw data for 2.4 µm of Nb_3Sn on EP treated Cu substrate.

Table 5.13: Using the linear $B_{fp}(T^2)$ fit, both $B_{fp}(0\,K)$ and T_c.

Sample	$\mathbf{K_2}$ **[10^{-3}]**	$\mathbf{B_{fp}}(0\,K)$ [mT]	$\mathbf{T_c}$ [K]	$\mathbf{B_{fp}}(0\,K)$ [mT]	$\mathbf{T_c}$[K]
		Method 3		$\boldsymbol{d^2(B_2)/d(B_1)^2}$	
Nb_3Sn (1)	7.9 ± 0.1	187.3 ± 2.1	12.36 ± 0.10	192.4 ± 1.9	12.40 ± 0.36
Nb_3Sn (2)	6.9 ± 0.1	147.1 ± 2.0	13.96 ± 0.14	150.4 ± 0.7	14.03 ± 0.13
Nb_3Sn (3)	7.7 ± 0.1	61.3 ± 1.9	10.72 ± 0.26	67.8 ± 0.7	10.96 ± 0.18

The samples were analysed using both the standard deviation and second derivative methods, with $B_{fp}(T)$ shown in Figs 5.17a and 5.17b respectively. Although the $B_{fp}(0\,K)$ comes out to be similar values, it is clear in Fig. 5.17 that there is greater scattering using the second derivative method. This is due to the gradual increase in B_2 rather than a sharp increase to indicate the field breaking through. Thus, it is considered that the reported B_{fp} is incorrect as any small change in B_2 could be misreported as B_{fp}. This further reinforces that for gradual transitions method 3 should be used to determine B_{fp}.

5.2.1.4 Discussion

It can be seen that the all three Nb_3Sn samples produce a lower T_c than the theoretical value, with the diamond turned sample producing the largest T_c (14.0 K). The Nb_3Sn

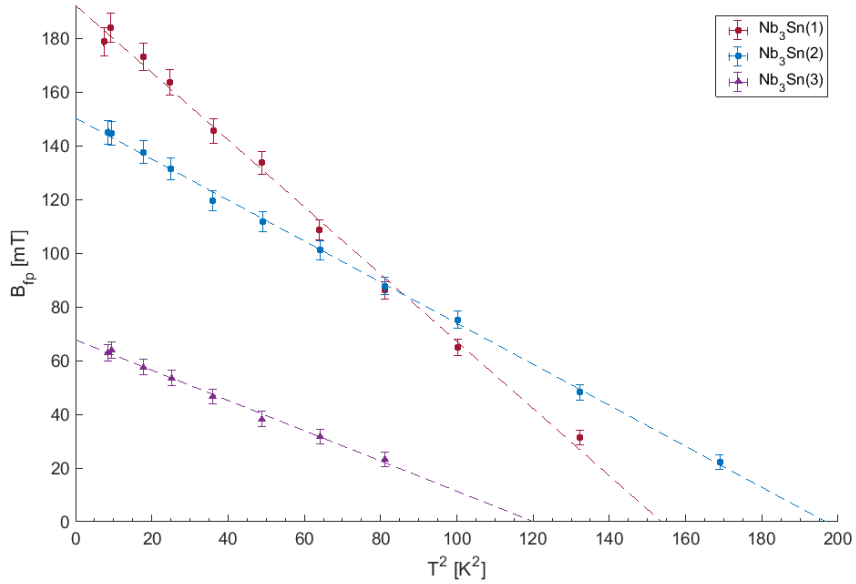

(a)

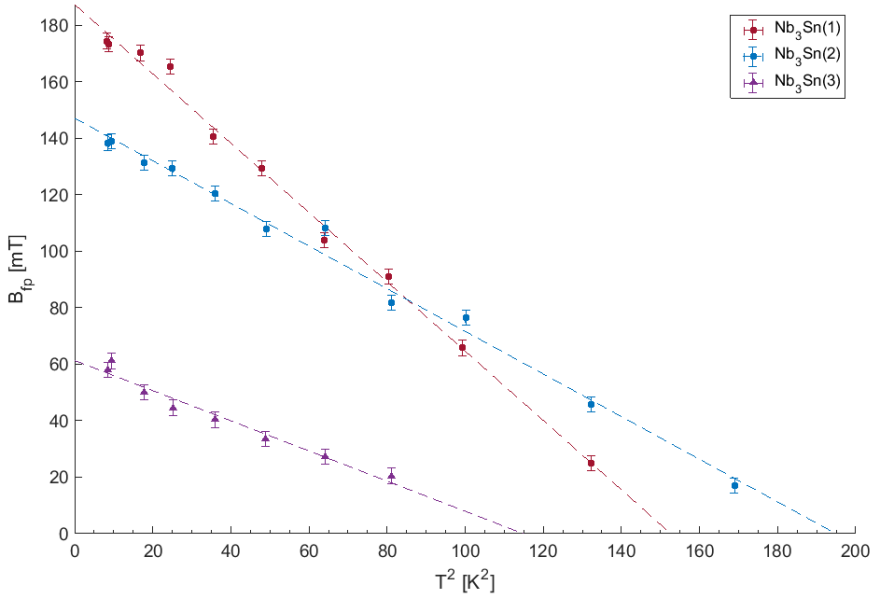

(b)

Figure 5.17: B_{fp} found using method 3 (5.17a) and the second derivative (5.17b) as a function of T^2 for the three 2.4 µm Nb3Sn(1), (2) and (3) (EP, diamond turned and SUBU polished Cu substrate respectively) deposited at Daresbury Laboratory.

(3) produced a T_c 10.7 K, which is much lower than the expected value for Nb_3Sn, but close to that of Nb. As $T \rightarrow T_c$, B_{fp} either becomes difficult to extract or is not visible, but does not persist up to the expected T_c of 18 K.

It has been determined by Godeke [35] and also shown in Ref. [142] that the T_c of Nb_3Sn greatly depends on the atomic Sn content, and T_c rapidly decreases for Nb_3Sn with atomic Sn percentages $< 23\,\%$. Using the graph presented in Ref. [142] it can be estimated from the T_c that Nb_3Sn films (1) and (2) contain between $\approx$ 22-22.5 atomic Sn percent. Similarly, the atomic Sn % is $\approx$ 21.5 for Nb_3Sn (3). Thus, the reported T_c could be close to the true value. To increase the T_c of the samples the Sn content must be increased up to 25 atomic Sn percent.

Another theory for this could be the range in T in which the T_c transition takes place. Whilst many institutes report T_c as the onset of superconductivity, the MFPF can only detect when the superconductor is fully in the Meissner state, such that the value reported by the MFPF is $T_c(0\,\%)$. Thus if the onset T is similar to that of the theoretical T_c, but the transition could take place over multiple K, and the MFPF is reports a different value. This is one explanation to the low extrapolated T_c. Further studies are required to determine if this is the case.

It was observed that the Nb_3Sn (1) sample produced the greatest $B_{fp}(0\,K)$ of the three samples (187.3 mT), which is similar to the values reported for Nb films produced by INFN and Siegen pre-laser treatment, reported in Section 5.1.3. The Nb_3Sn sample was $\approx$37 mT less than what was found for the EP polished Nb at a comparable thickness by Siegen. Similar to the micrometer thick Nb samples from Siegen, the best performing Nb_3Sn film was grown on EP polished Cu. The Nb_3Sn (3) film was deposited on SUBU polished Cu produced a much lower $B_{fp}(0\,K)$ compared to the EP sample than what was observed for the ARIES Nb samples. If the reduction in T_c is due to the low Sn content and not an error in the measurements, the low $B_{fp}(0\,K)$ for Nb_3Sn (3) could be due to a reduction in n_s present at each set T, thus reducing J_c.

The Nb_3Sn (3) was the sample which produced the lowest $B_{fp}(0\,K) = 61.3\,mT$, which is lower than both the Nb_3Sn (1) and (2) films, and also lower than the Nb samples presented in Section 5.1.3. Estimating the B_{fp} as a function of thickness from the sputtered Nb samples from Section 5.1 to 2.4 µm (for the thickness of the Nb_3Sn samples) found the $B_{fp}(2.4\,\mu m)\approx 81\,mT$. This is very similar to the values found for Nb_3Sn (3), and it is likely that the sample is Nb with Sn impurities rather than Nb_3Sn.

Surface characterisation was performed by Hitachi on the cross section of the samples. The charecterisation determined that the the grain structure of Nb_3Sn (3) were not well defined large grains, unlike Nb_3Sn (1) which produced large grains.

The Nb_3Sn (3) sample was one of the first high T_c samples deposited using the HIPIMS method with a V kick. Thus the deposition method had not been optimised, resulting in a poor quality of the film. This could be due to the V kicks producing

damage to the film. This could be one explanation for the reduced T_c, if the V kick reduced the atomic Sn percentage, thus reducing the T_c by a large amount compared to Nb_3Sn (1) and (2).

Measurements on the Nb_3Sn films indicate that strong Type II samples cause a slow, gradual transition in $B_2(B_1)$, which is different behaviour than previously observed for Pb as a Type I and even Nb as a weak Type II. Due to the gradual transition of the $B_2(B_1)$, it was found that the second derivative method was not reliable, and $B_{fp}(T)$ measurements were scattered. This indicates that the analysis technique was not correct, and for gradual transitions the standard deviation method must be used to determine B_{fp}. Measurements on the Nb_3Sn samples were also performed above the T's for previous measurements, and still produced a linear trend in $B_{fp}(T)$, indicating that the MFPF can reliably measure at higher T's. As the $T \rightarrow T_c$, B_{fp} becomes extremely small, and thus a B_{fp} could not be reported above 13 K. This could be an effect of the films having a lower T_c than expected. Or, as the critical fields depend on T, it is a possibility that the MFPF is limited to B_{fp} being greater than a minimum value to ensure B_{fp} can be extracted.

5.3 NbTiN

One alternative to Nb_3Sn is NbTiN, which is a B1 compound with the largest T_c (17.8 K [150]). The material NbN has multiple different phases which are characterised by different T_c [151]. The NbN phase of interest (δ-phase) is extremely sensitive to the N stoichiometry, and also has a high resistivity due to the presence of both metallic and gaseous vacancies which are randomly distributed [150].

Increasing the amount of Ti in NbN changes the structure to NbTiN, which presents many advantages. Titanium is a N getter, thus the greater the Ti composition, the lower the number of vacancies [150] present. Both NbN and NbTiN for a homogeneous mixture when added together, forming a SC NbTiN phase which is stable at T_{room}. The TiN phase has a reduced T_c of 5 K. It has been found that NbTiN with increased N content consistently produced $T_c \approx 16$ K, with a Nb/Ti target stoichiometry of 80/20 weight %, with the largest T_c found by Burton et al. [152] being deposited on AlN substrate. The increased N and Nb content increased the lattice parameters of the NbTiN, which had a good correlation to the induced T_c [152]. Common techniques to deposit NbTiN is to use magnetron sputtering [150], however other techniques are being investigated such as Plasma Enhanced Atomic Layer Deposition (PEALD) [153].

5.3.1 Micrometer thick NbTiN

Before multilayer structures consisting of thin films were deposited, it was beneficial to deposit a µm thick NbTiN film to ensure the parameters were correct before time was taken to produce thin film NbTiN. Although no samples had been tested which could be compared to the single thick layer, it had to be ensured the deposition parameters were correct such that the correct NbTiN phase was grown to help analysis with later results.

5.3.1.1 Sample preparation

A single thick layer NbTiN samples was deposited at STFC Daresbury laboratory using DC magnetron sputtering at 650 °C using a stoichiometric target onto a Cu substrate. This sample was deposited before the multilayers in Section 5.4 were deposited to ensure the NbTiN was SC. The NbTiN sample was deposited for 6 hours which has an estimated thickness of 1.2 µm. It should be noted here that these results were taken towards the end of the PhD such that further surface characterisation had not been performed. Thus, for this sample and the following multilayer results have estimated thickness' taken from the deposition parameters from previous samples.

5.3.1.2 Method

The sample was tested at a range of temperatures using the method shown in Section 4.5.3. The magnet was degaussed after each set T run, and the sample was heated to 30 K after each run to remove any trapped flux. The sample was tested up to 18 K, however this sample did not produce a B_{fp}. The samples were deposited as a comparison for the following multilayer samples in Section 5.4, thus the samples were investigated over a wide T range.

5.3.1.3 Results

An example of the raw data is shown in Fig. 5.18. Similar to the Nb_3Sn sample, the B_{fp} transition is a gradual transition and not a sharp jump.

Due to the smooth transition for B_{fp} and the high level of noise, the second derivative method could not be used to extract a reliable B_{fp}. Once again method 3 was used, discussed in Section 4.7, with an example shown in Fig. 5.19 for T=2.8 K with the standard deviation of B_1K_2 also indicated by the dashed line to determine B_{fp}.

Once again the $B_{fp}(T^2)$ was plotted with an assumed linear dependence, which is shown in Fig. 5.20, which shows some deviation away from the line of best fit. This is likely due to the noise produced during the tests obscuring the results.

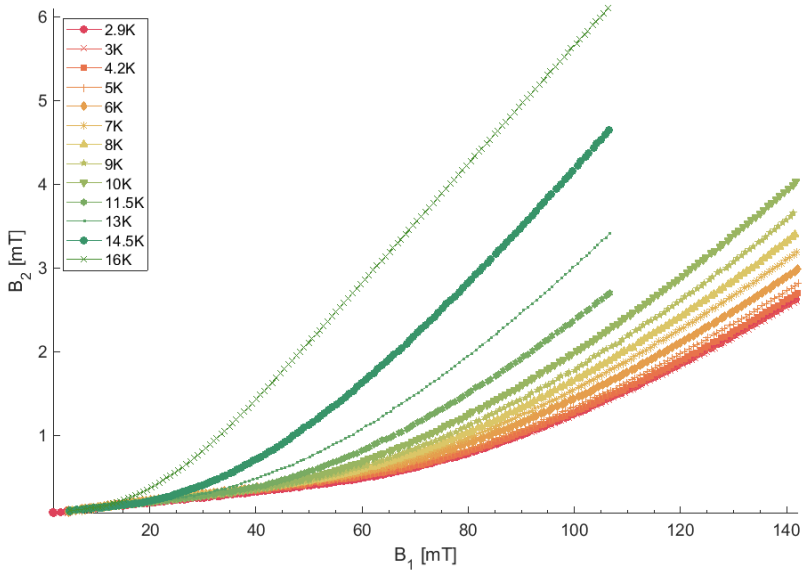

Figure 5.18: The raw data for a 6 hour deposition of NbTiN.

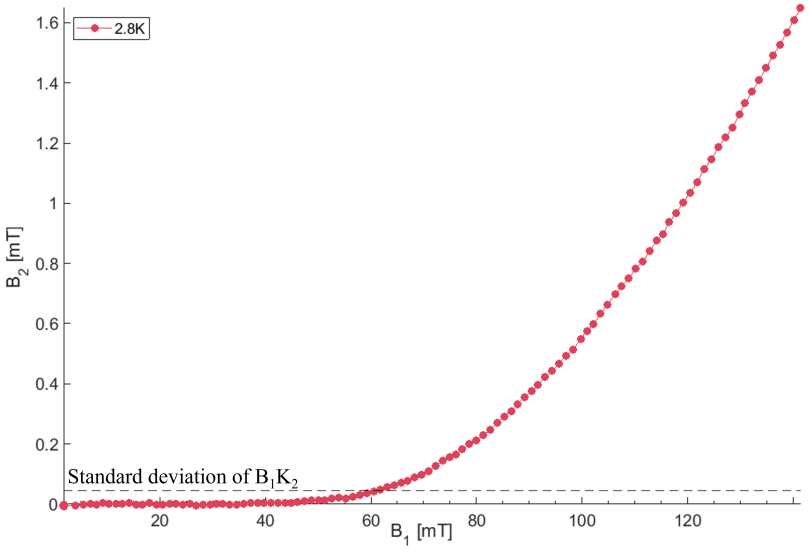

Figure 5.19: The $B_1(B_2)$ of the NbTiN sample at 2.8 K with the B_1K_2 slope removed. The standard deviation of the B_1K_2 slope is indicated by the dashed line.

Once again $B_{fp}(0\,K)$ and $T_c(0\,mT)$ were extracted from the graph and found to be $68.5 \pm 1.2\,mT$ and $18.3 \pm 0.3\,K$.

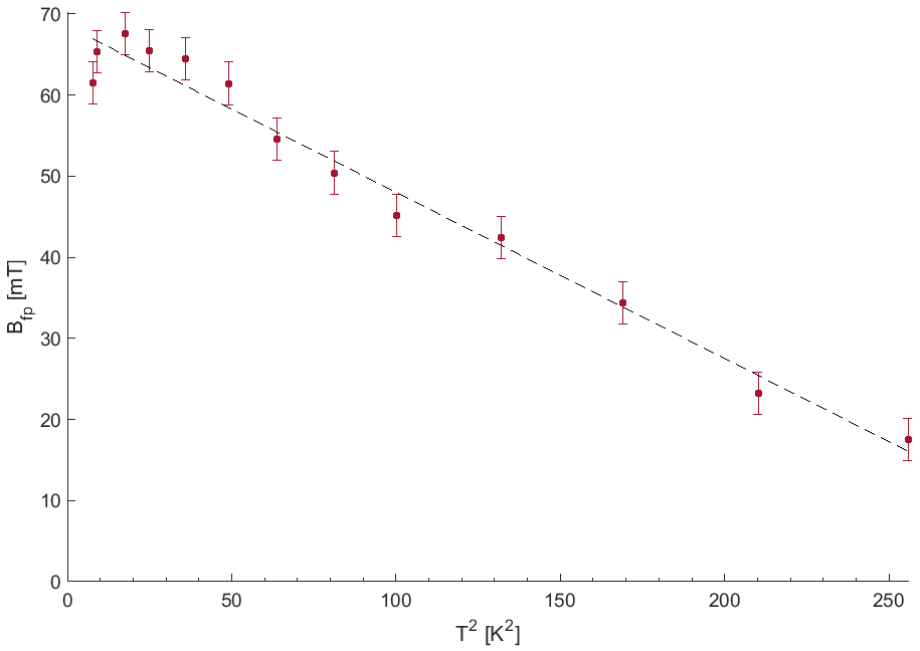

Figure 5.20: The B_{fp} as a function of T^2 for a 6 hour deposition of NbTiN.

5.3.1.4 Discussion

Not many conclusions can be drawn from these results due to no other samples with a similar thickness or material to compare the thick NbTiN sample too. The NbTiN produced a low $B_{fp}(0\,K)$. For Nb samples of a similar estimated thickness, the expected $B_{fp}(0\,K)\approx 56\,mT$, which is lower than what was found for this NbTiN sample. Assuming the sample thickness is 1.2 µm, calculating J_c using the theoretical value for B_{c1} (30 [39]) it was found that $J_c\approx 3.0\times 10^{10}\,A\,m^{-2}$. This is slightly below the depairing current density (J_d) for NbTiN $1.5\times 10^{11}\,A\,m^{-2}$ [154].

The measurements on the NbTiN are similar to the Nb_3Sn in the fact both produce a very gradual transition in $B_2(B_1)$. This confirms that for high T_c SC's, the MFPF should produce a slow transition and not a step increase. It is possible that this is an effect of the samples being deposited, however it is expected that this is a measurement feature for strong Type II SC's. The MFPF was able to measure a B_{fp} for the sample at 16 K, which produced a B_{fp}=17.6 mT. Thus further confirming that if the B_{fp} is large enough to form a reliable B_1K_2 line, it can be extracted. This further indicates that measurements can be performed as high as 16 K. Measurements could not be performed higher than this due to the T_c of the sample and low B_{fp} at this T. However, the extrapolated T_c of the NbTiN is close to the value of accepted T_c of NbTiN (17.8 K [150]).

5.3.2 Thin film NbTiN

Superconducting thin films which have a thickness d $< \lambda_L$ should not produce a B_{fp} in the MFPF, due to the B not reducing the 0 within the sample. Instead, the B will penetrate through the thin film as soon as it is applied, and decay exponentially as it passes through. The induced supercurrents screen the applied B as it passes through the sample whilst producing minimal RF losses within the film. As the film is so thin vortices cannot be thermodynamically stable within the sample. Thus, the thin films can remain in the Meissner state to a much greater applied B, whilst screening the B as it passes through. Thin films are a promising material for SRF applications due to screening the B, and thus can be utilised in multilayer structures to increase E_{acc} by increasing B_{surf} whilst the thick superconductor (under the thin films) is still witness to the same B. To investigate both the capabilities of the MFPF and the properties of sub-London penetration depth films, NbTiN thin film samples were deposited at the Deutsch Electron Synchrotron (DESY) in Hamburg.

5.3.2.1 Sample preparation

The team at DESY were investigating the deposition of NbTiN using PEALD onto AlN, on Si wafer substrates. The method and deposition parameters are described in Ref. [153]. Both samples (NbTiN (1) and (2)) looked very similar, with NbTiN (1) shown in Fig. 5.21.

Both samples consisted of 65 nm of NbTiN on 15 nm of AlN, deposited on 279±25 µm Si wafers. Thus, the total thickness of the samples were < 3 µm, and were extremely fragile. Both samples had a mirror like surface. The samples were deposited onto AlN layers, as AlN has shown to increase T_c for both NbN and NbTiN films which are grown on them [153], [155]. This is due to the AlN 'wurzite-hexagonal' phase having similar lattice parameters to that of NbN and NbTiN [155].

5.3.2.2 Method

The testing process was the same process as described in Section 4.5.3 with 1 K steps between tests. The samples were heated to 15 K in between each temperature test to remove any trapped flux. Whilst the theoretical T_c for NbTiN is 17.3 K [39], it was known before the tests started that these samples had a T_c lower than theoretical and a higher T was not required.

For accuracy, the first test was performed using only the sample (NbTiN (1)) with no spacers present. This lead to the sample forming a crack through the center. The crack was likely produced by stress generated by either the magnet or the S2 plate when the sample was heated/cooled. After the first test, to try and maintain the integrity of the samples, it was decided that a Cu disk (the same ones used for sample

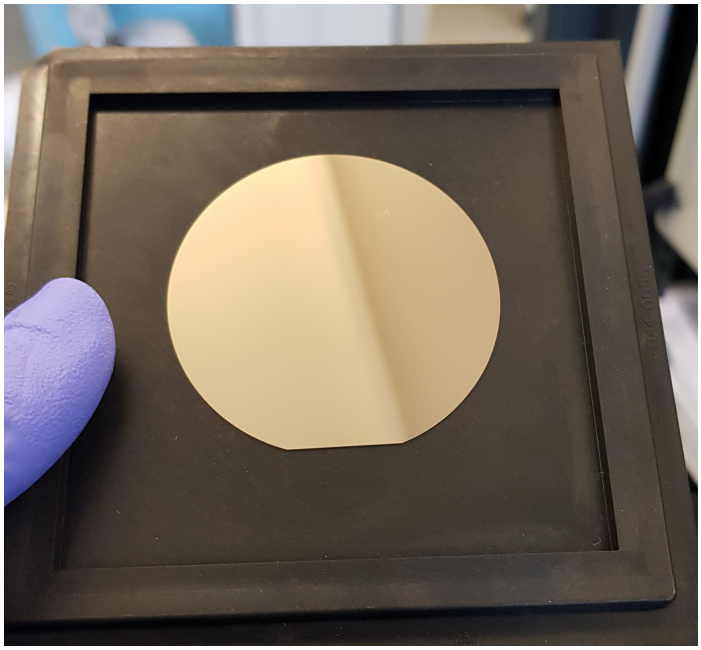

Figure 5.21: NbTiN (1) - NbTiN Thin film deposited on AlN on a silicon wafer.

deposition at STFC Daresbury laboratory) would be placed under the sample to try and reduce the stress on the thin film. The cracked sample was repeated, as it was uncertain when the crack formed or if it had affected the results. However, placing the sample back in the MFPF, the crack expanded, splitting the sample in half, thus only one half of the sample was placed in the facility for testing.

The NbTiN (2) sample was placed in the system the same way. Unfortunately, the sample shattered before the tests began, which was only determined once the system had been opened and the data analysed. Both samples are shown in Fig. 5.22 after they were removed from the MFPF.

5.3.2.3 Results

Due to the films having a d $< \lambda_L$, no B_{fp} was present in the results, as B would not decay to 0 within the sample, with the data for NbTiN (1) shown in Fig. 5.23. Due to the fragility of the samples, the samples could not be squashed onto the plate due to possibly causing damage to the samples. Thus, the thermal contact between the sample and the S2 plate was low, such that the minimum temperature that could be reached was 3 K.

As no B_{fp} was present, a different method was required to analyse the results. It can be assumed that the magnetic field will decay through the thin film with the relation $B = B_0 e^{-d/\lambda_L}$. The equation can be re-arranged for λ_L, $\lambda_L = -d/Ln(B/B_0)$,

Figure 5.22: The NbTiN samples after they had been tested in the MFPF.

where B is the gradient of $B_2(B_1)$ whilst the film is in the superconducting state, and B_0 is the gradient of $B_2(B_1)$ with a normal conductor present/a sample not in the superconducting state. In both cases, the same sample thickness must be kept consistent, as B also falls off with distance.

The London penetration depth was found for NbTiN (1) using the equation stated above and plotted as a function of T, shown in Fig. 5.24. The results shown in Fig. 5.24 do not produce the expected relationship for λ_L for increasing T.

5.3.2.4 Discussion

One main conclusion from this experiment is that the MFPF is not suited to test films with $d < \lambda_L$, as both of the thin films became damaged during testing. This could be mitigated by depositing the films directly onto thick substrates. A thick sample substrate would require to have similar lattice parameters to the thin film, whilst also providing a similar thermal properties to ensure that both the film and the substrate expand/contract at the same rate to mitigate any damage produced on the film.

Due to the thin films having a thickness $d< \lambda_L$ no B_{fp} was present. The results had to be analysed using a different method than those presented in Section 4.7. Hence the

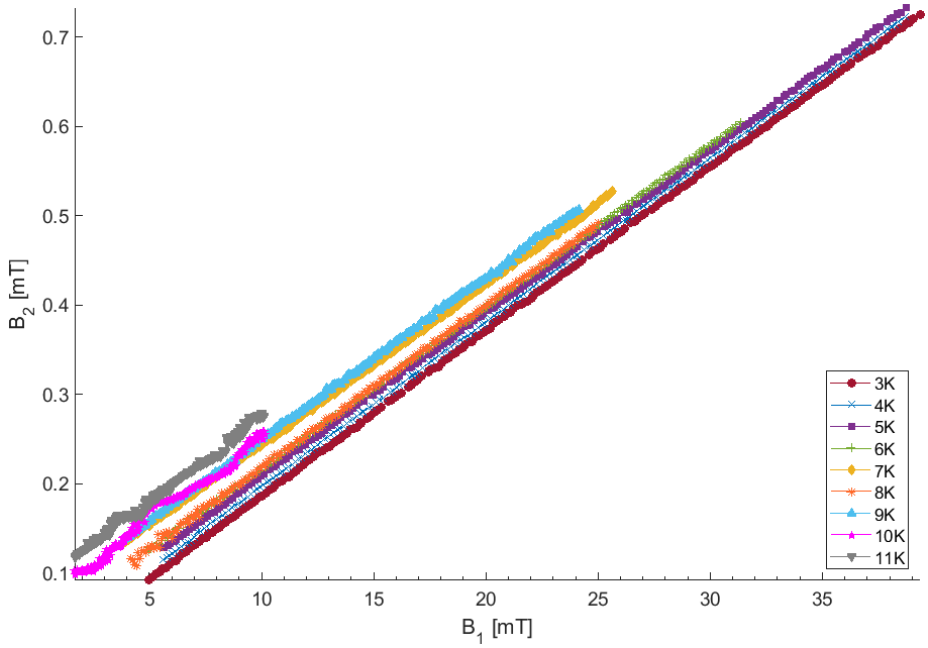

Figure 5.23: The B_2 on the opposing side the NbTiN (1) sample as B_1 was increased.

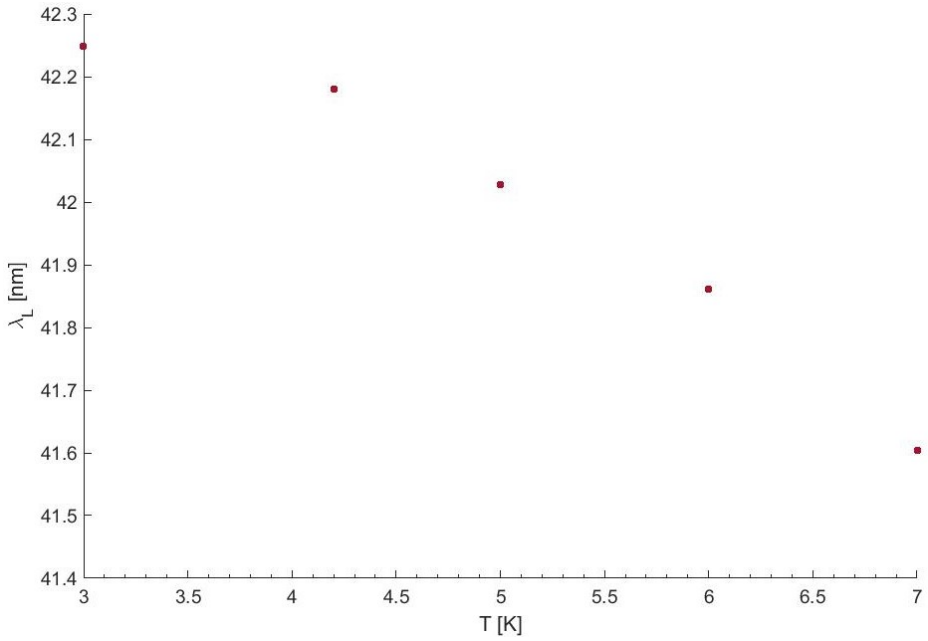

Figure 5.24: The calculated λ_L(T) for NbTiN(1) at a range of T.

gradient of $B_2(B_1)$ for the NbTiN film was compared to only the Cu substrate being

present, which resulted in a reduction in λ_L with increasing temperature. The T at which the results stopped following the trend was 7 K, which is slightly greater than the reported T_c reported by DESY [153]. The final result produced by the MFPF is within the T_c transition shown in Ref. [153].

The minimum T test produced a $\lambda_L \approx 42$ nm, which was much smaller than the expected $\lambda_L(0\,K)$=150-200 nm [39]. Whilst the T's are not the same, λ_L varies very little at low T, and therefore can be compared. However, the relation between λ_L and T does not agree with the relation shown in Eqn. 2.15. There are a number of possibilities that could explain the results:

- The magnet applies a small normal component as B diverges away from the poles. Thus, the normal component penetrates through the sample much easier than a parallel B, thus the field does not decay as expected.
- The film broke in between tests, thus more B 'penetrated' through the sample than expected.
- The reduced sample size produced an increased B_1K_2, such that more B leaked around the sample and not decayed through the film. This could also produce flux enhancements at the sample edges.
- The Hall probe sensors are not sensitive enough to determine extremely small changes in B_2.

The normal component of the magnetic field could be reduced by running further simulations to optimize the magnet poles for a more parallel B. Another possibility is to use a SC substrate. Thus, B would be forced parallel across the thick superconducting surface, hence forming an (almost) parallel B through the thin film on the surface. Thus, the B would be screened through the thin film. Additionally, this option may solve the limitation of damaging thin films, as superconductors have a low thermal conductivity, thus reducing the thermal stresses produced on the film during the change in temperature.

5.4 Multilayer samples

Thin films $d < \lambda_L$ are of great interest to aid thick Nb cavities. The thin films cause the B to decay exponentially through the films, whilst remaining in the Meissner state to much greater fields. Thus B_{surf} can be increased, whilst the thick Nb still witness' the same magnitude of B without thin films on the surface, allowing E_{acc} to be increased. Two kinds of multilayer exist: superconducting-insulating-superconducting (SIS) structures, and superconducting superconducting structures (SS bi-layers), the difference is the presence of a thin dielectric layer separating the superconductors. The dielectric layer is thought to intercept vorticies and localise the dissipation within

the thin film layer [78] where the RF losses are reduced, rather than in the thick superconducting layer, thus reducing the power dissipated in a multilayer cavity. Additionally, more energy is required at the following superconducting boundary to form new vortices, thus further increasing the maximum B_{surf}.

Whilst multilayer structures have been of great interest in the SRF field since they were first proposed in 2006 [16], few methods are suitable to investigate such structures. Planar multilayer samples cannot be reliably tested in a VSM (or similar set up) as B is applied over the whole sample. Thus, B will be applied not only to the face with the thin films, but also the face of the superconductor/substrate boundary, where no screening will take place. Furthermore, B can penetrate through the insulating layers, such that the thin films will not be investigated and the thick superconductor will witness the same B as if the thin films were not present. Finally, it is difficult to align the sample perfectly parallel to the applied B.

One method to investigate multilayers using commercial magnetometry is to use 3D structures with well known demagnetisation factors, which are then fully coated by a thin film. This has been performed by Tan et al. and Junginger et al. using multilayer ellipsoids [17], [18]. These structures require dedicated deposition facilities to be produced, and require different deposition parameters to ensure a quality film is deposited.

To investigate thin films and planar multilayer samples, a magnetometer must apply a local B from one side of a sample to the other to mitigate flux enhancements and ensure B does not penetrate through the insulating layers. The MFPF has already shown to be a powerful tool in investigating planar structures, thus it was decided to also investigate multilayer structures, which was the main aim for this facility.

To ensure the deposition parameters were correct a thick NbTiN sample was deposited and investigated to ensure the correct phase of NbTiN had been grown, which has been reported in 5.3.1. The data will be re-shown again in this section to allow a comparison between the samples.

5.4.1 Sample preparation

Investigations had already been performed on thin film NbTiN shown in Section 5.3.2, which were inconclusive due to damages being produced on the film, and the possibility of a normal component of B being applied to the thin film. It was determined that due to the damage of the thin films not having a thick substrate, the thin films must be deposited onto a thick substrate. Additionally, in the absence of a thick superconductor the B is not forced parallel across the sample surface. It is possible that B would penetrate through the thin film extremely easily, and not decay with an exponential dependence. All the multilayer structures were deposited onto a µm thick Nb film, which had the same deposition parameters and time as the 3.6 µm thick Nb

film previously presented in Section 5.1, which allows a comparison to the samples with thin films present on the surface. All 5 Nb films should have a similar thickness and should behave similar.

All samples were deposited at 650 °C by DC magnetron sputtering using a stoichiometric target. The Nb for each film was deposited under the exact same conditions as those in Section 5.1 onto a Cu substrate, and the NbTiN films were deposited under the same conditions as the sample presented in Section 5.3.1, with the deposition time being the only variation. The thin films were deposited for 1 hour which is estimated to be d ≈ 200 nm, where as the thick NbTiN films were deposited for 6 hours and estimated to be 1.2 µm.

The insulating layer was chosen to be AlN as it increases the T_c of the NbTiN thin film on the surface, has similar lattice parameters to both Nb and NbTiN, and also has a thermal conductivity slightly lower than Cu such that it can be assumed no thermal gradient is present through the SIS structures. The insulating layer was deposited for 3 minutes, and is expected to be on the order of nm's. The final multilayer samples are shown in Fig. 5.25. The 6 hour thick NbTiN sample has previously been shown in Section 5.3.1, but is being shown again as it was part of the multilayer investigation. All samples seem to have a consistent film across the surface except the Nb/AlN/NbTiN/AlN/NbTiN which shows a lighter colour in the centre of the sample. Any lines present on the surface of the samples were introduced by the magnet during testing.

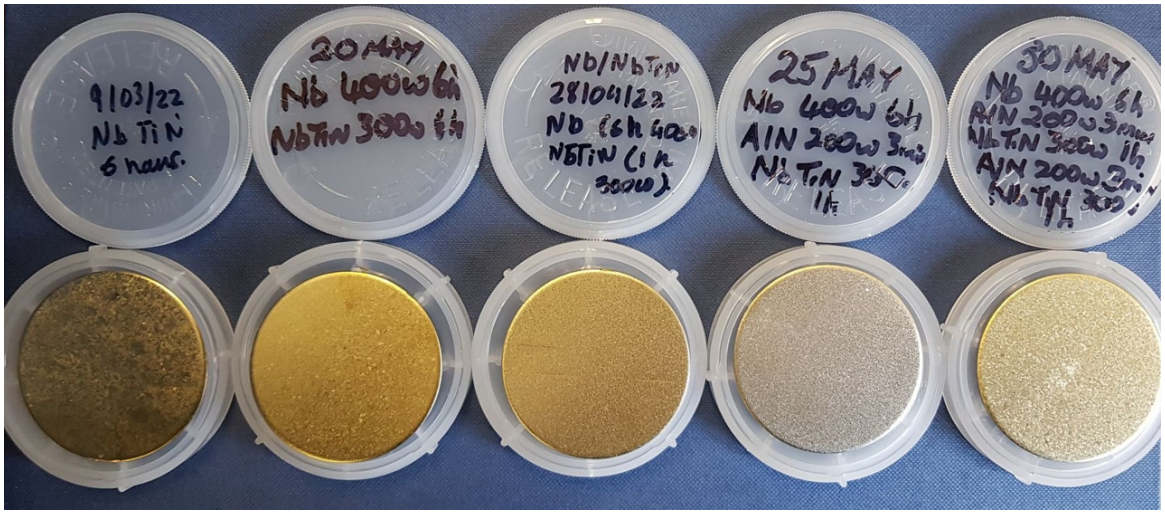

Figure 5.25: The NbTiN multilayer samples deposited to compare to Nb.

5.4.2 Method

All samples were tested using the method as described in Section 4.5.3 using the minimum step in I applied to the magnet. After each set temperature measurement the sample was heated to 25 K to remove any trapped flux that was present within the sample, as this was greater than the T_c of the NbTiN measured in Section 5.3.1, which was also greater than the theoretical T_c of 16-18 K [36], [37].

All the samples were investigated at as wide T range as possible, and was only limited by whether a B_{fp} was produced. Multilayers that consisted of thick NbTiN films were tested up to a T = 18 K, where as the multilayers consisting of thin NbTiN films were tested up to 10 K to ensure the Nb was no longer superconducting. The thin films were not tested at higher $T > T_c$ as the data analysis from section 5.3.2 did not produce meaningful results, and performing these tests would have extended the time of the tests.

5.4.3 Results

A comparison between every sample is shown at 4.2 K in Fig. 5.26. These samples produced a large amount of noise, such that the second derivative method could not be used to extract B_{fp}. It is clear in Fig. 5.26 that the thin films on the surface of the Nb increased B_{fp} significantly for samples that do not include an insulating layer.

After B_{fp}, there is a cross over between the thick and thin film for $B_2(B_1)\approx160$ mT. This indicates that whilst the thin film increased B_{fp}, the larger amount of material present produces a greater screening effect post B_{fp}.

Due to the large amount of noise, method 3 from Section 4.7 was to used to determine B_{fp}, which was then plotted as a function of T^2, shown in Fig. 5.27. Figure 5.27 shows that only 2 samples produced an increase in B_{fp} compared to the single layer 3.6 µm Nb sample, both a thin and a thick film of NbTiN without an insulating layer.

5.4.4 Discussion

As all samples were deposited on Cu substrates of the the same size for these investigations, it can be seen that B_1K_2 was the same for all samples. The additional films significantly alter B_{fp} in the MFPF. Due to the addition of the thin films, the only logical T_c values that can be extracted are for the single layer films which have already been previously presented. The $B_{fp}(0\,K)$ has been found using a linear fit of $B_{fp}(T^2)$, and a fit has been determined for both slopes produced by the thick Nb/NbTiN sample, which are all shown in Table 5.14.

The addition of a thick NbTiN layer produced 2 slopes. The slope at $T^2 > 76\,K^2$ (Nb/NbTiN (b)) is due to the Nb no longer being in the superconducting state, thus

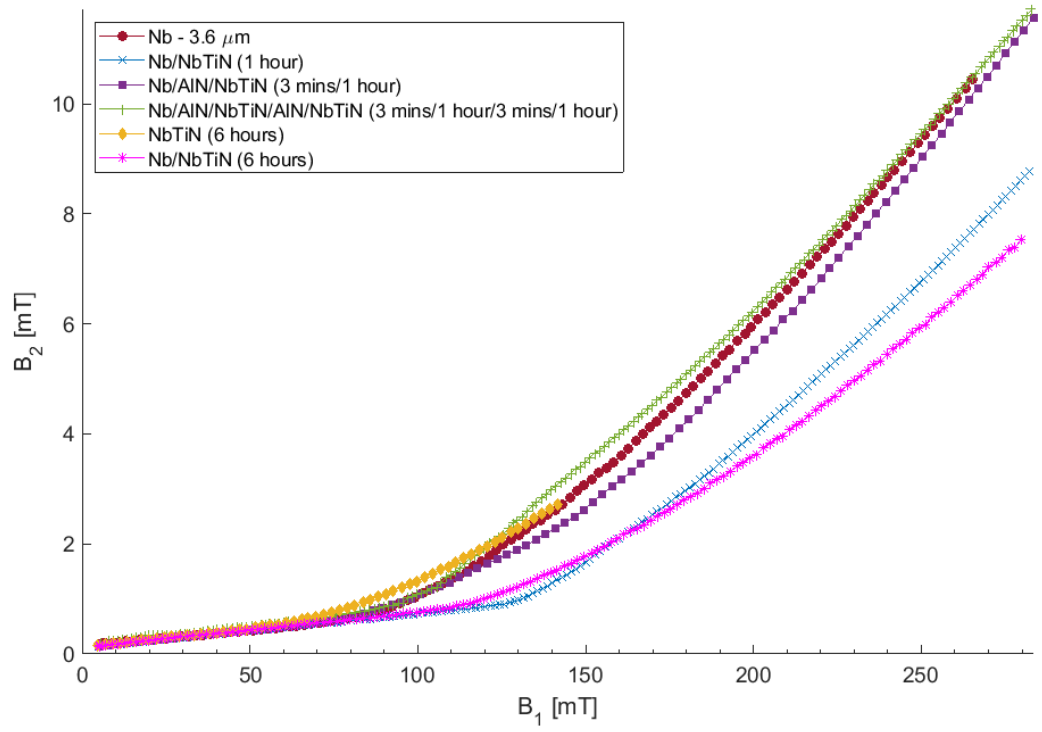

Figure 5.26: The $B_2(B_1)$ at 4.2 K for all the multilayer samples deposited. The deposition times are shown for each layer after the Nb respectively.

Table 5.14: The $B_{fp}(0\,K)$ found using the linear $B_{fp}(T^2)$ fit. The thick NbTiN has 2 values corresponding to both slopes. The results produced by the thick NbTiN on Nb produced 2 slopes depending on the T of the test, which are denoted as (a) for $T^2<76\,K^2$ and (b) for $T^2>76\,K^2$.

Sample	**Film deposition time [minutes]**	**B_{fp} (0 K) [mT]**
Nb (3.6 µm)	-	104.0 ± 0.2
Nb/NbTiN	60	153.6 ± 0.5
Nb/AlN/NbTiN	3/60	91.37 ± 0.92
Nb/AlN/NbTiN/AlN/NbTiN	3/60/3/60	102.6 ± 2.1
NbTiN	360	68.5 ± 1.2
Nb/NbTiN (a)	360	129.0 ± 1.4
Nb/NbTiN (b)	360	83.9 ± 9.0

only the NbTiN is measured. The Nb/NbTiN (b) slope is similar to that of the thick single layer NbTiN film.

At $T^2 > 76\,K^2$ (Nb/NbTiN (a)), the Nb is superconducting such that both superconductors expel B_1. The two slopes are expected due to the increase in SC

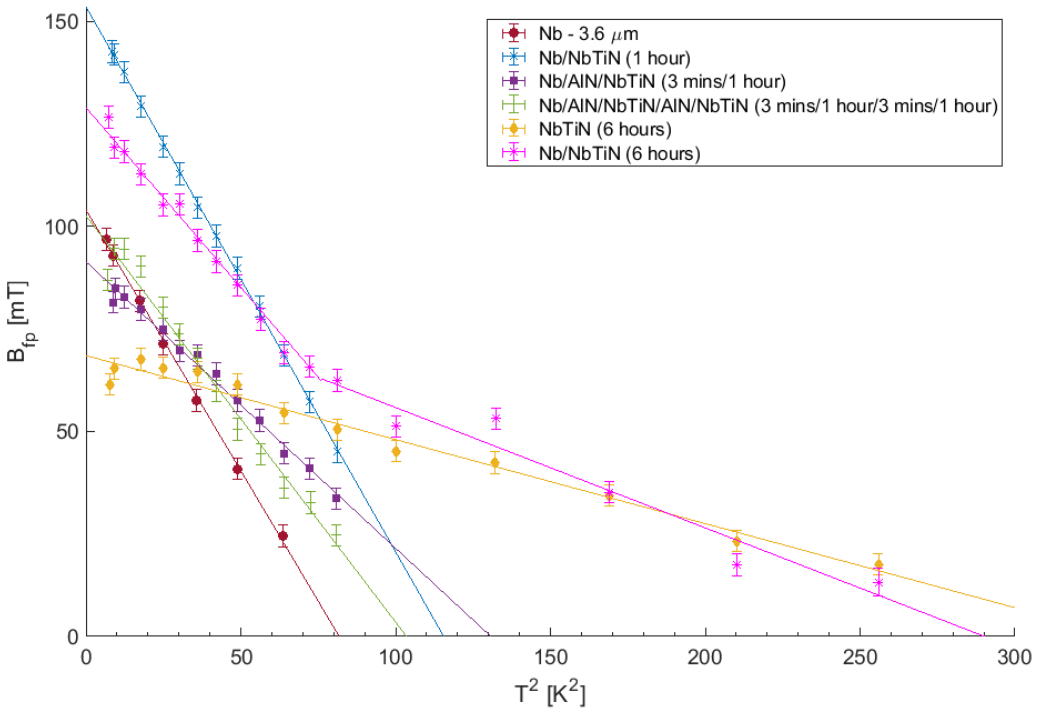

Figure 5.27: The $B_{fp}(T^2)$ for all the multilayer samples. The deposition times are shown for each layer after the Nb respectively.

d. Extrapolating to 0 K shows that the addition of a thick NbTiN film on the surface of the Nb produced an increase of 25 mT in B_{fp}. This increase is less than the sum of both the Nb and the NbTiN films individually, such that both superconductors must also be interacting with each other. Another possibility is that the lack of an insulating layer allowed vortices to avalanche through the structure [78], as NbTiN has a much lower B_{c1} than Nb, thus allowing the vortices to enter at a reduced B_1.

Both the NbTiN thin film (1 hour) and thick film (6 hour) samples produced an increase in B_{fp} at low T compared to the single layer of Nb, with the thin film producing a larger B_{fp} compared to the thick film. However, at $T>T_{c,Nb}$ the thin film did not produce a B_{fp} as the Nb was no longer in the Meissner state, thus B was not reduced to 0 within the film. Moreover, at $T>T_{c,Nb}$ the thick NbTiN film still produced a B_{fp} indicating that the Nb was no longer in the SC state, and that the NbTiN film was thick enough to reduce B to 0. This confirms that the 1 hour NbTiN deposition was a thin film as no B_{fp} was observed unlike what was seen in the thick film. The NbTiN thin film (1 hour) produced a 49.6 mT increase in B_{fp} compared to the Nb sample, which is a 47.7 % increase.

Figure 5.27 shows that the Nb/AlN/NbTiN/AlN/NbTiN sample did not show an increase in $B_{fp}(0\,K)$ when compared to the single layer of Nb, however did produce an

increase at higher T's. Similarly, the Nb/AlN/NbTiN sample also produced a reduced $B_{fp}(0\,K)$ compared to the single layer of Nb. The B_{fp} did not reduce with T as quickly as either the single Nb film or the SISIS structure.

It is possible that the NbTiN and AlN films produced pinning centres on the surface of the Nb, which skewed the measurements of B_{fp}, however as the remanence field within the magnet yoke is small and varies between each run, this should only skew single results. This theory is aided by the sample image in Fig. 5.25 where a change in the surface is present in the centre of the sample. Another possibility is that the NbTiN and the AlN are mixing, thus the thin film is not acting as a screening layer, and B_{fp} is not increased. This must be investigated using surface characterisation.

It should also be noted that the samples were only tested a single time, in a single area. Thus, the data is limited by single statistics. The samples should be repeated in both the same area to ensure the results are reliable, and also at various locations over the surface to investigate how the films vary over the sample surface.

Finding λ_L

The most interesting result is the single NbTiN thin film on Nb. As shown in Table 5.14, the addition of the thin film produced an increase of 49.6 mT, which is much larger than the increase produced by the thick NbTiN film, which is assumed to have 6 times the thickness. The λ_L can be estimated using $B = B_0 e^{-d/\lambda_L}$, where B is the change in B_1 due to the thin film, and the B_0 is what was expected on the micrometer thick Nb surface. Thus, the equation becomes:

$$\frac{d}{\lambda_L} = -\ln\left(\frac{B}{B_0}\right) = -\ln\left(\frac{B_{fp}(Nb/NbTiN) - B_{fp}(Nb)}{B_{fp}(Nb/NbTiN)}\right) = 1.13 \qquad (5.1)$$

Thus, it can be determined that d is $\approx$13 % $> \lambda_L(0\,K)$. Once surface analysis has been performed on the sample, λ_L could be determined precisely. Thus, the thin NbTiN film is not smaller than $\lambda_L(0\,K)$ but is a similar order of magnitude. For example if the deposited film d = 200 nm as assumed (1.2 µm/6 for the difference in deposition times), $\lambda_L(0\,K) = 177$ nm which agrees with literature values of $\lambda_L(0\,K)$ for NbTiN (150-200 nm [39]).

This method was also performed for the thick NbTiN film on Nb, using the increase of 25 mT at 0 K. This produces a $d = 1.64\lambda_L$. The 6 hour deposition of the NbTiN either produced a significantly reduced film thickness (due to not producing a film $\approx$ 6d), λ_L for both the thick and thin film are different, or that thick and sub-λ_L thick films behave differently.

Finding J_c

Using the increase in $B_{fp}(0\,K)$ J_c can also be determined by analysing the reduction of B through the NbTiN thin film, using $B = \mu_0 J_c d$ and re-arranging for J_c, where $B = B_{fp}(Nb/NbTiN) - B_{fp}(Nb)$. Assuming a film thickness between 100-200 nm produces a J_c of the NbTiN thin film to be 3.73×10^{11}-1.87×10^{11} A m^{-2} respectively, which is 2 orders of magnitude greater than what was found for the Nb in Section 5.1. These results are comparable to those determined by Stejic et al. [53] for the critical current on thin films with a $d = \lambda_L/2$ for NbTi in a parallel applied B, and is similar to the depairing current density (J_d) of NbTiN (1.5×10^{11} A m^{-2} [154]), which is expected due to the increase in J_c of a thin film in a parallel B.

Repeating this method for the for the µm thick NbTiN film on the surface and assuming d = 1.2 µm produced a $J_c = 1.66 \times 10^{10}$ A m^{-2}, which is an order of magnitude lower than for the thin film sample. As shown in the previous section, it is was thought that the film thickness is actually $d = 1.64\lambda_L$. Thus, assuming $\lambda_L(0\,K)$ = 150-200 nm, d ≈ 246-328 nm which thus produces values for J_c between 8.09×10^{10}-6.07×10^{10} A m^{-2} respectively. This is an order of magnitude lower than the thin NbTiN film, and reported values of J_d [154].

Stejic et al. [53] found that a NbTi film of $4\lambda_L$ produced a J_c an order of magnitude lower than that of a film with $d = \lambda_L/2$ whilst in a parallel B. Our results agree that the NbTiN film presented also shows a reduction in J_c by one order of magnitude in the presence of a parallel field. For a thorough, accurate analysis the thickness of the films need to be determined.

In the NC state, B diverges away from the poles, thus, a normal component is present on the sample surface of the samples. Thick films such as the Nb in the multilayer will force B parallel to the sample surface, however the orientation of B is not known through the thin films on the surface and is only assumed to be parallel. Hence, a perpendicular component of B could be present within the thin films such that B would not decay as expected, such that little to no increase in B_{fp} would be observed. This could be more prominent for samples which contain an insulating layer as B is not forced parallel until the Nb surface, and could explain the large difference between the samples with and without an insulating layer. The reduced B_{fp} of the films with an insulating layer could also be due to the NbTiN and AlN mixing, thus producing normal conducting islands or pinning centres, or the fact depositing thin NbTiN on AlN is more difficult than on a Cu.

The main conclusion from this study was that to fully investigate thin films ($d < \lambda_L$), the films need to be on the surface of a thick superconductor to produce the desired effect. This also includes the absence of an insulating layer, if this was not an artefact due to deposition. A comparison could be made between the samples due to all the films being deposited on a baseline substrate on Nb films that are expected to be identical.

More work needs to be performed on these multilayer samples such as surface analysis to determine the structure of the samples and the sample thickness. This can provide further information on why some samples do not show an increase in B_{fp}, and determine if the layers of AlN and NbTiN are distinct separate layers or if they are mixed. Determining the film d would allow values to be found for both λ_L and J_c, which can then be compared to theoretical values.

Chapter 6

Conclusions

6.1 Low temperature baked ellipsoid using DC magnetometry

The results produced for low temperature baked (LTB) ellipsoids suggest that the delay in the onset of the high field Q-slope is not due to an increase in the field of first vortex penetration (B_{vp}), but could be due to efficient pinning of vortices in the surface layers. Comparing the LTB measurements to bilayer samples that consist of 2 distinctly different superconductors suggest that LTB does not produce an effective interface energy barrier, as no increase in B_{vp} was observed. Experiments performed by Tan et al. and Junginger et al. [17], [18] suggest a superconducting surface layer with a larger London penetration depth (λ_L) than the substrate, and a thickness comparable to a dirty layer created by LTB, should generate an interface barrier.

Other potential mechanisms that may lead to an explanation for superconducting radio-frequency (SRF) cavities reaching magnetic fields greater than the lower critical magnetic field (B_{c1}) include; reduced RF heating due to a reduced surface current, mechanisms that suggest the removal of the cause for the HFQS such as [74], or effective pinning of vortices in the dirty layers. These mechanisms are neither supported or contradicted by the measurements produced in DC magnetometry.

6.2 Magnetic field penetration experiment

A magnetic field penetration experiment was first designed before I began my studies. The aim was to use a high carbon C-shaped magnet using a low temperature superconductor (LTS) solenoid to generate a magnetic field whilst reducing the heat load onto the experimental area. Two cryogenic facilities were designed to cool the samples down to an acceptable temperature for testing samples

6.2.1 C-shaped dipole magnet

A C-shaped dipole magnet had been designed by a previous student, and built by a team at the Rutherford Appleton Laboratory. A LTS solenoid was used to generate a DC magnetic field. To try and replicate conditions within a cavity, the magnetic field (B) is applied from one side of the sample to the other. The yoke was made out of C1020, a high carbon steel to maintain a high flux density to the gap in the poles, which are detachable to allow modification such that different sample geometries can be tested, for example curved surfaces and cavity cut outs. Both the applied and penetrated magnetic field are measured directly using Hall probe sensors, such that no modelling or calibration is required to determine B.

The magnet was tested at room temperature with a 1 A current applied to the solenoid, which generated a B=144 mT normal to the poles, and thus parallel to the sample surface. In the absence of a thick superconductor a normal component exists as B diverges away from the dipoles. With a 1 A current applied, the maximum normal component of B to the sample surface is 46 mT. Both components agree with simulated values. Thus B can be described as 31.6 % normal to a non-superconducting sample. In the presence of a superconducting sample in the Meissner state however, the superconductor behaves as a magnetic mirror, thus the normal components of B to the sample surface are cancelled at the sample surface and only the parallel components of B remain. It is expected that whilst a superconductor behaves as a magnetic mirror, any normal component is forced parallel to the sample surface.

The orientation of B should be investigated for B applied from one side of a sample using a localised B to determine if the applied B orientation does produce an effect on the field of first full flux penetration (B_{fp}). This could be performed by either altering the poles of the magnet, comparing B_{fp} values to other systems such as the solenoid field penetration facility at Old Dominion University, or increasing the distance between the poles and the magnet, thus altering the normal component on the surface of the sample. The reduction of B from the magnet onto the sample surface must also be accounted for. If the introduction of a normal component in the normal conducting state reduces B_{fp}, new poles should be made to ensure the applied B is parallel to the surface without a superconductor present.

The maximum applied field between the yoke (B_1) generated was 612 mT at 8 A, performed at 2.5 K. This was lower than the simulated values at 5 A, which is due to the yoke becoming saturated. However, this is more than sufficient for magnetic field penetration studies as the present limiting factor for SRF cavities is defined by the superconducting properties of Nb, which has a lower critical magnetic field, $B_{c1}(0\,K) = 174\,mT$ [34], [42] and superheating critical field, $B_{sh} \approx 240\,mT$.

Unlike other systems such as vibrating sample magnetometry [83] where a B is applied over the whole sample, the magnet is easy to align to the sample surface to ensure a parallel field. Due to the small gaps in the poles, B remains localised which

limits flux enhancements that can be produced on small samples. One limitation of using a high carbon steel yoke is that the yoke can become magnetised and therefore needs to be degaussed. The remanence field produced is $\leq 5\,\mathrm{mT}$, which is tolerable, but not ideal.

6.2.2 Variable temperature insert

One of the main aims was to have a fast sample turn around. The first cryogenic facility consisted of a variable temperature insert (VTI) which could be inserted/removed from a larger cryostat which remained cold. Thus, multiple samples could be tested a day with only the insert and the sample requiring to change temperature. The minimum T that the sample could reach was 7.5 K, which was not low enough for adequate testing.

To ensure the method worked, the VTI was tested using a liquid Helium (LHe) system. Only a few tests were performed due to the length of time taken and the rising cost of LHe. These tests determined that the magnetic field penetration method worked, however magnetic components consisting of long bolts to hold the magnet and the facility cage were present in the experimental area which skewed the results. Additionally, two diodes were present within the set up which limited B_1 in one polarity and not the other. It was decided that a new system should be built without the magnetic components present to ensure no parts became magnetised during testing.

6.2.3 Conduction cooled facility

A new field penetration facility was designed and built at Daresbury laboratory which cools the samples by conduction. The field penetration experiment is mounted directly onto a cold head. Due to the reduced heat load on the system the facility can reach a minimum $T = 2.5\,\mathrm{K}$. The sample T is controlled using a PID loop and varying the I applied to resistors placed either side of the sample. Thus, the facility can operate at a wide range of temperatures. Due to the nature of the compressor, the sample T fluctuates with a frequency of 0.2 Hz, with a fluctuation never greater than $\pm\ 20\,\mathrm{mK}$.

The conduction cooled facility provides a few specific benefits that makes it stand out from other systems such as being cryogen free. Thus the magnetic field penetration facility (MFPF) can operate full-time due to not relying on a supply of LHe. Additionally, the MFPF is integrated with LABView such that the system is automated and can be operated remotely.

The MFPF also has some limitations. Experimental observations have determined that some magnetic field leaks around the sample, which varies with sample size. However, the sample size is currently limited to a maximum of $50\times50\,\mathrm{mm}^2$, and thus

the minimum magnetic field leakage is also limited. This is $\approx 7 \times 10^{-3}$ of B_1. The only way to accommodate larger samples is to redesign the sample plate. Thus, the magnetic leakage must be taken into account when extracting B_{fp}.

It should be noted that this facility was not designed to report measurements of B_{c1}. This facility reports the field of first full flux penetration, the applied field at which the pick-up Hall probe indicated the field has broken through the sample. Several techniques to determine B_{fp} have been explored. A second derivative method produces the most accurate results, however it can only be used for samples that produce a sharp transition. For gradual transitions, or for noisier measurements a more robust method has to be used. The chosen method takes into account the magnetic field leaking around the sample (B_1K_2), and the noise of the measurements.

The measurements of the facility have multiple sources of error, such as the error in the Hall probes sensors, the step size of applied field, as well as the random error produced by the facility. These are summarised in Table 6.1. The random error of the facility was found by repeating measurements on 2 Nb foils procured from Goodfellows Ltd with a thickness of 50 and 100 µm. The 50 µm sample had 2 tests with repeated thermal cycling without removing the sample and the 100 µm had 3 tests without removing the sample. The 50 µm had the greatest random error of 0.9 %, where as for the 100 µm sample had an error of 0.4 %. The random error for the facility was taken to be the largest value of 0.9 %. Both samples were removed and placed back in the facility with a different sample surface area under the poles. This increased the error from 0.9 % and 0.4 % to 1.2 % and 0.7 % respectively with a change in $B_{fp}(0\,K)$. As a new area of the sample was tested, the change in B_{fp} could also be due to the samples. Future work should include if the homogeneity of the samples have an effect on B_{fp}, which can be investigated by testing different areas of a sample.

The system was commissioned by investigating two important properties; The effect of sample size, and the effect of sample thickness.

A Type I superconductor was used to determine how sample size affected how much B leaked around the sample whilst it was in the Meissner state. A Type I superconductor was chosen due to no intermediate state existing, such that B was either screened, or had penetrated through the sample. Thus, the transition was sharp, with a step away from B_1K_2 line, and produced a clear B_{fp}. The sample started with an area of $50 \times 50\,mm^2$, which was slowly reduced. As the sample size was reduced it was determined that more B leaked around the sample, increasing the gradient of B_1K_2. It was determined that the sample length (along the applied B direction) is the most critical whilst testing for B_{fp}, where as the width (perpendicular to the applied field) is less critical. These tests were also repeated (not as extensively) using a Nb sample, which agreed with the results produced by the Nb whilst and still indicated a clear B_{fp}. For large enough samples the B_{fp} becomes independent of of sample size. For accurate measurements a minimum sample size is required.

Table 6.1: A summary of all the errors found for the MFPF. Measured errors were taken using the standard deviation method.

Error Origin	[mT]	[%]
HP1 (1)	2.7	
HP1 (2)	5	
Step size (typical)	≈ 1	
50 Microns		
B_{fp} Average	409.6	
ΔB_{fp} Average	3.6	0.9
B_{fp} after moving sample	453.0	
ΔB_{fp} after moving sample	43.4	10.6
New B_{fp} average after moving sample	422.0	
New Standard Error after moving sample	4.9	1.2
100 Microns		
B_{fp} Average	230.6	
ΔB_{fp} Average	1.0	0.4
B_{fp} after moving sample	226.0	
ΔB_{fp} from moving sample	-4.6	-2.0
New B_{fp} average after moving sample	229.3	
New Standard Error after moving sample	1.6	0.7

Due to the MFPF applying B from one side of a sample to the other, it was expected that samples with a large thickness would increase B_{fp}, as B could enter and leave the superconductor from the same side. Multiple foils were procured from Goodfellows Cambridge Ltd, and three Nb films were deposited at Daresbury laboratory with the geometry and varying thickness to investigate the effect of sample thickness. These tests concluded that the B_{fp} does depend on sample thickness, with a large variation produced for low RRR samples. Finding a linear relation of $B_{fp}(d)$ for both the films and the foils to a minimum produced a similar value when extrapolated to d=0, where as it was expected that $B_{fp}(d=0)=B_{c1}$. Both the foils and the films have a low RRR, and it is expected that the films have a consistent grain growth for each sample, whilst the foils are all different samples that can have different grain boundaries between each sample. Thus, the possibilities that could lead to a B_{fp} less than the theoretical B_{c1} are:

- The foils and films are both low RRR, changing the mean free path and reducing the B_{c1} of the samples.

- The λ_L is large, such that B_2 is the B decay, and not vortices suddenly penetrating through the sample. This would require large λ_L, or films on the order of λ_L.
- The equation $B_{fp}=B_{c1}+J_c d$ does not apply to films in the µm range.
- Edge effects could still be present and be producing flux enhancements at the edges that can alter the results.

As the foils were 4 different foils with different RRR and grain boundaries for each sample, it is expected that each foil should have a different B_{c1} and J_c values. Although the sputtered films are also 3 different samples, they were all deposited under consistent conditions on Cu substrates and should have similar RRR and grain growth for each sample. The thin films produced a linear relationship with $B_{fp}(d)$ with much less scattering that what was seen for the Nb foils. This is likely due to the similarities between the films that may not be present in the foils. The thin film Nb samples produced similar B_{fp} for 1 and 3 µm compared to the foils, and a lower B_{fp} than for the 5 µm foil.

The J_c was calculated using the expected theoretical B_{c1}, and resulted in a J_c between 7×10^9-9×10^{10} A m^{-2} for the foils and 3×10^{10}-7×10^{10} A m^{-2} for the films, indicating that both the sample sets are of a similar quality with a low RRR. For a rough estimate a comparison in sputtered films can be compared to those of Nb films of a similar thickness, by comparing the B_{fp} and J_c. The limit for a comparison for film thickness is 10 µm. Further investigations on new novel materials require a baseline sample to first be tested for comparison, and it would be beneficial to investigate the behaviour as a function of thickness.

The magnetic field leakage was also compared with the Nb samples of varying thickness to determine if any normal component of B was produced on the surface of the superconducting sample which could cause early B_{fp}. No change was observed in B_1K_2 for the samples of varying thickness, thus it was expected that a normal component of B in the experimental set-up is negligible compared to the parallel component. This needs to be compared with future upgrades when the magnetic field leaking around the sample can be mitigated by increasing the sample size or by magnetic shielding.

6.3 Results

6.3.1 Micrometer thick Nb

The majority of the studies performed by the MFPF were performed on micrometer thick samples. As part of the ARIES WP15 collaboration 14 micrometer thick Nb films were deposited on Cu which had undergone various polishing techniques. The

films were deposited at the INFN LNL, the University of Siegen and STFC Daresbury laboratory, and were then tested in both the MFPF and the VSM. The samples were the laser treated, and the change in the films were compared.

Generally, the B_{fp} depends on the maximum Meissner screening and critical currents of the samples. Some samples produced an 'elbow' at the transition, and not a single step increase to indicates B_{fp}, whilst some samples produced a gradual transition. It is clear that different polishing techniques and the deposition institutes had a large effect on the B_{fp}. The samples were also tested in a VSM at IEE in Bratislava in both a parallel and perpendicular applied B, which allowed a comparison to the MFPF. The MFPF produced much larger B_{fp} than the entry magnetic field (B_{en}) for all samples, which was expected due to the physical properties each facility measures. Comparing B_{en} for both the parallel and perpendicular orientation of the samples to B showed that some normal components must have been present in the parallel set up due to both orientations producing similar values. This was also confirmed by the MFPF as the B_{fp} did not vary as much between samples.

The samples from Siegen and STFC were laser treated at RTU, and investigated by both the MFPF and the VSM. The MFPF facility determined that samples from STFC showed little change due to laser treatment, which could be attributed to a different location of the sample being tested, where as the films deposited by Siegen showed a large decrease in $B_{fp}(0\,K)$. No correlation could be made between the effect of substrate polishing and post deposition laser treatment.

The reduction in $B_{fp}(0\,K)$ is likely due to damage in the samples produced from Siegen as the reduction is large. This damaged can be attributed to the heat of the laser being deposited into the Cu substrate such that the substrate can mix with the Nb, or breaks through the film entirely. The damage is only witnessed in the films with a 3 µm thickness as the heat from the laser is deposited in the substrate rather than the film.

The VSM observed an increase in B_{en} for all irradiated samples except one by STFC. The enhancement may not be an effect of the post deposition laser treatment. As the VSM consists of limitations such as flux enhancements and normal components, which had already been observed in the investigation of substrate polishing. If these effects were present in the first round of testing and mitigated in later tests, all measurements will appear to have an improved B_{en}, thus appearing as improved qualities due to laser treatment. Thus, these studies show that due to the easy alignment of the MFPF allow a clear insight into the response of samples in a B. The reduction in B_{fp} after laser treatment could either due to a release of pinning or a decreased B_{c1}. With the current data it is not possible to distinguish between these two interpretations. Upgrades to the facility could provide further insight into this.

Some samples indicated similar values in B_{fp} compared to the rapid change in the magnetic moment produced by the VSM. This indicates there may be some similarities

between the systems if the conditions are similar to B_{fp} or B_{vp} have a similar extraction method chosen.

Further studies should be performed to determine how post deposition laser treatment varies as a function of thickness. A number of samples should be deposited with thickness varying from 1-10 µm and tested in the MFPF both before and after laser treatment to remove the effect from different laboratories depositions.

6.3.2 Micrometer thick NbTiN and Nb_3Sn

One potential method to increase SRF performance is to replace Nb with new materials with larger critical fields, or greater T_c. This can enable higher E_{acc} to be reached, or increase the operating T of the cavity to reduce the operating costs.

Three 2.4 µm Nb_3Sn samples were deposited at STFC Daresbury on substrates which had been treated by either EP, diamond turned or SUBU polishing, and one 1.2 µm NbTiN sample on untreated Cu. None of the samples produced a sharp transition in B_{fp} that was present for Pb and Nb samples, and this behaviour could be intrinsic of strong Type II superconductors. The gradual transition leads to issues in reporting the B_{fp}, as there is not a single clear step at the transition. The results must be analysed using a technique to ensure a reliable B_{fp} is reported, which at this moment, discounts using the second derivative method. Thus the point of B_{fp} can only be reported as a deviation away from the Meissner screening/leakage line.

Samples could be tested up to a higher T (as the samples were still superconducting), and points still produced a linear $B_{fp}(T^2)$. As $T \rightarrow T_c$, the B_{fp} became small such that a clear B_{fp} could not be reported.

All the samples produced a $B_{fp}(0\,K)$ larger than the theoretical B_{c1} for their respective material. One Nb_3Sn film deposited on the SUBU polished substrate also produced a low B_{fp} (61.3 mT), as well as a low T_c (10.7 K). This sample produced similar results to sputtered Nb for the same thickness, and could be a Nb only sample.

It is hard to distinguish the difference for B_{fp} between high T_c materials and Nb. This could be an effect due to the deposition institute, or a limitation of the MFPF for samples with a low thickness ($d<10$ µm). Further analysis on bulk high T_c materials should be performed by investigating the effect of thickness dependence on B_{fp}. This can also help determine if the films are good quality, whilst also determining $B_{fp}(d=0)$ is similar to what is expected.

6.3.3 Thin film NbTiN

Two NbTiN 65 nm thin films were deposited at DESY using Plasma enhanced atomic layer deposition (PEALD) [153] to determine if the MFPF was sensitive enough to characterise thin films. However, both thin films received damage due to the extremely

thin, coupled with the stress' produced whilst the facility cooled/warmed up. One sample was able to be tested using half the film. However, the sample which had been annealed (and thus have an increased T_c) was too damaged to be tested.

The amount of screening the NbTiN produced was found by comparing the gradient of B_2/B_1 to that of the same set up without a superconductor present. No comparison was made to above T_c as an accurate T_c measurement was not made, as the T_c of sample was at the lower T limit of the the RRR facility at STFC. Additionally, the RRR facility had not been compared to other systems to ensure the T_c results were reliable. Comparing the gradient of B_2/B_1 without a superconductor present allowed the penetration depth to be calculated. However, λ_L did not become extremely large as $T \rightarrow T_c$, as expected, but rather reduced as $T \rightarrow T_c$. This could be due to a number of reasons:

- The film had broken, such that a smaller portion of B was being screened compared to a full sample. I.e - B_1K_2 is larger, thus less B was being screened.
- The sample was found to have a low T_c, and thus may have not been a good quality NbTiN film.
- The normal component of B_1 was not forced parallel to the film (due to not being a thick film), thus B could pass through the film much easier, thus producing a reduced λ_L.

As both samples were damaged during these tests, it was determined that for future work on thin films, the films must be deposited on a thick substrate such that the films are less likely to break. Additionally, the substrates must have a similar thermal conductivity as the films to ensure no stress is generated on the film during cooling. If the low λ_L was produced by a normal conducting component penetrating through the film, the film should be deposited onto a well known thick superconductor that will force B parallel within the thin film, causing the B to decay as expected.

This study concluded that the MFPF could not test thin films with a thickness d $< \lambda_L$, and is a limitation of the facility. This is due to the applied field not being forced parallel through the superconductor. To investigate thin films, a bulk superconductor is required to force the B field to be parallel within the thin film.

6.3.4 Multilayer NbTiN on Nb

One promising method to aid bulk Nb is the use of multilayer structures, first proposed by A. Gurevich [16] in 2006. Multilayer structures utilise superconducting thin films (d$< \lambda_L$) on the surface of a thick superconductor. A B applied parallel to a thin film decays exponentially as it passes through the film, such that the surface of the thick superconductor underneath is witness to a $B<B_{surf}$. Parallel vortices are

not thermodynamically stable within the thin film, thus reducing the RF losses. Additionally, thin films can remain in the Meissner state up to much larger B.

Multilayer structures can also have a thin dielectric layer separating the thin films from the substrate, and are known as superconducting-insulating-superconducting (SIS) structures. Insulating layers are not always present in multilayer structures, such that the thin film is directly grown on the thick superconductor, which are known as SS bi-layers. The insulating layer interrupts any vortices that could be present within the multilayer, thus increasing B_{vp} [78].

Multilayer structures cannot be accurately measured by commercial magnetometry systems such as VSM as B is applied over the whole sample producing many unwanted effects such as:

- B penetrates through the insulating layer such that the screening effect produced by the thin films will not be observed.
- B penetrates through the opposing side of the thick superconductor, thus the thin films do not have any effect on the magnetic field of first flux entry.
- The sample is not aligned such that the sample surface is parallel with B, thus producing a lower field of first flux entry.

The aim of the MFPF was to reduce these limitations to allow multilayer samples to be tested, such that it would be a powerful tool to investigate multilayer structures. Measurements performed on thin films on the order of λ_L indicated that thin films by themselves are a limitation of the MFPF. Thus, the thin films must be deposited onto a thick substrate that would fully screen the field.

A range of multilayer samples were deposited at STFC Daresbury laboratory. All the samples were deposited by DC magnetron sputtering micrometer thick Nb onto Cu substrates, followed by depositing NbTiN films on the surface. Both thick and thin films were deposited on the Nb under the same conditions to allow comparison between the varying thickness by comparing the results to the Nb sample. Some samples consisted of thin films seperated by AlN insulating layers.

All the samples were tested in the conduction cooled MFPF at a wide range of T set points. It was found that all multilayer samples which contained an insulating layer of AlN did not produce an increase in $B_{fp}(0\,K)$, however they did increase B_{fp} at higher T's. One explanation for the reduction in B_{fp} for multilayers with an AlN layer could be due to the AlN and NbTiN films had mixed, producing normal conducting islands or reducing the quality of the NbTiN.

This should be investigated by depositing micrometer thick NbTiN film on AlN on Cu, and comparing to the sample without AlN. Alternatively, the new multilayer could be deposited on Nb with an insulating layer to determine if the difference is caused by the interaction between the AlN and the Nb. Thus eliminating the thin film and the unknown orientation of B, such that the only variable is the insulating layer.

Thick NbTiN on Nb produced interesting results. A clear change in regime can be seen when the Nb is no longer superconducting, portrayed by two slopes. At higher T's where the Nb is no longer superconducting, the slope is comparable to the single thick NbTiN sample as expected, however there is a greater deviation in the B_{fp}. At low T's, the Nb becomes superconducting and the B_{fp} increases due to an increased superconducting volume. The thin NbTiN film produced an increase in B_{fp} by 49.6 mT compared to the Nb only sample, which was an increase in B_{fp} of 47.7 mT. The increase in B_{fp} for the thick NbTiN was almost half of that compared to the thin NbTiN film, with an increase of 25 mT. This indicates that other effects are present other than just an increase in superconducting volume increasing B_{fp}.

Using a relationship of $B_{fp}(d)$ for Nb and extrapolating to 4.8 µm (3.6 µm for the Nb film, and the estimated 1.2 µm), the expected $B_{fp}(d{=}4.8\,\mu m){\approx}130.8$ mT. This is very similar to what was found for the thick NbTiN on Nb sample (129 mT). This could be that the effect of thickness is not correlated to sample material, or that the sample thickness is so thin that the material does not matter, or a coincidence.

It has been estimated that the thin NbTiN film on the surface of the Nb has a $d \approx 13\,\% > \lambda_L$. It has been estimated that the thickness of the thin film is $\approx$ 150-200 nm, such that $\lambda_L(0\,K)$ is $\approx$ 133-177 nm. These values are similar to the theoretical values of $\lambda_L(0\,K)$ = 150-200 nm [39]. The analysis was also repeated on the thick NbTiN layer on Nb, which produced a $d{=}1.64\lambda_L$. This was unexpected as the deposition time was 6 hours longer, and it was expected the film would be 6 times the thickness of the thin film. Another possibility is that λ_L is different for the thicker film due to the lattice structure becoming more uniform at greater thickness.

The J_c was determined for both the thin and thick film using the change in $B_{fp}(0\,K)$ when compared to the Nb sample. The thin film produced a $J_c = 1.9 \times 10^{11}\,A\,m^{-2}$. This is comparable to the J_c of a NbTi film with a $d = \lambda_L/2$ in a parallel field [53], and is also comparable to the J_d of a thick NbTiN ($1.5 \times 10^{11}\,A\,m^{-2}$ [154]). This agrees that the MFPF produced a parallel field during these tests. The 6 hour NbTiN sample had an estimated $d = 1.2\,\mu m$, which produced a $J_c = 1.7 \times 10^{10}\,A\,m^{-2}$.

The films should undergo thorough surface characterisation to determine if the the films are of good quality, or if during the deposition process the films had become damaged. Additionally, the films could also be tested in commercial magnetometry to determine if any correlation is present, and also accurately determine the T_c of the superconductors present.

Taking all experimental results into consideration it can be concluded that the MFPF can be used to test the added Meissner screening of thin thin films on the order of the λ_L if deposited on sufficiently large and thick substrate which have been tested with the facility before deposition.

6.4 Future work

It has been shown that the MFPF is a powerful tool to investigate superconducting thin films. To determine if these results are relaible, they should be compared to other local magnetometer techniques such as the field penetration measurement at Old Dominion University to determine if any correlation can be made between the facilities. It is clear that samples must have a similar thickness to allow a comparison, and they can only be compared to results of the MFPF that have been analysed using the same methods as this can change the B_{fp} significantly.

The orientation of B should also be investigated. A superconductor in the Meissner state will force B parallel to the sample surface. Normal components may allow vortices to enter the sample at a lower applied magnetic field (B_{app}), thus producing a lower B_{fp}. Thus, the effect of normal components on the surface should also be investigated.

A remanence field is present due to using a magnetic yoke. Although degaussing was performed to demagnetise the yoke, a small B was still present. Removing the remanence field would further improve the reliability of the measurements as less B would be trapped within the samples during the cool down transition.

The bi-power supply should be used to ramp the B in both polarities to perform hysteresis loops. Thus allowing the MFPF to distinguish between Meissner screening and pinning within the samples, as is performed in a VSM. This would allow the MFPF to directly determine the J_c, and can be also combined with B_{fp} to determine if the samples are good quality.

The B leaking around the sample should be removed, as it is possible that the stray B is producing magnetic flux enhancements at the sample edges, or also obscuring the B_{fp}. It is possible that the B_1K_2 has no effect on the results, however this needs to be proved experimentally. This can be done by a few methods.

1. Increase the size of the sample such that all stray fields remain on one side of the sample, such that B_1K_2 is removed. This requires the stage 2 (S2) plate to be re-designed to accommodate larger samples.
2. Install magnetic shielding to re-direct the stray fields away from the opposite side of the sample. Great care must be taken if this method is chosen as flux enhancements could occur at the edges of the shield, or more importantly the shield could become magnetised similarly to in the VTI, thus skewing the measurements.
3. Install flux gates around the sample to determine if there is any flux enhancement at sample edges causing early flux penetration.

Recent studies on the MFPF have been performed with the pick up Hall probe (HP2) shielded using mu-metal, such that the B_1K_2 curve was completely removed [156]. The measurements were performed on sputtered Nb with a size of

$30\times30\,\mathrm{mm}^2$, that were shown in Section 4.9, and it produced a $B_{fp}(0\,K)=193.3\pm1.8\,mT$, with measurements performed between 5-9 K. This indicates that the B_1K_2 line did not have an effect on the extraction of B_{fp}.

The MFPF produced promising results for multilayer samples, however thorough surface charecterisation should be performed to determine why the films with an AlN layer did not behave as expected. Additionally, once the thickness of the films has been determined, a more accurate analysis can be made for both the λ_L and J_c. Further investigations of a thin film on the surface of a well known thick superconductor should be performed to determine how the film d alters B_{fp}, and can be compared with the theoretical calculations performed by Kubo [78].

One aim of the MFPF was to increase the sample turn around to quickly determine materials for SRF applications. Thus, a comparison between the MFPF should be made to RF measurements such as a quadrupole resonator or the RF choke cavity at STFC Daresbury Laboratory [157] to determine if there is any correlation between devices, or any correlation between DC and RF measurements. The same sample must be tested in both facilities to allow a comparison to be made between the two types of measurements. No tests had been completed at the time of writing. If the MFPF is modified such that larger samples can be accommodated to reduce B_1K_2, the samples do not have to be cut between measurements, thus minimising any damage or impurities that can be introduced to the samples. Additionally, it can be ensured that the same area on the sample is investigated in both the DC and RF case to ensure the results are comparable.

The purpose of the MFPF was to investigate multilayer and thin film structures. It was determined that the MFPF is not sensitive to single layer thin films, thus films were deposited on the surface of Nb with a thickness similar to a previously tested Nb sample. This was to ensure that B would be forced parallel to the surface of the sample, to ensure the B would decay exponentially as it passed through the film. It was determined that samples with an insulating layer did not produce an increase in B_{fp} which must be investigated, such that it can be accounted for in future depositions and tests. These tests need to be repeated to ensure the reliability of the measurements.

Using the same method, the effect of thickness on thin films can be investigated by depositing the films directly onto sufficiently thick Nb. Comparing the results to the single layer Nb can allow the properties of the film to be investigated. Performing these measurements can therefore allow a comparison to be made to theoretical values calculated by Kubo [78]. Whilst NbTiN is of great interest for multilayer structures, other materials should also be investigated to determine the effect of thickness, such as Nb_3Sn. Thus, a comparison can be made between the two (or more) materials for thin films, which can be implemented for SRF cavities.

List of Acronyms

AFM	Atomic force microscopy
B	Magnetic flux density
B_1	The applied magnetic field in the gap of the yoke
B_2	The magnetic field read the opposing side of the sample
B_{app}	The applied magnetic field (generic)
B_c	The thermodynamic critical field
B_{c1}	The lower critical field
B_{c2}	The upper critical field
B_{c3}	The surface critical magnetic field
B_{sh}	The superheating critical magnetic field
BCP	Buffer chemical polishing
BCS	Bardeen, Cooper, Schreiffer
B_{en}	The entry magnetic field defined by IEE
B_{eq}	The magnetic field at the equator of the ellipse
B_{ext}	The external magnetic field
B_{fp}	The magnetic field of first full flux penetration
B_{surf}	The surface magnetic field
B_{vp}	The field of first vortex penetration
C_e	Electronic specific heat
d	Sample thickness
DC	Direct current
E	Electric field
e^-	The charge of an electron
e^*	The charge of a Cooper pair
E_{acc}	The accelerating gradient
EBSD	Electron back scattered diffraction
E_c	Condensation energy of a Cooper pair
EP	Electro-polishing
F	Gibbs free energy in superconducting and normal state
f	Gibbs function for enthalpy
fi	Impurity content
FNAL	Fermi national laboratory
G	Geometry factor
GL	Ginzburg Landau
GLAG	Ginzburg Landau Abrikosov Gor'kov
h	Planck's constant
$\hbar$	Reduced Planck's constant
HFQS	High field Q slope
HTS	High temperature superconductor

IEE	The institute of electrical engineering, Bratislava
INFN LNL	National Institute for Nuclear Physics, National Laboratories of Legnaro
J_c	Critical current
J_d	Depairing current density
J_s	Superconducting current, also known as supercurrent
K_1	The relationship between B1 and B2 for a given distance
K_2	The magnetic field leakage constant
LHe	Liquid helium
LT	Laser treated
LTB	Low temperature baking
LTS	Low temperature Superconductor
m	Magnetic moment
m^*	Mass of a Cooper pair
m_e	Mass of an electron
MFPE	Magnetic field penetration experiment
MFPF	Magnetic field penetration facility
MPMS	Magnetic property measurement system
μSR	Muon spin rotation
n_s	Number of superconducting charge carriers
ν	Velocity of an electron
ODU	Old Dominion University
OFHC	Oxygen free high conductivity
p	Pressure
P_c	Power dissipated in the cavity walls
PCB	Printed circuit board
PEALD	Plasma enhanced atomic layer deposition
PID	Proportional integral differential
PVD	Physical vapour deposition
Q_0	Quality factor
QPR	Quadrupole resonator
R	Resistance
R_a	Roughness
ri	Relevant resistivity of an impurity
RRR	Residual resistance ratio
R_{surf}	Surface resistance
RTU	Riga technical university
S	Entropy
$S1$	Stage 1
$S2$	Stage 2
SEM	Scanning electron microscope
SQUID	Superconducting quantum interference device

SRF	Superconducting radio frequency
STFC	Science and technology facilities council
SUBU	A chemical polishing solution
T	Temperature
T_c	Critical temperature
T_{room}	Room temperature
TMP	Turbo molecular pump
TRS	Thermal radiation shield
U	Stored energy
VSM	Vibrating sample magnetometer
VTI	Variable temperature insert
ZFC	Zero field cool down

Symbols

ξ_0	The BCS coherence length
ξ_{GL}	The GL coherence length
Δ	The superconducting energy band gap
κ_{GL}	Ginzburg-Landau parameter
k_b	Boltzmann constant
λ_L	London penetration depth (for infinite mean free path)
ϕ_0	One magnetic flux quantum
Ψ	Phase order parameter
Ψ^*	Phase order parameter

Bibliography

[1] D. A. Turner, G. Burt, and T. Junginger, "No interface energy barrier and increased surface pinning in low temperature baked niobium," *Scientific reports*, vol. 12, no. 1, pp. 1–9, 2022.

[2] D. A. Turner, O. B. Malyshev, G. Burt, T. Junginger, R. Valizadeh, and L. Gurran, "A facility for the characterisation of planar multilayer structures with preliminary niobium results," *Superconductor Science and Technology*, vol. 35, no. 9, p. 095 004, 2022.

[3] D. A. Turner, O. B. Malyshev, G. Burt, *et al.*, "Investigating the superconducting properties and surface morphology of sputtered Nb films on Cu due to laser treatment," *IEEE Transactions on Applied Superconductivity*, vol. 33, no. 4, pp. 1–12, 2023. DOI: 10.1109/TASC.2023.3243459.

[4] D. Turner, O. Malyshev, G. Burt, *et al.*, "Characterization of flat multilayer thin film superconductors," in *Proc. SRF 2019*, 2019.

[5] R. Valizadeh, A. Hannah, S. Aliasghari, *et al.*, "PVD depostion of Nb3Sn thin film on copper substrate from an alloy Nb3Sn target," *Proc. IPAC'19*, pp. 2818–2821, 2019.

[6] O. Malyshev, R. Valizadeh, D. Turner, *et al.*, "Final report on thin film technology, ARIES delivery report D15.4," *Horizon 2020 Research Infrastructures*, 2021. [Online]. Available: available%20at:%20https://edms.cern.ch/document/1820620/1.0 (visited on 03/14/2022).

[7] Á. Faus-Golfe and R. Edgecock, "Applications of particle accelerators in europe," 2017.

[8] M. Vretenar, "Linear accelerators," in *CERN Accelerator School on High Power Hadron Machines*, Mar. 2013. DOI: 10.5170/CERN-2013-001.225. arXiv: 1303.6766 [physics.acc-ph].

[9] H. S. Padamsee, "Superconducting radio-frequency cavities," *Annual review of nuclear and particle science*, vol. 64, pp. 175–196, 2014.

[10] R. Kleiner and W. Buckel, *Superconductivity: an introduction*. John Wiley & Sons, 2016.

[11] J. W. Bray, "Superconductors in applications; some practical aspects," *IEEE Transactions on Applied Superconductivity*, vol. 19, no. 3, pp. 2533–2539, 2009. DOI: 10.1109/TASC.2009.2019287.

[12] H. Padamsee, *RF Superconductivity - Science, Technology, and Applications*. Wiley-VCH, 2009.

[13] H. Padamsee, J. Knobloch, and T. Hays, *RF superconductivity for accelerators*.

[14] G. Ciovati, "Where next with SRF," in *Paper presented at IPAC2013,Shanghai, China p. 3124*, 2013.

[15] A. Grassellino, A. Romanenko, Y. Trenikhina, *et al.*, "Unprecedented quality factors at accelerating gradients up to 45 MVm^{-1} in niobium superconducting resonators via low temperature nitrogen infusion," *Superconductor Science and Technology*, vol. 30, no. 9, p. 094 004, 2017.

[16] A. Gurevich, "Enhancement of rf breakdown field of superconductors by multilayer coating," *Applied Physics Letters*, vol. 88, no. 1, p. 012 511, 2006.

[17] T. Tan, M. A. Wolak, X. Xi, T. Tajima, and L. Civale, "Magnesium diboride coated bulk niobium: A new approach to higher acceleration gradient," *Scientific reports*, vol. 6, p. 35 879, 2016.

[18] T. Junginger, W. Wasserman, and R. Laxdal, "Superheating in coated niobium," *Superconductor Science and Technology*, vol. 30, no. 12, p. 125 012, 2017.

[19] Quantum Design, "Magnetic property measurement system MPMS 3 user's manual," *Quantum Design Inc*, 2016.

[20] V. L. Ginzburg and E. A. Andryushin, *Superconductivity*. World Scientific, 2005.

[21] M. Tinkham, *Introduction to superconductivity*. Courier Corporation, 2004.

[22] F. London and H. London, "The electromagnetic equations of the supraconductor," *Proceedings of the Royal Society of London. Series A-Mathematical and Physical Sciences*, vol. 149, no. 866, pp. 71–88, 1935.

[23] M. Cyrot, "Ginzburg-landau theory for superconductors," *Reports on Progress in Physics*, vol. 36, no. 2, p. 103, 1973.

[24] W. Meissner and R. Ochsenfeld, "Ein neuer effekt bei eintritt der supraleitfähigkeit," *Naturwissenschaften*, vol. 21, no. 44, pp. 787–788, 1933.

[25] R. K. W. Buckel, *Superconductivity*, 2nd ed. Wiley-VCH.

[26] W. Corak, B. Goodman, C. Satterthwaite, and A. Wexler, "Exponential temperature dependence of the electronic specific heat of superconducting vanadium," *Physical Review*, vol. 96, no. 5, p. 1442, 1954.

[27] R. Glover III and M. Tinkham, "Conductivity of superconducting films for photon energies between 0.3 and $40\kappa T_c$," *Physical Review*, vol. 108, no. 2, p. 243, 1957.

[28] E. Maxwell, "Isotope effect in the superconductivity of mercury," *Physical Review*, vol. 78, no. 4, p. 477, 1950.

[29] J. Bardeen, L. N. Cooper, and J. R. Schrieffer, "Theory of superconductivity," *Physical review*, vol. 108, no. 5, p. 1175, 1957.

[30] A. Knapton, "Niobium and tantalum alloys," *Journal of the Less Common Metals*, vol. 2, no. 2-4, pp. 113–124, 1960.

[31] A.-M. Valente-Feliciano, *2016 supercond. sci. technol. 29 113002*, 2016.

[32] R. F. Gasparovic and W. L. McLean, "Superconducting penetration depth of lead," *Phys. Rev. B*, vol. 2, pp. 2519–2526, 7 Oct. 1970. DOI: 10.1103/PhysRevB.2.2519. [Online]. Available: https://link.aps.org/doi/10.1103/PhysRevB.2.2519.

[33] G. Chanin and J. Torre, "Critical-field curve of superconducting lead," *Physical Review B*, vol. 5, no. 11, p. 4357, 1972.

[34] D. Finnemore, T. Stromberg, and C. Swenson, "Superconducting properties of high-purity niobium," *Physical Review*, vol. 149, no. 1, p. 231, 1966.

[35] A. Godeke, "Nb3Sn for radio frequency cavities," Lawrence Berkeley National Lab.(LBNL), Berkeley, CA (United States), Tech. Rep., 2006.

[36] T. Courtney, J. Reintjes, and J. Wulff, "Critical field measurements of superconducting niobium nitride," *Journal of Applied Physics*, vol. 36, no. 2, pp. 660–661, 1965.

[37] C. Yen, L. Toth, Y. Shy, D. Anderson, and L. Rosner, "Superconducting H_c-J_c and T_c measurements in the Nb–Ti–N, Nb–Hf–N, and Nb–V–N ternary systems," *Journal of Applied Physics*, vol. 38, no. 5, pp. 2268–2271, 1967.

[38] R. Blaschke, J. Ashkenazi, O. Pictet, D. Koelling, A. van Kessel, and F. Muller, "The influence of band structure on the electromagnetic properties of superconducting Nb and Nb3Sn," *Journal of Physics F: Metal Physics*, vol. 14, no. 1, p. 175, 1984.

[39] A.-M. Valente-Feliciano, "Superconducting RF materials other than bulk niobium: A review," *Superconductor Science and Technology*, vol. 29, no. 11, p. 113 002, 2016.

[40] T. Orlando, E. McNiff Jr, S. Foner, and M. Beasley, "Critical fields, pauli paramagnetic limiting, and material parameters of Nb3Sn and V3Si," *Physical Review B*, vol. 19, no. 9, p. 4545, 1979.

[41] L. Yu, N. Newman, and J. M. Rowell, "Measurement of the coherence length of sputtered Nb/sub 0.62/Ti/sub 0.38/N thin films," *IEEE transactions on applied superconductivity*, vol. 12, no. 2, pp. 1795–1798, 2002.

[42] T. Junginger, S. Abidi, R. Maffett, *et al.*, "Field of first magnetic flux entry and pinning strength of superconductors for rf application measured with muon spin rotation," *Physical Review Accelerators and Beams*, vol. 21, no. 3, p. 032 002, 2018.

[43] T. Junginger, T. Prokscha, Z. Salman, A. Suter, A.-M. Valente-Feliciano, *et al.*, "Critical fields of SRF materials," in *Proc. 9th International Particle Accelerator Conference (IPAC'18), Vancouver, BC, Canada*, 2018, pp. 3921–3924.

[44] M. K. Transtrum, G. Catelani, and J. P. Sethna, "Superheating field of superconductors within ginzburg-landau theory," *Physical Review B*, vol. 83, no. 9, p. 094 505, 2011.

[45] "73 - on the theory of superconductivity," in *Collected Papers of L.D. Landau*, D. TER HAAR, Ed., Pergamon, 1965, pp. 546–568, ISBN: 978-0-08-010586-4. DOI: https://doi.org/10.1016/B978-0-08-010586-4.50078-X. [Online]. Available: https://www.sciencedirect.com/science/article/pii/B978008010586450078X.

[46] A. A. Abrikosov, "On the magnetic properties of superconductors of the second group," *Soviet Physics-JETP*, vol. 5, pp. 1174–1182, 1957.

[47] L. P. Gor'kov, "Microscopic derivation of the ginzburg-landau equations in the theory of superconductivity," *Sov. Phys. JETP*, vol. 9, no. 6, pp. 1364–1367, 1959.

[48] M. Checchin, *Physics of limiting phenomena in superconducting microwave resonators: Vortex dissipation, ultimate quench and quality factor degradation mechanisms*. Illinois Institute of Technology, 2016.

[49] C. Bean and J. Livingston, "Surface barrier in type-II superconductors," *Physical Review Letters*, vol. 12, no. 1, p. 14, 1964.

[50] J. Matricon and D. Saint-James, "Superheating fields in superconductors," *Physics Letters A*, vol. 24, no. 5, pp. 241–242, 1967.

[51] D. Saint-James and P. d. Gennes, "Onset of superconductivity in decreasing fields," *Physics Letters*, vol. 7, no. 5, pp. 306–308, 1963.

[52] A. Abrikosov, "On the lower critical field of thin layers of superconductors of the second group," *Soviet Physics JETP*, vol. 19, pp. 988–991, 1964.

[53] G. Stejic, A. Gurevich, E. Kadyrov, D. Christen, R. Joynt, and D. Larbalestier, "Effect of geometry on the critical currents of thin films," *Physical Review B*, vol. 49, no. 2, p. 1274, 1994.

[54] A. Gurevich, "Maximum screening fields of superconducting multilayer structures," *AIP Advances*, vol. 5, no. 1, p. 017 112, 2015.

[55] P. Hasan, K. Jens, and H. Tom, "Rf superconductivity for accelerators," *New York. A Wiely-Interscience Publication*, pp. 129–144, 1998.

[56] W. Singer, A. Ermakov, and X. Singer, "RRR-measurement techniques on high purity niobium," *TTC report*, vol. 2, 2010.

[57] P. Bauer, T. Berenc, C. Boffo, *et al.*, "RRR measurements on niobium for superconducting RF cavities at fermilab," in *Proceedings of 11 th Workshop on RF superconductivity, Lübeck, Germany*, 2003.

[58] M. Hörmann, "Production of high thermal conductivity niobium on a technical scale for high-frequency superconductivity," *Journal of the Less Common Metals*, vol. 139, no. 1, pp. 1–14, 1988.

[59] H. Umezawa, "Impurities analysis of high purity niobium in industrial production," *Materiaux & Techniques*, vol. 91, no. 7-8-9, pp. 33–37, 2003.

[60] K. Saito *et al.*, "Critical field limitation of the niobium superconducting RF cavity," in *Proceedings of the 10th International Conference on RF Superconductivity, Tsukuba, Japan*, 2001.

[61] R.-L. Geng, H. Padamsee, A. Seaman, and V. D. Shemelin, "World record accelerating gradient achieved in a superconducting niobium RF cavity," in *Proceedings of the 2005 Particle Accelerator Conference*, IEEE, 2005, pp. 653–655.

[62] R. Geng, G. Eremeev, H. Padamsee, and V. Shemelin, "High gradient studies for ILC with single-cell re-entrant shape and elliptical shape cavities made of fine-grain and large-grain niobium," in *2007 IEEE Particle Accelerator Conference (PAC)*, IEEE, 2007, pp. 2337–2339.

[63] M. Vretenar, "A high-intensity H-linac at CERN based on LEP-2 cavities," *arXiv preprint physics/0008142*, 2000.

[64] P. Brown, O. C. Brunner, A. Butterworth, *et al.*, "Performance of the LEP200 superconducting RF system," CERN, Geneva, Tech. Rep., 1999. [Online]. Available: `https://cds.cern.ch/record/420404`.

[65] A. D'Elia, R. Jones, and M. Pasini, "HIE-ISOLDE high beta cavity study and measurements," *arXiv preprint arXiv:0910.0409*, 2009.

[66] P. Dhakal, G. Ciovati, and A. Gurevich, "Flux expulsion in niobium superconducting radio-frequency cavities of different purity and essential contributions to the flux sensitivity," *Physical Review Accelerators and Beams*, vol. 23, no. 2, p. 023 102, 2020.

[67] S. Posen, M. Checchin, A. Crawford, *et al.*, "Efficient expulsion of magnetic flux in superconducting radiofrequency cavities for high Q applications," *Journal of Applied Physics*, vol. 119, no. 21, 2016.

[68] M. Checchin, M. Martinello, A. Romanenko, *et al.*, "Quench-induced degradation of the quality factor in superconducting resonators," *Phys. Rev. Appl.*, vol. 5, p. 044 019, 4 Apr. 2016. DOI: 10.1103/PhysRevApplied.5.044019. [Online]. Available: https://link.aps.org/doi/10.1103/PhysRevApplied.5.044019.

[69] T. Kubo, "Flux trapping in superconducting accelerating cavities during cooling down with a spatial temperature gradient," *Progress of Theoretical and Experimental Physics*, vol. 2016, no. 5, 053G01, 2016.

[70] R. Appleby, G. Burt, J. Clarke, and H. Owen, *The science and technology of particle accelerators*. Taylor & Francis, 2020.

[71] A. Macpherson, R. Torres-Sanchez, C. Jarrige, *et al.*, "CERN's bulk niobium high gradient SRF programme: Developments and recent cold test results," 2015.

[72] M. Checchin and A. Grassellino, "High-field Q-slope mitigation due to impurity profile in superconducting radio-frequency cavities," *arXiv preprint arXiv:2005.05396*, 2020.

[73] P. G. De Gennes and J. Matricon, "Collective modes of vortex lines in superconductors of the second kind," *Reviews of Modern Physics*, vol. 36, no. 1, p. 45, 1964.

[74] A. Romanenko, F. Barkov, L. Cooley, and A. Grassellino, "Proximity breakdown of hydrides in superconducting niobium cavities," *Superconductor Science and Technology*, vol. 26, no. 3, p. 035 003, 2013.

[75] G. Ciovati, "Effect of low-temperature baking on the radio-frequency properties of niobium superconducting cavities for particle accelerators," *Journal of applied physics*, vol. 96, no. 3, pp. 1591–1600, 2004.

[76] A. Grassellino, A. Romanenko, D. Bice, *et al.*, "Accelerating fields up to 49 MV/m in TESLA-shape superconducting RF niobium cavities via 75C vacuum bake," *arXiv preprint arXiv:1806.09824*, 2018.

[77] A. Romanenko, A. Grassellino, F. Barkov, A. Suter, Z. Salman, and T. Prokscha, "Strong meissner screening change in superconducting radio frequency cavities due to mild baking," *Applied Physics Letters*, vol. 104, no. 7, p. 072 601, 2014.

[78] T. Kubo, "Multilayer coating for higher accelerating fields in superconducting radio-frequency cavities: A review of theoretical aspects," *Superconductor Science and Technology*, vol. 30, no. 2, p. 023 001, 2016.

[79] T. Wang, C. Reece, and R. Sundelin, "DC field emission studies on Nb," Thomas Jefferson National Accelerator Facility, Newport News, VA (US), Tech. Rep., 2001.

[80] C. Durand, W. Weingarten, P. Bosland, and J. Mayer, "Non quadratic RF losses in niobium sputter coated accelerating structures," *IEEE Transactions on Applied Superconductivity*, vol. 5, no. 2, pp. 1107–1110, 1995. DOI: 10.1109/77.402745.

[81] C. Pira, C. Antoine, A. Katasevs, *et al.*, "Evaluation of cleaning process, ARIES delivery report D15.1," *Horizon 2020 Research Infrastructures*, 2018. [Online]. Available: available%20at:%20https://%20edms.cern.ch/document/1820617/1.0 (visited on 03/14/2022).

[82] C. Pira, C. Antoine, E. Chyhyrynets, *et al.*, "Impact of the Cu substrate surface preparation on the morphological, superconductive and RF properties of the nb superconductive coatings," *in Proceedings of SRF*, 2019.

[83] D. Turner and et al, "Magnetic field penetration of niobium thin films produced by the ARIES collaboration," in *Proc. SRF 2021*, 2021, SUPFDV007.

[84] C. Benvenuti, S. Calatroni, I. Campisi, *et al.*, "Study of the surface resistance of superconducting niobium films at 1.5 GHz," *Physica C: Superconductivity*, vol. 316, no. 3, pp. 153–188, 1999, ISSN: 0921-4534. DOI: https://doi.org/10.1016/S0921-4534(99)00207-5. [Online]. Available: https://www.sciencedirect.com/science/article/pii/S0921453499002075.

[85] A. Cubero, E. Martinez, L. A. Angurel, *et al.*, "Effects of laser-induced periodic surface structures on the superconducting properties of niobium," *Applied surface science*, vol. 508, p. 145 140, 2020.

[86] L. Zhao, J. M. Klopf, C. E. Reece, and M. J. Kelley, "Laser polishing for topography management of accelerator cavity surfaces: Laserpolieren als topographiemanagement zur schnellen herstellung von oberflächen mit mulden," *Materialwissenschaft und Werkstofftechnik*, vol. 46, no. 7, pp. 675–685, 2015.

[87] A. Medvids, P. Onufrijevs, J. Kaupuzs, *et al.*, "Improvement of Nb/Cu adhesion and increase of Nb crystal size by laser radiation," *Applied Surface Science*, vol. 525, p. 146 528, 2020.

[88] E. Radicioni, C. Benvenuti, M. Bianconi, and L. Correra, "Laser annealing of Nb coatings for superconducting RF accelerating cavities," *Nuclear Instruments and Methods in Physics Research Section A: Accelerators, Spectrometers, Detectors and Associated Equipment*, vol. 365, no. 1, pp. 28–35, 1995.

[89] Y. Yang, X. Lu, W. Tan, L. Xiao, L. Zhu, and D. Xie, "Study on laser annealing of niobium films deposited on copper for RF superconducting cavities," *Nuclear Instruments and Methods in Physics Research Section A: Accelerators, Spectrometers, Detectors and Associated Equipment*, vol. 964, p. 163 803, 2020.

[90] R. Ries, E. Seiler, F. Gömöry, A. Medvids, C. Pira, and O. Malyshev, "Superconducting properties and surface roughness of thin Nb samples fabricated for SRF applications," in *Journal of Physics: Conference Series*, IOP Publishing, vol. 1559, 2020, p. 012 040.

[91] R. Ries, E. Seiler, F. Gömöry, *et al.*, "Improvement of the first flux entry field by laser post-treatment of the thin Nb film on Cu," *Superconductor Science and Technology*, vol. 34, no. 6, p. 065 001, 2021.

[92] S. Posen, J. Lee, D. N. Seidman, *et al.*, "Advances in Nb3Sn superconducting radiofrequency cavities towards first practical accelerator applications," *Superconductor Science and Technology*, vol. 34, no. 2, p. 025 007, 2021.

[93] S. Keckert, T. Junginger, T. Buck, *et al.*, "Critical fields of Nb3Sn prepared for superconducting cavities," *Superconductor Science and Technology*, vol. 32, no. 7, p. 075 004, 2019.

[94] S. Foner, "Versatile and sensitive vibrating-sample magnetometer," *Review of Scientific Instruments*, vol. 30, no. 7, pp. 548–557, 1959.

[95] J. Clarke and A. I. Braginski, *The SQUID handbook*. Wiley Online Library, 2004, vol. 1.

[96] C. Böhmer, G. Brandstätter, and H. Weber, "The lower critical field of high-temperature superconductors," *Superconductor Science and Technology*, vol. 10, no. 7A, A1, 1997.

[97] E. H. Brandt, "Superconductors in realistic geometries: Geometric edge barrier versus pinning," *Physica C: Superconductivity*, vol. 332, no. 1-4, pp. 99–107, 2000.

[98] S. Candia and L. Civale, "Angular dependence of the magnetization of isotropic superconductors: Which is the vortex direction?" *Superconductor Science and Technology*, vol. 12, no. 4, p. 192, 1999.

[99] S. Roy, G. Myneni, and V. Sahni, "On the reliable determination of the magnetic field for first flux-line penetration in technical niobium material," *Superconductor Science and Technology*, vol. 21, no. 6, p. 065 002, 2008.

[100] A. Zhukov, G. Perkins, Y. V. Bugoslavsky, and A. Caplin, "Geometrical locking of the irreversible magnetic moment to the normal of a thin-plate superconductor," *Physical Review B*, vol. 56, no. 5, p. 2809, 1997.

[101] A. S. Dhavale, P. Dhakal, A. A. Polyanskii, and G. Ciovati, "Flux pinning characteristics in cylindrical niobium samples used for superconducting radio frequency cavity fabrication," *Superconductor Science and Technology*, vol. 25, no. 6, p. 065 014, 2012.

[102] O. Malyshev, L. Gurran, R. Valizadeh, *et al.*, "First results of magnetic field penetration measurements of multilayer SIS structures," 2016.

[103] O. B. Malyshev, L. Bizel-Bizellot, K. Dumbell, *et al.*, "Design, assembly and commissioning of a new cryogenic facility for complex superconducting thin film testing," in *Proc. 9th Int. Particle Accelerator Conf.(IPAC'18)*, 2018, pp. 3859–3861.

[104] C. Antoine, M. Aburas, A. Four, *et al.*, "Progress on characterization and optimization of multilayers," in *Proc. 18th Int. on RF Superconductivity Conf.(SRF'17)*, 2017, pp. 368–373.

[105] H. Ito, H. Hayano, T. Kubo, and T. Saeki, "Lower critical field measurement system based on third-harmonic method for superconducting RF materials," *arXiv preprint arXiv:1906.08468*, 2019.

[106] R. Katayama, Y. Iwashita, H. Tongu, *et al.*, "Evaluation of superconducting characteristics on the thin-film structure by NbN and insulator coatings on pure Nb substrate," in *Proc. 9th Int. Particle Accelerator Conf.(IPAC'18)*, 2018, pp. 3653–3655.

[107] R. Katayama, Y. Iwashita, H. Tongu, *et al.*, "Precise evaluation of characteristic of the multi-layer thin-film superconductor consisting of NbN and insulator on pure Nb substrate," in *Proc. 29th Linear Accelerator Conf.(LINAC'18)*, 2019, pp. 391–394.

[108] N. Katyan and C. Antoine, "Characterization of thin films using local magnetometer," Tech. Rep., 2015.

[109] C. Z. Antoine, M. Aburas, A. Four, *et al.*, "Optimization of tailored multilayer superconductors for RF application and protection against premature vortex penetration," *Superconductor Science and Technology*, vol. 32, no. 8, p. 085 005, 2019.

[110] I. Senevirathne, A. Gurevich, and J. Delayen, "Direct current magnetic hall probe technique for measurement of field penetration in thin film superconductors for superconducting radio frequency resonators," *Review of Scientific Instruments*, vol. 93, no. 5, p. 055 104, 2022.

[111] S. Wilde, R. Valizadeh, O. Malyshev, G. Stenning, T. Sian, and B. Chesca, "DC magnetometry of niobium thin film superconductors deposited using high power impulse magnetron sputtering," *Physical Review Accelerators and Beams*, vol. 21, no. 7, p. 073 101, 2018.

[112] S. Senoussi, "Review of the critical current densities and magnetic irreversibilities in high Tc superconductors," *Journal de physique III*, vol. 2, no. 7, pp. 1041–1257, 1992.

[113] R. French, "Intrinsic type-2 superconductivity in pure niobium," *Cryogenics*, vol. 8, no. 5, pp. 301–308, 1968.

[114] H. Hart Jr and P. Swartz, "Studies of surface transport currents in type-II superconductors; a surface-flux-pinning model," *Physical Review*, vol. 156, no. 2, p. 403, 1967.

[115] C. Furtado, "DC magnetization measurements on pure niobium," *Cryogenics*, vol. 13, no. 11, pp. 639–643, 1973.

[116] B. Walton, B. Rosenblum, and F. Bridges, "Nucleation of vortices in the superconducting mixed state: Nascent vortices," *Physical Review Letters*, vol. 32, no. 19, p. 1047, 1974.

[117] B. Mangum, "Determination of the indium freezing-point and triple-point temperatures," *Metrologia*, vol. 26, no. 4, p. 211, 1989.

[118] *High linearity hall probe for room and cryogenic temperatures*, 2625, Electrical specifications of the Hall probe, Arepoc s.r.o., 2020.

[119] *High linearity hall probe for room and cryogenic temperatures*, 2395, Electrical specifications of the Hall probe, Arepoc s.r.o., 2020.

[120] *High linearity hall probe for room and cryogenic temperatures*, 2205, Electrical specifications of the Hall probe, Arepoc s.r.o., 2020.

[121] *High linearity hall probe for room and cryogenic temperatures*, 2207, Electrical specifications of the Hall probe, Arepoc s.r.o., 2020.

[122] *A new cryogenic diode thermometer*, DT-600, Lakeshore cryotronics.

[123] C. Lin, X. Wei-Ping, L. Ming-Yang, *et al.*, "Development of high purity niobium used in SRF accelerating cavity," *Chinese Physics C*, vol. 32, no. 12, p. 1003, 2008.

[124] MATLAB. "Gradient." Accessed: 17 January 2021. (), [Online]. Available: %5Curl%7Bhttps://uk.mathworks.com/help/matlab/ref/gradient.html#bvhp8_m%7D.

[125] MATLAB. "Filtering and smoothing data." Accessed: 17 January 2021. (), [Online]. Available: %5Curl%7Bhttps://uk.mathworks.com/help/curvefit/smoothing-data.html#bq_6ys3-8%7D.

[126] J. Jackson, Private Communication, 2024.

[127] A. Das Gupta, W. Gey, J. Halbritter, H. Küpfer, and J. Yasaitis, "Inhomogeneities in superconducting niobium surfaces," *Journal of Applied Physics*, vol. 47, no. 5, pp. 2146–2153, 1976.

[128] M. Krishnan, E. Valderrama, B. Bures, *et al.*, "Very high residual resistivity ratios of heteroepitaxial superconducting niobium films on MgO substrates," *Superconductor Science and Technology*, vol. 24, no. 11, p. 115 002, 2011.

[129] A. Mayadas, R. Laibowitz, and J. Cuomo, "Electrical characteristics of RF-sputtered single-crystal niobium films," *Journal of Applied Physics*, vol. 43, no. 3, pp. 1287–1289, 1972.

[130] J. Sosniak and G. Hull Jr, "Superconductivity of niobium thin films deposited by DC diode sputtering," *Journal of Applied Physics*, vol. 38, no. 11, pp. 4390–4392, 1967.

[131] A. Valente-Feliciano, H. Phillips, C. Reece, *et al.*, "RF and structural characterization of SRF thin films," 2010.

[132] R. Russo, L. Catani, A. Cianchi, S. Tazzari, and J. Langner, "High quality superconducting niobium films produced by an ultra-high vacuum cathodic arc," *Superconductor Science and Technology*, vol. 18, no. 7, p. L41, 2005.

[133] J. Langner, M. J. Sadowski, P. Strzyzewski, *et al.*, "Purity of Nb and Pb films deposited by an ultrahigh vacuum cathodic arc," *IEEE transactions on plasma science*, vol. 35, no. 4, pp. 1000–1003, 2007.

[134] S. Wolf, S. Qadri, J. Claassen, T. Francavilla, and B. Dalrymple, "Epitaxial growth of superconducting niobium thin films by ultrahigh vacuum evaporation," *Journal of Vacuum Science & Technology A: Vacuum, Surfaces, and Films*, vol. 4, no. 3, pp. 524–527, 1986.

[135] S. Morohashi, N. Takeda, S. Tsujimura, *et al.*, "Characteristics of superconducting Nb layer fabricated using high-vacuum electron beam evaporation," *Japanese Journal of Applied Physics*, vol. 40, no. 2R, p. 576, 2001.

[136] S. Calatroni, R. Cosso, J. Bacher, *et al.*, "Influence of copper substrate treatments on properties of niobium coatings," P00019441, Tech. Rep., 1993.

[137] I. H. Senevirathne, "Measurements of magnetic field penetration of materials for superconducting radiofrequency cavities," 2023.

[138] O. Kugeler, D. Tikhonov, O. Malyshev, *et al.*, "Evaluation of system 3 and SIS, ARIES delivery report D15.3," *Horizon 2020 Research Infrastructures*, 2020. [Online]. Available: `available%20at:%20https://edms.cern.ch/document/1820619/1.0` (visited on 06/10/2022).

[139] D. A. Turner, O. B. Malyshev, G. Burt, T. Junginger, R. Valizadeh, and L. Gurran, "A facility for the characterisation of planar multilayer structures with preliminary niobium results," *Superconductor Science and Technology*, 2022.

[140] A. Medvid and P. M. Lytvyn, "Dynamic of laser ablation in SiC," in *Silicon Carbide and Related Materials 2003*, ser. Materials Science Forum, vol. 457, Trans Tech Publications Ltd, Jun. 2004, pp. 411–414. DOI: `10.4028/www.scientific.net/MSF.457-460.411`.

[141] O. H. Siegmund, "7. amplifying and position sensitive detectors," in *Experimental Methods in the Physical Sciences*, vol. 32, Elsevier, 1998, pp. 139–175.

[142] S. Posen and D. L. Hall, "Nb3Sn superconducting radiofrequency cavities: Fabrication, results, properties, and prospects," *Superconductor Science and Technology*, vol. 30, no. 3, p. 033 004, 2017.

[143] W. Schneider, P. Kneisel, and C. Rode, "Gradient optimization for SC CW accelerators," in *Proceedings of the 2003 Particle Accelerator Conference*, IEEE, vol. 5, 2003, pp. 2863–2868.

[144] G. Ciovati, J. Anderson, B. Coriton, *et al.*, "Design of a CW, low-energy, high-power superconducting linac for environmental applications," *Phys. Rev. Accel. Beams*, vol. 21, p. 091 601, 9 Sep. 2018. DOI: `10.1103/PhysRevAccelBeams.21.091601`. [Online]. Available: `https://link.aps.org/doi/10.1103/PhysRevAccelBeams.21.091601`.

[145] R. C. Dhuley, R. Kostin, O. Prokofiev, *et al.*, "Thermal link design for conduction cooling of SRF cavities using cryocoolers," *IEEE Transactions on Applied Superconductivity*, vol. 29, no. 5, pp. 1–5, 2019. DOI: `10.1109/TASC.2019.2901252`.

[146] M. Peiniger, M. Hein, N. Klein, G. Müller, H. Piel, and P. Thuenus, "Work on Nb3Sn cavities at wuppertal (no," ANL-PHY–88-1-VOL, Tech. Rep., 1988.

[147] E. Saur and J. Wurm, "Präparation und supraleitungseigenschaften von niobdrahtproben mit nb3sn-überzug," *Naturwissenschaften*, vol. 49, no. 6, pp. 127–128, 1962.

[148] B. Hillenbrand and H. Martens, "Superconducting Nb3Sn cavities with high quality factors and high critical flux densities," *Journal of Applied Physics*, vol. 47, no. 9, pp. 4151–4155, 1976.

[149] G. V. Eremeev, M. J. Kelley, C. E. Reece, U. Pudasaini, and J. Tuggle, "Progress with multi-cell Nb3Sn cavity development linked with sample materials characterization," Thomas Jefferson National Accelerator Facility (TJNAF), Newport News, VA ..., Tech. Rep., 2015.

[150] A. Valente-Feliciano, G. Eremeev, H. Phillips, *et al.*, "NbTiN based SIS multilayer structures for SRF applications," *TUP088 SRF*, pp. 664–667, 2013.

[151] L. Toth, *Transition metal carbides and nitrides*. Elsevier, 2014.

[152] M. C. Burton, M. R. Beebe, K. Yang, R. A. Lukaszew, A.-M. Valente-Feliciano, and C. Reece, "Superconducting NbTiN thin films for superconducting radio frequency accelerator cavity applications," *Journal of Vacuum Science & Technology A: Vacuum, Surfaces, and Films*, vol. 34, no. 2, p. 021 518, 2016.

[153] I. G. Díaz-Palacio, R. Blick, W. Hillert, M. Wenskat, and R. Zierold, "ALD-Based NbTiN Studies for SIS R&D," in *Proc. IPAC'21*, (Campinas, SP, Brazil), ser. International Particle Accelerator Conference, https://doi.org/10.18429/JACoW-IPAC2021-THPAB320, JACoW Publishing, Geneva, Switzerland, Aug. 2021, THPAB320, pp. 4420–4421, ISBN: 978-3-95450-214-1. DOI: 10.18429/JACoW-IPAC2021-THPAB320. [Online]. Available: https://jacow.org/ipac2021/papers/thpab320.pdf.

[154] A. Klimov, W. Słysz, M. Guziewicz, V. Kolkovsky, I. Zaytseva, and A. Malinowski, "Characterization of the critical current and physical properties of superconducting epitaxial nbtin sub-micron structures," *Physica C: Superconductivity and its Applications*, vol. 536, pp. 35–38, 2017.

[155] T. Shiino, S. Shiba, N. Sakai, *et al.*, "Improvement of the critical temperature of superconducting NbTiN and NbN thin films using the AlN buffer layer," *Superconductor Science and Technology*, vol. 23, no. 4, p. 045 004, 2010.

[156] O. Malyshev, L. Smith, D. Seal, and G. Burt, Private Communication, 2024.

[157] P. Goudket, T. Junginger, and B. Xiao, "Devices for SRF material characterization," *Superconductor Science and Technology*, vol. 30, no. 1, p. 013 001, 2016.